Quasifree Knockout of Charged Particles from ^{4}He with 100 MeV Protons

D. M. Whittal

A thesis submitted in partial fulfilment of the requirements
for the degree of Doctor of Philosophy
in the Department of Physics
University of Cape Town

October 1989

Quasifree Knockout of Charged Particles from ^{4}He with 100 MeV Protons

David Mark Whittal

National Accelerator Centre, P.O.Box 72, Faure, 7131, South Africa

October 1989

Abstract

Exclusive measurements have been made of the reactions ^{4}He(p,2p), (p,pd), (p,pt) and (p,ph) at 100 MeV. The primary protons were measured at two angles, 45° and 60°, in coincidence with secondary protons, deuterons, tritons or helions covering a wide range of angles on the opposite side of the beam, from $-15°$ to $-90°$ in plane, and from 0° to 30° out-of-plane.

The purpose of the experiment was to explore the validity of the Distorted Wave Impulse Approximation (DWIA) as a description of these quasifree knockout reactions, at all geometries where the knockout cross section is significant.

Six particle telescopes, each consisting of two silicon detectors and a NaI detector, were used to measure the coincident particles. The experimental data are presented in the form of energy-sharing distributions, which were generated by projecting the two-dimensional quasifree knockout loci onto the energy axis of the primary proton.

The comparison between these energy-sharing distributions and the curves calculated by means of the DWIA is satisfactory for all geometries, except at the most forward secondary angles for the (p,pt) and (p,ph) reactions. It is concluded that the DWIA is an adequate formalism for modelling the quasifree knockout reactions induced by 100 MeV protons on ^{4}He.

Based on this conclusion, the total contribution of quasifree knockout to the existing *inclusive* (p,p′) spectra has been calculated by integrating the DWIA cross sections over the solid angles of the secondary particles. The spectroscopic factors used were those extracted from the coincidence data. For the (p,pn) reaction, it was assumed that the spectroscopic factors were the same as for (p,2p).

It is found that $70 \pm 10\%$ of the inclusive continuum yields is attributable to quasifree scattering, with ~30% arising from multiple scattering. At low energies of the scattered proton, the knockout of nucleons constitutes over 90% of the quasifree component, whereas at high energies the knockout of deuterons, tritons and helions dominates the yield. Thus the absence of discernable quasifree peaks in the inclusive spectra is probably due to the cluster knockout contributions filling in the yield at higher energies.

Acknowledgements

I am extremely grateful to Dr Anthony Cowley for his imaginative supervision of this work. Not only has he taught me a great deal of physics, but he has also demonstrated, by frequent example, the value of a tenacious approach to research.

I thank my university supervisor, Professor F. D. Brooks, for originally stimulating my interest in nuclear physics, and for his continued encouragement over the years.

The assistance of my colleagues, Dr John Pilcher, Dr Ricky Smit and Siegfried Förtsch in running the experiment is gratefully acknowledged. I am particularly indebted to John Pilcher, who was never too busy to help me with my computing problems. Also, the fact that he trod the thesis path just a few months ahead of me was of immense benefit.

My thanks go to Charles Stevens for the great effort he put into getting the hardware ready on time, and for drawing some of the figures in this thesis.

I am also grateful to Dr Adriaan Botha and the cyclotron operators for reliable proton beams; to my colleague, Dr Kobus Lawrie, for explaining some of the intricacies of the theoretical calculations; to Charles Wikner for his efficient maintenance of the electronic equipment; to Dick Raavé for assembling the gas handling system; and to Annamarie de Goede for her assistance with the typing.

Many other people at the National Accelerator Centre contributed towards the completion of this thesis, and I express my gratitude to them all.

Thanks also go to Professor David Aschman of the University of Cape Town for arranging the remote computing facilities.

I am deeply appreciative of the support I have received from my wife Alix, who has single-handedly run the home for so many months, put up with my moodiness, and endured a miserable social life. I am also grateful to my friends, Bill and Julie, for their support and encouragement, and to my mother for the faith which she has always maintained in my ability.

Finally I thank my son Louis for reminding me daily that life can be fun too.

Contents

List of Figures

List of Tables

Chapter 1

Introduction

1.1 Quasifree Scattering

Some of the most useful models in nuclear physics are those which simplify a problem by relating it to concepts with which we are already familiar. It is reassuring, for example, to discover that some of the elementary principles of optics are applicable to nuclear scattering, or that particle emission from a compound nucleus is analogous to evaporation from a hot body.

The seeking of appropriate analogies continues within the confines of nuclear physics itself. The quasifree scattering model [Wol52], for instance, assists us by relating certain scattering problems in which there are three particles in the final state, to the simpler two-body picture.

Thus quasifree scattering may be defined as the interaction between an incident projectile and a nucleon (or cluster of nucleons) in a target nucleus, which proceeds in an analogous way to free scattering; the remaining "spectator" nucleons in the nucleus have negligible influence on the direct interaction itself [Tyr66], although they may distort the incident or scattered waves.

For many years it has been known that this simplistic picture provides a satisfactory framework for modelling knockout reactions at medium energies (the most recent review is by Kitching *et al.* [Kit85]).

Historically, the main interest in proton-induced knockout reactions such as (p,2p) and (p,pn) has been in the investigation of single-particle states through the extraction of distorted momentum distributions [Jac66]. Similarly, the knockout of composite particles, particularly α-particles, has been used to study the cluster parentage of nuclei (for example, [Roo76] [Roo77a] [Sam82] [Car84]).

Unlike pickup reactions, quasifree knockout reactions have the advantage of being able to remove nucleons with low nuclear momentum from inner shells, as the production of three particles in the final state allows for

less restrictive momentum matching.

The quasifree model is expressed theoretically in the Distorted Wave Impulse Approximation (DWIA) [Jac65] [Jac76], and has usually been applied to situations in which the kinematics have been carefully chosen to probe the desired momentum range of the single-particle states being studied, while staying within bounds which ensure the validity of the various approximations (for example, [Tyr66] [Hou71] [Bho76] [Dev79] [Kit80] [Sam86]).

Reasonable agreement in shape has been found between measured distorted momentum distributions and theoretical calculations, but it has not been possible to extract very reliable spectroscopic factors, which is hardly surprising for reactions containing strong (hadronic) distortions in the entrance channel and in both exit channels.

Recently, there has been a rapid improvement [Fru84] [Den88] [Kra89] in the ability to extract similar information on nuclear structure from the (e,e'p) reaction, which is inherently superior for this purpose in that the only important distortions are for the single outgoing proton. With the advent [Fru84] of high-duty-factor electron accelerators, the major drawback of small reaction cross sections is being eliminated.

It is interesting to note, however, that a better description of the (e,e'p) reaction requires a thorough understanding [Den88] [Gee89] [Mag89] of the hadronic final state interaction, which can be gained partly from complementary proton-induced reactions [Tak89]. Furthermore, it has recently been shown [Pun88] that for light targets, a carefully executed (p,2p) experiment can provide data of comparable quality to that obtainable with electron beams.

In the meantime, a keen interest has evolved in proton-induced quasifree scattering from a reaction dynamics point of view. This has its roots in

several aspects of the phenomenon:

1. The extent to which the signature of quasifree scattering is seen in inclusive measurements of proton continuum spectra is the subject of some debate. These measurements are discussed more fully in the next section.

2. Considerable progress has been made with the notion that the first step in any reaction leading to the continuum consists of a quasifree scattering, either as a pure knockout or as a doorway [Ale80] to more complex processes. One approach which works well [Cow80a] [Cia83] [Cia84a] [Cow88] [Pil89b] is to treat the first step as a quasifree reaction, followed by inelastic scattering of the struck nucleon, which behaves as an intranuclear projectile incident on the residual nucleus.

   Further support for the quasifree doorway interpretation of continuum processes comes from Anderson *et al.* [And81] [Kal83], who found that the inclusive proton and neutron spectra from 90 MeV protons on various targets are similar in shape, and that the ratio of (p,p′) to (p,n) cross sections is very close to what one might expect for N-N scattering.

3. The impressive successes of the DWIA in reproducing angular correlation and energy-sharing distributions over a wide range of energies and target masses have encouraged refinements to the formalism and the inevitable temptation to test it to the limits of its range of applicability. Thus some measurements have been made for geometries [Kit80] [Cow89] and energies [Sam86] [Kud88] at which the DWIA is not expected to describe the quasifree reaction accurately, which in turn should lead to further theoretical stimulus.

Currently, there is a pressing need to determine just how far one may reliably use the model: firstly, estimates of the quasifree component in inclusive spectra rely on integrating over that part of phase space of the unobserved particle which might be expected to contribute to the yield. Thus one requires an accurate description of the distorted momentum distributions out to at least 200 MeV/c, and also knowledge of the off-shell behaviour of the two-body interaction at extreme geometries. Secondly, for studies in which the quasifree reaction is assumed to create a doorway state leading to more complex processes, the kinematic conditions required in the model [Cia84b] need to span regions of phase space which have not yet been studied explicitly under controlled (kinematically complete) conditions.

4. The continuum background underlying collective states such as Gamow-Teller and giant resonances limits the accuracy to which the strengths of these states may be determined [Spe81]. An understanding of the reaction mechanisms leading to continuum excitations is thus vital for the proper subtraction of the background. This problem appears to pose more of a challenge than was first envisaged, because of recent indications [Yoo89] of coherent interference between the amplitudes of giant resonances and quasifree scattering.

5. One of the limitations in the use of these reactions for extracting nuclear structure information is their sensitivity [Red70] [Jac73] to off-shell effects; this makes them the ideal vehicle [Roo87] for investigating the fundamental nucleon-nucleon interaction in the presence of a modifying nuclear medium.

In this study, we shall address some of the issues pertinent to points 1 and 3, i.e. the origin of inclusive proton spectra, and the range of applica-

bility of the DWIA.

1.2 Inclusive Spectra

Inclusive proton spectra at medium energies are characterized by three regions: at low energy, there is a broad bump due to evaporation from a fully equilibrated compound nucleus; at the highest energies, there are the sharp discrete states and the broader collective resonances; and in between lies the "continuum" or "preequilibrium" region of the spectra (see, for example, [Ber73]).

For incident energies above a few tens of MeV, the continuum contains most of the inclusive yield [Ber73], yet an understanding of the physics leading to continuum emission is not as well in hand as it is for the regions on either side of it. This is not surprising, since the continuum exhibits characteristics of both extremes. Forward-peaked emission of high-energy particles (as for direct reactions) implies that equilibrium statistical approaches are invalid, yet the mechanisms are obviously more complicated than in single-step direct reactions.

Most of the theoretical approaches to the problem [Bla75] [Mac85] [Gru86] have envisaged continuum emission as resulting from a sequence of particle-hole excitations, with a certain probability of emission after each step. The semiclassical exciton model [Gri66] is the best known of these and it has enjoyed a fair amount of success [Mac85] in describing certain types of continuum spectra, as has [Gru86] [Tra89] the quantum statistical formalism of Feshbach, Kerman and Koonin [Fes80].

The quasifree model, on the other hand, is appealingly simple in that it describes only that part of the continuum which arises from single-step processes. In the modelling of inclusive spectra, its usefulness thus depends

on what proportion of the yield is composed of single-step events ("quasifree scattering"), as opposed to multistep events ("multiple scattering").

The answer to this question for incident energies of 100–200 MeV has turned out to be rather elusive in the light of contradictory experimental evidence over the last twenty-odd years.

Naïvely, one might expect [Jac66] the problem to be very simple: as this type of quasifree scattering is essentially nucleon-nucleon scattering, with one of the nucleons bound in the nucleus, one would expect to see a peak in the inclusive spectra which moves with N-N kinematics, but is broadened by the momentum distribution of the struck nucleon. The strength of this quasifree peak would thus quantify the contribution of quasifree scattering to the continuum spectra.

However, calculations of the inclusive yield due to quasifree scattering do not always predict a noticeable quasifree peak [And81] [Kal83]; thus the failure to observe a strong quasifree peak does not necessarily mean that the reaction mechanism is dominated by multiple scattering. On the other hand, the observation of a strong quasifree peak which moves with N-N kinematics must indicate the presence of single-step processes.

Consequently, when Wall and Roos [Wal66] observed strong quasifree peaks in (p,p′) spectra at 160 MeV, they claimed that the continuum was dominated by quasifree scattering at that energy. Subsequently, other experiments [Che81] [Seg82] [Mac84] contradicted these results and it is now generally believed that the earlier results were in error.

Segel *et al.* [Seg82] [Seg85] measured featureless continuum spectra for ^{58}Ni at 150 MeV, even at forward angles, whereas other measurements [Wu79] [Cow80b] have yielded quasifree peaks for the same target at lower energies (90 and 100 MeV), which should be less likely. Nevertheless, they did see quasifree peaks for lighter targets, which is confirmed by Förtsch

et al. [För88] who found quasifree peaks from ^{12}C(p,p′) at both 90 and 200 MeV.

Below 60 MeV, distortion effects seem to be severe enough [Ber73] to obscure the signature of quasifree scattering altogether.

In an attempt to clarify the importance of quasifree scattering around 100 MeV, Wesick *et al.* [Wes85] measured cross sections and analyzing powers from the reactions ^{2}H, ^{3,4}He(p,p′) and ^{3,4}He(p,d) for 100 and 150 MeV protons. They chose light targets in order to minimize the contributions of multiple scattering to the continuum yields and to remove most of the contributions from evaporation at low energies, and from collective states at high energies of the outgoing protons.

They found quasifree peaks which tracked with N-N kinematics in the yields from the ^{2}H and ^{3}He targets, but in the case of ^{4}He, there was no clear quasifree peak, which disagreed with their DWIA calculations.

Analyzing power data were also taken, but these were not as fruitful as had been hoped in distinguishing quasifree scattering from multiple scattering contributions, because the expected multiple scattering signature of small analyzing power at low outgoing energy was also predicted by the DWIA calculations for the one-step process.

These results are discussed further in Section 1.4, where we explain the purpose of the present measurements, but first we need to set down the rudiments of the DWIA.

1.3 The Distorted Wave Impulse Approximation

In order to simplify the theoretical description of quasifree knockout reactions, it is necessary to develop the distorted wave formalism within the

impulse approximation [Che50] [Tyr66], which is chiefly the assumption that the momentum of the recoiling residual nucleus is just the opposite of the momentum which the struck particle had in its bound state at the time of the interaction. In other words the residual nucleus is merely a "spectator" to the knockout process, and its presence is only felt indirectly via the distorting optical potentials for the initial and final scattering states, and in the binding energy of the struck particle, which causes the N-N interaction to be half off-the-mass-shell.

Thus, the knockout cross section is roughly proportional to the product of the N-N cross section and the momentum distribution of the struck nucleon in the target nucleus [Jac65] [Jac66] [Jac73]:

$$\frac{d^3\sigma}{d\Omega_1 d\Omega_2 dE_1} \propto \frac{d\sigma}{d\Omega}_{NN} \times |\phi(\vec{q})|^2 \tag{1.1}$$

where $\vec{q}$ is the bound state momentum of the struck nucleon. It is this simplified picture which makes the quasifree knockout reaction a useful tool for studying nuclear structure.

Since the mean free path of medium-energy protons in nuclei decreases with decreasing energy, the impulse approximation is expected to break down at low energies [Jac66]. Although incident energies > 200 MeV have been recommended [Tyr66] [Kit85] for using this approximation "safely", many satisfactory comparisons have been made with lower-energy data.

We have used the computer program THREEDEE [Cha82] for the DWIA calculations which we describe in Chapter 4. As the theoretical basis of this program is prominently documented [Cha77] [Cha79] [Cha83], we shall give only a brief description here.

We consider a (p,2p) reaction denoted by $A(a,cd)B$ where $A = B + b$. The differential cross section is given by

$$\sigma_{BA} = \frac{2\pi}{\hbar v}|T_{BA}|^2 \omega_B$$

where v is the relative velocity of a and A in the entrance channel, T_{BA} is the reduced transition amplitude and ω_B is the phase space factor.

Applying the factorization approximation, which requires [Cha77] the effect of the distorting potentials on the two-body (N-N) interaction to be negligible, we may write (for an unpolarized beam)

$$|T_{BA}|^2 = C^2S \sum_{\rho_a\rho'_c\rho''_d JM} \frac{1}{(2J+1)(2S_a+1)} \Big| \sum_{\sigma_a\sigma'_c\sigma''_d\Lambda\sigma_b} (2L+1)^{\frac{1}{2}}(L\Lambda S_b\sigma_b|JM) \times T^{L\Lambda}_{\sigma_a\sigma'_c\sigma''_d\rho_a\rho'_c\rho''_d}\langle\sigma'_c\sigma''_d|t|\sigma_a\sigma_b\rangle\Big|^2,$$

where C^2S is the spectroscopic factor for the final state in B, L is the relative angular momentum (projection Λ) of b and B, J is the angular momentum (projection M) of the target, S_i are the spins, with projections ρ_i and σ_i for particles i (as defined by Chant and Roos [Cha83]), t is the two-body operator for the free N-N scattering process (by the impulse approximation), and the primes indicate quantities which are expressed with respect to different sets of axes, as follows: the unprimed $\hat{z}$-axis is along the beam direction, whereas the $\hat{z}'$- and $\hat{z}''$-axes are in the directions of propagation of particles c and d respectively.

The quantity $T^{L\Lambda}$ is defined by

$$T^{L\Lambda}_{\sigma_a\sigma'_c\sigma''_d\rho_a\rho'_c\rho''_d} = (2L+1)^{-\frac{1}{2}} \int \chi^{(-)*}_{\sigma'_c\rho'_c}(\vec{r}')\chi^{(-)*}_{\sigma''_d\rho''_d}(\vec{r}'')\phi_{L\Lambda}(\vec{r})\chi^{(+)}_{\sigma_a\rho_a}(\gamma\vec{r})d\vec{r}, \quad (1.2)$$

where the χ_{ij} are distorted waves, ϕ is the spatial part of the bound state wave function of particle b, and $\gamma = B/A$.

The conventional approach would now be to expand the distorted wave integral in a linear combination of one-dimensional integrals. As the name of the program implies, however, THREEDEE performs a direct Gaussian integration of Equation 1.2. Typically less than 20 Gaussian points are needed (in each dimension) for convergence [Cha83], which results in substantial savings in computing time.

The final result for the triple differential cross section is thus

$$\frac{d^3\sigma}{d\Omega_c d\Omega_d dE_c} = C^2S\,K \sum_{\rho_a\rho'_c\rho''_d JM} \Big| \sum_{\sigma_a\sigma_c\sigma'_c\sigma_d\sigma''_d\sigma_b\Lambda} (L\Lambda S_b\sigma_b|JM) \times D^{(1/2)*}_{\sigma_c\sigma'_c}(R_{ac})\, D^{(1/2)*}_{\sigma_d\sigma''_d}(R_{ad})\, T^{L\Lambda}_{\sigma_a\sigma'_c\sigma''_d\rho_a\rho'_c\rho''_d} \times \langle\sigma_c\sigma_d|t|\sigma_a\sigma_b\rangle\Big|^2, \quad (1.3)$$

where K is a kinematic factor (also containing constant terms which drop out of the summations for a specific final state in B), the D_{mn} are rotation matrices, and the R_{aj} are rotations of the sets of axes which were defined for particle j into the set of axes for particle a.

The half off-shell two-body t matrix is approximated by interpolation of on-shell nucleon-nucleon phase shifts, with a choice of two prescriptions [Jac66] [Red70] for the centre-of-mass energy: in the final energy prescription (FEP), E_{cm} is taken as the relative cm energy of the emitted particles c and d; in the initial energy prescription (IEP), E_{cm} is the relative cm energy of the incident particle a and the struck particle b, where the fact that b is off-the-mass-shell is ignored, and the scattering angle is taken to be the same as in the FEP.

Kudo *et al.* [Kud86] [Kud88] [Kud89] have achieved improved agreement between experimental data and DWIA calculations by calculating the off-shell t matrix with an effective N-N interaction, which illustrates the shortcomings of evaluating the t matrix at the asymptotic on-shell momenta. Nevertheless, in many situations the results calculated with each of the extreme on-shell prescriptions are similar, which shows that off-shell effects are not always important.

THREEDEE calculates Equation 1.3 with $C^2S = 1$. The spectroscopic factor is thus determined by normalization of the calculated cross sections to the experimental values.

If spin-orbit interactions are ignored, the expression may be simplified, as it is no longer necessary to sum the elements of the two-body t matrix coherently with the distorted wave integral; this leads to the appearance of the two-body cross section as a multiplicative factor [Cha77] (which recovers the simplicity of Equation 1.1):

$$\frac{d^3\sigma}{d\Omega_c d\Omega_d dE_c} = C^2 S\, K' \frac{d\sigma}{d\Omega}_{1-2} \sum_{\Lambda} |T_{BA}^{\alpha L\Lambda}|^2, \tag{1.4}$$

where K' is a different kinematic factor from K. The factor $|T_{BA}^{\alpha L\Lambda}|^2$ is the distorted momentum distribution, where α represents unneeded quantum numbers. The particles 1 and 2 in the two-body cross section are a and b for the IEP or c and d for the FEP approximation.

Although the so-called factorization approximation is used in the derivation of both Equations 1.3 and 1.4 (it allows the two-body t matrix to be evaluated outside the distorted wave integral), we shall refer to Equation 1.4 as the "factorized cross section" because of the additional factorization of the t matrix with respect to the sum over quantum numbers, whereas Equation 1.3 (the amplitude-factorized form) will be called the "coherent cross section".

It is a simple matter to generalize this formalism to encompass cluster knockout as well.

Finally, to obtain inclusive cross sections, the triple differential cross sections 1.3 or 1.4 may be integrated over the solid angle of the unobserved particle:

$$\frac{d^2\sigma}{d\Omega_c dE_c} = \int \frac{d^3\sigma}{d\Omega_c d\Omega_d dE_c} d\Omega_d. \tag{1.5}$$

1.4 Purpose and Scope of this Experiment

In Section 1.2, we described the inclusive measurements of Wesick *et al.* [Wes85] for 100 and 150 MeV protons on light targets. The questions left open by that experiment inspired the present coincidence measurements.

Most important of these questions is the reason why no clear quasifree peaks were seen in the ^{4}He(p,p′) spectra at either 100 or 150 MeV, even through they were predicted by DWIA calculations for quasifree nucleon knockout. In all cases, the high-energy portions of the measured spectra were enhanced with respect to the calculations.

Some of the discrepancies were reduced by the incoherent addition of a (p,pd) contribution to the (p,pN) predictions, which filled in part of the "missing" high-energy yield and also gave a better fit to the analyzing power data. It was speculated that the inclusion of other cluster knockout reactions (p,pt) and (p,ph) might contribute further toward explaining the flat spectra from ^{4}He, by filling in even higher-energy portions of the inclusive cross sections.

Another possible source of high energy protons is from the unbound states [Fia73] [Fuk86] [Bla87] of ^{4}He with excitation energy between 20 and 30 MeV.

Furthermore, it was not known to what extent multiple scattering affected the shapes of the inclusive continuum spectra; presumably it would contribute mainly to the low-energy regions.

The contributions from multiple scattering were also put forward as a possible explanation for the angle-dependent normalizations: the ratio that was required to normalize the theoretical cross sections to the data increased with increasing detection angle, which is consistent with the notion of multiple scattering contributions being mainly at low energies. However, the explanation could as easily be that the DWIA is inadequate for

modelling quasifree reactions in such light systems.

Clearly, much of the interesting physics is inaccessible with single-detector inclusive measurements. We have thus extended these studies to exclusive particle-particle correlation measurements.

Now, in order to plan the measurements, we need to consider the manner in which the inclusive DWIA cross section is calculated, i.e. the triple differential cross section is integrated over the solid angle of the unobserved particle (Equation 1.5). In practice the range of integration is cut off at some sensible value for the solid angle which encompasses most of the coincidence yield but comprises a small fraction of 4π. Not only does this save on computing time, but, more importantly, it reduces the risk of extending the DWIA into regions of phase space for which it is no longer valid. [As an aside, we note that the evaluation of Equation 1.5 for the inclusive cross section $\sigma(\Omega_1, E_1)$ places more demands on the validity of the DWIA than do the usual calculations of $\sigma(\Omega_1, \Omega_2, E_1)$, for which the geometries are commonly chosen such that the various approximations are safely within their ranges of applicability.]

Experimentally, the corresponding exercise is thus to measure protons at the same "primary" angles as Wesick *et al.*, in coincidence with "secondary" particles over a solid angle range which is similar to that used for integrating Equation 1.5.

The main objectives of the experiment were:

- to determine whether the DWIA is valid over the angular ranges required for calculating the inclusive spectra (and if so, to extract spectroscopic factors);

- to determine the relative contributions of nucleon and cluster knock-out to the inclusive cross sections;

- to determine the proportion of multiple scattering in these reactions;
- to explain the angle dependence [Wes85] in the normalizations of the DWIA calculations to the inclusive yields.

Although an explanation of the flat continuum spectra for ^{4}He(p,p′) was the inspiration for this experiment, the investigation of the range of validity of the DWIA is in itself an interesting problem with broader implications, particularly for models [Cia84b] in which the quasifree scattering is viewed as a doorway to more complex processes, and also with regard to the current interest [För88] [Tak89] [Smi89] in the composition of inclusive proton spectra.

Previous measurements [Pug73] [Fra75] of ^{4}He(p,2p) below 200 MeV have been for quasifree symmetric angles only, i.e. geometries for which zero recoil momentum is possible at equal energies of the detected protons.

The measurements which are presented here are for ^{4}He(p,2p), (p,pd), (p,pt) and (p,ph) at 100 MeV, for primary proton angles of 45° and 60°, secondary in-plane angles ranging from $-15°$ to $-90°$, and secondary out-of-plane angles extending from 0° to 30° .

In Chapter 2 we present details of the experiment. Although it would have been interesting to perform the experiment also at 150 MeV, and for further primary angles, we explain the reasons for concentrating on 45° and 60° at 100 MeV.

Chapter 3 covers the replay of the data. We present the experimental results in the form of energy-sharing distributions for which the quasifree knockout locus has been projected onto the axis of the primary proton energy. The energy-sharing cross sections are tabulated in the Appendix.

In Chapter 4 we describe the DWIA calculations which are compared with the experimental energy-sharing distributions. By normalizing to the data, we extract spectroscopic factors. We then integrate over the solid an-

gle of the secondary particle for each reaction channel, thus reconstructing the quasifree part of the inclusive (p,p′) spectra. We show that quasifree scattering accounts for most of the yield. Upon adding a multiple scattering contribution, which we estimate from our data, we reproduce the inclusive spectra of Wesick *et al.* to within ∼10%.

Chapter 5 contains a discussion of our findings and the conclusions which may be inferred from them.

The final chapter consists of a summary of this work.

Chapter 2

The Experiment

2.1 Design Considerations

The overall design of the experiment is explained in this section. The detailed designs of specific components such as the gas cell and detector telescopes will be discussed in the following sections.

From an experimental point of view, our primary objective was to make exclusive measurements of the ^{4}He(p,p'x) reaction under the same experimental conditions for which Wesick *et al.* [Wes85] made their inclusive measurements: at 100 and 150 MeV incident proton energies and at "primary" proton detection angles of 17.5°, 30°, 45° and 60°.

For the measurement of the primary protons, we decided to use two detector telescopes, each consisting of two silicon surface barrier detectors and a NaI(Tl) detector. One of these telescopes (at the more forward angle) would be equipped with active collimation in order to reduce contributions due to slit penetration by scattered particles.

The "secondary" particles, undetected by Wesick *et al.*, would be measured over as much of phase space as possible. The choice of detectors for these particles was not as easy. In order to know which regions of laboratory coordinate space we should be planning to cover, we started by assuming that the production of secondary particles is dominated by quasifree knockout, so most of these particles would be emitted towards the opposite side of the beam from the primary protons. Furthermore, since the distorted momentum distribution for a particle bound in ^{4}He drops at least an order of magnitude [Pug73][Fra75] from the peak at zero MeV/c to the value at 200 MeV/c, we concluded that most secondary particles would be concentrated into that region of laboratory coordinate space for which recoils of momentum less than 200 MeV/c are kinematically possible.

In Figure 2.1 we show the loci for secondary particles within which minimum recoil momenta of <200 MeV/c are possible, for (p,2p) and (p,pd)

quasifree knockout at 100 MeV with primary detection angles of 45° and 60°. Only half the loci are shown (for positive out-of-plane angles β_S) as the reactions are symmetric with respect to the two out-of-plane hemispheres.

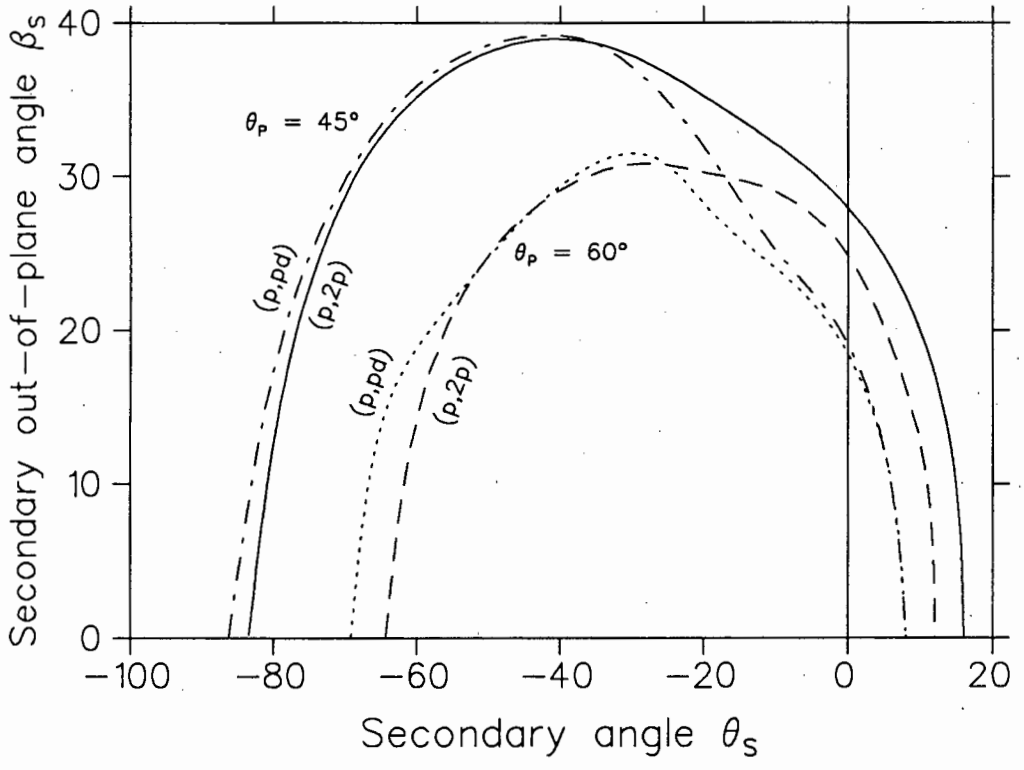

Figure 2.1: *Loci within which recoil momenta of <200 MeV/c are possible. The solid curve is the locus for the (p,2p) reaction at a primary angle of 45° and primary proton energy ≥ 10 MeV. The dash-dotted curve is for the (p,pd) reaction at 45°. For the primary angle of 60°, the (p,2p) and (p,pd) reactions are represented by the dashed and dotted curves respectively.*

The loci corresponding to the primary angles of 17.5° and 30° are much larger: for 30°, the locus extends from −156° to 60° in the reaction plane and right out to 90° out-of-plane.

Of the inclusive spectra measured by Wesick *et al.* [Wes85], the agreement between the data and the theoretical calculations was poorest for proton angles of 45° and 60° at 100 MeV, which makes these angles the more interesting ones to investigate further by means of exclusive measurements. Because most of the secondary particles associated with protons detected at these angles would be more tightly localized (Figure 2.1) than for primary angles of 30° and 17.5° , we decided that it would be expedient to concentrate our efforts on acquiring as complete a set as possible of coincidence data at primary angles of 45° and 60°.

Thus, our requirements were for a secondary particle detection system that could cover the region from close to 0° out to −90° in-plane, and from 0° to ∼ 30°–40° out-of-plane.

We considered constructing a large-solid-angle detector such as a plastic hodoscope which would be able to cover the region of interest in relatively few steps. It would have consisted of thick slabs of plastic scintillator, viewed at each end by photomultiplier tubes, with a thin sheet of scintillator mounted in front for particle identification. Angular resolution would have depended on measuring the time difference between the light reaching the top and bottom phototubes of each slab. However , when we considered the investment in time and money which would have been required to build such a detector, the complex electronic setup (increasing the risk of breakdowns during beam time) and the possibility that we may not have been able to achieve adequate angular resolution, we chose instead to use an array of four detector telescopes consisting of silicon surface barrier and NaI(Tl) detectors.

The compromise, of course, was that we would require more beam time to effect the same measurements. Furthermore, we had to assume that cross sections would vary smoothly enough to enable interpolation between

measured angles on not too fine a grid. Nevertheless, our estimates of expected count rates indicated that we would be able to achieve the goals of this experiment within the allocated beam time (65 eight-hour shifts) by using NaI detectors. This choice of detector telescope also yields the advantage that gas target collimators may be used to exclude the detection of reaction products from the entrance and exit windows of the gas cell.

To summarize, we decided to use six detector telescopes (two primary and four secondary) for these measurements. The thicknesses of the silicon surface barrier detectors were chosen to yield good particle identification over a wide dynamic range. To enable the subtraction of accidental coincidences, the event-by-event data would include coincidence timing parameters in addition to all the detector energy parameters.

With reference to the (p,pn) reaction, we decided that it would be adequate to extrapolate the neutron knockout contribution from the (p,2p) data.

The run took place during October 1987, with 100 MeV protons. The cyclotron delivered beam for a total of 63 shifts ($\sim$ 500 hours), just two shifts short of the time allocated.

2.2 Accelerator and Beam Characteristics

The k=200 MeV separated-sector cyclotron (SSC) of the National Accelerator Centre [Bot86a] delivers a diverse range of beams for experimental physics, radiotherapy and isotope production. [k is a constant of proportionality, such that the maximum energy E of an accelerated particle with charge state q and mass number m is given by $E = kq^2/m$]. The layout of the facility is shown in Figure 2.2. At present, the SSC is served by a single injector (SPC1), which is a k=8 MeV solid-pole cyclotron with an

internal ion source, capable of producing unpolarised light ions. A second injector cyclotron (SPC2), presently under construction [Bot86b], will be able to produce polarised beams and heavy ion beams.

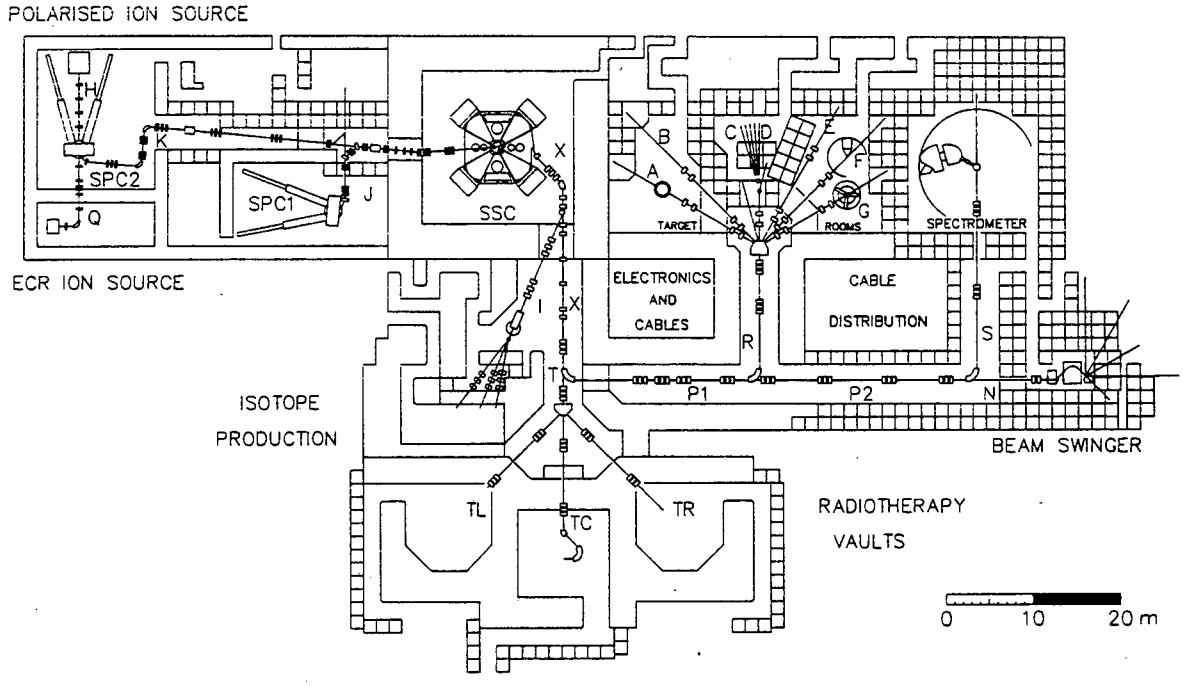

Figure 2.2: *The cyclotron facility of the National Accelerator Centre.*

For this experiment, we used a beam of 100 MeV protons with a typical intensity of ~60 nA. Operating characteristics of the SSC during production of this beam are summarised in Table 2.1.

The determination of the energy of the extracted beam would preferably be by NMR measurements on one of the 90° magnets in the high-energy beamline, but as this was not available at the time of the run, we had to rely on cyclotron parameters. The energy was calculated from $v_p = l_e/T$, where v_p is the speed of the protons at extraction, l_e is the length of the extracted orbit and T is the period of the beam in the SSC. The uncertainty

Injection energy		4.6 MeV
Rf Dee-Voltage		~220 kV
Frequency		19.7 MHz
Mode of Acceleration		$N = 2$
No. of turns in SSC		~110
Length of extracted orbit		$l_e = 26.1$ m
At Extraction:	Orbit separation	~18 mm
	Energy	100.0 ± 0.4 MeV
	Energy spread	$\pm$ ~100 keV
	Emittance	~14 mm.mr
	Period of beam pulses	51 ns
	Pulse length	~0.8 ns

Table 2.1: *Operating characteristics of the SSC during production of a beam of 100 MeV protons; and properties of the extracted beam.*

of 0.4 MeV (Table 2.1) arises from uncertainties in the centering of the beam and in the beam phase relative to the rf phase. The energy spread in the extracted beam was estimated to be ~100 keV and would probably have been reduced somewhat by emittance-limiting slits during transport to the target. We did not attempt to determine the energy dispersion because even the upper limit of ~100 keV is negligible in comparison with the energy resolution of the NaI detectors.

The beam was transported along beamline X (see Figure 2.2), through 90° into beamline $P1$ and through another 90° into beamline R. The double monochromator (the two 90° magnets) was operated in achromatic mode, and the emittance of the beam was cut by slits in beamline $P1$. Halo produced by the beam striking these slits was reduced by a set of "clean-up" slits in line R. The beam was focused to a waist in the centre of the

switching magnet by the quadrupole magnets of line R.

From the switching magnet, a pair of doublet quadrupoles on beamline A focuses the beam at the centre of the scattering chamber. Steering magnets on line A were switched off during the entire run, because it was considered inadvisable to steer the beam so close to the scattering chamber.

The spot size was generally smaller than 4 mm wide by 2 mm high and the divergence of the beam was $\sim$0.2° in the reaction plane and $\sim$0.3° out-of-plane. The position of the spot was never more than a $\frac{1}{2}$-mm off-centre and, from monitoring the beam distribution on the elements of the beam stop (see below), we estimate a directional stability of $\leq$0.1°. The monitoring of halo on the beam is discussed in Section 2.9.

Because of the adequate angular acceptance of the beam stop, the beam is not refocused after passing through the target. It is stopped at a distance of 6.34 m from the target by sections of aluminium with a total thickness of 22.8 cm and a diameter of 18.4 cm. Viewed along the beam direction, these beam stop elements are split into four quadrants to enable the use of the current integrator as a monitor of beam distribution over the face of the beam stop. These elements are preceded by three sections of aluminium pipe, each 80 cm long, 16 cm in internal diameter and 12 mm thick. All these beam stop elements are separated from one another and from ground by machinable-glass-ceramic insulation. During tuning of the beam, the proportion of beam current collected by each of the seven elements (four quadrants and three pipe sections) may be recorded separately and represented on an LED display. Of course, for a well-directed beam and thin targets, the contributions from the pipe sections are negligible, as the back of the beam stop subtends $\pm$0.7° and the entrance to the first pipe section subtends $\pm$1.2° at the target. The entire assembly is packed around with steel shielding and hand-stacked concrete blocks.

The current integrator (Brookhaven Instruments Corporation Model 1000C) has "no measurable non-linearity" and can be calibrated to ±0.02%, according to the instruction manual.

2.3 Scattering Chamber

The high-precision scattering chamber was acquired from the University of Maryland after their own cyclotron was shut down, and refitted [Raa87] in this laboratory with more modern stepper motors and shaft encoder readouts. The vacuum tank (see Figure 2.3) is 1.52 m in diameter and 0.76 m high, measured from the upper detector arm. As it is supported independently from the table carrying the detector arms and target mechanism, the precision alignment of components on the detector arms is preserved irrespective of whether the tank is open or under vacuum.

In order to prevent noise on the signal lines due to earth loops, the scattering chamber is electrically isolated from the beamline, the vacuum pumps and the floor. It is connected to the same "clean earth" as the detector electronics, which find "clean earth" via the earth straps on the NIM-bins.

Six of the side ports and two top ports have vacuum feedthroughs for signals and voltage supplies. At present, there are 51 BNC feedthroughs (of which we used 45 in this experiment), 27 SHV feedthroughs and a feedthrough for preamplifier power. Clamps on the inside walls of the scattering chamber keep cables out of the way of the moving arms.

The two independent arms may be locally controlled, which is useful during setup, or operated remotely from the data room. The shaft encoder readouts have a resolution of 0.01°; the overall accuracy in the positioning of each arm is estimated to be ±0.02°. In the case of the target ladder,

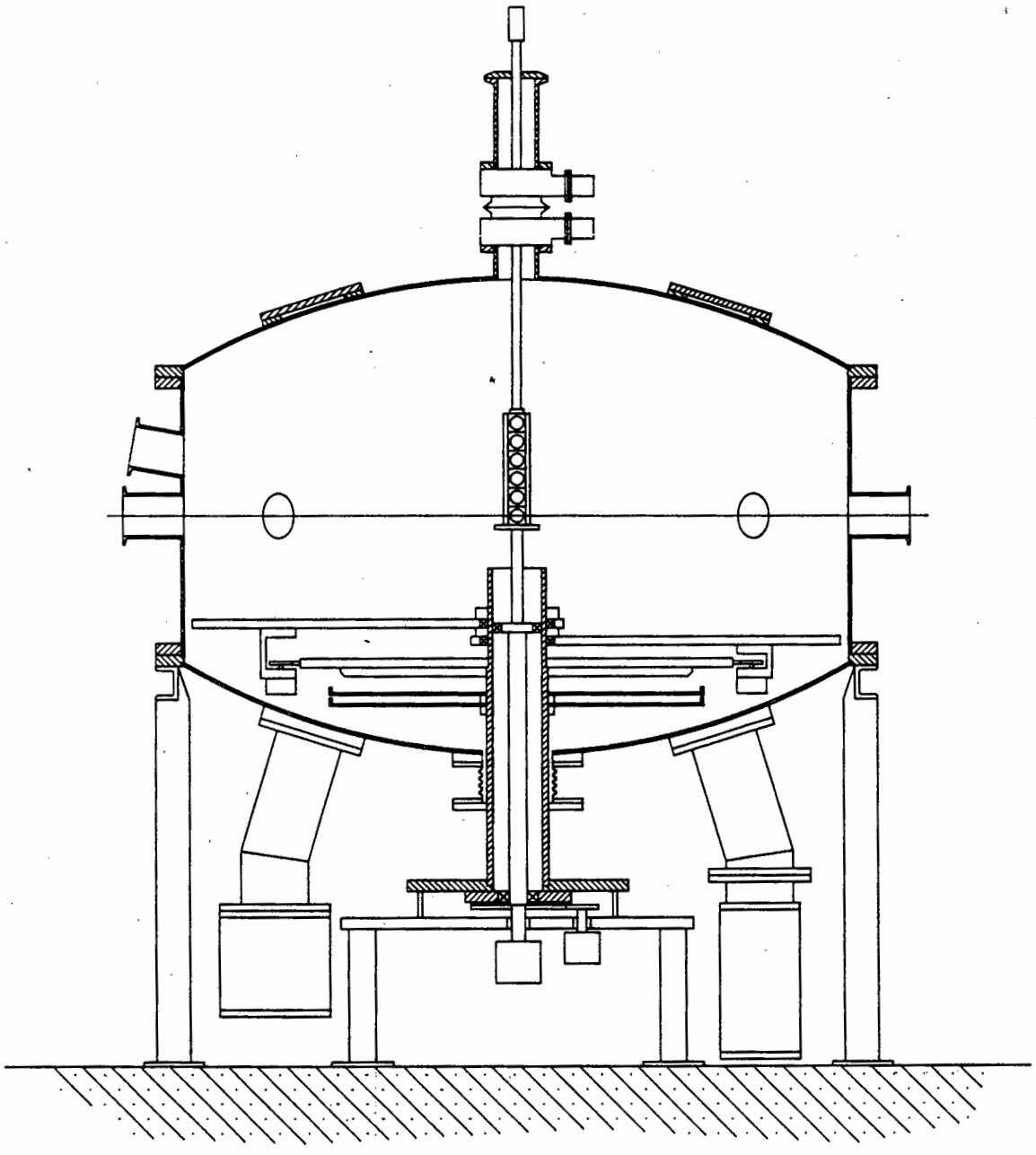

Figure 2.3: *The 1.5 m scattering chamber.*

the vertical position and target angle are controlled in a similar manner, to an accuracy of ± 0.3 mm and $\pm 0.1°$ respectively. The target ladder can accommodate five solid targets or a gas cell plus three solid targets.

The operating vacuum during this experiment was typically 6×10^{-5} mbar.

2.4 Targets

Figure 2.4 is a drawing of the gas cell and target ladder which were constructed for this experiment; the gas cell is bolted to a table on top of the ladder and there is room below it for three solid targets. We mounted, in descending order, a beryllium oxide scintillator, an empty target frame and a 1.8 mg.cm^{-2} polythene target, all of diameter 25 mm. The utilisation of these targets is described in Section 2.9.

The design criteria for the dimensions of the cylindrical gas cell are discussed in Section 2.5, as these dimensions were considered as variables in the design of the gas target collimators. The cell was constructed from a single block of aluminium, which was chosen for lightness yet would distort only negligibly at a pressure difference of one or two bar.

O-rings form the seals between the Havar windows and the body of the gas cell. These windows are unusually high (50 mm) because of the requirement for out-of-plane measurements. Calculations based on manufacturer's specifications for tensile strength indicated that 6 μm thick Havar windows would be able to withstand a pressure difference of about 2 bar, which should have given us a safe enough margin to operate the cell at just over 1 bar. However, having tested three sets of windows to destruction at 1.2 bar, 0.7 bar and 1.1 bar successively, we had no choice but to fit thicker 25 μm windows, resulting in higher thresholds for the detection of

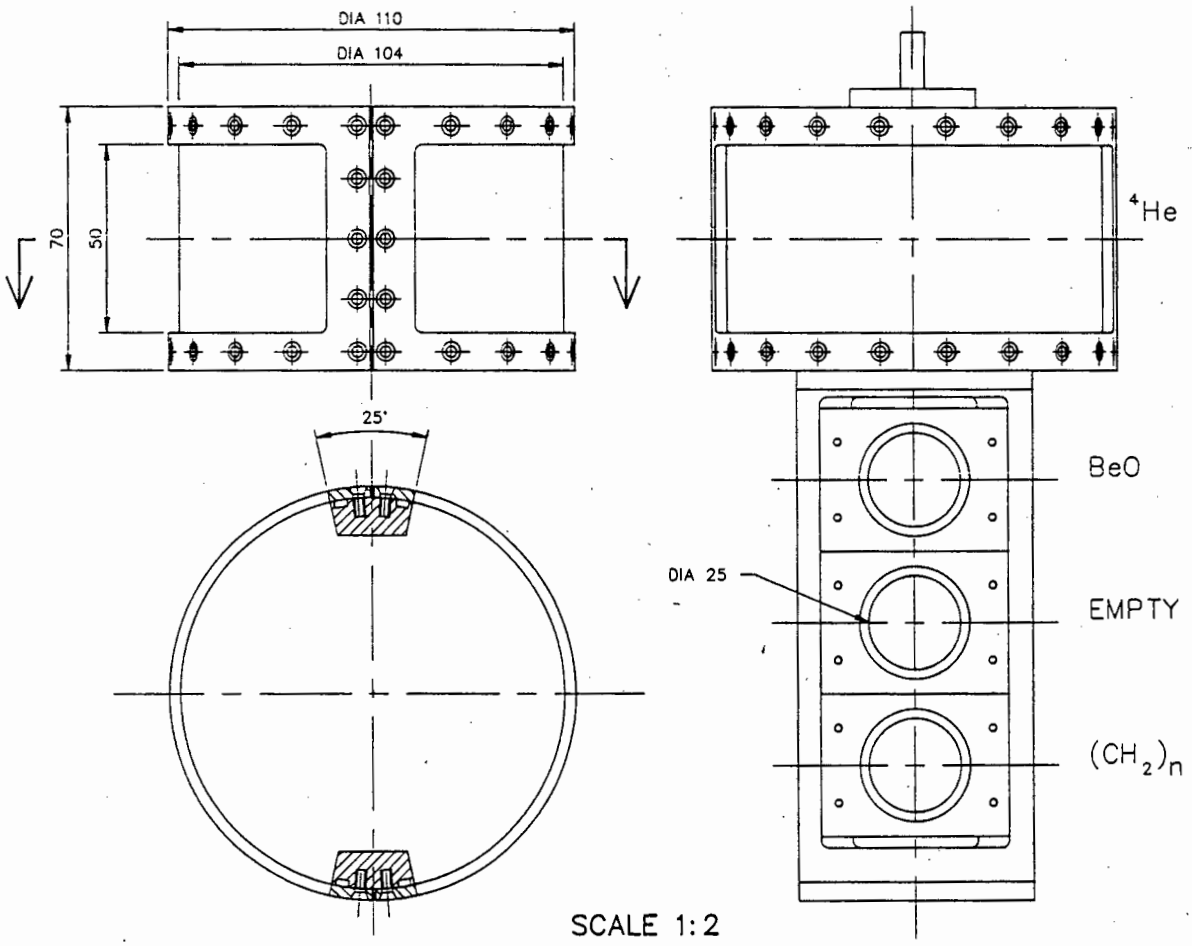

Figure 2.4: *Side view and top view of the gas cell; front view of the cell mounted on the target ladder.*

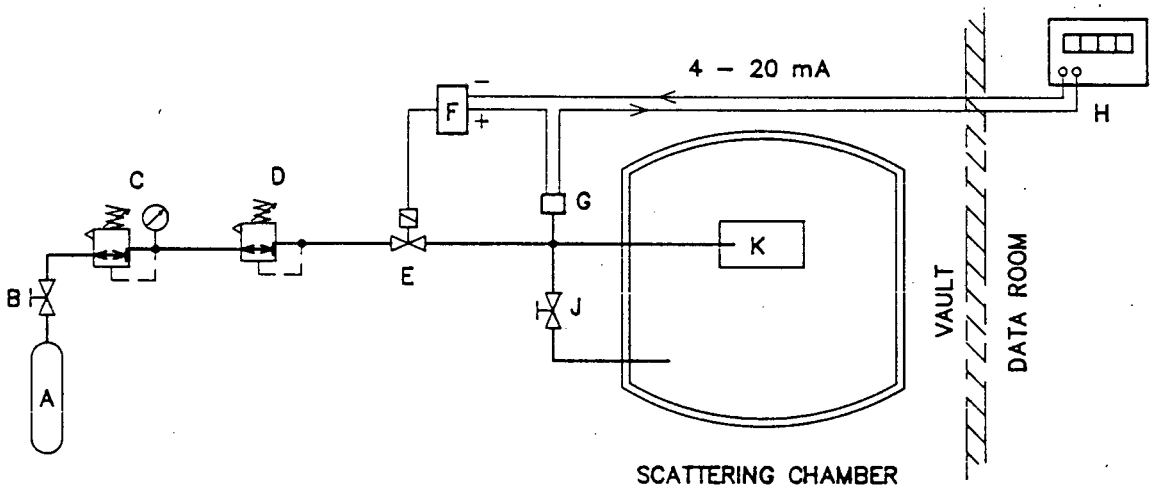

Figure 2.5: *Gas handling system. The components are described in the text.*

low-energy particles. As the detector telescopes had thresholds of ~10 MeV for helions (the heaviest particles of interest in this experiment), the overall thresholds then corresponded to 14 MeV helions losing 4 MeV in the Havar.

A relatively thick Havar window also has implications for energy calibration and resolution. However, as projections of the data would always be performed onto the energy axis of the primary proton (see Section 3.8), we were only really concerned about good energy calibration for the primary protons. Thresholds in this case corresponded to 5 MeV protons losing 1 MeV in the Havar, with the energy loss decreasing rapidly to only 100 keV for 100 MeV protons. Corrections for these losses were applied to the proton energy scales during analysis of the data (see Section 3.8.3).

Figure 2.5 is a schematic representation of the gas handling system. The components are:

A Disposable cylinder of high-purity helium (99.995%), initially ~400 l under pressure of 126 bar.

B Isolating hand valve.

C Air Products Single-Stage Regulator E11-M-N145D for coarse adjustment of pressure.

D Negretti & Zambra Precision Regulator R/182. According to the specifications, the change of regulated pressure is less than 1% of any variation in the supply pressure.

E Solenoid valve.

F Quanta Alarm Power Supply Model 1200. The "Alarm" part of the power supply consists of two relays with adjustable set-points. One of these was used to arm the solenoid valve so that it would close in the event of a sudden loss of pressure, e.g. rupture of the gas cell window.

G Fuji Absolute Pressure Transmitter Model FBA30WA1-00Y. The specified accuracy is "better than $\pm 0.25\%$". We confirmed this figure during calibration and testing over a number of days.

H Optelec $3\frac{1}{2}$-digit Indicator, which allowed us to monitor the gas cell pressure continuously during the run. It was connected to the power supply and pressure transmitter in a 4–20 mA current loop.

J Hand-operated valve. The gas cell was evacuated via the scattering chamber vacuum system before being filled with helium.

K Gas cell.

The gas cell was not tested independently for leaks; we suspect that most of the leakage rate of 10% hr^{-1} (from the entire system) was due to

leaky connections or even diffusion through the polythene tubing which was used to connect these components.

Despite the high leakage rate, we never saw any evidence of significant contamination in the target, probably for two reasons: firstly, the gas cell pressure was maintained at a level higher than atmospheric, 1.1 bar, and secondly, the system was probably much more leak-tight for other gases than it was for helium.

It was obvious that the precision regulator was coping easily with the leakage, which after all was only $\sim$1 cm^3/min., because the pressure variation during data acquisition at each angle setting was always within the accuracy of the gauge ($\pm$0.25%) and it changed by only 2% over the course of the entire run, a period of three weeks.

The gas temperature was not monitored directly; it was assumed to be in thermal equilibrium with the air in the vault which was monitored by means of an ordinary thermometer.

2.5 Gas Target Collimators

Collimation becomes a complex problem when coincidence measurements need to be made over a wide angular range with a gas target. The "raw" target is the path traversed by the beam, and in this experiment it consisted of two Havar foils (the entrance and exit windows) and a line through the helium gas. In order to prevent window-scattered particles from entering the detectors and to establish adequate angular resolution, it is necessary to use a double-aperture collimator to define an appropriate length of the line target. Unfortunately, suitable aperture dimensions are strongly dependent on the detector angle and the situation is complicated by the need to maintain an appropriate "coincidence target length" between pairs of

detectors, both of which need to change angle during the experiment.

We based our design work on the approach outlined by Carey [Car79] for vertical front slits and circular rear apertures, extending his formulae to include out-of-plane detector configurations, finite beam diameters and finite aperture thicknesses. Provision for the latter was necessary because the collimators were chosen to stop 150 MeV protons (due to anticipated use at higher incident energy), which required aperture thicknesses of 30 mm, a significant dimension in these calculations.

Most of the parameters which are used in the following calculations are introduced in Figure 2.6 which for simplicity shows the situation of a collimator with thin apertures at 90° to a pencil beam.

Although the detector telescope sees a total target length $z_f - z_a$, only the length $z_d - z_c$ corresponds to maximum detector response, as the rear aperture is not fully illuminated by particles coming from the "penumbra" beyond z_c and z_d. Carey [Car79] has shown that $z_e - z_b$ constitutes an "effective target length", t_{eff}. Furthermore, in coincidence experiments, the way to ensure an easily calculable coincidence target length is to require that the total target length $(z_f - z_a)$ seen by one telescope lies entirely within the maximum response region of the other telescope (see Figure 2.7). The first telescope thus defines the coincidence overlap region, and the coincidence target length is trivially given by t_{eff} of this defining telescope. Thus in order to design the collimators, one needs to use the following relationships, in which β is the out-of-plane angle and all other symbols are defined in Figure 2.6:

$$z_a = -\frac{R_0 w_f}{2h \sin\theta_0} \frac{\left[1 + \left(1 - \frac{h}{R_0}\right)\frac{w_r}{w_f}\right]}{\left[1 - \frac{\cot\theta_0 \cos\beta}{2h}(w_r + w_f)\right]},$$

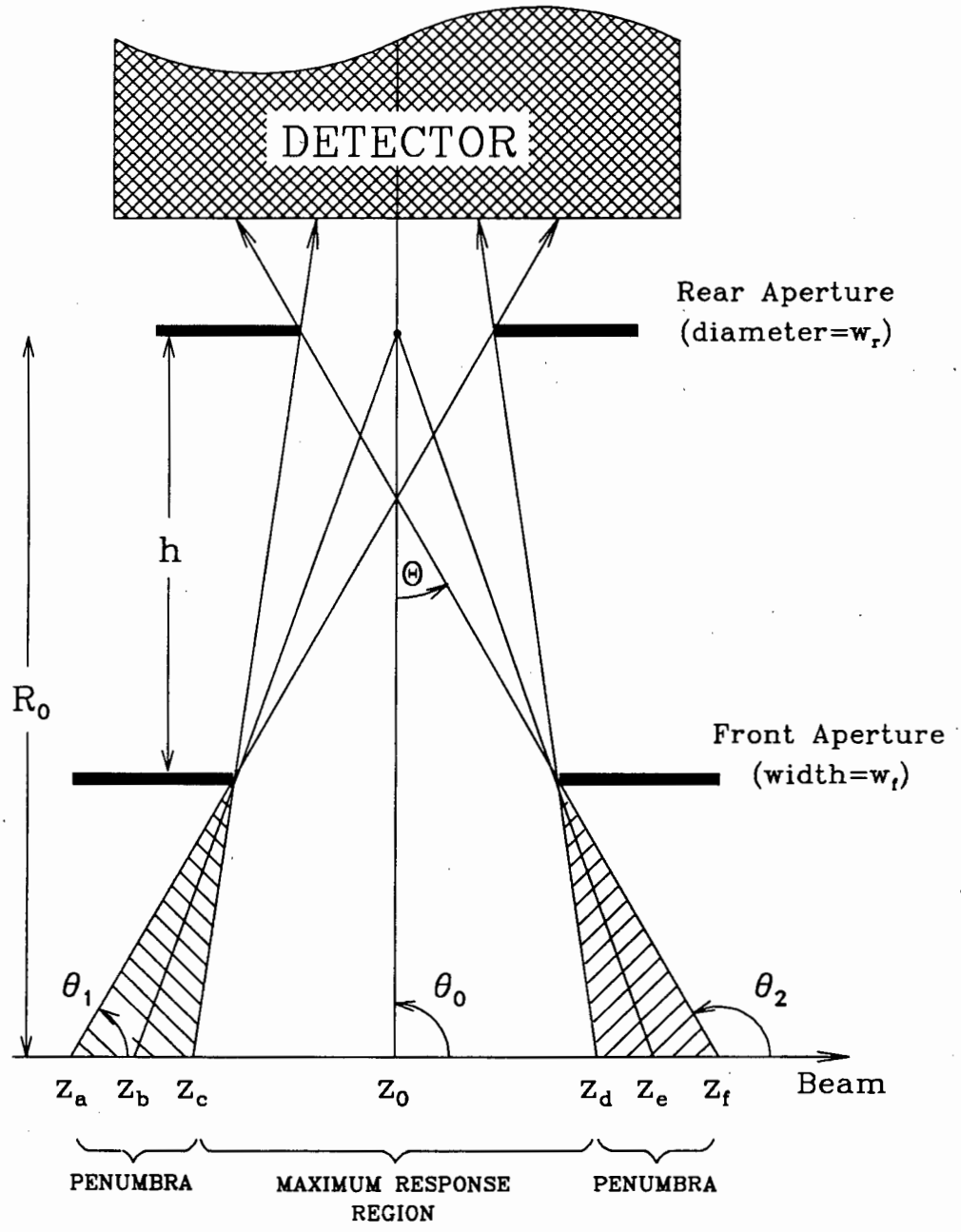

Figure 2.6: *Ray diagram for a gas target collimator*

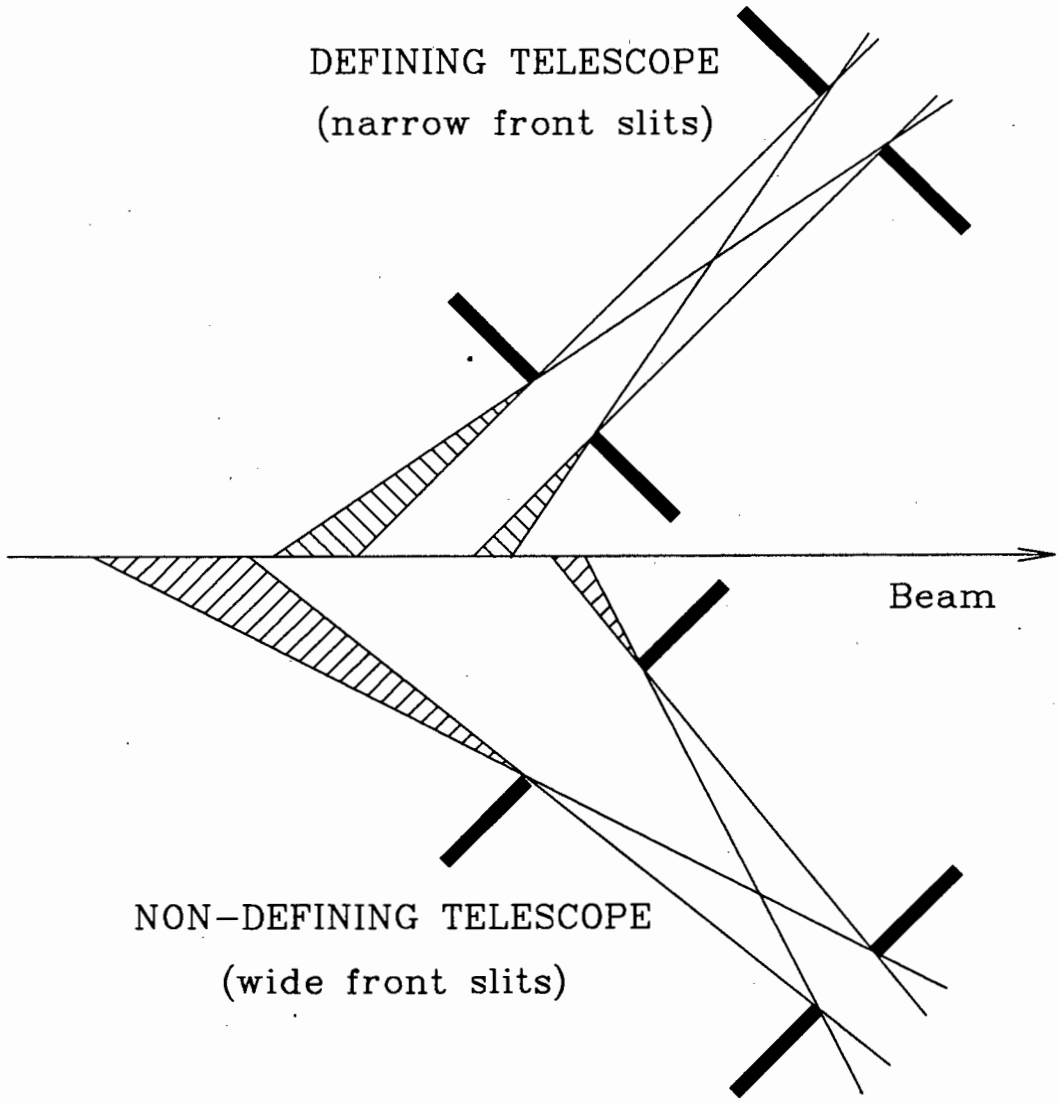

Figure 2.7: *The coincidence target length is easy to calculate in the situation illustrated here because the total target length of the defining telescope lies entirely within the maximum response region of the non-defining telescope.*

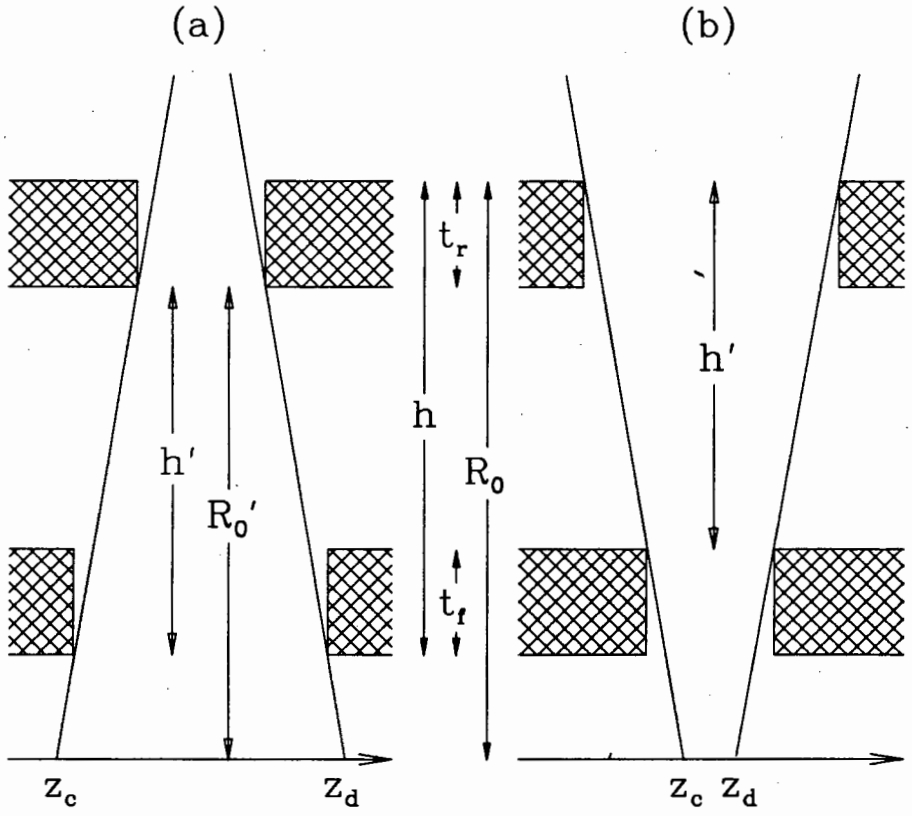

Figure 2.8: *The effect of finite aperture thicknesses on the evaluation of the length parameters R_0 and h, for (a) front aperture wider than rear aperture, and (b) vice versa.*

$$z_f = \frac{R_0 w_f}{2h \sin\theta_0} \frac{\left[1 + \left(1 - \frac{h}{R_0}\right)\frac{w_r}{w_f}\right]}{\left[1 + \frac{\cot\theta_0 \cos\beta}{2h}(w_r + w_f)\right]}.$$

The effect of finite aperture thicknesses on the determination of z_c and z_d is illustrated in Figure 2.8:

$$z_c = -\frac{R_0' w_f}{2h' \sin\theta_0} \frac{\left[1 - \left(1 - \frac{h'}{R_0'}\right)\frac{w_r}{w_f}\right]}{\left[1 + \frac{\cot\theta_0 \cos\beta}{2h'}(w_r - w_f)\right]},$$

$$z_d = \frac{R_0' w_f}{2h' \sin\theta_0} \frac{\left[1 - \left(1 - \frac{h'}{R_0'}\right)\frac{w_r}{w_f}\right]}{\left[1 - \frac{\cot\theta_0 \cos\beta}{2h'}(w_r - w_f)\right]},$$

where, for $w_f > w_r$, $R_0' = R_0 - t_r$
and $h' = h - t_r$;
and, for $w_f < w_r$, $R_0' = R_0$
and $h' = h - t_f$.

The effective target length is given by

$$t_{eff} = \frac{R_0 w_f}{h \sin\theta_0} \frac{1}{1 - \left[\left(\frac{w_f}{2h}\right)\cot\theta_0 \cos\beta\right]^2}. \tag{2.1}$$

These relationships assume a perfectly aligned pencil beam. In Figure 2.9, we show how the inclusion of the beam radius r_b leads to the definition of maxima and minima for each of these parameters on either side of the central values:

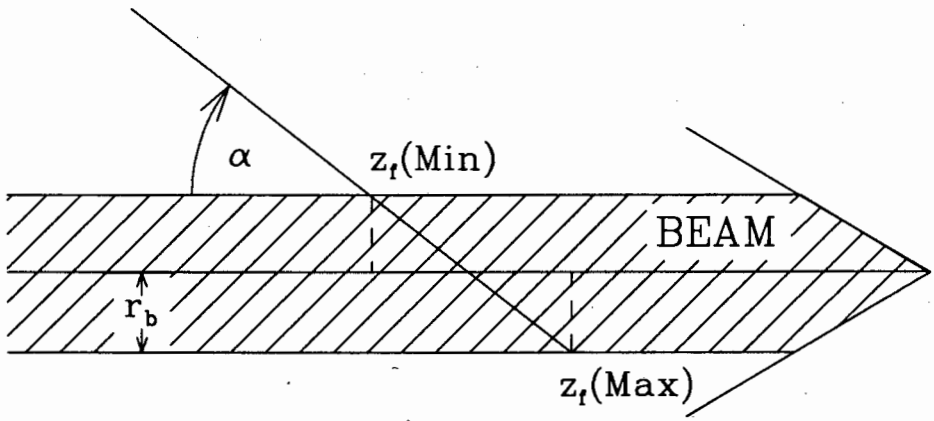

Figure 2.9: *The effect of finite beam dimension r_b on the evaluation of the target length parameters z for rays intersecting the target at angle α.*

$$\begin{aligned} z_f(Max) &= z_f + r_b \tan\alpha, \\ z_f(Min) &= z_f - r_b \tan\alpha, \\ &\text{etc.} \end{aligned}$$

where $\alpha = \arccos(\cos\theta_2 \cos\beta) \approx \arccos(\cos\theta_0 \cos\beta)$.

The parameter r_b can be thought of as a measure of the extent of the beam with respect to the centreline, i.e. the combined effect of alignment inaccuracies and spot size.

The angular resolution is defined [Car79] with respect to the angles shown in Figure 2.6 to be

$$\Theta = \frac{1}{2}(\theta_2 - \theta_1) = \arctan\left[\frac{w_f + w_r}{2h}\right].$$

As a rule of thumb, we aimed to keep $\Theta < 3°$ in the design of the collimators, but this was not always practical. In one case it was over 4°. However the *effective* angular resolution [Car79] in such a coincidence experiment is determined by the defining telescope and was always $\leq 3°$.

As we have mentioned in Section 2.1, we employed two primary detector telescopes, one of which was equipped with active collimation, and four secondary telescopes. We wished to cover the four primary angles 15°, 30°, 45° and 60° in two sets of measurements (15° being considered close enough to the 17.5° of Wesick *et al.* [Wes85]). Space limitations prevented our placing the primary detectors 15° apart, so they were placed 30° apart in order that the measurements could be performed at the two settings (15°;45°) and (30°;60°).

We wanted the four secondary telescopes to be placed in a fairly tight cluster, and finding that a spacing of 15° was feasible, we thus decided on the configuration illustrated in Figure 2.10: two in-plane telescopes, 15° apart, and two out-of-plane telescopes placed 15° and 30° directly above the forward in-plane detector telescope.

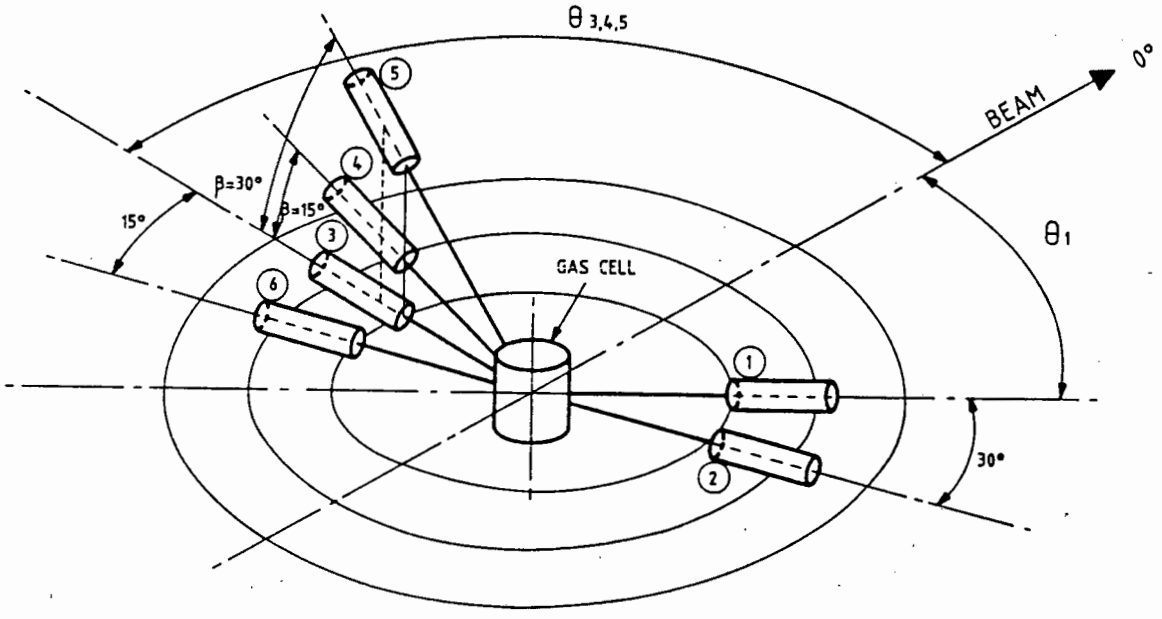

Figure 2.10: *The configuration of the detector telescopes. Primary telescopes 1 and 2 are coplanar with both the beam and secondary telescopes 3 and 6. Secondary telescopes 4 and 5, mounted directly above telescope 3, are out-of-plane by 15° and 30° respectively.*

In the following list, we discuss some further design criteria in the choice of the collimator dimensions.

R_0, the total distance from the target to the back of the collimator, was chosen to be as large as possible, allowing for a safe clearance between the photomultiplier base of the NaI detector and the cables strapped to the sidewall of the scattering chamber.

h, the distance between the front and back apertures, should be as large a proportion of R_0 as possible for best angular resolution and to minimize the fraction of penumbra in the total target length. In

practice, it is limited by the radius of the gas cell, which is thus chosen to satisfy the best compromise:

$\mathbf{r_{cell}}$, the radius of the gas cell, needs to be a sensible balance between

(i) the requirements for h as mentioned above,

(ii) the need to provide a long enough line target to facilitate the design of the collimator apertures, and

(iii) the need to keep the size of the Havar windows within reasonable limits; a larger r_{cell} results in a lower safe operating pressure for a gas cell with Havar windows of a given thickness.

$\mathbf{t_f}$ and $\mathbf{t_r}$, the thicknesses of the front and back apertures were chosen to stop up to 150 MeV protons; for brass apertures, 30 mm is adequate.

$\mathbf{w_r}$, the diameter of the rear aperture, determines the solid angle subtended by the telescope:

$$\Delta\Omega = \frac{\pi w_r^2}{4R_0^2}.$$

$\Delta\Omega$ should be large enough to ensure a satisfactory yield. We could have tolerated $\Delta\Omega$ up to $\sim$2 msr while maintaining adequate angular resolution, but were limited to $\sim$1.5 msr by the surface area of the silicon detectors. This limit is reached long before possible outscattering from the NaI detectors becomes a problem.

$\mathbf{w_f}$, the width of the front aperture (which consists of vertical slits), is the principal factor in determining the target length parameters. It was impossible to satisfy all the desired requirements for the collimators at all geometries with a single set of front slits. However, with two sets of slits we found that we could satisfy most of the requirements most of the time, which seemed the best compromise if we could thus

count on stopping the experiment only once in order to break vacuum and change slits.

We tried to adhere to the following guidelines in choosing the slit widths:

1. $|z_a|$ and $|z_f|$ should be $< \frac{3}{4} r_{cell}$ to ensure that no particles generated in the Havar windows could enter the telescopes. In some cases we had to forfeit some of the margin of safety, and at two extreme geometries (the data from which are not amongst those presented here) one telescope partially viewed the entrance window.

2. In order to define a simple coincidence target length as shown in Figure 2.7, we tried to keep $|z_a(Max)|$ and $|z_f(Max)|$ of the defining telescope less than $\frac{3}{4}$ of $|z_c(Min)|$ and $|z_d(Min)|$ of the non-defining telescope. Here also, the margin of safety was compromised in some geometries, but even in the worst case the error in the calculated coincidence target length due to imperfect overlapping of response regions is estimated to be negligible (see Section 3.9.2).

3. In pursuit of "good overlap", one should be careful not to make the front slits of the defining collimator too narrow, as this increases the proportion of slit-scattered particles in the total yield and causes most of the response region to be penumbra (an obvious consequence of having $w_f << w_r$). We thus kept $w_f > w_r/3$ in all cases. Also, bearing in mind that the slits had to be 30 mm *thick*, it can be easily imagined that $w_f < 5$ mm would result in a very undesirable slit shape.

4. The real coincidence count rate is proportional to $(t_{eff})^2$ of

the defining telescope, whereas the random rate is proportional to $t_{eff}(defining) \times t_{eff}(non-defining)$, so we tried to keep $t_{eff}(defining) > 0.2\, t_{eff}(non-defining)$. Once again, this was not always possible at some extreme geometries. Of course, during the experiment we compensated for this design problem by adjusting the beam current for satisfactory real-to-random coincidence rates.

In satisfying these four guidelines, we arrived at coincidence target lengths in the range 6–11 mm, which seemed to be reasonable values. The secondary telescopes defined the coincidence target length when they were at angles $|\theta_S| \geq 35°$; at smaller angles, it became necessary to change slits so that the primary telescopes could define the coincidence target length.

y_f, the height of the front slits, was large enough to be effectively infinite for the in-plane telescopes. For the two out-of-plane telescopes, however, the projection of the line target onto the front face of the collimator is horizontal at $\theta = 90°$ but becomes increasingly diagonal as θ is reduced until at $\theta = 0°$ it is vertical. Thus at some point, y_f starts to determine the target length parameters rather than w_f. Although there were severe space limitations between the front slits of telescopes 3,4 and 5, values of y_f could be chosen such that they did not impose serious restrictions on the choice of good overlap conditions.

r_b, the allowable "extent" of the beam with respect to the centreline, was dictated by necessity: we could not guarantee good overlap unless r_b was ≤ 2 mm, so we insisted on beams of at least this standard.

The collimators were constructed from brass. Table 2.2 gives their dimensions, along with their distances from the target and solid angle defined.

Collimator	w_f (mm)	w_r (mm)	h (cm)	R_0 (cm)	$\Delta\Omega$ (msr)
1	4.8, 17.9	13.98	22.14	31.61	1.536
2	4.9, 23.9	14.10	24.94	31.50	1.574
3	5.2, 13.0	14.01	25.04	31.50	1.554
4	4.8, 12.8	13.97	25.16	31.56	1.543
5	4.8, 13.0	14.00	24.15	31.52	1.549
6	5.0, 13.0	14.02	25.08	31.50	1.556

Table 2.2: *Principal dimensions of the collimators (w_f, w_r and h), distances R_0 from the target, and solid angles $\Delta\Omega$ subtended.*

In order to ensure that any particles generated in the target could enter the detectors only after passing through both apertures, the sidewalls had to be thick enough to stop 150 MeV protons and the block containing the rear aperture had to be wide enough to shield the entire NaI crystal from the gas cell (see Figure 2.11). The range of 150 MeV protons in brass is $\sim$ 30 mm; the maximum angle ϕ for which particles could enter a detector via a sidewall and the back aperture was $\sim$ 15°; thus the sidewalls were made 30mm $\times \sin 15° =$ 8mm thick. For the out-of-plane telescopes, some shielding material also had to be provided for the top and bottom sides of the collimators.

Inner surfaces of the apertures were polished and checked for alignment and uniformity. The positioning of the removable front slits was found to be repeatable to within the accuracy of measurement, $\pm$0.1 mm.

Telescope 1, the forward primary telescope, was equipped with active collimation. The apertures were machined in 6 mm-thick pieces of NE-102A scintillator which were optically coupled via perspex light-guides to 19 mm-diameter photomultiplier tubes (Thorn EMI 9826B with built-in base). The assemblies were made light-tight with a coating of NE 560 Reflector Paint.

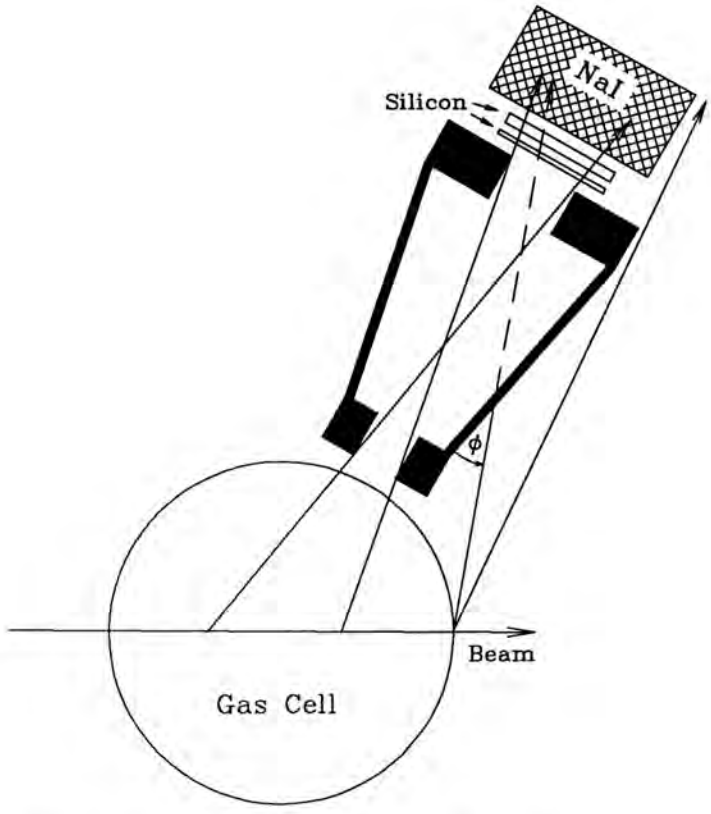

Figure 2.11: *Illustration of how the sidewalls and rear aperture blocks of the collimators prevent unwanted particles from entering the detectors.*

To reduce the count rates in these veto detectors, brass shielding masked most of the surface area (the brass apertures were approximately twice the area of the active collimator apertures).

Photographs of the six collimators mounted in the scattering chamber are shown in Figure 2.12.

Alignment was achieved with the aid of a precision-machined steel rod which passed through the circular rear aperture, and a theodolite was used to determine the final position of each collimator with respect to the arm on which it was mounted.

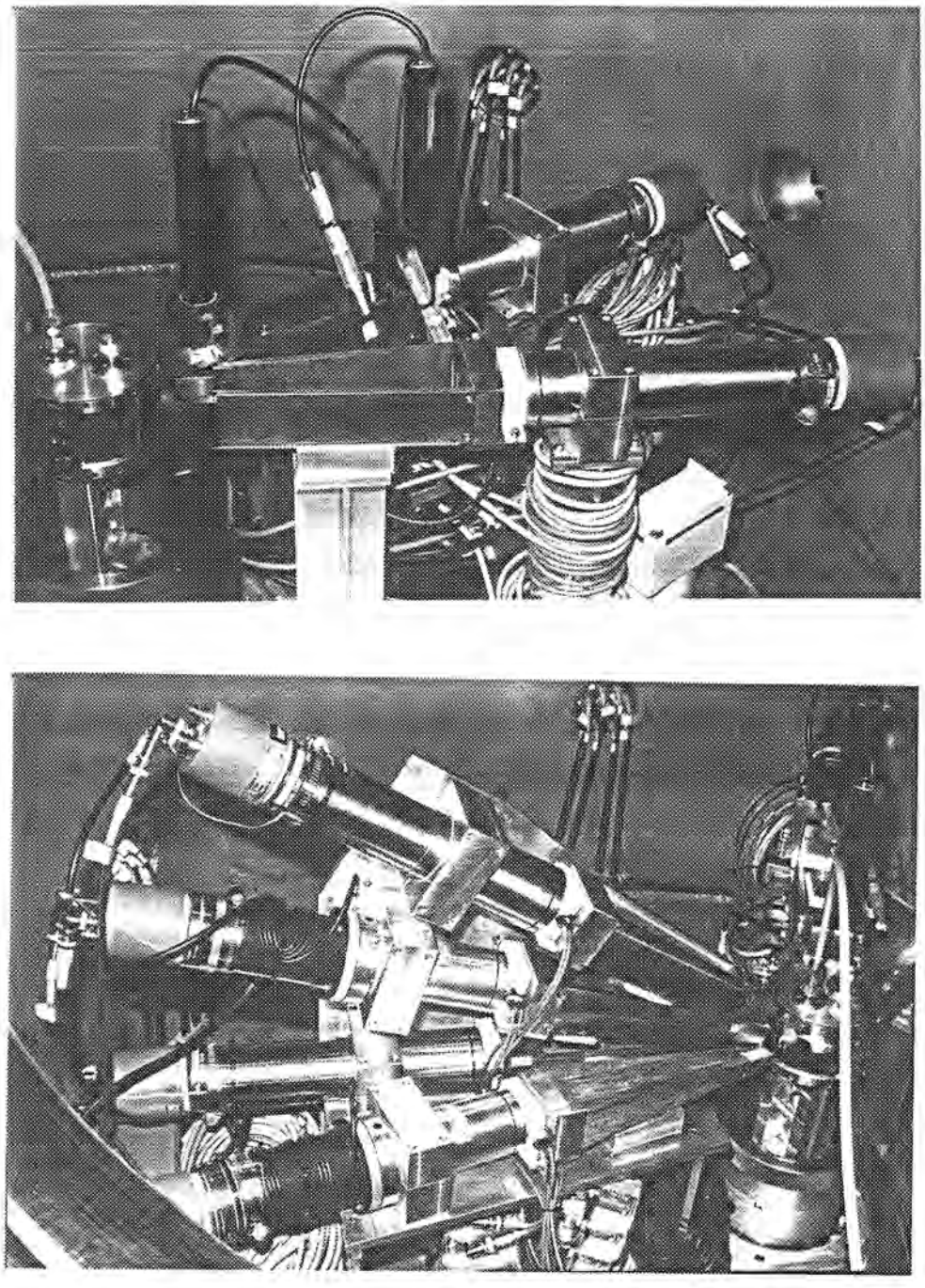

Figure 2.12: *The two primary telescopes are shown above, with the gas cell on the left. The photomultiplier tubes of the active collimators are mounted vertically on the forward telescope. The four secondary telescopes (on the opposite side of the beam) are shown below, two in-plane and two out-of-plane.*

Because solid targets were also to be used (for calibration purposes) each collimator had a foil of 8μm-thick Kapton stretched across one of the apertures in order to reduce the flux of secondary electrons impinging on the surface barrier detectors.

2.6 Detector Telescopes

In order to permit particle identification over a wide dynamic range for protons, deuterons, tritons and helions, we chose to use triple-element detector telescopes. As shown in Table 2.3, each telescope consisted of two silicon surface barrier detectors, both of area 300 mm^2, followed by a 51 mm diameter by 127 mm long NaI(Tl) crystal.

<table>
<tr><th>Telescope</th><th>A (silicon)</th><th>B (silicon)</th><th>C (NaI)</th></tr>
<tr><td>1</td><td rowspan="6">ORTEC
100 μm</td><td rowspan="3">ORTEC
1000 μm</td><td rowspan="3">BICRON</td></tr>
<tr><td>2</td></tr>
<tr><td>3</td></tr>
<tr><td>4</td><td rowspan="2">Q-PAR ANGUS
500 μm</td><td>HARSHAW</td></tr>
<tr><td>5</td><td>BICRON</td></tr>
<tr><td>6</td><td>HARSHAW</td></tr>
</table>

Table 2.3: *Detectors* A-B-C *in the triple-element telescopes.*

Elements $B5$ and $B6$ were originally 1000 μm thick detectors, but their performance deteriorated early in the run and they were replaced by 500 μm thick detectors. Similarly, the NaI detectors are not all identical, because we did not have six of the same make in stock.

The silicon detectors (elements A and B) formed a ΔE-E combination for particle identification of low energy particles stopped in the second detector: for telescopes 1–4 (5 and 6) protons with energies up to 12 MeV

(9 MeV) or helions with energies up to 45 MeV (32 MeV) were stopped. For higher energies the ΔE-E combination was formed by elements B and C. All the detectors were electrically isolated from the scattering chamber by means of teflon holders or sleeves. The silicon detectors were mounted with their gold-layered surfaces facing each other in order to minimize the dead layer between them. The surface contacts themselves constitute negligible dead layers (40 μg.cm^{-2}), but regions of undepleted silicon will form behind the aluminium contacts if the applied voltage becomes too low (usually caused by an increase in leakage current). A further benefit of having the grounded surfaces facing each other is that capacitive effects between the two detectors are eliminated.

The NaI detectors were integral line assemblies with thin (6 μm) Havar entrance windows and mu-metal shielding. A crystal length of 127 mm is sufficient to stop protons of energy in excess of 200 MeV. The four Bicron assemblies contained SRCB50B01 photomultiplier tubes and the two Harshaw detectors were supplied with EMI 9956 tubes. For improved linearity the signal was taken from the fifth dynode in the chain. Gain drifts and non-linearities in response functions are discussed in Sections 3.4.5 and 3.3.2.

2.7 Electronics

All the preamplifiers were mounted on the detector arms inside the scattering chamber in order to minimize the cable capacitance on the inputs. In the data room, the timing and energy signals from the preamplifiers were fed into Timing Filter Amplifiers and Linear Amplifiers respectively.

A block diagram of the electronics for processing the slow linear signals is shown in Figure 2.13.

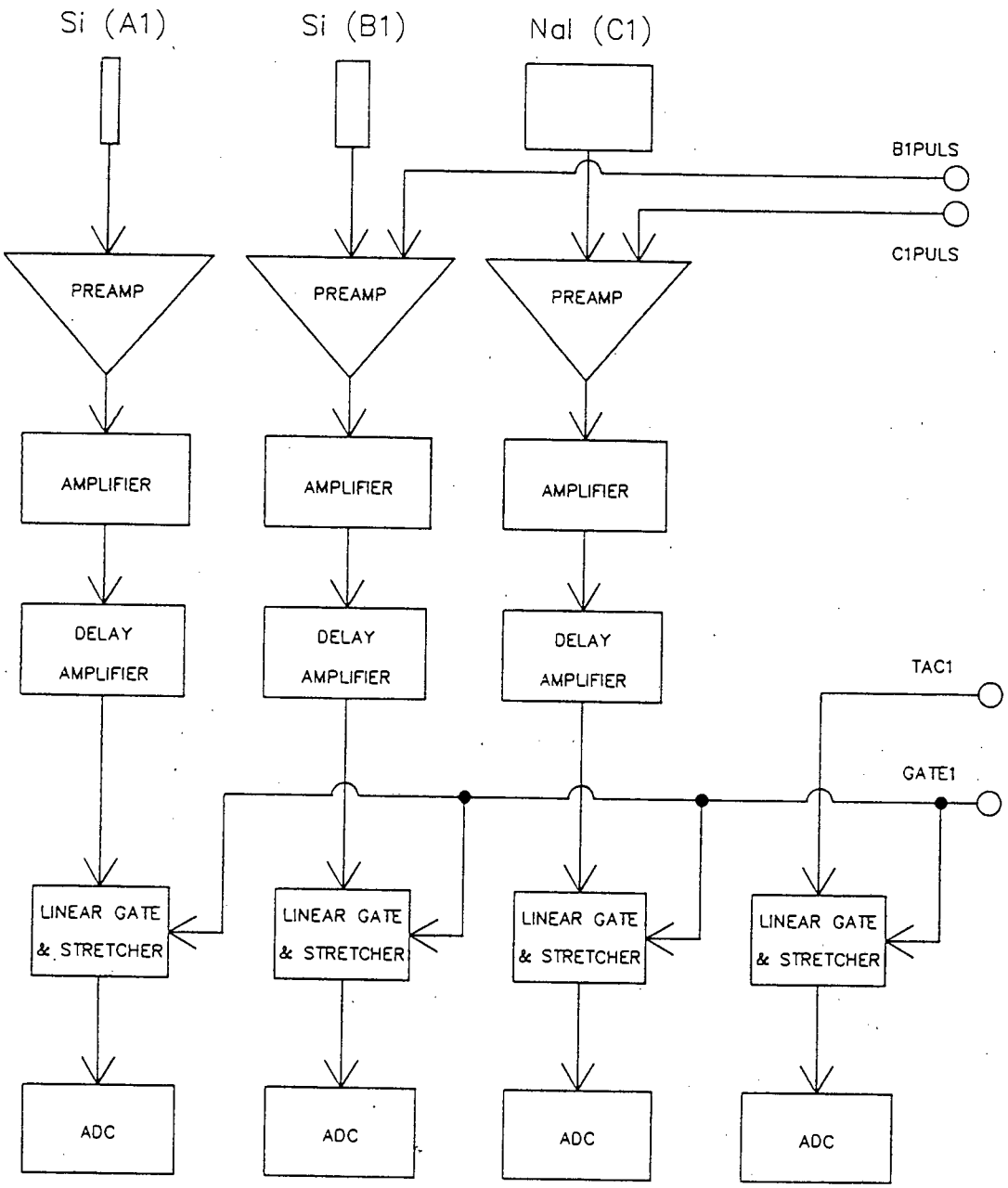

Figure 2.13: *Linear electronics for telescope 1. The setup for the other five telescopes was similar.*

For each of the two primary telescopes, there was an additional linear signal to be processed, namely the TAC (Time-to-Amplitude Convertor) signal for the relative timing between the event in the primary telescope and whichever secondary telescope had fired in coincidence with it. The time range of each TAC was set to 500 ns. With a period of ~50 ns between beam bursts, this setting allowed for the inclusion of several "random" peaks on either side of the "real" peak (see Figure 3.3), which would be necessary for the subtraction of random coincidences during replay of the data (see section 3.8.1). [The "random" peaks can contain only accidental coincidences, as the timing indicates that the two coincident telescopes fired on events from different beam bursts. The "real" peak contains the true coincidences superimposed on a background of accidental coincidences.]

Associated with each telescope was a gate signal which was generated by the logic circuitry for events involving that telescope. The gated linear energy signals were digitized in fast Analogue-to-Digital Convertors (ADCs) at a conversion gain of 1024 channels for the energy signals and 512 channels for the timing signals.

Figure 2.14 is an overview of the logic circuitry. As it is intended merely as an introduction to the essential features, many important aspects are not shown in order to simplify the illustration.

We now proceed with a more detailed description, commencing with the circuitry for Telescope 1 (the forward primary telescope) which is shown in Figure 2.15.

Timing signals from the Timing Filter Amplifiers were fed into Constant Fraction Discriminators which produced fast logic pulses. The logic circuitry then followed two stages, viz. "telescope logic" and "event logic".

Telescope Logic In order for the telescope to register a valid count, we required a signal from B (the thicker silicon detector) in coincidence

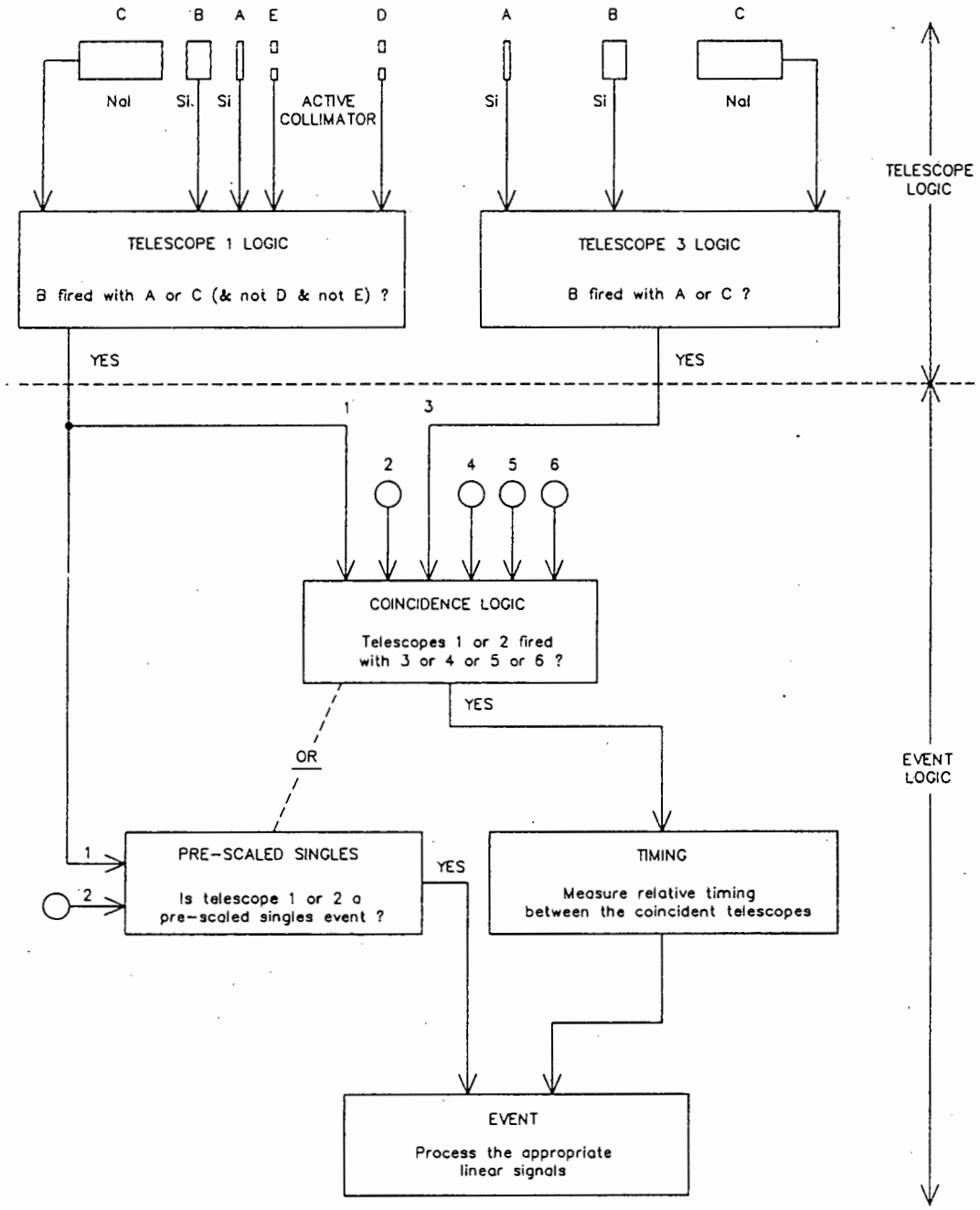

Figure 2.14: *Overview of the logic circuitry.*

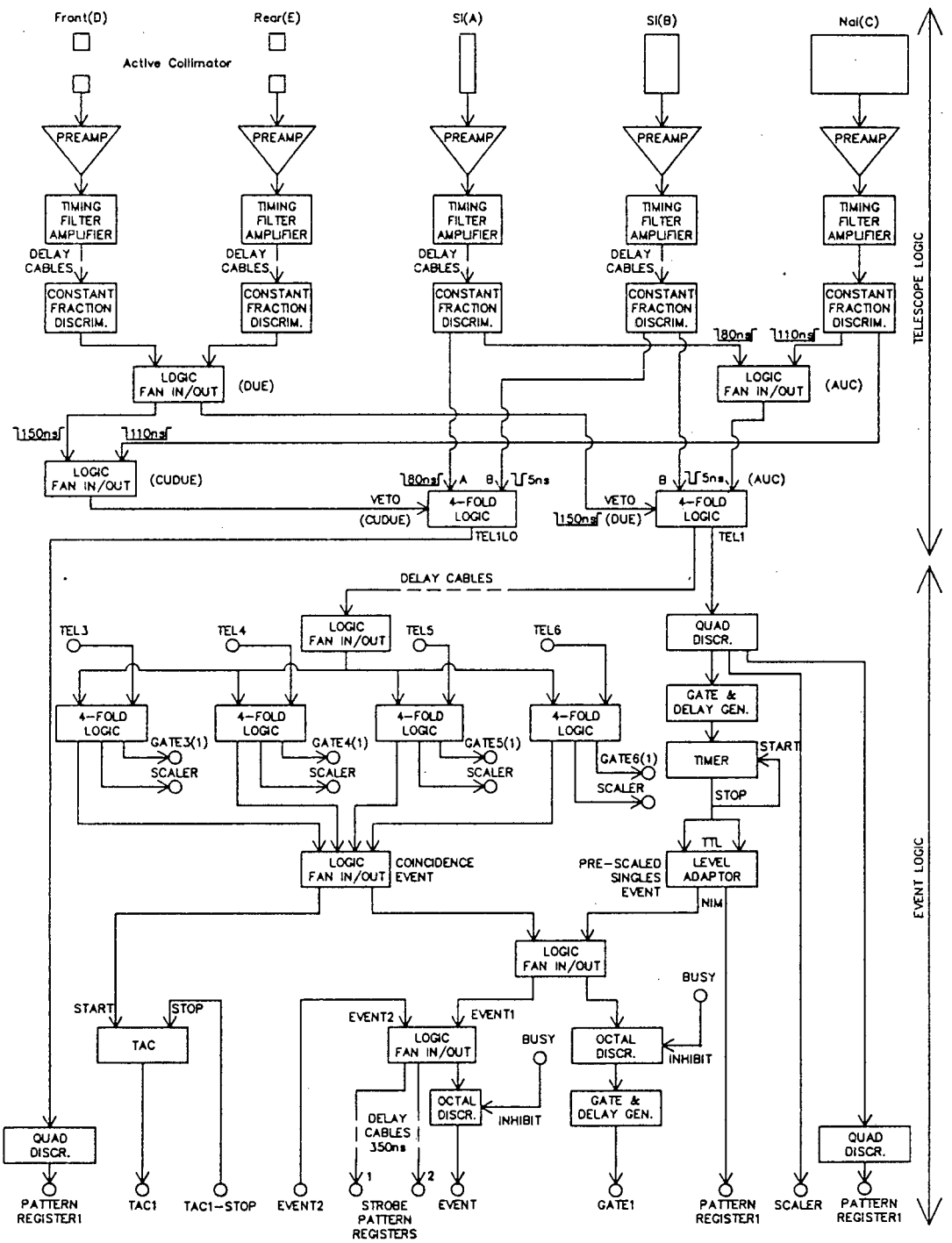

Figure 2.15: *Timing electronics for Telescope 1.*

with either A (thin silicon detector) or C (NaI detector). A signal from either the front(D) or back (E) element of the Active Collimator served as a veto. Thus a valid count required: $B \cap (A \cup C) \cap (\overline{D \cup E})$.

Whenever this condition was satisfied, a "TEL1" pulse was produced for the "event logic" stage of the circuitry, a scaler was incremented and a level was set in an Input ("Pattern") Register for use by the event sorting program. In addition, the logic test $A \cap B \cap \overline{C} \cap (\overline{D \cup E})$ was performed in order to identify the low energy particles "TEL1LO" which were stopped in detector B. Whenever TEL1LO was true, a further level was set in the Pattern Register.

The timing of detector B was used to determine the timing of pulse TEL1; in other words it was a narrow pulse which arrived at the coincidence unit within the overlapping periods of the wide pulses $(A \cup C)$ and $(D \cup E)$.

Event Logic There were two ways in which a TEL1 pulse could eventually lead to the recording of a valid event: it could become a coincidence event or a "pre-scaled singles" event. The "pre-scaled singles" data were taken because we wanted to monitor the inclusive spectra from the primary detectors (for comparison with the spectra of Wesick *et al.* [Wes85]) simultaneously with the coincidence data; we pre-scaled the singles rate by a factor of 1000 so that it would be compatible with the coincidence data rate.

The pre-scaling was achieved by feeding the TEL1 pulse through a Gate and Delay Generator into the External Clock Input of a Timer. The Timer was set to provide a Stop pulse for every 1000 clock pulses. This Stop pulse then restarted the Timer, set a level in a Pattern Register to signal a "Pre-scaled Singles Event" and was fanned in with

"Coincidence Event" pulses to perform the remaining logic functions for a valid "Event".

If a pulse from any one of the Telescopes 3,4,5 or 6 was present in coincidence with pulse TEL1, then the following functions were performed:

- A scaler was incremented for the appropriate pair of telescopes which had fired in coincidence.
- The linear gates were opened for the secondary telescope involved.
- The TAC for Telescope 1 was started by a pulse which derived its timing from pulse TEL1 and it was stopped by a pulse derived from whichever secondary telescope had fired.
- The Coincidence Event pulse was fanned in with the Pre-Scaled Singles pulse to open the linear gates for Telescope 1, to generate an Event Trigger and to strobe the two Pattern Registers.

The other primary telescope (Telescope 2) had no Active Collimator. Apart from this difference events involving Telescope 2 were processed in a similar way to that described for Telescope 1. The timing electronics for Telescope 3 are shown in Figure 2.16. Apart from some small details, the circuitry for all four secondary telescopes was identical. The "telescope logic" functioned in the same way as in the primary telescopes, except that levels were set in *both* Pattern Registers (each Register was associated with one of the two primary telescopes). The "event logic" was simpler than in the primary telescope because there were no pre-scaled singles events recorded.

The remaining components of the electronic setup are shown in Figure 2.17.

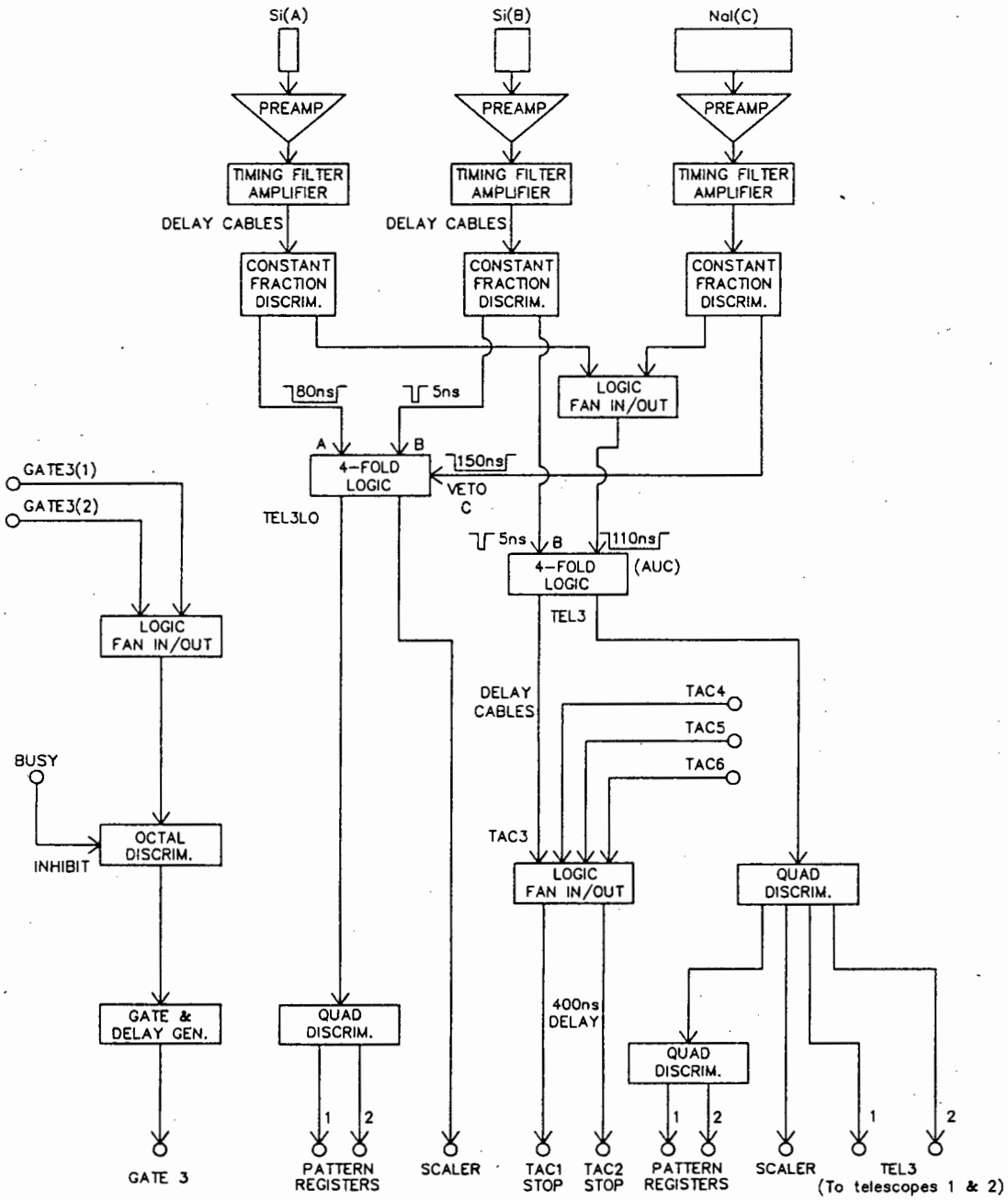

Figure 2.16: *Timing electronics for Telescope 3.*

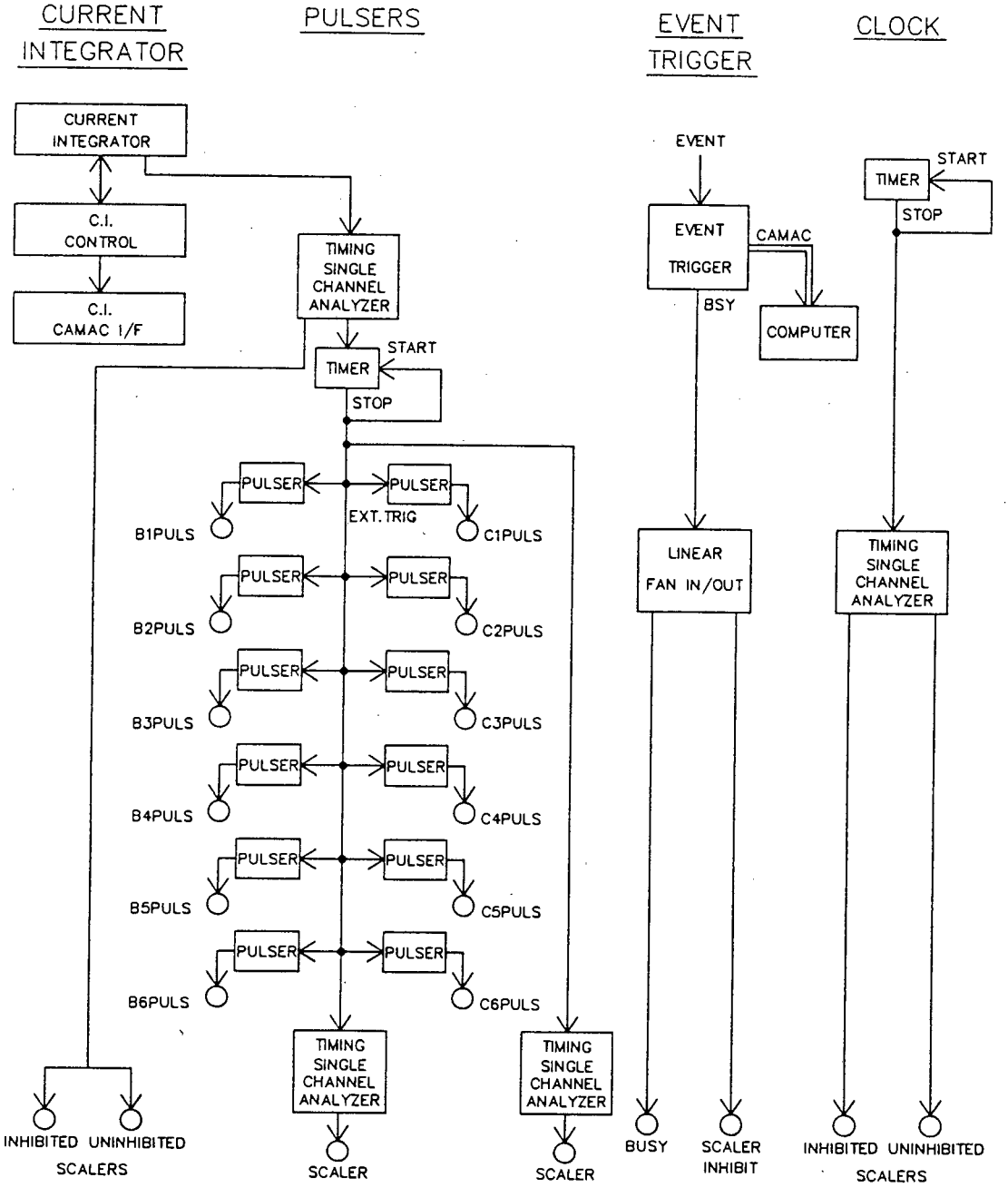

Figure 2.17: *Electronics for the Current Integrator, the Pulsers, the Event Trigger and the Clock.*

Current Integrator A locally-built Control Module allows selection of the Current Integrator range, i.e. the number of output digital pulses corresponding to every coulomb of collected charge. The Range setting was communicated to the computer via a CAMAC interface.

Pulsers Twelve tail pulse generators fed pulses into the preamplifiers of the six B- and six C-detectors for the purpose of correcting for pile-up and electronic dead time during replay (see Section 3.7). The pulsers were triggered at a rate proportional to the beam current by means of the pre-scaled digital output from the current integrator.

Event Trigger The Event Trigger module communicates (via the CAMAC crate) with the computer and also provides a BUSY signal, which was used to inhibit any further event triggers, all the linear gates and one of the two scaler modules for a period exceeding the time required by the computer to process an event.

Clock A continuous-running Timer served as a real-time clock on the "uninhibited" scaler module and as a computer live-time clock on the other module which was "inhibited" by the BUSY signal.

The signals recorded by the scaler modules and the levels set in the pattern registers are summarised in Table 2.4. By inspecting the contents of the Pattern Registers, the event sorting program was able to identify which telescopes had fired, whether the event was a "pre-scaled singles" or "coincidence" event and whether the detected energies were low (particles stopping in detector B) or high (particles stopping in detector C).

Bit	Uninhibited Scalers	Inhibited Scalers	Pattern Register 1	Pattern Register 2
1	Clock	Clock	TEL1LO	TEL2LO
2	Current Integr.	Current Integr.	TEL3LO	TEL3LO
3	TEL1	TEL1∩TEL3	TEL4LO	TEL4LO
4	TEL2	TEL1∩TEL4	TEL5LO	TEL5LO
5	TEL3	TEL1∩TEL5	TEL6LO	TEL6LO
6	TEL4	TEL1∩TEL6	TEL3	TEL3
7	TEL5	TEL2∩TEL3	TEL4	TEL4
8	TEL6	TEL2∩TEL4	TEL5	TEL5
9	TEL3LO	TEL2∩TEL5	TEL6	TEL6
10	TEL4LO	TEL2∩TEL6	TEL1 Pre-scaled	TEL2 Pre-scaled
11	TEL5LO	Current Integr. Pre-scaled	TEL1	TEL2
12	TEL6LO	Pulser Triggers		

Table 2.4: *Scaler and Pattern Register input definitions.*

2.8 Data Acquisition System

2.8.1 Hardware

The Data Room of the National Accelerator Centre is presently provided with two computers: the VAX 11/730 is dedicated to data acquisition, whereas the VAX 11/750 is used for off-line data analysis and general computing tasks. The two computers communicate with each other via an Ethernet-based network. The VAX 11/730 is interfaced to the CAMAC crates through a Bi-Ra microprogrammed branch driver (MBD-11). For a more detailed description of the VAX computers and the MBD-11, the

reader is referred to Pilcher's Ph.D. thesis [Pil89a]. In this experiment, event-by-event data were written to tape at a density of 6250 bpi and subsequently backed up at 1600 bpi. For setting up the experiment and for monitoring its progress, we also made extensive use of a colour graphics terminal to display the spectra produced by the sorting of data on-line. Some of these spectra were saved on disk, which was the only medium of storage for some of the calibration runs for which event-by-event recording was disabled.

2.8.2 Software

The software package which is used for data acquisition on the VAX 11/730 and for replay of data on either of the VAX computers is called XSYS. Pilcher [Pil89a] gives a comprehensive description of the origins and structure of XSYS, its operation with the MBD-11, and the facility for sorting event data. As for all experiments which run under XSYS, there were basically three major tasks to be performed during setup of this experiment, namely allocation of memory to the required list of histograms and gates, implementation of the Data-Acquisition Program (DAP) and loading of the EVAL program for event analysis.

Memory Allocation A command procedure was written which allocated 3072 pages of global memory (the maximum allowed) to this experiment (see Table 2.5).

Each of the 18 detector elements (6 telescopes of 3 elements each) was allocated a one-dimensional histogram of 1024 channels for the recording of coincidence events. Pre-scaled singles events were recorded in separate histograms, a total of 6 for the two primary telescopes. Coincidence timing (TAC) spectra were recorded in 512-channel his-

Number of histograms	Size of histograms	Contents
18	1024	Pulse height spectra for detector elements (coincidence events)
6	1024	Pulse height spectra for detector elements (pre-scaled singles events)
8	512	Coincidence timing spectra
2	2048	Pattern Registers
12	64 × 64	ΔE-E spectra
40	128 × 128	2-D energy-sharing spectra
32	64 × 64	Particle gates for ΔE-E spectra
16	—	1-D gates for timing spectra
27	—	Scalers

Table 2.5: *Memory allocations for histograms, gates and scalers*

tograms. There were 8 of these histograms corresponding to the eight possible coincidence-pair combinations between the two primary and four secondary telescopes. The two pattern registers were each allocated 2048-channel histograms, which corresponded to the full range of their bit patterns.

In order to save space in memory, the channels of all the two-dimensional histograms were restricted to storage in 16-bit words instead of 32-bit longwords. These histograms were cleared often enough, however, that overflows did not present a problem in the displaying of the data. Two types of 2-D histograms were allocated:

1. ΔE-E (64 × 64 channel) histograms for particle identification (see Section 3.4.1), of which there were two for each telescope,

i.e. between detectors A (ΔE) and B (E) and between detectors B (ΔE) and C (E).

2. Energy-sharing spectra in 128×128 channel histograms in which the axes represent the total detected energy in a primary telescope, and in a secondary telescope respectively. There were separate histograms for each type of secondary particle of interest, viz. protons, deuterons, tritons or helions. These 32 histograms (eight telescope combinations with four types of secondary particle) occupied most of the available memory. There was room for a further eight histograms of the same size, which was used for inspecting a sample of the "ungated TAC" and "random-gated TAC" spectra, which will be explained more fully in Section 3.4.2.

Two 1-D gates were allocated to each TAC histogram, for selecting real and random coincidences respectively (see Section 3.4.2). Each 2-D particle-identification histogram had the appropriate gates available for the selection of protons, deuterons, tritons or helions (secondary telescopes) or protons only (primary telescopes).

Finally, data areas were allocated to the scalers. In addition to those scaler variables listed in Table 2.4, the EVAL program used information from the Current Integrator interface to provide the additional quantities "Current", "Current Integrator Range" and "Charge".

Data Acquisition Program (DAP) The DAP file contains the list of instructions to be loaded into the MBD-11, which controls the CAMAC crates and reads event data from the interfaces mounted in the crates [Pil89a]. Data were read event-by-event; scalers were read every ten seconds.

EVAL Program The EVAL program controls the incrementing of the histograms based on the analysis of the data event-by-event. The analysis may include gate tests and simple arithmetic and logical manipulations (for more complicated analysis, FORTRAN code may be called by the lower level Event Analysis Language). The EVAL program which was used during the experiment was very similar to that used for the subsequent replay of the data, which is explained in some detail in Section 3.4.4.

2.9 Experimental Procedure

2.9.1 Setting up the Scattering Chamber

After mounting and aligning the collimators and detectors, we patched the cables between the detectors and the ports of the scattering chamber in such a way that the arms would have the maximum freedom to move over the angular ranges required. There were over sixty signal and high voltage cables inside the chamber and it was essential to ensure that the various bunches would not snare or become pinched during remote operation. Using the local-control box in the vault to operate the arms, we established the limits to the angular ranges of the two arms and the minimum allowable separation angle between them. The arm carrying the primary telescopes was able to move through to the same side of the beam as the secondary telescopes, a feature which we would need in order to determine the angular offset of the beam.

Before closing the scattering chamber we illuminated the BeO scintillator and switched on the TV-camera so that the position of the crosshairs, pencilled on the face of the scintillator, could be marked on the monitor screens in the Control Room. Later, this would enable the proper position-

ing of the beam spot.

2.9.2 Tuning the Electronics

Initial tuning of the electronics was performed with the 100 MeV proton beam on a polythene target. The gains of the linear amplifiers were set as follows:

For the A ΔE-detectors (100 μm silicon), we needed to consider only those particles transmitted to the B-detectors. For the particles of interest (p, d, t and h), the highest energy-loss in the A-detectors would be helions only just punching through at $\sim$ 10 MeV, so the gains were set such that 1024 channels $\longleftrightarrow$ 12–16 MeV, except for detector $A5$ (1024 channels $\longleftrightarrow$ 7 MeV). The unintentionally high gain for $A5$ raised the helion energy threshold by $\sim$ 3 MeV (to $\sim$ 13 MeV) i.e. $\Delta E_h = 7\,\mathrm{MeV} \longleftrightarrow E_h =$ 13 MeV.

The B-detectors (1000 μm or 500 μm silicon) were required to cover a wide dynamic range: 1000 μm Si stops up to 43 MeV helions, yet the energy loss for 100 MeV protons is only 1.4 MeV. We feared that if we were to set the gains low enough to include all the helions, lower-level thresholds in the linear electronics might cut into the high-energy proton locus corresponding to low ΔE in the particle identification (PID) spectra. As confidence in the high-energy proton data was crucial to this experiment, we set the gains at what we considered to be safe values: for the 1000 μm detectors, 1024 chann.$\longleftrightarrow\sim$ 30 MeV, with the result that there was a large gap in the measured energy distributions for ^{4}He(p,ph), extending from $\sim$ 30–43 MeV.

Using the elastically-scattered protons from carbon as a guide, we set the amplifier gains for the NaI detectors such that 1024 chann.$\longleftrightarrow\sim$ 100 MeV. A shaping time constant of 1 μs was employed in all the linear amplifiers.

The Delay Amplifiers were then adjusted so that the signals would arrive

at the ADCs synchronously. DC-levels in the Linear Gate & Stretchers were eliminated and the ADC zero-channels were set to ~0 MeV. This completed the setup of the linear electronics.

On the logic side of the electronics, the biggest problem was the setting of the thresholds in the Constant Fraction Discriminators associated with the A- and B-detectors. Ideally, these thresholds should sit safely above the noise but below the level of the highest energy (lowest ΔE) protons. However we were obliged to allow some of the noise through so as not to cut into the proton locus in the PID spectra. Consequently, in the early part of the run, some of the timing (TAC) spectra were "dirty" as a result of timing jitter and a few thresholds were raised again. In one case (Telescope 5) high energy protons were then lost from the PID spectrum. In the next chapter (Sections 3.4.2 and 3.4.6) these problems with the TAC spectra and with the PID cutoff in Telescope 5 are discussed further.

Delays were introduced, firstly to synchronize the timing of the three elements of each telescope (telescope logic), and then to put all six telescopes in coincidence, including the pre-scaled-singles branches of Telescopes 1 and 2 (event logic). The Stop pulse to each TAC was delayed such that "real" events would stop the TAC roughly in the middle of the selected timing range. Gate pulses were aligned with their respective linear signals in the Linear Gate & Stretchers, and the Strobe signal to the Pattern Registers was delayed to ensure the prior arrival of all the input signals (discriminators were employed to stretch these signals).

Finally, all the pulsers were adjusted to satisfy the timing requirements for a six-fold telescope coincidence (of course only two were needed to signal a coincidence "event") and their amplitudes were set such that the pulser peaks would appear clearly on the PID spectra, well above the dense proton, deuteron and triton loci.

2.9.3 Setting up the Software

The various PID gates were set by means of the cursor on the graphics terminal, to select protons in the primary telescopes, and protons, deuterons, tritons or helions in the secondary telescopes. 1-D gates in the TAC spectra selected the "real" peak and a peak containing only random events. The utilization of these gates in the event-by-event processing of data will be discussed more fully in the next chapter.

2.9.4 Calibrating the detectors

Calibration of the NaI detectors was done towards the end of the run; the coincidence requirement in the event logic was disabled so that singles spectra could be acquired from the polythene and helium targets with the telescopes at various angles between 15° and 90°.

In order to calibrate the silicon detectors, the scattering chamber was vented at the end of the run, and ^{228}Th α-sources were placed a few centimetres from the gold (grounded) surface of each detector. Calibration spectra were acquired once a suitable vacuum had been attained. As we had only three ^{228}Th sources available, it took four pump-down cycles to complete the calibration of all 12 silicon detectors.

2.9.5 Determining the Angular Offset

After acquiring the data for the NaI energy calibrations, we moved the arm carrying the secondary detectors to a backward angle so that the primary telescopes could be swung from one side of the beam to the other. With the polythene target in position and Telescope 1 at $\sim 50°$, short runs were recorded for a cluster of angle settings, separated by $\sim 0.4°$. This procedure was then repeated with Telescope 1 at $\sim 50°$ on the opposite side of the

beam. The angle chosen for this exercise could not be more forward than 50° because Telescope 2 had to be well clear of the beam when on the opposite side (see Figure 2.10). The angular offset between the beam direction and the zero-degree readout of the shaft encoder on the detector arm would then be determined from a comparison of the positions (energies) of the hydrogen elastic peak at the various angle settings and/or from a comparison of the various elastic and inelastic cross sections for $^{12}C(p,p')^{12}C^*$.

On our first attempt at these measurements, bizarre inconsistencies were apparent in the above comparisons. We soon realised that the shaft encoder on the detector arm was behaving in an unreliable manner, possibly owing to prolonged operation in vacuo (although it had been specifically designed for vacuum conditions). Fortunately, a careful investigation of the data from the last few runs leading up to this catastrophe (some coincidence runs and the NaI energy calibrations) convinced us that the problem had not existed earlier. It was also easy to determine that on the few occasions that this detector arm was moved, prior to the problem, the readout could still be trusted. Thus we suspect that the breakdown in the encoder was precipitated by our moving the arm through a large angle to the opposite side of the beam.

A few hours later, the encoder reverted to normal operation and we were able to determine the angular offset in a self-consistent manner (see Section 3.2). This offset could then be used to correct the readout angles of *both* arms, as the separation angle between the arms had earlier been shown (by checks with a theodolite) to be exactly the difference between the readout angles.

Only one coincidence angle setting remained to be covered before the end of the experiment; once again, the encoder readout started behaving strangely, with the result that the value for the last angle setting is not

known accurately. It was not an important angle, however, and the data are not presented here. The faulty encoder has since been replaced with a simpler and (hopefully) more reliable model.

2.9.6 Taking Data

We started taking data on 11 October 1987 and finished on 2 November, a little over three weeks later.

At frequent intervals during the run, we checked the quality of the beam by replacing the gas cell with the empty frame and comparing raw count-rates (we had ratemeters connected permanently to several of the linear amplifiers). Although beam halo is not as troublesome in a coincidence experiment as it is in a singles experiment, we tried to keep it as low as reasonably possible. Occasionally it was necessary to look at the beam spot on the BeO scintillator. We always found it to be well centred, except after major breakdowns (and one other time, when it was $\sim$1 mm too high). The size of the beam spot was typically 2 mm $\times$ 2 mm, well within our requirements for "good overlap" of telescope response regions (see Section 2.5). During acquisition at two of the angle settings, the spot was somewhat wider (up to 4 mm), but the angles were such that "good overlap" was ensured.

Some of the angle settings took two or three days to complete but we split the data into several runs by stopping and re-starting the acquisition every few hours. This made the subsequent task of replaying the data simpler, e.g. in monitoring gain drifts on a run-by-run basis. It also enabled us to adjust the supply voltage to the preamplifiers of the silicon detectors in order to maintain constant bias voltages across the detectors themselves under conditions of changing leakage currents, which are very sensitive to slight changes in ambient temperature, and degradation due to

surface deposits and radiation damage. Towards the end of the experiment the leakage current in detector $B6$ started increasing quite rapidly and we decided not to maintain full depletion bias on this detector. The effect on the data was negligible.

At the start of each run we recorded the pressure in the gas cell. We also continuously monitored the performance of the detectors and the electronics by scrutinizing the XSYS histograms as the data came in. Fortunately the electronics were very reliable: although there were a few breakdowns during setup, not one of the 158 NIM modules gave problems for the remaining three weeks! Three of the ADC-to-CAMAC interface modules and one of the CAMAC crates had to be replaced during the experiment.

The choice of beam current was governed by two factors: firstly, the need to keep pile-up and other sources of electronic dead time down to a reasonable level (<10% in each telescope); and secondly, the need to maintain a good ratio of real-to-random coincidences. By keeping the raw count-rates in the NaI detectors $< 10^4\,s^{-1}$, and monitoring the pulser peaks in the PID spectra for excessive pile-up, we were able to satisfy the first consideration (during replay we discovered that the dead time in Telescope 6 had been a little high, 11–14%, but in all the other telescopes it was <10%).

The real-to-random ratio was generally >2:1, which we expected to result in a 10–15% component of random coincidences in the region of interest (the ground state knockout locus). However, during the experiment we underestimated the effect of the macroscopic structure in the beam (see Section 3.8.1) and the random coincidences turned out to be a larger component than we would have liked, typically 20–30%.

The initial intention, as described in Section 2.5, was to cover the primary angles in two sets of measurements, i.e. with Telescopes 1 and 2 at (15°;45°) and at (30°;60°). Early in the experiment, it became apparent

that in order to obtain adequate statistics at 45°, the beam current would have to be such that any data acquired at 15° would be of limited use because of high random coincidence rates and dead times. As we were more interested in the data at 45° than at 15°, we decided to abandon 15° and run the pair of primary telescopes at (45°;75°) and (30°;60°) instead. The measurements at 45° thus benefited from the active collimator mounted on Telescope 1.

With the primary telescopes at (30°;60°) a similar problem arose, although it was less serious than at (15°;45°). The beam current was optimized for the telescope at the more "interesting" angle, 60°, with the result that dead times and real-to-random ratios are not good in the data collected at 30°. Although the 30° data may be of some interest, they have not been analyzed at this time, because the range of secondary angles is somewhat restricted. With hindsight, then, this experiment could have been performed in the same time with a single primary telescope, which would have greatly simplified the setup!

Chapter 3

Replay and Results

3.1 Overview

In replaying the data, the aim was to produce cross sections for the quasifree knockout (to the ground state of the residual nucleus) of protons, deuterons, tritons and helions as a function of the energy of the proton detected at the primary angle. These "energy-sharing" spectra form the data base for comparisons with theoretical calculations, which are discussed in Chapter 4.

The presentation of the data analysis in this chapter follows in more-or-less chronological order the various tasks which were performed in order to render the experimental results in final form. Thus we start with the determination of the angular offset of the beam, which was a prerequisite for performing the energy calibrations of the detectors, the subject of the section following that. Further preparations for the sorting of event data included setting the software gates and tailoring the event-analysis (*EVAL*) program for offline analysis. After explaining the flow chart for sorting, we describe the replay of the event data, during which corrections were applied for gain drifts in the NaI detectors. During replay, the effects of electronic thresholds on the analyzed data were also monitored continuously.

A selection was then made of a subset of the replayed data for further analysis. We describe how the two-dimensional energy spectra were converted to summed-energy spectra and how the quasifree knockout locus was selected for projection onto the energy axis of the primary proton.

During projection of the two-dimensional data to yield energy-sharing spectra, a normalization factor was introduced which converted the relative yields to absolute cross sections. The various quantities which contribute to this factor are discussed; then the projections themselves are described, along with an account of the subtraction of random coincidences and the corrections for reaction tail losses in the NaI detectors.

This is followed by a discussion of the systematic errors in the analysis

of the data.

The final results may then be presented (along with the statistical errors, which have been propagated consistently throughout the analysis).

3.2 Angle Calibrations

The positions of the scattering chamber arms are given by shaft encoders which are read out on digital display panels in the Data Room. In order to relate these readout angles to the actual scattering angles of each detector telescope, one needs to know firstly, the relative angle between each telescope and the centre of the arm on which it is mounted, and secondly, the angular offset of the beam with respect to the zero-degree readout position of each arm.

During setup of the scattering chamber, a theodolite was used to measure the former relative angle. Normally, the angular position of a collimator is quite simply defined by an imaginary line passing through the centre of the target and through the centre of the exit hole in the back of the collimator, and it was the angle between this line and the centre of the arm which was measured. However, the portion of a gas target seen by a detector is determined by both apertures of the double-aperture collimator, and the centre of this portion of target only corresponds to the centre of the scattering chamber if the front slits are symmetrically positioned with respect to the imaginary line defined above, as of course they should be. Because of dimensional tolerances encountered in the manufacture of the slits which were used, this was not always the case, and corrections of the order of 0.1° had to be made to some of the scattering angles. It followed that, for a particular readout angle, the telescope defined slightly different scattering angles depending on which of the two sets of front slits was in

use, or on whether the target was solid or gaseous. Nevertheless, care was taken in the analysis always to work with the correct scattering angles for each situation.

The quantity which we call the "angular offset of the beam" is actually the difference between two offsets:

1. The horizontal component of the angle between the beam and the centreline of beamline A, which is the true "beam offset"; and

2. The angle between the detector arm when the readout is indicating zero degrees and the centreline of beamline A, which is an alignment error of the scattering chamber.

For our purposes, however, the relative contributions of these two components are irrelevant and we may determine an overall angular offset. Either of the arms may be used for this purpose provided that the two arms have no relative offset between them, which was confirmed by means of the theodolite.

As explained in Section 2.9.5, measurements were taken at $\sim 50°$ on either side of the beam with Telescope 1 and the polythene target. At these large angles, the elastic and inelastic peaks from $^{12}C(p,p')^{12}C^*$ were fairly small and gave inconsistent results because of uncertainties in subtracting backgrounds. However, the centroid of the hydrogen elastic peak could be determined well enough for us to measure the offset as $-0.5° \pm 0.1°$.

The out-of-plane angles β for Telescopes 4 and 5 were measured by means of a precision protractor to be 15.3° and 30.8° respectively. Although kinematic quantities have been calculated with the correct angles throughout this work, the angles quoted in the text and figures have been left uncorrected in order to simplify the presentation. For the record, the corrected primary angles were 45.5° and 60.5° (quoted as 45° and 60°), and the corrected secondary angles differ by up to 0.6° from the quoted values.

3.3 Energy Calibrations

3.3.1 Silicon detectors

Seven of the peaks in the energy spectrum of α-particles from ^{228}Th, between 5.3 and 8.8 MeV, were used for the calibration of the silicon detectors. The *CAL ENER* command of XSYS was used to obtain linear fits—the worst point on the calibration curves for the twelve detectors deviated by only 0.2% from the fitted line.

3.3.2 NaI detectors

A simplified version of the EVAL sorting program was used for replaying the calibration runs, with particle identification gates set (see Section 3.4.1) on protons and deuterons. Peaks from elastic scattering off hydrogen, helium and carbon, and inelastic scattering to several of the excited states of carbon, were identified in the proton spectra obtained at various angles from the polythene and helium gas targets. In calculating the energy deposited in a NaI detector by protons arising from these events, the energy lost in the silicon detectors and in the Havar foils of the gas cell (for the helium target) was taken into account.

Linear fits to various sets of calibration points were found to be more consistent with one another when (0;0) was assumed to be one of the calibration points. Even though the response function of NaI for protons in the energy range up to 100 MeV is slightly non-linear, the linear fits were found to be adequate for the purposes of this experiment—all the points, including those not used in the fitting routine, generally lay within 2% of the lines.

The response of the NaI detectors to deuterons was determined from the reactions ^{4}He(p,d)^{3}He(g.s.) and ^{12}C(p,d)^{11}C*(g.s. and 2.00 MeV) at

various angles for the detected deuterons.

The calibration of one of the detectors for protons and deuterons is shown in Figure 3.1. The response to deuterons is consistently ~4% greater than to protons of the same energy, which is the opposite trend to that for α-particles and heavier ions, but in agreement [Bir64][Mei87] with that found for deuterons in CsI(Tl).

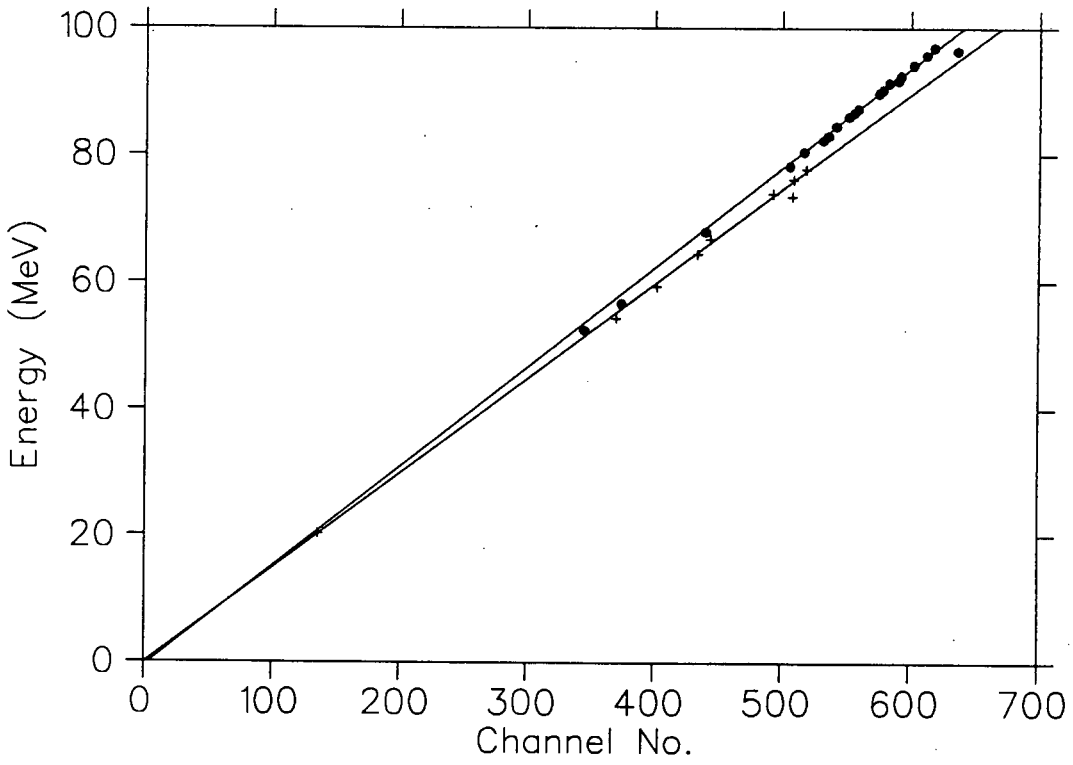

Figure 3.1: *Response of one of the NaI detectors to protons (dots) and deuterons (crosses). The lines are least-squares fits to the data points.*

As we had no peaks upon which to base a direct calibration for the response to tritons, we assumed it to have the same trend as for deuterons,

with twice the difference in slope as between the proton and deuteron responses, which is roughly the trend [Mei87] found in CsI; i.e. the triton response was assumed to be ~8% greater than that for protons. Although this procedure might seem rather arbitrary, it should be noted that the energy-sharing spectra (Section 3.8) were obtained from projections onto the energy axis of the *primary proton*; calibrations for the other particles merely needed to be good enough to ensure reasonably straight knockout loci in the summed-energy spectra (Section 3.6).

The response to helions was assumed to be the same as that to α-particles, for which some calibration points were obtained from elastic scattering on the helium target. Probably because of the large energy losses and straggling of the elastically-scattered α-particles in the Havar window and silicon detectors, the calibration was not as reliable as for the lighter particles. Nevertheless, the response of the NaI detectors was clearly ~20% *less* than that for protons of the same energy, which is the opposite trend to that for deuterons, but in agreement with other work at lower energies [Bir64] and with the trends found [Mei87] in CsI.

3.4 Replay

3.4.1 Particle Identification

The thickness of each detector in the three-element telescopes was chosen to enable the identification of protons, deuterons, tritons and helions over a wide dynamic range: for the lower energies, the 100 μm silicon detectors (elements A) provided the ΔE values for particles stopped with energy E in the 1000 μm (or 500 μm) silicon detectors (elements B); for the higher energies, the B detectors provided ΔE values for particles punching through to the NaI detectors (elements C). There were thus two sets of

2-D histograms for ΔE vs E particle identification (PID), the "AB" spectra and the "BC" spectra.

Typical examples of each are shown in Figure 3.2. Also shown in the figure are some of the software gates which were set to select the particles of each type (only protons were selected from the primary telescopes).

In regions where the particle loci were not well separated, adjacent gates overlapped each other, so that in some cases a particle would be double-counted, e.g. as a deuteron *and* as a triton. However, most of the wrongly-identified particles would fall outside the quasifree knockout locus in the corresponding summed-energy spectra (see Section 3.6) and would thus not contribute to the wrong energy-sharing distributions. A certain amount of double-counting was considered preferable to making the gates too narrow, with the danger of cutting into the loci at some energies more than at others, which would affect the shapes of the energy-sharing distributions.

3.4.2 Time Gates

For each of the eight coincident pairs of telescopes (two primary with four secondary), a coincidence timing (TAC) spectrum was generated, which consisted of the "real" coincidence peak with several "random" coincidence peaks on either side of it. Two software gates were set on each spectrum: one on the "real" peak and the other on one of the "random" peaks, so that subtraction of random coincidences could be performed at a later stage (Section 3.8.1). In Figure 3.3, a typical TAC spectrum with its associated gates is shown.

In the early stages of the experiment, a few of the electronic thresholds were set too low, with the result that, in some TAC spectra, real coincidences were spread over two peaks due to noise-related timing jitter. For the replay of those runs, the gate was set over both peaks and the gate on

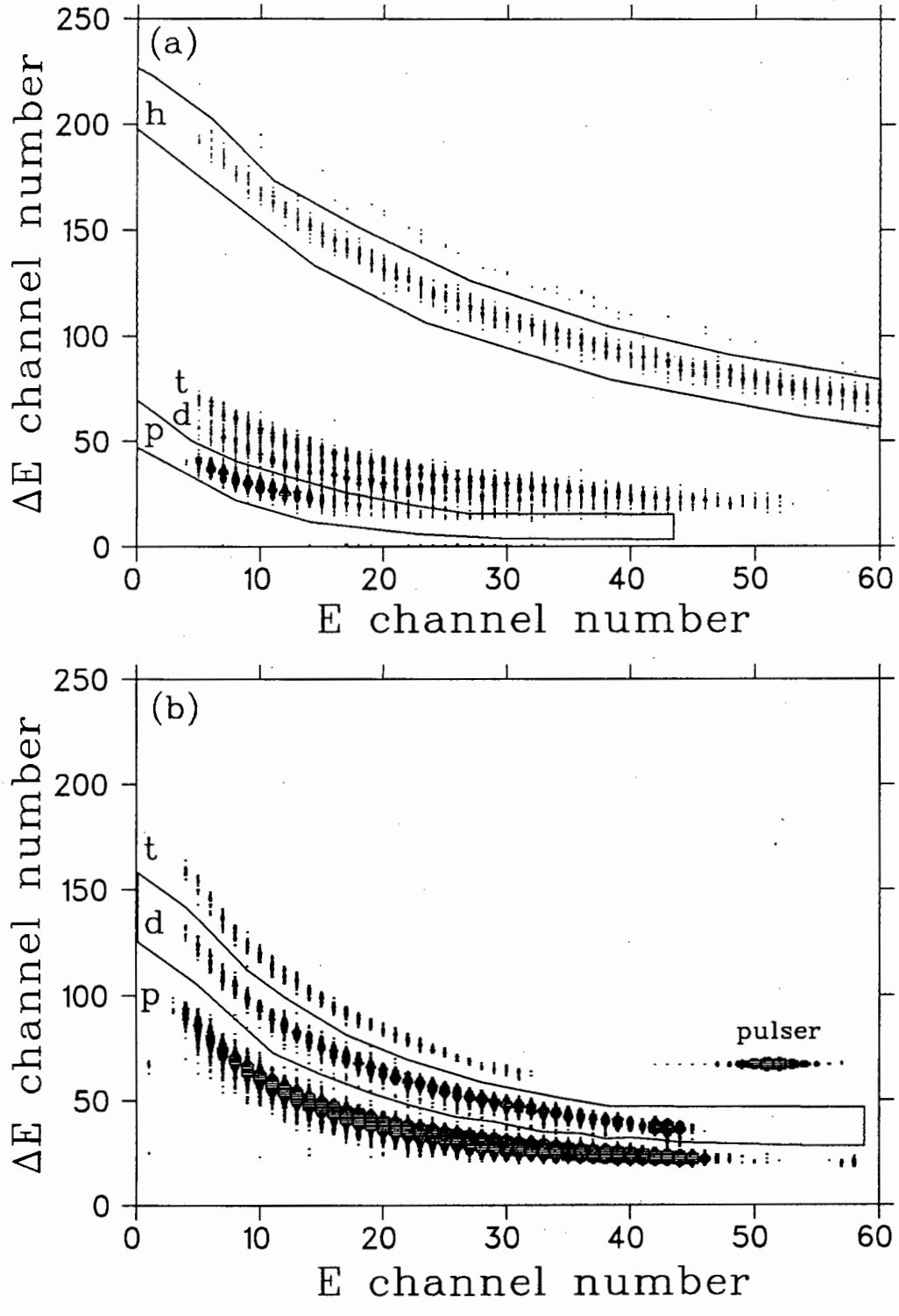

Figure 3.2: *Typical particle identification spectra, (a)* AB *for lower energies and (b)* BC *for higher energies. In order to keep the figure uncluttered, not all the PID gates are illustrated.*

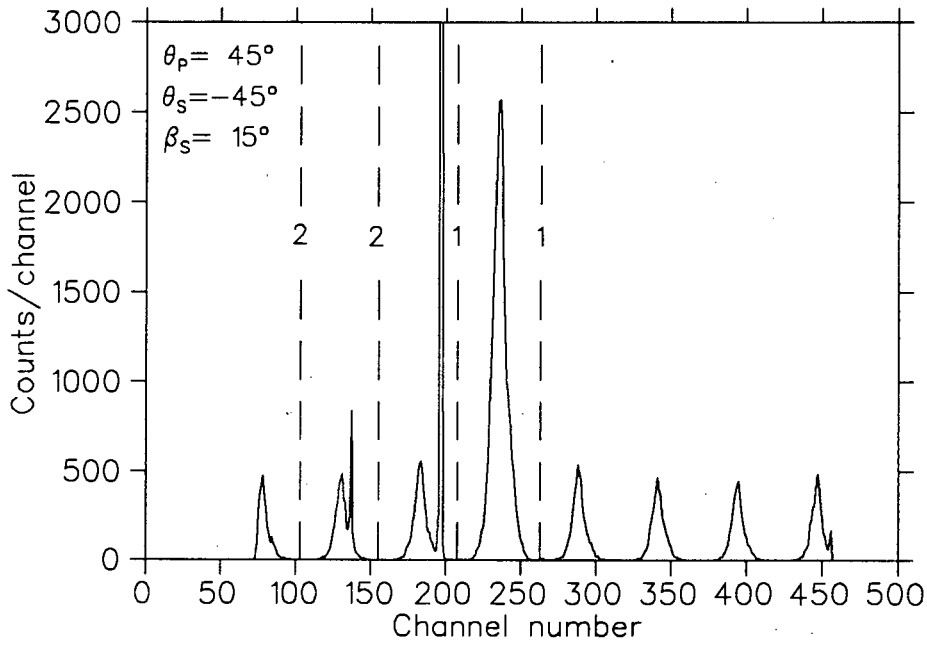

Figure 3.3: *A coincidence timing (TAC) spectrum, with Gate 1 set on the "real" peak and Gate 2 set on a "random" peak. The fall-off in successive peaks on either side of the "real" peak is due to macrostructure in the beam. The sharp peaks at channel numbers 140 and 190 are caused by different types of pulser coincidences.*

random coincidences was also widened to include two peaks. Even after eliminating most of the timing jitter, we avoided the peaks adjacent to the "real" peak in setting the gate on a "random" peak, so that we could be confident that the events within this gate consisted of random coincidences only.

3.4.3 Pattern Registers

In Section 2.7, it was explained how different levels would be set in the Pattern Registers by each of the detector telescopes when they fired; other levels would identify those events which were of low energy; yet other levels labelled the pre-scaled singles events. In the sorting of event data it is normal to use the bit pattern recorded by these registers, in conjunction with various tests on software gates, to control the flow of the sorting program (EVAL). However, during replay of the energy calibration runs, a few anomalies became apparent in the bit patterns, e.g. in some cases, the bit signifying a "low-energy event" in a particular telescope would not be accompanied by the expected bit signifying an "event" in that telescope (for some telescopes, this happened for up to 10% of the total counts). Such events would not have been processed and recorded at all if the problem had lain in the "telescope logic" electronics (see Section 2.7), so it must have been in the setting of levels for the Pattern Registers themselves (or in reading from them).

Consequently, in the version of EVAL used for replaying the data, and described below, the test for whether a particular telescope had fired was based on there being a non-zero value in the ADC for element B of that telescope. As the gate on the Linear Gate & Stretcher was opened only if that telescope had fired and as a value for element B was required for both low- and high-energy events, this was an equivalent test.

3.4.4 Event Sorting (EVAL)

Before replaying the event tapes, we altered the memory allocation somewhat from that used during acquisition of the data (Section 2.8):

- Whereas previously we had stored only a *sample* of the "random" and "ungated" energy-sharing spectra for comparison with the "real" spectra, now all the "random" spectra were required (for later subtraction from the "real" spectra). Because of the limitation on total global memory size (within XSYS) of 3072 pages, we were forced to split the replay into four separate runs, one for each selected type of secondary particle.

- The pre-scaled singles histograms were no longer required—they had been used during acquisition to monitor the quality of the incoming data and to confirm the shapes of the inclusive spectra of Wesick *et al.* [Wes85]. Instead, pre-scaled singles events were simply combined with the coincidence events in the "singles" energy spectra of Telescopes 1 and 2.

- The size of the ΔE vs E histograms was increased from 64×64 channels to 64×256 channels in order to improve the ΔE channel-resolution for regions in which the particle loci were poorly separated. This allowed the particle identification gates to be set more accurately.

Figure 3.4 is a flow chart for the version of the event analysis (EVAL) program in which secondary deuterons were selected in coincidence with the primary protons. The nomenclature for the energy histograms is "element; telescope" e.g. $A3$ means element A (thin silicon detector) of Telescope 3; $TIME13$ means the TAC spectrum for coincidences between Telescopes 1 and 3.

It should be noted that the flow of the program is such that multiple coincidences are handled as a series of separate two-telesope coincidences. One might have expected these to be so few that a more efficient flow, ignoring multiple coincidences, could have been used in the program. However,

our earlier inspection of the Pattern Register histograms (Section 3.4.3) had revealed a significant number (~3%) of such events, probably due to the fact that count rates were at times higher than optimum in some of the telescopes.

The other versions of EVAL, for secondary protons, tritons and helions respectively, differed only in the choice of particle identification gates and in the energy calibration variables for the response of the NaI detectors to the different secondary particles (see Section 3.3.2).

3.4.5 Gain Drifts

The photomultiplier tubes of the NaI detectors are susceptible to significant gain drifts [Leo87] when the count-rate changes, for instance on moving to a new angle. Even at a steady count-rate, they may suddenly drift for a short period before stabilizing at a new gain. Over the course of the experiment, drifts of the order of 10% in gain were typical; one of the Harshaw detectors (Telescope 4) was particularly unstable, with a change of over 30% from the initial value! Fortunately, however, the gain tended to "jump" to a new value, i.e. it would take only a few minutes to stabilize (a short period of time in a typical coincidence run of several hours). Consequently, the energy resolution of a telescope could be kept within reasonable limits as long as these drifts were monitored and the appropriate corrections were applied to the calibration variables used by EVAL.

We adopted the following procedure for handling these drifts. On the first scan of the tapes, the peaks due to elastically scattered protons from the ^{4}He target and also, when they were discernible, the peaks from the (p,d)(g.s.) reaction were continuously monitored. These peaks were visible because of random coincidences and, for Telescopes 1 and 2, pre-scaled singles events. Whenever one of the gains had drifted by more than ~3 MeV

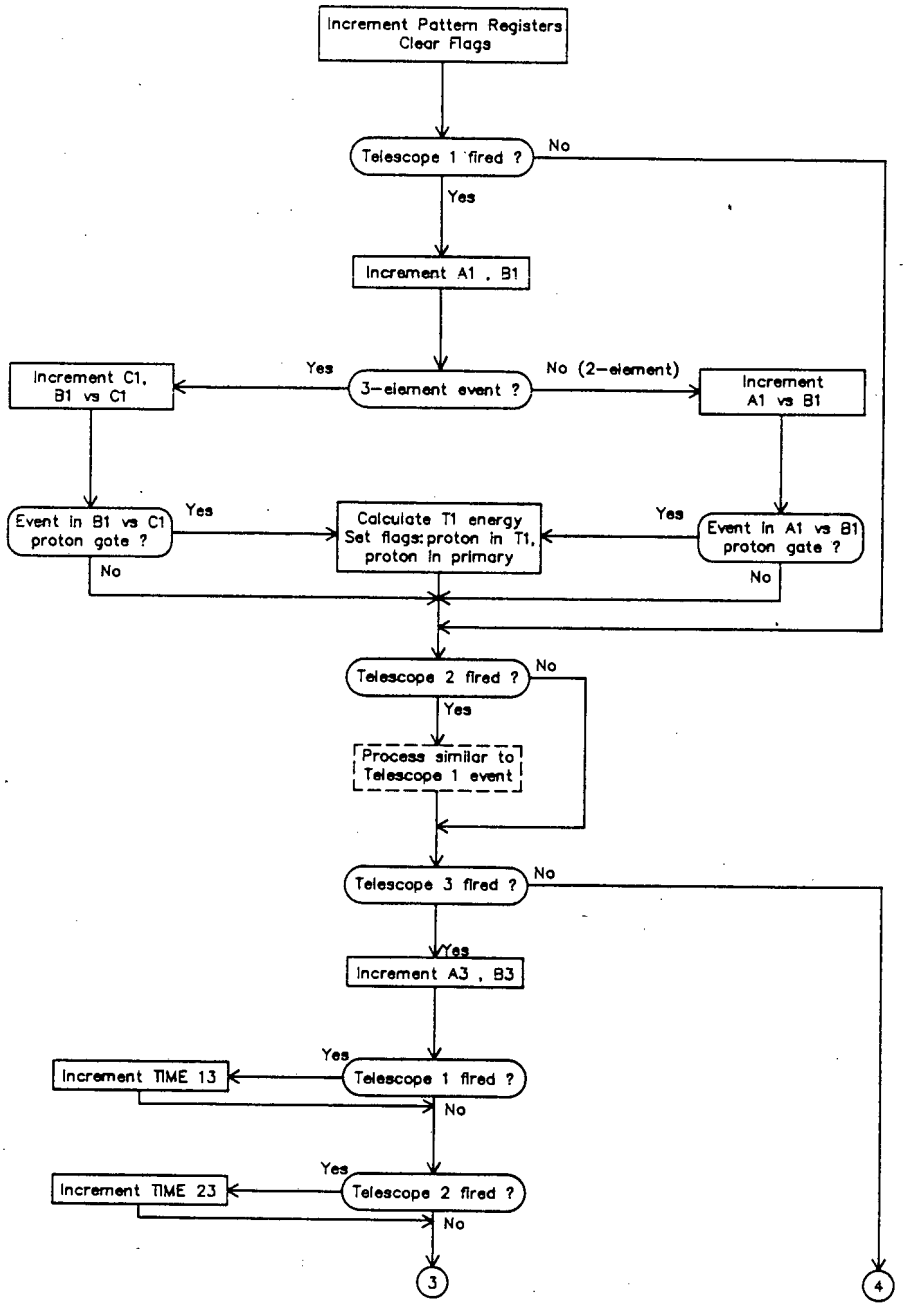

Figure 3.4: *Flow chart for the event analysis (EVAL) program. In the version depicted here, the proton-deuteron coincidences are selected. The versions which select the other secondary particles are similar to this one.*

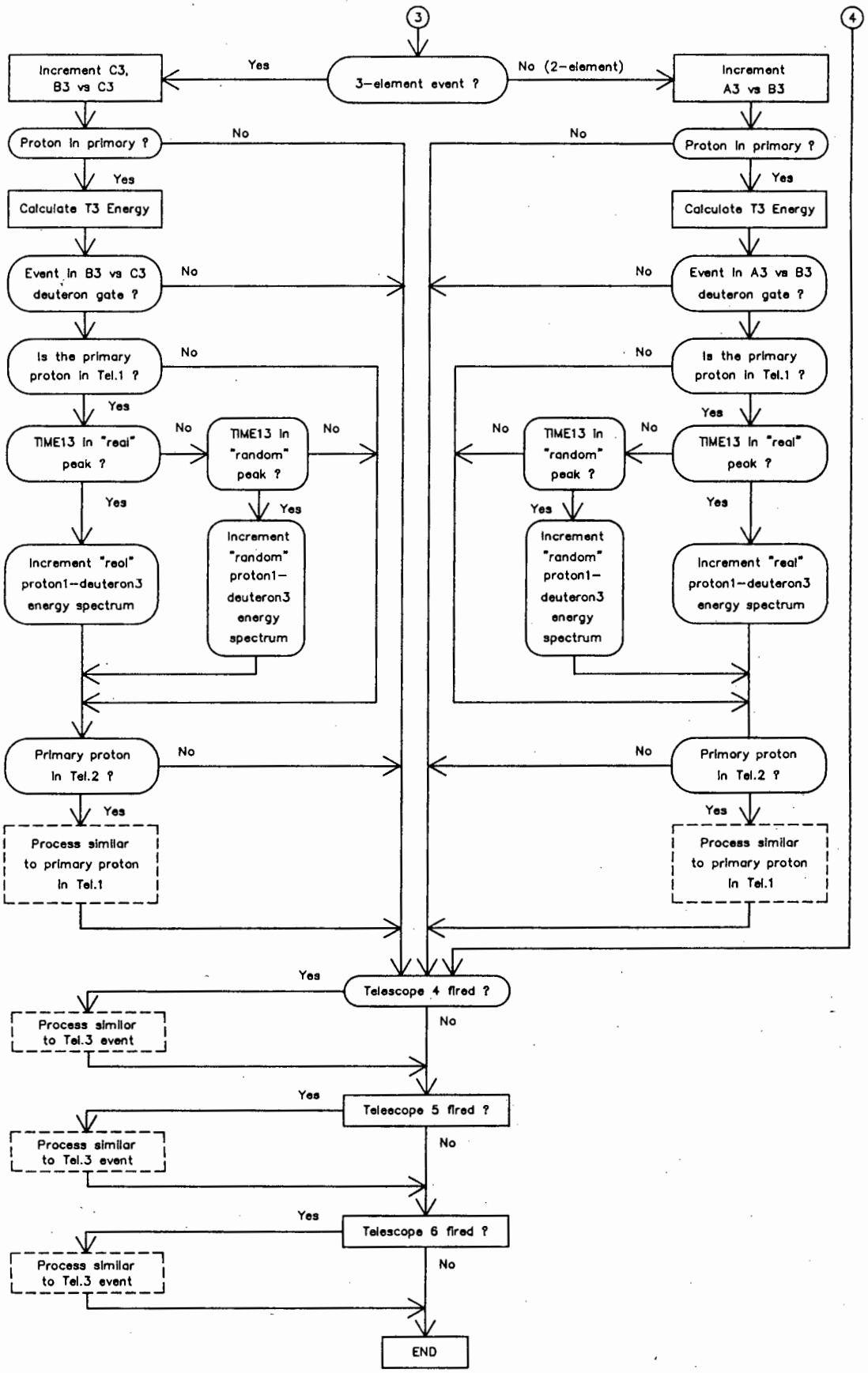
3
4
3-element event ?
Yes
No (2-element)
Increment C3, B3 vs C3
Increment A3 vs B3
Proton in primary ?
No
Yes
Calculate T3 Energy
Event in B3 vs C3 deuteron gate ?
Event in A3 vs B3 deuteron gate ?
Is the primary proton in Tel.1 ?
TIME13 in "real" peak ?
TIME13 in "random" peak ?
Increment "real" proton1–deuteron3 energy spectrum
Increment "random" proton1–deuteron3 energy spectrum
Primary proton in Tel.2 ?
Primory proton in Tel.2 ?
Process similar to primary proton in Tel.1
Telescope 4 fired ?
Process similar to Tel.3 event
Telescope 5 fired ?
Telescope 6 fired ?
END

(3–5%) from the calibrated value, we "back-tracked" a little and restarted the scan with corrected values for the calibration variables. Because this procedure was so tedious and involved inherent inaccuracies so much greater than in the calibrations described in Section 3.3.2, we simplified those calibrations by forcing the lines through (0;0), so that only one variable, the slope, would need to be changed to compensate for gain drifts. For each case, an average factor was determined which gave the best correction to the proton and deuteron calibrations, and the slopes for the triton and helion calibrations were assumed to need correcting by the same factor.

Subsequent scans were much less time-consuming, as we were able to set up a command procedure file to make these corrections automatically.

3.4.6 Cutoffs in PID spectra

As mentioned in Section 2.9, the thresholds of the Constant Fraction Discriminators had to be increased in some cases because of excessive noise causing jitter in the timing of the fast logic pulses. In the case of detector $B5$, the threshold then cut into the proton locus in the $B5$ vs $C5$ PID spectrum . The onset of the cutoff is gradual, however, so instead of rejecting the data from that region, which may still be useful in indicating general trends, we have retained them in the results which we present (although they are clearly indicated, as a reminder that they should be treated with suspicion). As the effect of the cutoff worsens towards higher energies of the *secondary* proton, it is the *lower* energy data points which are affected most in the "cutoff" regions indicated on the energy-sharing spectra of Figures 3.9 to 3.11.

The PID histograms of all the telescopes were monitored during replay of the data; none of the other thresholds was high enough to cause the same cutoff phenomenon as in spectrum $B5$ vs $C5$.

3.5 Selection of Spectra

After replaying all the data, we chose a subset of the 408 energy-sharing spectra for further analysis. Firstly, we decided to concentrate only on those data for primary angles θ_P of 45° and 60° (204 spectra), i.e. neglecting the primary angles 30° and 75°. Of these, 42 spectra were selected for $\theta_P = 45°$ and 20 for $\theta_P = 60°$ (there were fewer spectra at $\theta_P = 60°$ because the major yield of coincident secondary particles was confined to a smaller region of laboratory coordinate space). The selection of proton-proton spectra is shown in Figure 3.5.

The main criterion was to choose a set of spectra which was not so large as to be too time-consuming and unwieldy to analyze, but was large enough to enable us to follow the trends in the data. The reason for neglecting the most forward-angle spectra was the poor statistical accuracy of those data.

At the secondary angles $(\theta_S; \beta_S) = (-35°; 0°)$, there were two entirely independent sets of data involving different telescopes and slit widths, which was a useful indication of the systematic error (see Section 3.9.2).

For the proton-deuteron coincidence spectra, the same set of angles was chosen as for the proton-proton spectra, except for $(\theta_P; \theta_S; \beta_S) = (45°; -80°; 0°)$, $(45°; -90°; 0°)$ and $(60°; -70°; 0°)$, which were left out because of poor statistical accuracy.

The angle sets $(45°; -90°; 0°)$ and $(60°; -50°; 0°)$ were left out of the set of proton-triton spectra, because electronic thresholds cut into the knockout loci too severely; otherwise the set of angles was the same as for proton-proton coincidences.

Most of the spectra for the ^{4}He(p,ph) reaction were of no practical use because so much of the quasifree knockout locus was lost in the wide gap between the regions corresponding to "low-energy" and "high-energy" helions, which was explained in Section 2.9. At four geometries, however, the en-

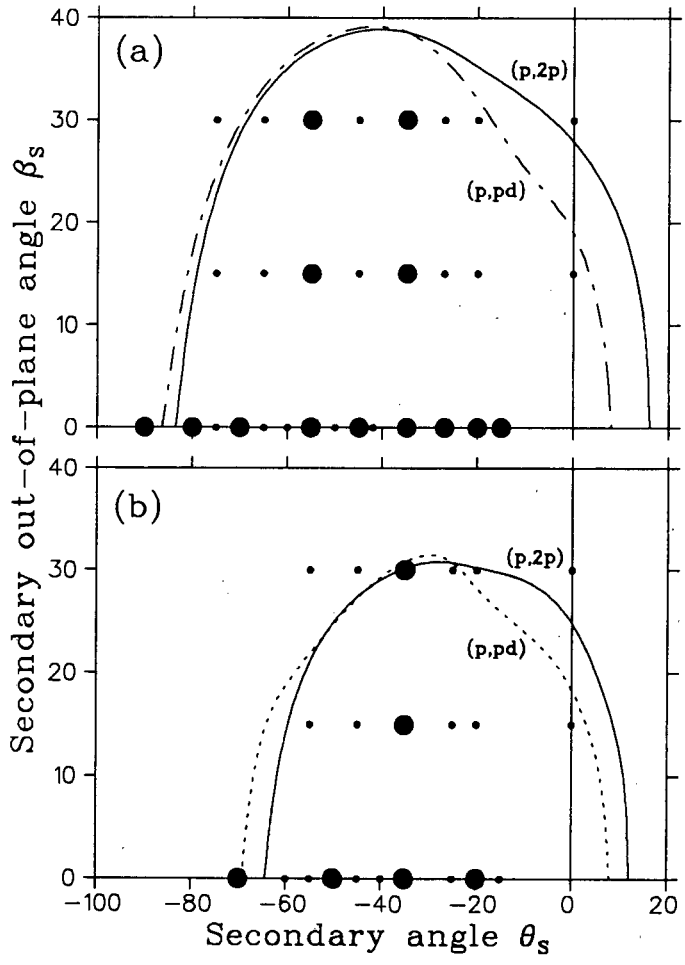

Figure 3.5: *Selection of a subset of the data. The available geometries for (a)* $\theta_P = 45°$ *and (b)* $\theta_P = 60°$ *are indicated by the dots, with the selected spectra shown as large dots. The loci within which recoils of* < 200 MeV/c *are possible, are indicated as in Figure 2.1.*

tire locus fell within the low-energy region, so these were chosen for further analysis: $(\theta_P; \theta_S; \beta_S) = (45°; -55°; 15°)$, $(45°; -65°; 0°)$, $(45°; -65°; 15°)$ and $(60°; -55°; 15°)$.

3.6 Summed-energy Spectra

A FORTRAN program was written to convert the 2-D energy-sharing spectra into spectra of summed-energy vs primary proton energy.

$$E_{Sum} = E_P + E_S + E_R - Q,$$

where the subscripts P, S and R refer to the primary, secondary and recoil particles respectively. E_R was calculated with the use of relativistic kinematics. The locus for quasifree knockout to the ground state should thus be a straight line at constant $E_{Sum} = 100$ MeV.

Sample 2-D energy-sharing spectra and their corresponding summed-energy spectra are shown in Figure 3.6. The width of the locus is an indication of the missing mass resolution, whereas deviations from the straight line at 100 MeV reflect calibration errors and non-linearities.

Also shown in the figure are the ranges which were selected for projecting the knockout locus onto the primary proton energy axis. Each summed-energy range was subjectively chosen to include the full width of the locus. Although the loci were typically ~6 MeV wide, inaccuracies in the energy calibrations caused them to be skew, which resulted in some ranges having to be somewhat wider (up to 17 MeV in the worst case).

The vertical dashed lines on the plots indicate the ranges of primary proton energies which were included in projecting the spectra onto that axis. Firstly, data below 4 MeV were discarded because they fell within the lower threshold region of the primary telescope. Then at ~14 MeV, there is a gap in the data between the "low-energy" and "high-energy" portions of

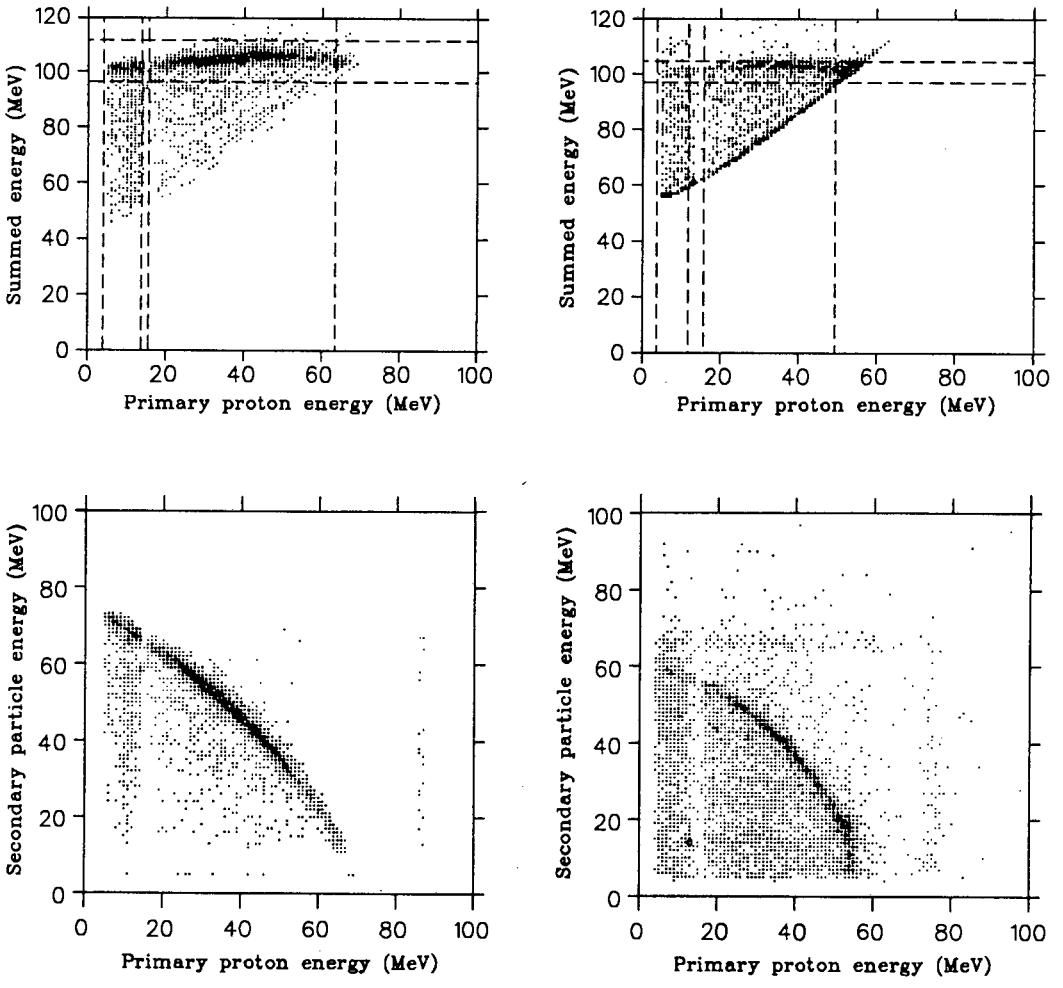

Figure 3.6: *Examples of 2-D energy-sharing spectra (below) which were converted to summed-energy spectra (above) as described in the text. The quasifree knockout loci are clearly visible. The dashed lines indicate the regions of the loci that were chosen for projection onto the energy axis of the primary proton.*

the primary proton spectrum, caused by electronic thresholds for the NaI detectors. This gap was typically 2–4 MeV wide, including the broadening due to binning effects (the energy bins are 1 MeV wide).

For the secondary telescope, the corresponding low-energy threshold is seen on the summed-energy plots as the diagonal high-energy cutoff to the data. In the plot on the left, the diagonal energy gap corresponding to the NaI detector threshold of that secondary telescope is also visible. On the right, where data from a different telescope are presented, the threshold was lower and the gap is not discernible.

Because these latter thresholds and gaps run diagonally, some of the data at highest primary proton energies must inevitably be discarded, as indicated by the uppermost vertical lines in the figure. In order to retain these data, one would need to perform the projections in a different way (against a different dependent variable) as, for example, has been done by Darden *et al.* [Dar88], who project against an energy ordinate along the kinematic locus of interest itself.

3.7 Conversion to Absolute Cross Sections

The conversion to absolute cross sections was done at the same time as the projections, by the inclusion of normalization factors in the command procedure files. In this section, we describe how these factors were determined.

The triple differential cross section for the (p,p'x) reaction is given in the laboratory system by

$$\frac{d^3\sigma}{d\Omega_{p'}d\Omega_x dE_{p'}} = \frac{YC_{DT}}{\Delta\Omega_P\Delta\Omega_S\Delta E_P N_0 n_t t_{eff}},$$

where Y is the number of counts in a bin at primary energy E_P,
C_{DT} is a correction factor for electronics dead time,
$\Delta\Omega_P$ is the solid angle subtended by the primary detector telescope,
$\Delta\Omega_S$ is the solid angle subtended by the secondary telescope,
ΔE_P is the width of the energy bin,
N_0 is the number of protons incident on the target,
n_t is the number of target nuclei per unit volume, and
t_{eff} is the effective thickness of the target along the direction of the beam.

Some of these quantities are not measured directly, but may be expressed in terms of those that are:

$$N_0 = \frac{C}{e}$$

where C is the total charge of the beam collected in the beamstop and e is the charge of a proton;

$$n_t = \frac{P}{k(T + 273.2)}$$

where, from the Ideal Gas Law, P is the pressure in the gas target cell,
k is Boltzmann's Constant, and
T is the temperature of the gas, in °C.

As the current integrator scaler (CI) is incremented at a rate of 1000 s^{-1} for full-scale current on the selected range, the charge C is calculated from

$$C(\text{coulomb}) = CI \times \text{Range(nA)} \times 10^{-12}.$$

Expressing these quantities in convenient units and collecting constant terms, we arrive at a normalization factor F for converting the yield to absolute cross section:

$$\sigma(\text{mb.sr}^{-2}.\text{Mev}^{-1}) = F \times Y$$

$$\text{where } F = \frac{22116 \times [273.2 + T(^\circ\text{C})] \times C_{DT}}{\Delta\Omega_P(\text{msr}) \times \Delta\Omega_S(\text{msr}) \times \Delta E_P(\text{MeV}) \times P(\text{bar})} \times \frac{1}{CI(\text{coulomb}) \times \text{Range}(\text{nA}) \times t_{eff}(\text{cm})}.$$

Corrections to the yield Y for reaction losses in the detectors, and the subtraction of random coincidences will be discussed in the next section. For the remainder of this section, we concentrate on the separate quantities which go into F.

Solid Angles

The solid angles $\Delta\Omega$ (see Table 2.2) were small enough to be well approximated by

$$\Delta\Omega = \frac{A}{R_0^2}, \tag{3.1}$$

where A is the plane area of the back hole the collimator, and R_0 is the distance from the centre of the target cell to the back of the collimator.

Target Parameters

As discussed in Section 2.4, T was taken to be the room temperature of the vault. Readings varied from 19.5° to 22°C during the run. The temperature was assumed to vary linearly between readings, which were taken on the few occasions on which we entered the vault.

The pressure P was recorded in the logbook approximately every two hours. As the value in the current integrator scaler at each recording time was recovered during replay of the event tapes, it was a simple matter to calculate a weighted average pressure for each angle setting. For data presented here, the average pressure varied from 1.115 to 1.126 bar.

The effective coincidence target length was calculated from Equation 2.1 as t_{eff} for the defining telescope, with the assumption of "good overlap"

of the coincident telescope response regions. It varied with angle setting in the range 0.71–1.13 cm.

Dead Time Corrections

The values for CI were taken from the scaler which had been inhibited by the BUSY signal (see Table 2.4), and so the correction for computer dead time was made automatically.

In order to estimate the electronics dead time for each pair of coincident telescopes, we replayed the event tapes with a "particle" gate set on each of the pulser peaks in the ΔE vs E histograms. For each pair of telescopes, the ratio of pulser events appearing in the energy-sharing histogram, to the number of pulser triggers recorded by the inhibited scaler, was taken as a measure of the dead time.

It is always advisable to keep the dead time at a reasonably low level, as using pulsers for estimating it is inherently inaccurate as a result of several assumptions which need to be made. The most obvious of these is the assumption that the various components in the electronic setup respond to pulser signals in the same way as they respond to real signals. In this experiment, there was one stage in the processing of the signals where this was clearly a poor assumption, namely in the gated TAC spectra: the jitter in the timing which was responsible for throwing some real events outside the TAC gate would probably affect pulser signals in a different way. Consequently, we analyzed the pulser events with a wide-open gate on the TAC spectrum, and then estimated the TAC losses independently.

On the 2-D energy-sharing histograms, the pulser events appeared as a dense blob, with tails (caused by pile-up) extending towards higher and lower energies in both dimensions. In counting the number of pulser events, the decision on how much of these tails to include was made in the same

subjective way as the choice, for projection purposes, of the limits of the knockout locus, i.e. the pulser blob was treated as if it were a portion of kinematic locus. This was considered to be the most consistent way of estimating the losses from the projected knockout locus due to pile-up.

The dead time correction factor at various coincident angles ranged from 4% to 30% (with a typical value of ~10% in most cases), depending on count rates and on which telescopes were involved.

Correction for TAC losses

For a small fraction of the data, we had to contend with losses from the "real" peak of the TAC spectra, due to timing jitter. These were estimated from a comparison of the total number of counts in the "random" peaks on either side of the "real" peak. Normally these peaks should be symmetric. However, timing jitter in a particular telescope would throw real coincidence events into the region of one of these peaks and not the other; thus the asymmetries caused by this phenomenon could be used to deduce the percentage of real events affected. In the early part of the experiment, the problem had been severe enough to warrant setting the gate widths to span two TAC peaks (see Section 3.4.2); after the troublesome thresholds had been adjusted, however, our investigations show that the problem persisted only in Telescopes 4 and 5, resulting in corrections for TAC losses of 1% and 14% respectively. Where they occurred, they were treated as additional dead time corrections, and were thus included in C_{DT}.

3.8 Projections

Having determined which regions of each summed-energy spectrum to project (Section 3.6) and the appropriate factor for conversion to absolute cross

sections (Section 3.7), we were able to set up command procedure files to project the data onto the energy axis of the primary proton, for presentation in their final form (Section 3.10) and comparison with theoretical calculations (Chapter 4). Included in these command files were procedures for the subtraction of random coincidences and for performing the reaction tail corrections, which are explained in more detail below.

In order to improve the statistical accuracy of the data points, the energy bins were generally chosen to be 2 MeV wide, but for coincident angle pairs at which the statistical accuracy was poorest, they were 4 MeV or even 8 MeV wide.

Our use of the term "energy-sharing spectra" now refers to these one-dimensional projected spectra, as opposed to the "2-D energy-sharing spectra" described previously.

3.8.1 Subtraction of Random Coincidences

Usually one would simply take the projected data derived from a "random" TAC peak and subtract them from the corresponding "real" data (consisting of real coincidences with a background of random coincidences), which would then yield a corrected spectrum of real coincidences only. At the time of this experiment, however, the cyclotron physicists had not yet had the time to study the behaviour of the ion source in relation to the macrostructure in the beam (intensity fluctuations from one beam pulse to another), and ways of optimizing it; consequently, this beam structure was not very good, which caused the successive "random" peaks on either side of the "real" peak to decrease in magnitude in an unpredictable way (see Figure 3.3).

Thus, before performing each subtraction, it was necessary to multiply the data derived from the chosen "random" peak by a factor which compen-

sated for the fall-off due to beam structure. The appropriate multiplicative factor was determined as follows:

On the 2-D energy-sharing spectra (see Figure 3.6), there are regions which can be populated only by random coincidences, i.e. those regions at higher total energy than is kinematically possible for real coincidences. Therefore, different portions of these randoms-only regions were selected from the "real" spectra for comparison with the corresponding areas in the "random" spectra, in order to determine the factor required.

In addition to the proton-proton data at each coincidence angle, the proton-deuteron, -triton and -helion spectra provided independent means of determining the same factor. The consistency of the factors determined from these different sets of data was good enough to inspire confidence in the procedure. The factor by which the projected "random" data had to be multiplied before subtraction from the "real" data varied with coincidence angle from 1.3 to as high as 2.4.

As mentioned before, another consequence of the structure on the beam was that, during data acquisition, we underestimated the random-to-real ratio by about a factor of 2. The average ratio for the (p,2p) data was 20%, whereas we had intended to keep it at about the 10% level. Nevertheless, the estimated errors in the subtraction of random coincidences are still reasonable, as will be shown in Section 3.9.2.

3.8.2 Reaction Tail Corrections

All detectors which measure the energy of a charged particle by quantifying the ionization track which it leaves in matter suffer from the problem of reaction tails. The accurate determination of the full energy relies on the particle losing all its energy by Coulombic interactions with atomic electrons, and by small angle multiple scattering from the atomic nuclei.

At energies below the Coulomb barrier, only large angle Rutherford scattering competes with these processes, but as the energy increases, there is a growing probability that the particle will undergo some large angle and/or nonelastic interaction with a nucleus in the detector before it reaches the end of its range, resulting in some of the energy going undetected, for example in the form of Q-values, and the escape of one or more energetic particles (particularly neutrons) from the detector volume. Thus for every portion of an energy spectrum measured in this way, there is an associated reaction tail extending from the full energy downwards to zero energy.

In our FORTRAN routine which corrects for the reaction tails, we have assumed that the stopping material is all Sodium Iodide. This is a reasonable approximation because at high energies, where the tail is most pronounced, the particles do indeed lose almost all of their energy in the NaI detectors, whereas at lower energies for which the energy lost in the silicon detectors is proportionately higher, the corrections become, in any case, very small.

Furthermore, we assume that having subtracted the random coincidences, there is no tailing into the quasifree knockout locus from higher energy bins, as the locus lies along the kinematic limit for three particles in the final state. Thus, the corrections simply consist of adding to the quasifree locus the yield lost to the tails which extend downwards from the measured energy in both coincident telescopes.

We used the empirical formula of Green *et al.* [Gre83] to correct the yield Y at primary proton energy E_P and secondary particle energy E_S:

$$Y_c(E_P, E_S) = \left(1 + \left(\frac{E_P}{354}\right)^{1.8}\right)\left(1 + \left(\frac{E_S}{354}\right)^{1.8}\right) Y(E_P, E_S).$$

This functional form gives values for the reaction tail within 2% of Cameron *et al.* [Cam77] at 89 and 104 MeV, and a value within 2% of that quoted

in the Janni tables [Jan82] for 100 MeV protons in NaI. The corrections required for the secondary deuterons, tritons and helions were assumed to be the same as for protons of the same energy. This is a similar approach to that of Segel *et al.* [Seg82], except that they ignored altogether the tails due to helions, which is justifiable on the grounds of the shorter ranges for Z = 2 particles.

3.8.3 Corrections for Energy Loss in Foils

Although energy losses in the 25 μm Havar foil of the gas cell window, and in the 8 μm Kapton foil on each collimator, hardly affected the accuracy of the energy scale over most of the range, for the lowest points in the energy-sharing spectra it was considered worthwhile to make at least a crude correction. For the low-energy data points in the range 5–11 MeV (below the energy gap), the energy loss in the foils was $\sim$1 MeV, so those points were shifted up by 1 MeV. Above the energy gap ($\geq$17 MeV) the energy loss was $<$0.4 MeV, decreasing rapidly with increasing energy, so these points were left unchanged.

3.9 Error Analysis

3.9.1 Statistical Errors

In the results to be presented, the error bars on the data points represent the statistical counting errors only. These errors have been propagated in the usual way during subtraction of the random coincidences, compression of the data into fewer points, and all the other operations which determine the relative normalization of each datum.

In a fastidious approach, the error bars representing one standard de-

viation above and below each datum should be asymmetric, reflecting the Poisson distribution appropriate to small numbers of counts (some of the data points represent only 3 counts). With only one exception, however, the peaks of the distributions represent data of >30 counts; in these regions of the most interest, the difference between standard deviations on a Poisson or a Gaussian distribution (for which one may use the more convenient expression $N \pm \sqrt{N}$) is barely noticeable. Consequently we have assumed that all the data are normally distributed.

3.9.2 Systematic Errors

In this section, we describe firstly the non-statistical errors which may also affect the shapes of the energy-sharing distributions, and then the errors which affect only the normalizations. We conclude by attempting to lump all these diverse errors into an overall estimate of the systematic uncertainty in each energy-sharing distribution. Although some of the errors described here are more correctly classified [Lyo86] as "random" than "systematic", insufficient sampling leads us to treat them as if they were systematic.

Finite Resolution Effects

Each datum in the energy-sharing distributions is represented by a point plotted at a specific value for the cross section and primary proton energy. However, the coincidence events from which such a datum is derived correspond to a range of energies spanning the width of the bin (usually 2 MeV), which is broadened further by the energy resolution of the detectors. Similarly, the distribution represents an average over the coincident angles $(\theta_P \pm \Theta_P; \theta_S \pm \Theta_S)$, where the Θ are the angular resolutions of the collimators, typically 3°. It is thus necessary to accept a systematic error for the extent to which these average values of the cross section do not

represent the true cross sections at the specified angles and energies.

In a similar situation to ours, Carey [Car79] calculated the finite resolution effects for various portions of energy-sharing distributions, and found that in most cases the average value in a range was a good approximation to the actual value at the centre. However, at the peak of a distribution, this smearing effect results in lower than true values.

Now, when one makes comparisons with theoretical model calculations, it is often the value at the peak which determines the extracted spectroscopic factor. Consequently, we investigated this effect on the peak of the (p,2p) distribution for (45°;-27°), which is a quasifree angle, i.e. an angle where zero recoil momentum is possible. The cross section was calculated (as described in Chapter 4) for the primary proton energy corresponding to zero recoil momentum, and also for ± 1 MeV of this value, which changed the cross section by 3–4%. The calculation was repeated with both angles more forward by an amount equal to the angular resolution of the respective collimators, which reduced the cross section by 6%.

Assuming therefore that the energy resolution and the two angular resolutions each contribute a maximum 4% change to the cross section (7% total when added in quadrature), it seems unlikely that the average value for the finite range would differ by more than $\pm 3\%$ from the central value.

Slit Penetration

A drawback of using passive collimators to define the solid angle of acceptance is that some particles slice into the edges of the collimator material, but do not traverse enough of the absorber to be stopped, thus emerging to be detected with a degraded energy. For inclusive measurements of continuum spectra (such as the pre-scaled singles data in this experiment), distortions due to slit penetration may be severe, particularly [Cow80b]

in the regions below strong elastic peaks at forward angles. It is for this reason that we equipped the forward-angle primary telesope with active collimation, which limits the phenomenon to negligible edge regions of the plastic scintillator.

For coincidence measurements of the quasifree knockout locus, passive collimators are sufficient at these energies. Tailing into the locus from higher-energy events is limited to the random coincidences which we assume to be treated well enough in the subtraction procedure described earlier (Section 3.8.1), with no additional systematic error for slit penetration.

There remains the problem that some *real* coincident particles will be included in the measured locus after traversing part of a collimator, thus causing an effective increase in the solid angle of acceptance. The fraction of such particles in the total yield depends [Ber72] on the geometry and alignment of the collimators, the extent of the target, and the range of the particles in the collimator material. Bertrand *et al.* [Ber72] find that for single-aperture collimators and solid targets, this fraction approaches $2R/L$ under ideal conditions, where R is the range and L is the target-collimator distance. Applying their methodology to the situation of double-aperture collimators, we find that this fraction is of the order R/h, where h is the distance between apertures (see Section 2.5). For protons in the energy range of our quasifree knockout loci, the fraction can be up to 4%. These extra particles, however, have an energy distribution which extends from the undegraded energy all the way down to zero energy. Consequently the fraction included in the projected region of the summed-energy spectra would be $\ll 1\%$ and may thus be neglected.

Reaction Tail

In Section 3.8.2, we saw that the functional form [Gre83] which we used for reaction tail corrections agrees within 2% with the estimates of other authors [Cam77][Jan82]. The magnitude of the correction for the (p,2p) knockout locus varies from 4–6%; the error in the final data due to uncertainties in the correction is thus assumed to be $\ll$1%, and can be safely ignored.

PID gates

We investigated the errors associated with the particle identification gates by replaying two of the angle sets with gates set at extreme values, firstly as wide as could be considered reasonable, and then as narrow. One of the angle sets was chosen as representative of the average, whereas the other was known to be sensitive to the exact limits of the gates because we had noticed that some tritons were leaking into the deuteron locus at a summed-energy value where the two knockout loci overlapped (in most situations, one type of particle leaking into the gate of another did not present a serious problem as they would still be kinematically separated in the summed-energy spectra).

In the worst case, the largest variation in a particular energy bin was 23%, with the overall normalization for that distribution changing by 6%. Normalizations for the other distributions changed by 2–7%, and they also suffered some shape changes of up to $\sim$10%. Assuming therefore that the worst possible error in absolute normalization was $\sim$7% and that generally the gates are set much more sensibly than in these tests, we take an average error due to the PID gates of 3%.

Energy Scale

Uncertainties in both the width and central energy of each bin contribute to shape uncertainties in the distributions and may even be thought of as affecting the normalization, for instance by introducing a shift in the peak relative to the peak in a theoretical calculation which is being normalized to the data.

The energy of the incident protons, corrected for energy loss in the Havar entrance window, was taken to be 99.9 ± 0.4 MeV.

The energy scales were corrected to within 0.5 MeV (see Section 3.8.3) for losses in the Havar exit window and the Kapton foils. Uncertainties due to further dead layers in the detectors (windows and undepleted regions of silicon) are negligible in comparison with this figure.

The largest energy uncertainties come from the calibration ($\sim$1 MeV) and compensation for gain drifts ($\sim$2 MeV) of the NaI detectors. In comparison with these errors, nonlinearities in the electronics and calibration errors in the silicon detectors may be neglected.

There is one error, namely foldback, which affects a very limited region of the low-energy data. When a proton has enough energy to penetrate both silicon detectors ($\sim$13 MeV) but not enough to overcome the threshold in the electronics for the NaI detector (corresponding to total energy $\sim$15 MeV), it is wrongly identified as a low-energy proton stopping in the silicon detectors. Protons of energy 13–15 MeV thus fold back onto the data for 9–12 MeV protons. In the results to be presented, therefore, the last two data points before the energy gap should not be trusted.

Uncertainties in the angles arise from the determination of the beam offset ($-0.5° \pm 0.1°$), temporal drifts in the beam direction with respect to this measured value (estimated to be $< 0.2°$), and errors in the alignment of the collimators ($\pm 0.1°$), and in the positioning of the removable front slits

($\pm 0.1°$). Assuming that these uncertainties are uncorrelated, we accept a total uncertainty in the angle of 0.3°, which adds < 0.5 MeV to the uncertainty in the energy.

The overall uncertainty in the central energy of each bin (except for the small region of foldback) is estimated to be $\sim$2 MeV, and the width of the bins is uncertain by $\sim$4%. The effect of this uncertainty on the absolute normalization of each energy-sharing distribution is estimated to be 4%.

Solid Angles

For double-aperture collimators viewing gas targets, the yield in a detector is related [Sil59] to the cross section by means of a complicated "G factor" incorporating all the geometry parameters appropriate to a particular angle of measurement. Carey [Car79] points out that the use of an "effective target length" (Equation 2.1) in conjunction with solid angles calculated in the usual way (Equation 3.1) is equivalent to taking the lowest order term in the expansion of the G factor.

We have calculated the G factor to first order for our least favourable geometry and find that the correction required is $\sim$0.1%. Consequently, we ignore the full G factor and consider instead the uncertainties associated with determining the solid angles of acceptance, as defined in Equation 3.1 to lowest order.

The uncertainty in the exit hole diameter of each collimator is $\sim$0.1% ($\sim$0.5% for the active collimator, owing to nonuniformities of the painted surface). The distance from the centre of the scattering chamber to the back of each collimator is uncertain to $\sim$0.5 mm ($<$0.2%), but a larger uncertainty arises from the position and width of the beam relative to the centreline, $\sim$1 mm (0.3%). Even larger is the uncertainty caused by the asymmetric front slits, which may shift the distance from the collimator

to the centre of the effective target length by as much as 3 mm (1%) for measurements at 15°. All these errors combine in quadrature to give an uncertainty in the solid angles $\Delta\Omega$ of up to 2%.

Effective target length

There are two contributions to the error in t_{eff}, firstly the uncertainty in the effective target length seen by the defining telescope (see Section 2.5) and secondly the uncertainty in the overlap condition for coincident telescope response regions. The former quantity arises from the same collimator and beam alignment errors which have already been discussed in relation to the energy scale and the solid angles, and is estimated (by partial differentiation of Equation 2.1 and summing of terms in quadrature) to contribute up to 3% uncertainty in t_{eff}.

In the design of the apertures, we allowed as much margin of safety as practically possible in overlapping the coincident response regions. Consequently, even when alignment errors shift the response regions of the coincident telescopes in opposite directions, we calculate an error of $< 1\%$ in the overlap depicted in Figure 2.7. The total uncertainty in t_{eff} is thus estimated to be 3%.

Pressure

The pressure transmitter was calibrated before the experiment to better than 0.2%. As the indicated pressure varied by less than the stated accuracy of the gauge during acquisition at any one angle pair, we could use the manufacturer's value ($\pm 0.25\%$) as an estimate of the systematic error in the gas pressure. The measured pressure is not necessarily the correct value for the helium gas, however, as there may be partial pressure contributions from gaseous contaminants. The energy spectra of pre-scaled singles events

indicated the presence of hydrogen, but there was little evidence of any heavier elements, so we allow an uncertainty of 2% on the partial pressure of ^{4}He.

Temperature

Although several days passed between temperature readings in the vault, the change was never more than 1.5°C. We take the uncertainty in the average temperature estimated for each angle pair to be ±1°C, which is ~0.3% absolute.

Integrated Charge

The beam stop described in Section 2.2 was designed to stop 200 MeV protons and to suppress the escape of secondary electrons. The efficiency has not been measured, but we presume that for a beam of 100 MeV protons it is effectively 100%. Any systematic uncertainty in the total integrated charge is more likely to originate in the current integrator, for which intrinsic inaccuracies are negligible, but calibration errors (in particular, setting the zero-point) may be ~0.2%.

Dead Time Corrections

The major uncertainty in the dead time correction is in what proportion of the tails due to pile-up should be included in the pulser peak (see Section 3.7). To get an estimate of the maximum possible error for each energy-sharing distribution we compared the total pulser counts, including all of the pile-up regions, with the number of pulser counts in the regions which we actually summed to make the correction. Assuming that the error in the procedure would be not more than ~40% of this maximum differ-

ence, we found values varying from 1% to 4% for the uncertainty in this part of the dead time correction.

In addition, there is the uncertainty in the correction for losses from the TAC gates due to timing jitter, which we estimate to be no more than 1%, with perhaps a further 1% uncertainty due to the position of the gates with respect to the TAC peaks. Thus, we take an average uncertainty in the overall correction to be ~4%.

Subtraction of Random Coincidences

As described in Section 3.9.1, statistical errors due to the subtraction of random coincidences are propagated in the usual way and lead to increased error bars on the data points. However, there is also a systematic uncertainty, in the estimate of the factor for multiplying each spectrum of random coincidences before subtracting it from the real coincidence spectrum (see Section 3.8.1). As this factor was determined from an average over several independent sets of data, the error could be reliably estimated: it varied quite widely (mainly as a result of different real-to-random ratios) from as little as 0.1% in some energy-sharing spectra to a maximum of 2.8%. We assign an average uncertainty of 2% to this procedure, which in most cases is an overestimate of the actual uncertainty.

Summary

The systematic errors are summarized in Table 3.1. If we assume that they are uncorrelated, they add in quadrature to give an overall systematic error of 8%.

There are obviously some correlations, however, particularly amongst the uncertainties in the energy scale, the solid angles, and the effective target length, which have common components in misalignments of the

	% Error
Finite Resolution Effects	3
Slit Penetration	$\ll 1$
Reaction Tail correction	$\ll 1$
PID gates	3
Energy Scale	4
Solid Angles	2
Effective Target Length	3
Pressure	2
Temperature	0.3
Integrated Charge	~ 0.2
Dead Time corrections	4
Subtraction of Randoms	2
Linear Sum	24
Total Systematic Error	8

Table 3.1: *Summary of the systematic errors.*

beam and collimators. Adding these three uncertainties linearly and then summing in quadrature raises the total figure to 11%, which is bound to be an overestimate of the effect of correlations.

Consequently, we may be reasonably confident that the total systematic error is <10%. [It is interesting to note that, although a gas target is more difficult to use than most solid targets, and is accompanied by a string of uncertainties, our total systematic error is less than in many solid-target experiments for which the only significant error might be a 10% uncertainty in the target thickness.]

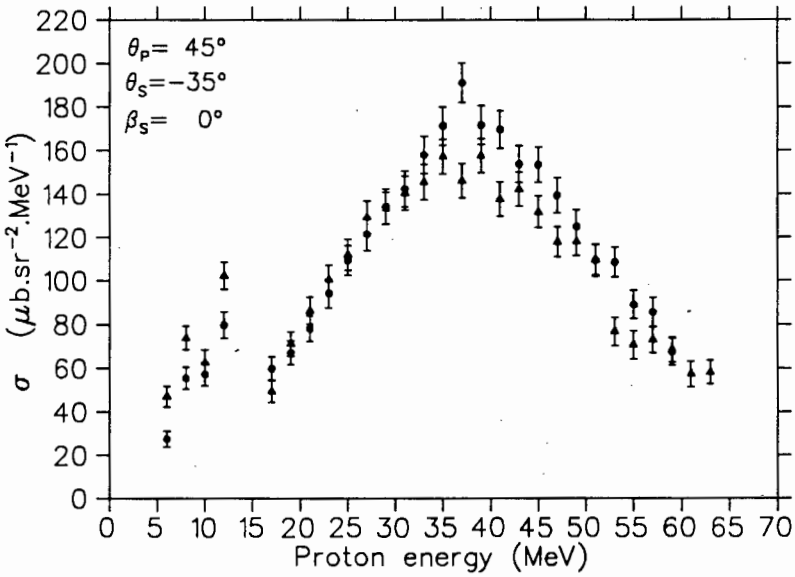

Figure 3.7: *Overlapping sets of data for $\theta_P = 45°$. The dots represent measurements of protons in Telesope 1 (with 18 mm front slits) in coincidence with protons in Telescope 3 (with 5 mm slits); the triangles represent proton-proton coincidences at the same angles, but between Telescope 1 (with 5 mm slits) and Telescope 6 (with 13 mm slits).*

Overlapping sets of data

In Figure 3.7, we overlay the energy-sharing distributions from two independent measurements at $(\theta_P; \theta_S; \beta_S) = (45°; -35°; 0°)$. This duplication came about as a result of an intentional overlap between those sets of angle pairs for which the secondary telescopes defined the coincident target length ($|\theta_S| \geq 35°$) and those for which the primary telescopes defined the target length ($|\theta_S| \leq 35°$).

Thus the front slits of primary Telescope 1 were 18 mm wide for one set of data, and 5 mm wide for the other; the secondary protons were measured

in Telescope 3 (with 5 mm slits) in one set, and Telescope 6 (with 13 mm slits) in the other. As one of the measurements was made eight days after the other, almost all the other sources of systematic uncertainties are also tested by this comparison. It is gratifying to note that most of the data points lie within overlapping statistical error bars. The data below 15 MeV fluctuate more rapidly with energy and are thus more sensitive to systematic differences in the energy scales, and they also suffer in varying degrees from the foldback problem discussed earlier.

A similar comparison for $(60°; -35°; 0°)$ is shown in Figure 3.8, where once again the front slits were different for each set, and the secondary protons were measured in two different telescopes. The agreement is generally better than at $\theta_P = 45°$, possibly because the photomultiplier tube of Telescope 2 (at 60°) was more stable than that of Telescope 1 (at 45°), resulting in a more stable energy scale.

Similar inter-comparisons for the (p,pd) and (p,pt) data give the same type of agreement. Although there are several systematic uncertainties which remain correlated amongst all these sets of data and are thus not tested by the comparisons, it seems likely that the overall error is indeed <10%, as predicted.

3.10 Experimental Results

3.10.1 ^{4}He(p,2p)^{3}H

The energy-sharing distributions for the primary angle $\theta_P = 45°$ are shown in Figures 3.9 and 3.10.

At the most forward angle $(\theta_P; \theta_S; \beta_S) = (45°; -15°; 0°)$ the statistical accuracy is poor and no clear trend is apparent in the data. From $\theta_S = -20°$ outwards the data exhibit a broad bump which is characteristic of quasifree

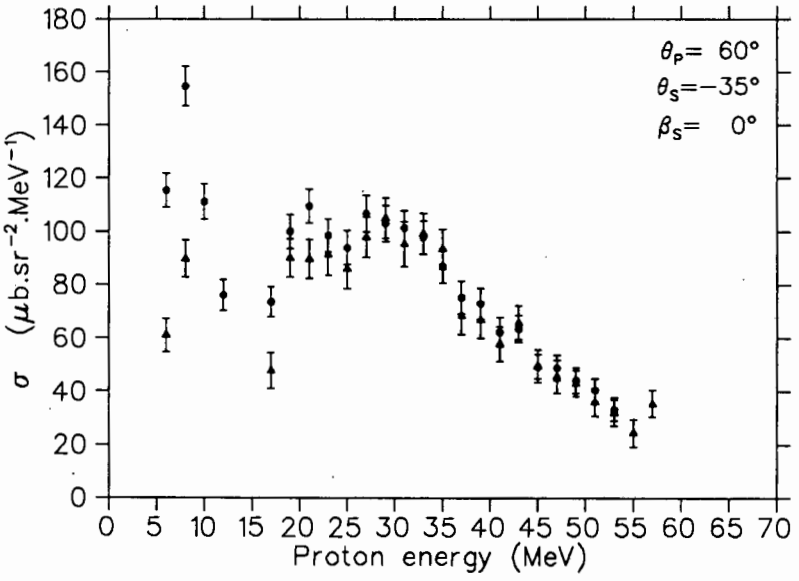

Figure 3.8: *Overlapping sets of data for $\theta_P = 60°$. The dots represent proton-proton coincidences between Telesope 2 (with 24 mm slits) and Telescope 3 (with 5 mm slits); the triangles represent similar data for Telescope 2 (with 5 mm slits) and Telescope 6 (with 13 mm slits).*

knockout from an s-state, as expected. As $|\theta_S|$ increases, the kinematic dependence is clearly seen: the position of the peak moves from primary proton energy T_P ~30 MeV up to ~55 MeV at $\theta_S = -70°$ and it disappears above the high-energy cutoff for $|\theta_S| \geq 80°$.

At the quasifree angle $(45°; -27°; 0°)$ the point $T_P = 24$ MeV corresponds to zero recoil momentum, but the yield peaks at T_P about 7 MeV higher than this. It should be noted, too, that the peak cross section continues to rise beyond the quasifree angle to a maximum of ~160 μb.sr^{-2}.MeV^{-1} for $|\theta_S| \sim 35°$ to 45°, and then falls rapidly with increasing angle.

The fall-off with out-of-plane angle β_S is also quite sharp, and the quasifree bump becomes less pronounced, as can be seen at $\theta_S = -35°$ and $-55°$ (a factor of 2 between $\beta_S = 0°$ and 15°, and for $\beta_S = 30°$, a factor of 3–5 with respect to the in-plane values). Clearly, most of the yield is indeed concentrated in the region of laboratory coordinate space corresponding to recoil momenta <200 MeV/c (see Figure 2.1), as expected.

At T_P below the energy gap (<12 MeV), the fluctuating cross section may be associated with sequential decay from ^{4}He(p,p')^{4}He*; several states [Fia73] in the excitation region of 20–22 MeV have been observed [Fuk86] [Bla87], and would yield low-energy protons in this region of T_P.

At $(45°; -45°; 0°)$, tailing from the strong ^{1}H(p,p)^{1}H locus affects two regions of the data. Unfortunately, this background is too large to be subtracted reliably, so data points have been deleted in the most-affected region (48–54 MeV); and other regions (22–40 MeV; 55–58 MeV) are identified on the plot as sitting on this background. The other problematic regions of data are for $\beta_S = 30°$ at $T_P < 42$ MeV. Here the effect of the PID cutoff progressively worsens towards lower energies (see Section 3.4.6), and these data points, too, should be treated with circumspection.

The corresponding energy-sharing distributions for primary angle $\theta_P = 60°$

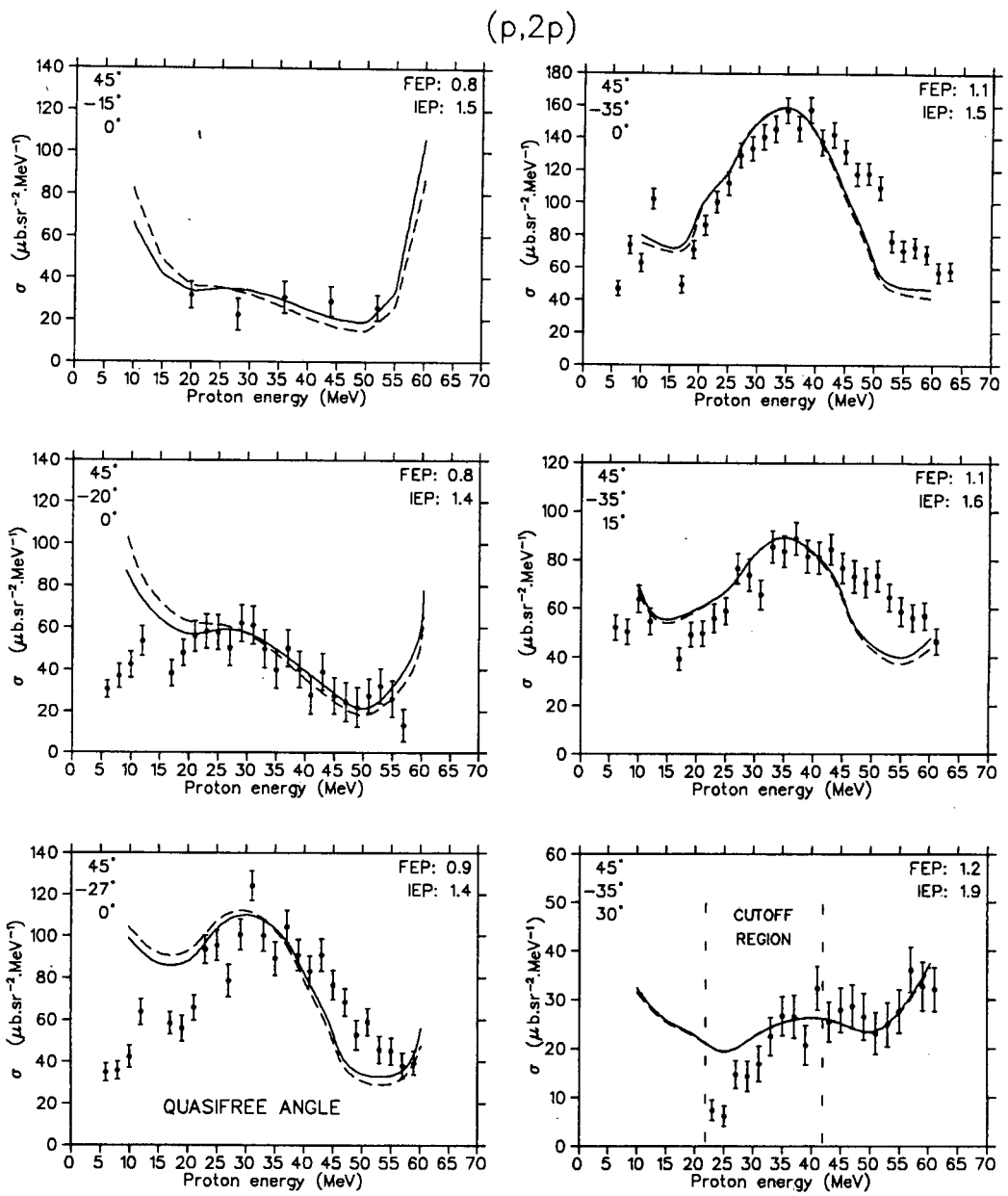

Figure 3.9: *Cross sections for the quasifree knockout reaction $^4He(p,2p)^3H$ at primary angle $\theta_P = 45°$ are shown as points with statistical error bars. The angles given in each plot are, from top to bottom: θ_P, θ_S and β_S. DWIA calculations with the FEP (solid curves) and the IEP (dashed curves) are normalized to the data with the indicated spectroscopic factors.*

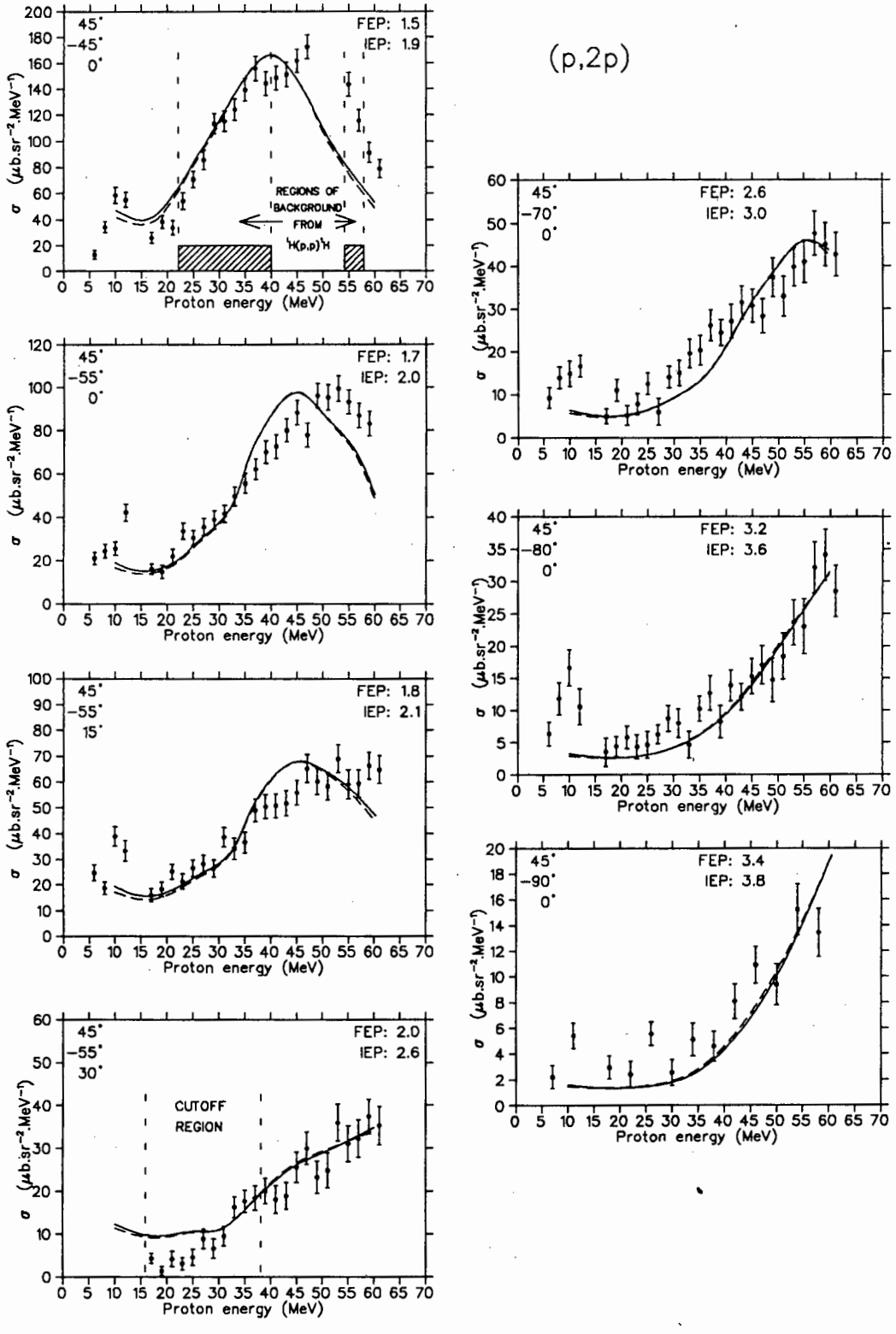

Figure 3.10: *See caption to Figure 3.9.*

are shown in Figure 3.11. There is no quasifree angle in this case, but the recoil momentum reaches a minimum of 23 MeV/c at $\theta_S = -12°$. Thus the minimum recoil momentum at each angle increases with $|\theta_S|$ for the entire set of data presented. The characteristic quasifree bump is not as clear in this set of data, and the peak yield (ignoring the very low-energy points) is lower than at $\theta_P = 45°$, reaching $\sim$100 μb.sr^{-2}.MeV^{-1} at $(60°; -35°; 0°)$. The fall-off towards out-of-plane angles is about as rapid as for $\theta_P = 45°$, and towards increasing $|\theta_S|$ it is even more rapid than for $\theta_P = 45°$, which is consistent again with the interpretation of Figure 2.1.

3.10.2 ^{4}He(p,pd)^{2}H

The energy-sharing distributions are shown in Figures 3.12, 3.13 and 3.14. The general trends are similar to those for (p,2p), except that the yield tends to peak towards higher primary proton energies. The quasifree angles are $(45°; -44°; 0°)$ and $(60°; -36°; 0°)$; in both cases the yield reaches a maximum at those angles ($\sim$90 μb.sr^{-2}.MeV^{-1} and $\sim$60 μb.sr^{-2}.MeV^{-1} respectively).

The most striking feature of these data is that the cross sections at the higher primary proton energies are often comparable with the (p,2p) cross sections. Clearly, the (p,pd) contribution is an important component of the total (p,p′) yield at the higher p′ energies, as postulated by Wesick *et al.* [Wes85]. It should be noted, however, that the major yield appears to be more concentrated in laboratory coordinate space than for (p,2p), so one should not overestimate the relative contribution to the inclusive (integrated) cross section.

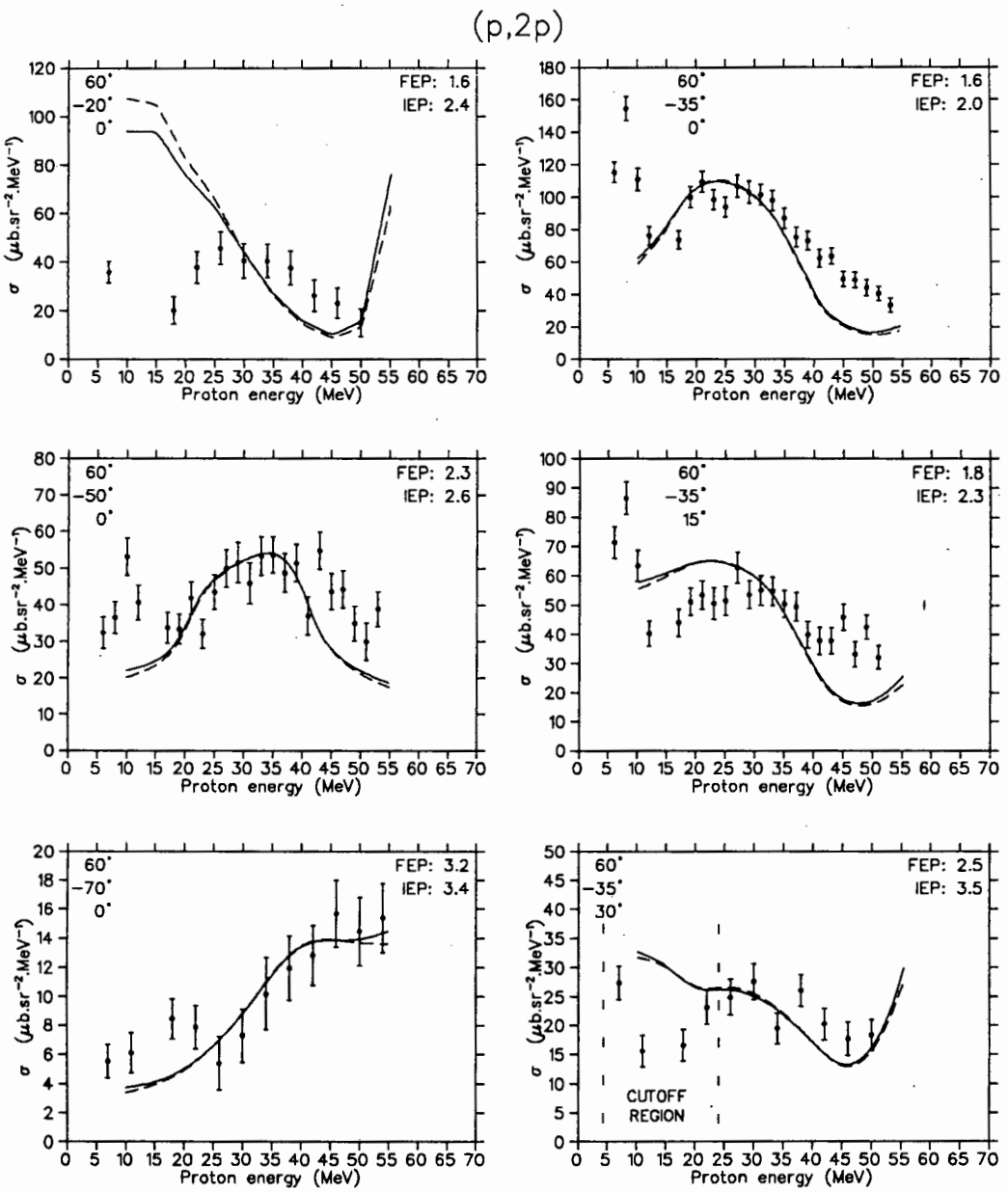

Figure 3.11: *Cross sections for the quasifree knockout reaction $^4He(p,2p)^3H$ at a primary angle of 60° are shown as points with statistical error bars. The DWIA calculations are presented as in Figure 3.9.*

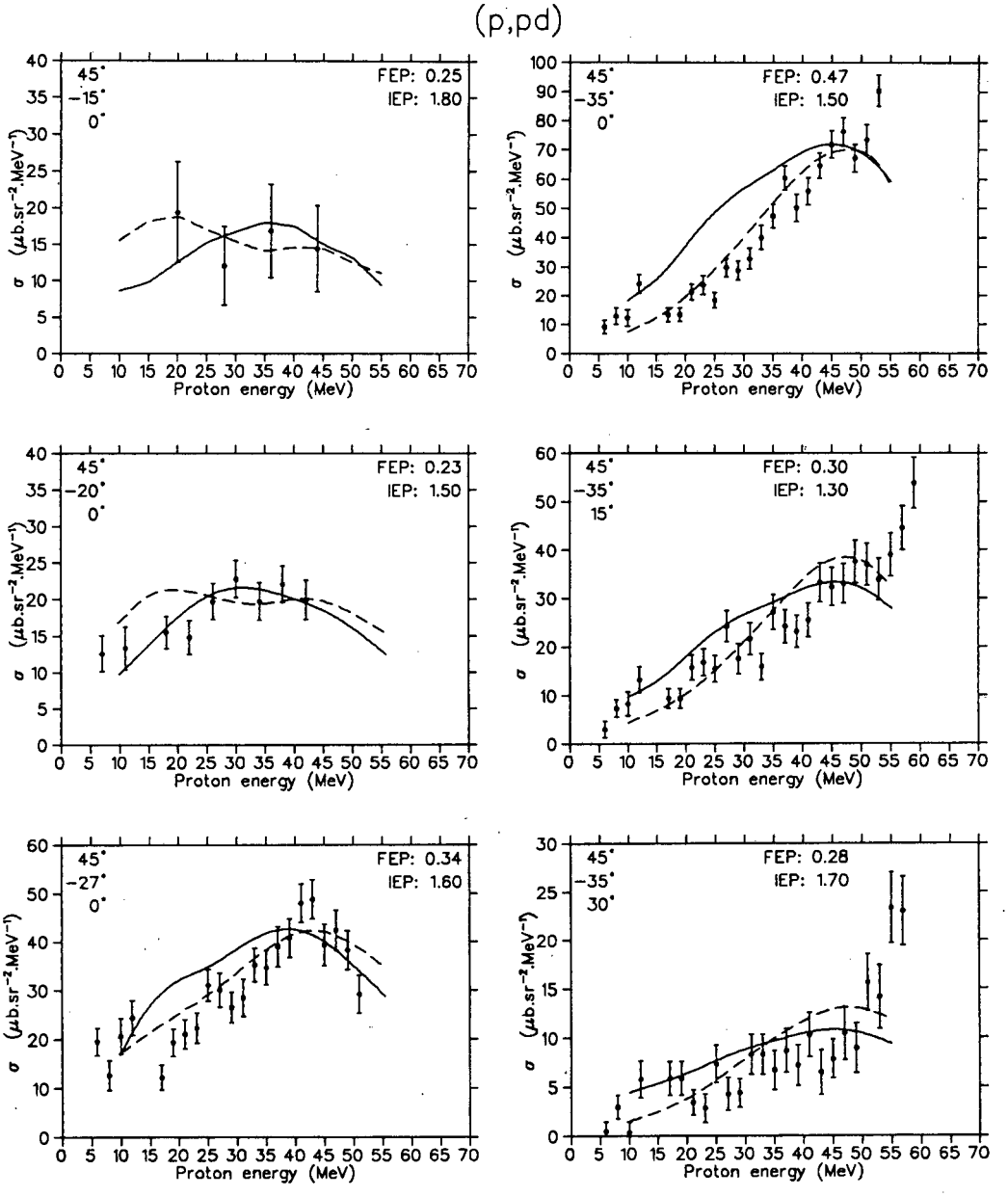

Figure 3.12: *Cross sections for the quasifree knockout reaction* $^4He(p,pd)^2H$ *at primary angle* $\theta_P = 45°$ *are shown as points with statistical error bars. The angles given in each plot are, from top to bottom:* θ_P, θ_S *and* β_S. *DWIA calculations with the FEP (solid curves) and the IEP (dashed curves) are normalized to the data with the indicated spectroscopic factors.*

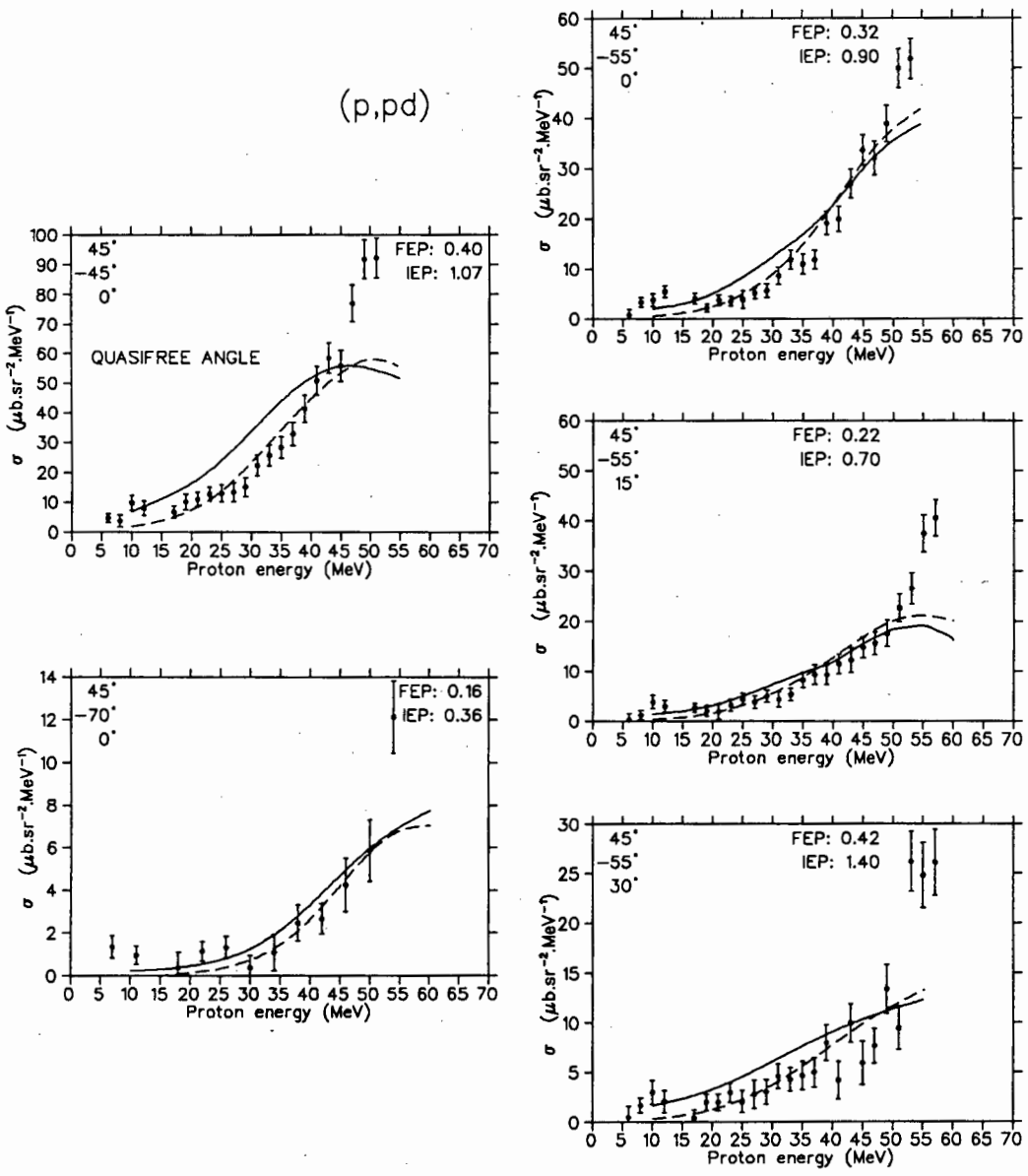

Figure 3.13: *See caption to Figure 3.12.*

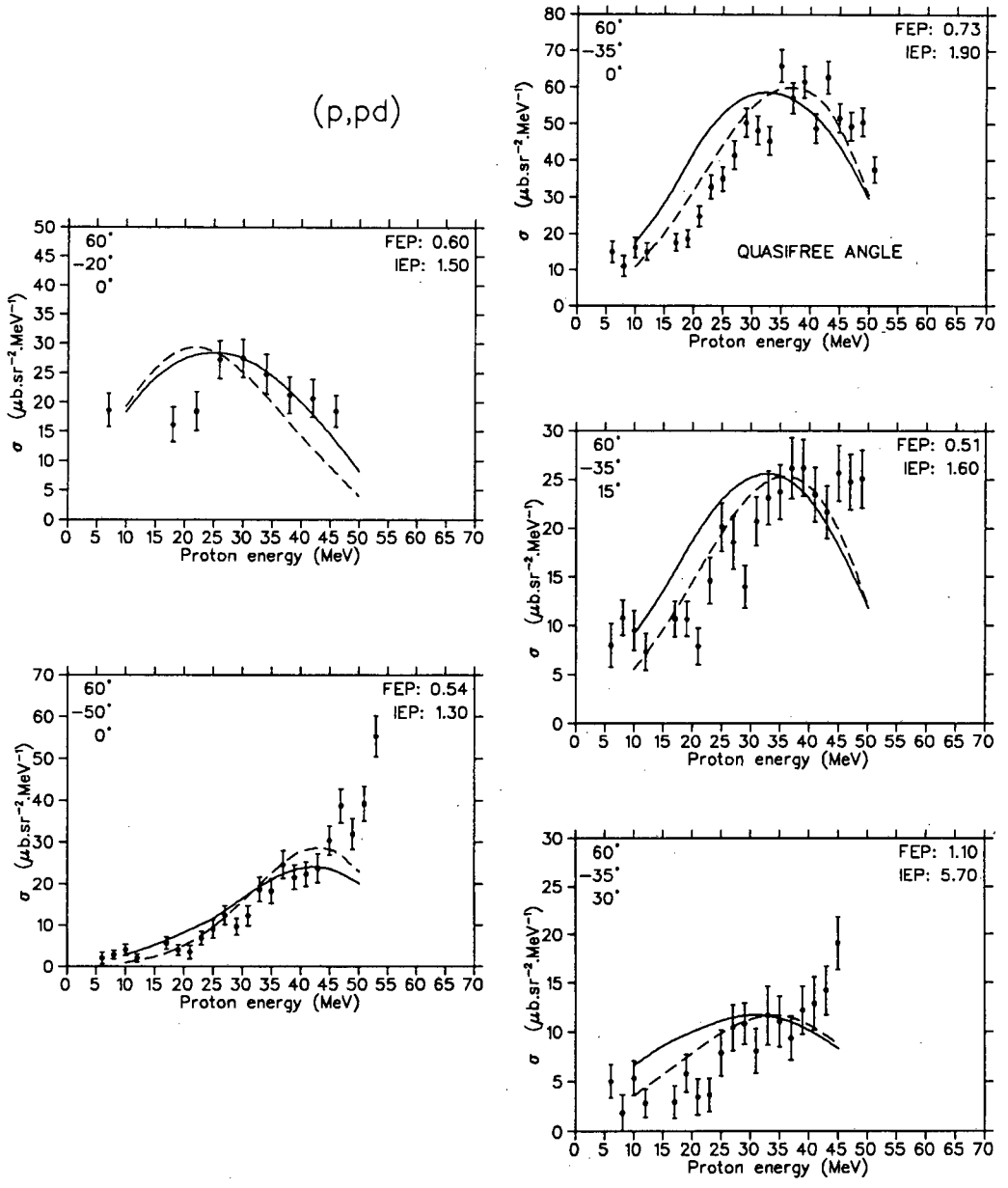

Figure 3.14: *Cross sections for the quasifree knockout reaction $^4He(p,pd)^2H$ at a primary angle of 60° are shown as points with statistical error bars. The DWIA calculations are presented as in Figure 3.12.*

3.10.3 ^{4}He(p,pt)^{1}H

Energy-sharing distributions for the knockout of triton clusters are shown in Figures 3.15, 3.16 and 3.17. As for (p,pd), the yield is greatest at high energies T_P and is at places comparable with (p,2p); furthermore it does not fall off as rapidly as (p,pd) towards large angles $|\theta_S|$. As for (p,pd), the yields peak at $(45°; -45°; 0°)$ and $(60°; -35°; 0°)$, but at higher energies. The quasifree angles for triton knockout are a little further out, at $(45°; -51°; 0°)$ and $(60°; -44°; 0°)$. At large angles $(45°; -70°; 0°)$ and $(60°; -70°; 0°)$ the central regions of the distributions are enhanced by final state interactions between the primary and recoil protons (see Section 4.9).

3.10.4 ^{4}He(p,ph)n

The few distributions that were worth analyzing from the helion-knockout data (see Section 3.5) are presented in Figure 3.18. Generally, they seem similar to the (p,pt) distributions, which is to be expected, as the physics and kinematics involved are much alike. At $(45°; -65°; 0°)$, most of the yield is due to final state interactions between the scattered proton and recoil neutron.

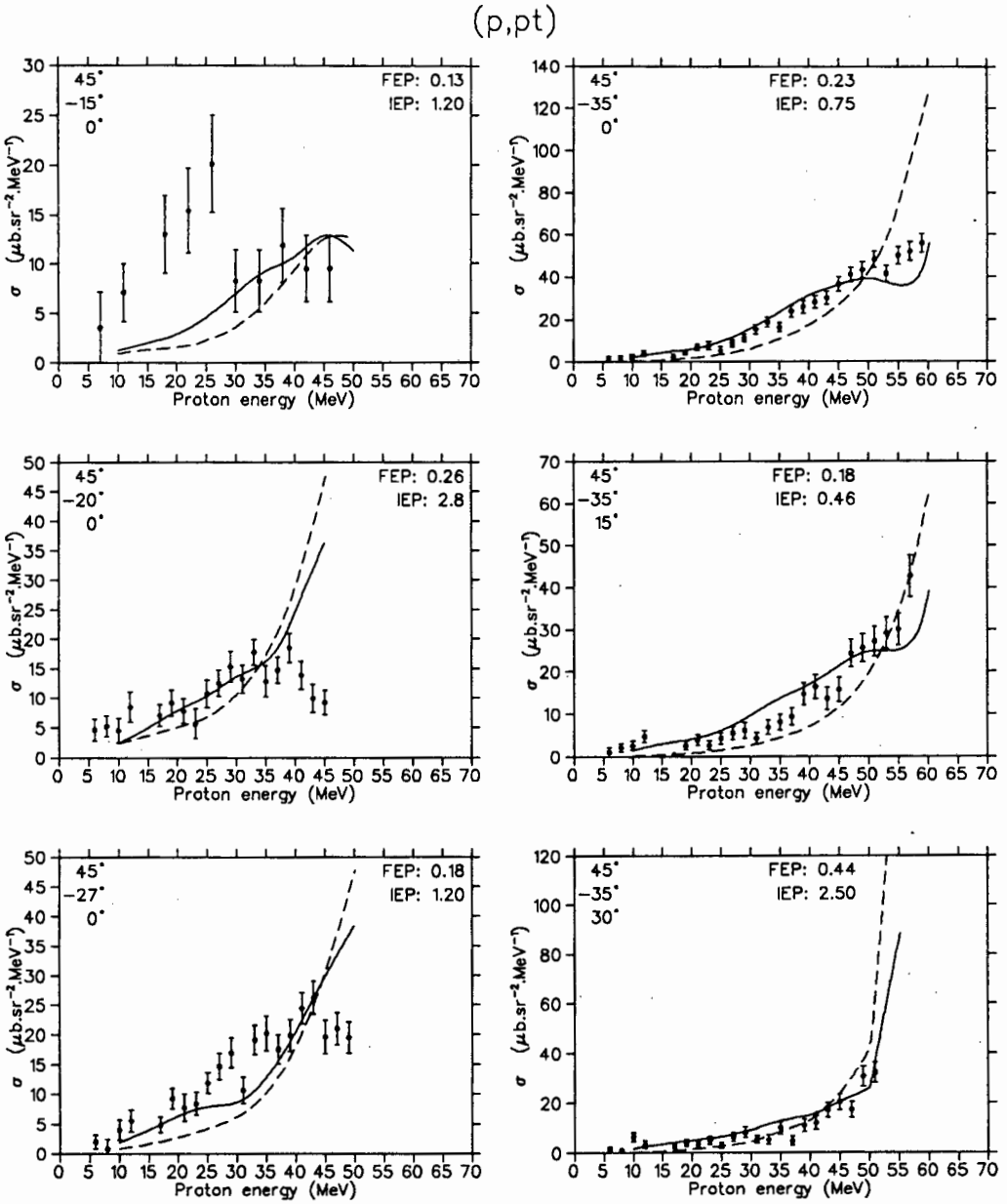

Figure 3.15: *Cross sections for the quasifree knockout reaction $^4He(p,pt)^1H$ at primary angle $\theta_P = 45°$ are shown as points with statistical error bars. The angles given in each plot are, from top to bottom: θ_P, θ_S and β_S. DWIA calculations with the FEP (solid curves) and the IEP (dashed curves) are normalized to the data with the indicated spectroscopic factors.*

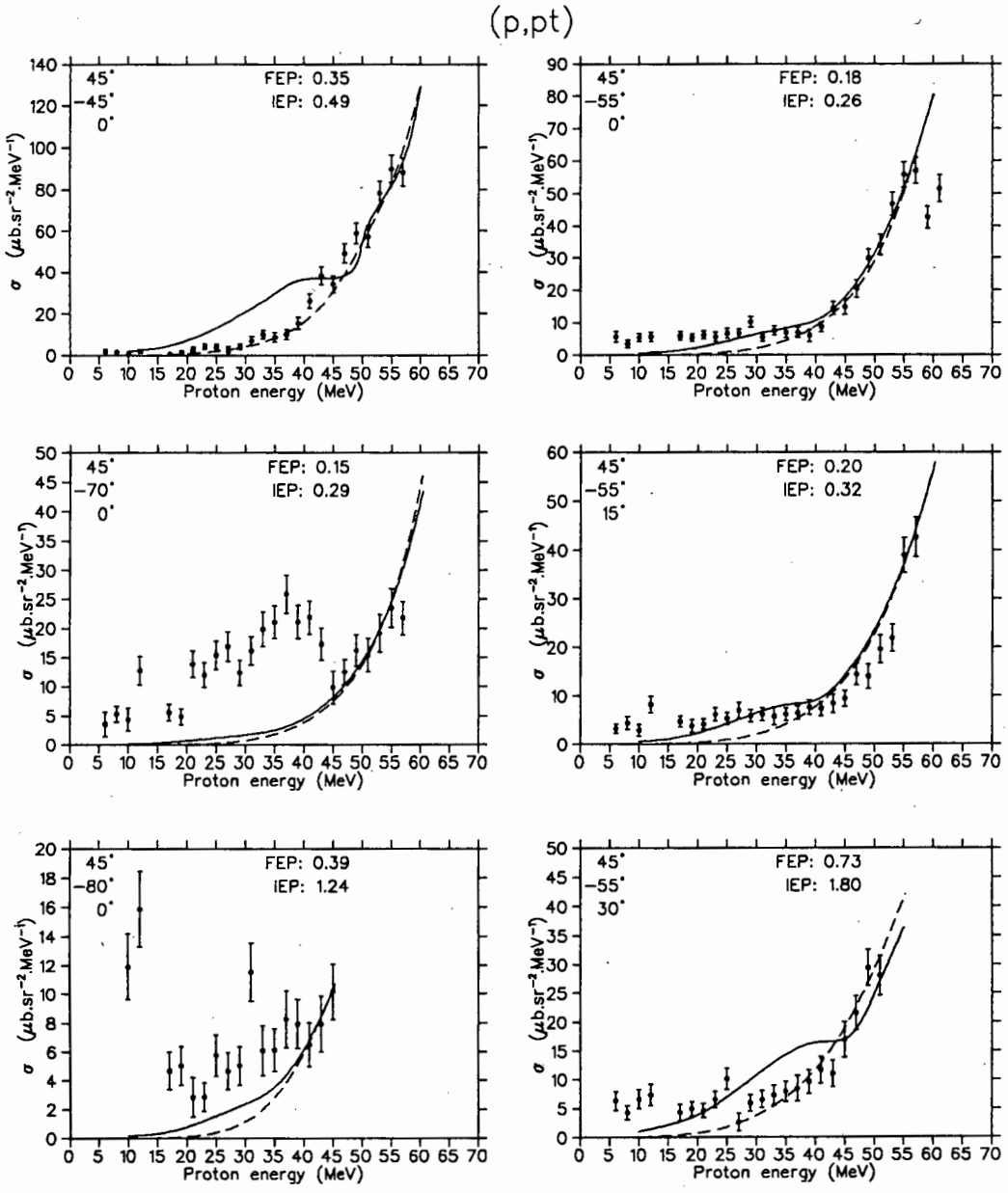

Figure 3.16: *See caption to Figure 3.15.*

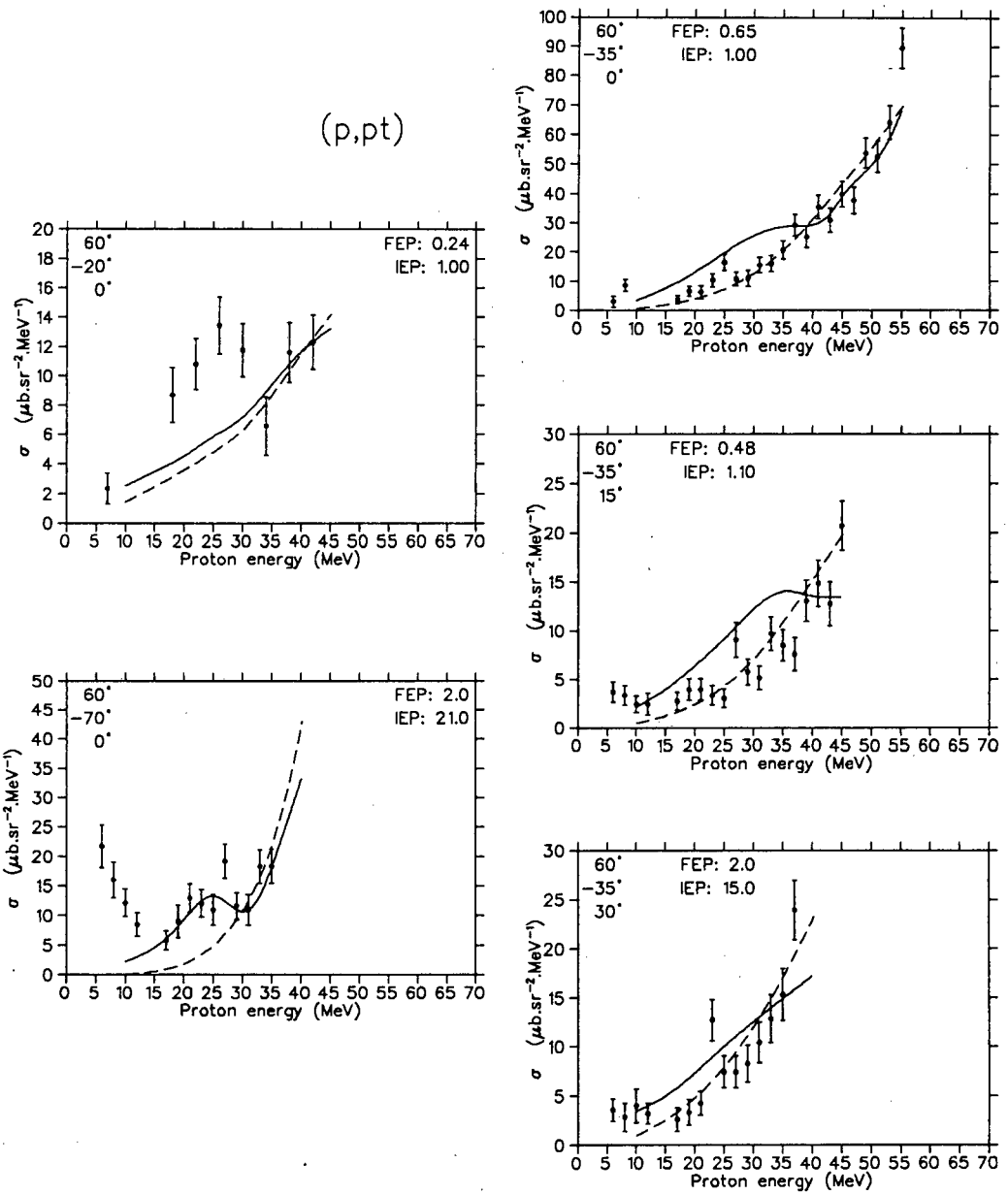

Figure 3.17: *Cross sections for the quasifree knockout reaction* $^4He(p,pt)^1H$ *at a primary angle of 60° are shown as points with statistical error bars. The DWIA calculations are presented as in Figure 3.15.*

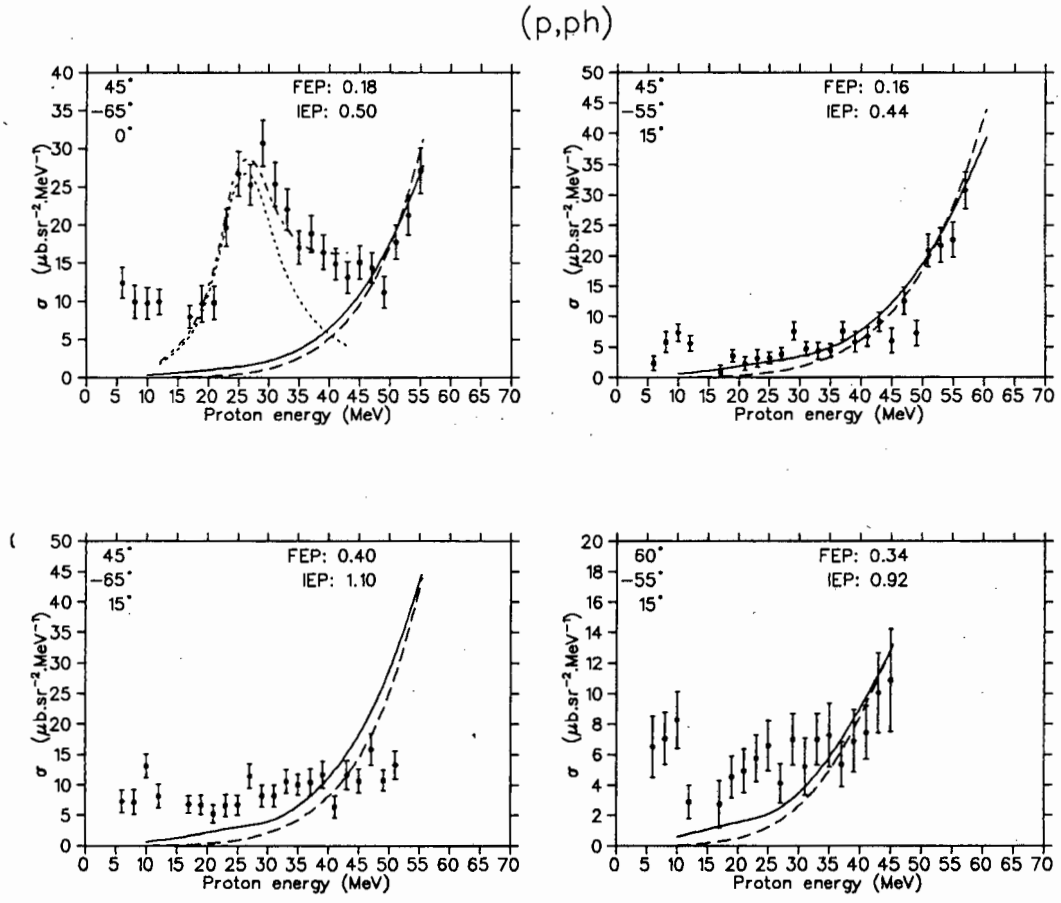

Figure 3.18: *Cross sections for the quasifree knockout reaction $^4He(p,ph)n$ are shown as points with statistical error bars. The angles given in each plot are, from top to bottom: θ_P, θ_S and β_S. DWIA calculations with the FEP (solid curves) and the IEP (dashed curves) are normalized to the data with the indicated spectroscopic factors. At* $(45°; -65°; 0°)$*, the final state interactions are fitted with a Watson-Migdal calculation (dotted curve). The dash-dotted curve represents the sum of the Watson-Migdal and FEP curves.*

Chapter 4

Calculations

4.1 Overview

Two types of DWIA calculations are described in this chapter: firstly, calculations of the triple differential cross sections for comparison with the coincidence energy-sharing distributions in Chapter 3 (for the quasifree knockout of protons, deuterons, tritons and helions); and secondly, calculations based on these comparisons, of the inclusive (p,p′) cross sections for comparison with the inclusive spectra from Wesick *et al.* [Wes85].

The various ingredients which were required for the calculations are described first. We start with the form of the optical potentials which distort the wave functions in the entrance and exit channels, and we tabulate the parameters which were used to define these potentials.

For the bound state wave functions, we discuss the ways in which the overlap integrals may be calculated, and justify using simple parametrizations. Then the elastic scattering data which were required for the evaluation of the two-body t matrices are discussed, and there is a brief explanation of how all the input parameters were optimized for calculational efficiency.

In Section 4.6, the theoretical calculations are compared with the data for each of the knockout reactions (p,2p), (p,pd), (p,pt) and (p,ph). The quality of agreement is discussed in relation to both the shapes and the spectroscopic factors.

The sensitivity of the distorting potentials to changes in the well-depth parameters is investigated, and we compare the results obtained with two different parametrizations for the the bound state wave function.

Then it is shown that the nonlocality corrections to the optical potentials make a moderate difference to the shapes and magnitudes of the calculated distributions. The effect of the spin-orbit terms in the optical potentials is also shown to be small.

Proceeding to other mechanisms, we show that some of the cluster knockout data have competing contributions from final state interactions which are calculated well in the Watson-Migdal formalism.

Next, we prove that it is safe to ignore the problem of double-counting, which is caused by the coincident detection of the primary proton with the *recoil* particle, instead of the knocked-out particle.

The calculation of the inclusive cross sections concludes this chapter. We show that by integrating over the solid angle of all possible knocked-out particles and by adding the contributions incoherently (using the spectroscopic factors extracted from the coincidence data) we can account for most of the inclusive yields. As a check on the consistency of these results, we then demonstrate that the multiple scattering component in the coincidence data can be integrated to provide the remaining yield within ~10% in magnitude, and in good shape agreement with the experimental inclusive yields.

4.2 Optical potentials

In the program THREEDEE [Cha82], the distorted wave functions $\chi_{ij}^{(\pm)}$ (see equation 1.2) are generated [Cha83] from spin-dependent optical potentials

$$\begin{aligned} V_{OPT}(r) &= -V\, f(r, r_R, a_R) - i(W - 4W_D a_I \frac{d}{dr})\, f(r, r_I, a_I) \\ &\quad -(-1)^l V_{ex}\, f(r, r_{ex}, a_{ex}) \\ &\quad + \left(\frac{\hbar}{m_\pi c}\right)^2 \vec{l}.\vec{\sigma} \frac{1}{r}(V_{SO} + iW_{SO}) \frac{df(r, r_{SO}, a_{SO})}{dr} + V_C \end{aligned}$$

where the Woods-Saxon form factor

$$f(r, r_i, a_i) = \left[1 + \exp\left(\frac{r - r_i A^{1/3}}{a_i}\right)\right]^{-1},$$

and V_C is the Coulomb potential between a point scattered particle and a uniformly charged sphere of radius $r_c A^{1/3}$.

Parameters for the real and imaginary well depths V and W, the potential radii r and diffuseness a are chosen from optical model analyses of elastic scattering data at the appropriate relative energy for each of the scattering states.

When spin-dependent potentials are used for these scattering states, it is no longer possible [Jac76] [Cha83] to factorize the DWIA cross section as given in Equation 1.4. Rather, the expression 1.3 for the coherent cross section should be used. However, for cluster knockout, as we shall see in Section 4.4, we have replaced the two-body t matrix directly with experimental cross section data for elastic scattering; thus we can only calculate the factorized cross section, because THREEDEE requires phase shifts in order to integrate the spin-space elements of the two-body t matrix coherently with those of the distorted wave integral $T^{L\Lambda}$. For consistency we have used the factorized form of the DWIA cross section for *all* the calculations, including those for nucleon knockout.

Nevertheless, we have retained the spin-orbit terms in some of the potentials, arguing that one should rather use the best available optical potentials than restrict the parameters for the sake of theoretical rigour. Thus we still allow the coherent mixing of spin amplitudes in the distorting potentials while decoupling the spin-orbit dependence of the two-body interaction (in Section 4.8, we shall show that this is probably the best option).

The assumption that the distorting potentials are local has been shown [Kit80] [Sam86] to be a poor approximation in some situations. Consequently, a nonlocality correction of the form derived by Perey and Buck [Per62] has been incorporated as an option in THREEDEE:

$$\chi_{ij}(r) = \exp\left[-\frac{\mu\beta^2}{4\hbar^2}V_{OPT}(r)\right]\chi_{ij}^{LOCAL}(r),$$

where the wave function $\chi_{ij}^{LOCAL}(r)$ is that obtained from the local potential $V_{OPT}(r)$, μ is the reduced mass, and β is the range of the nonlocality. Although we used this approximation for simulating properly non-local potentials, we show in Section 4.8 that the effects of nonlocality in these calculations are not severe, as might be expected for such light systems—there is not much nuclear interior to generate the damping of the wave function associated with nonlocality.

For the entrance channel, $p + {}^4He$ at a lab energy of 100 MeV, we used the optical potential [Van82] given in Table 4.1; although it is written in an energy-dependent form, it was of course used at only one energy in these calculations.

V	$27.35 - 5.046 \ln E$	r_R	1.577	a_R	0.2
W	$6.55 + 6.977 \times 10^{-2} E$	r_I	1.493	a_I	0.315
	$-6.250 \times 10^{-5} E^2$				
W_D	0				
V_{ex}	0.051 at 100 MeV	r_{ex}	0.930	a_{ex}	0.657
V_{SO}	$25.37 - 3.243 \ln E$	r_{SO}	0.879	a_{SO}	0.303
W_{SO}	$5.69 - 1.355 \ln E$	r_C	1.36		
		β_{NONLOC}	0.85		

Table 4.1: *Optical potential for the entrance channel [Van82]. The well depths (in MeV) were multiplied by m_B/m_A (see text). Length parameters are in units of fm.*

Because the distorting potential is actually supposed to describe the scattering from the *residual* nucleus B rather than the target A (the interaction with the knocked-out particle being explicitly included in the two-body t matrix), we adjusted the well depths [Jac65] [Roo76][Roo77a] by the ratio m_B/m_A. The entrance channel potential strengths of Table 4.1

were thus multiplied by 0.75 for (p,2p) calculations, 0.5 for (p,pd) and 0.25 for (p,pt) and (p,ph).

For the exit channels of the (p,2p) reaction, the energy-dependent optical potentials [Pod75] [Van82] given in Table 4.2 were used.

In the case of the (p,pd) reaction, we used the energy-dependent potentials [Wes83] [Roo86] listed in Table 4.3 for the p + d leg of the final state. For the d + d scattering, a folding model potential [Cow77] was used (see Table 4.4). The parameters are intended for a deuteron energy of ~65 MeV, which is close enough to an "average energy" for these calculations, as the energy dependence is weak.

For the (p,pt) reaction, the final state interactions are p + p and t + p, whereas for (p,ph) they are p + n and h + n. We considered two ways of treating the nucleon-nucleon legs of the final states. The simpler option would be to assume that distortions were minimal, and use plane waves for these exit channels (this would seem to be a reasonable approximation—Wesick *et al.* [Wes85] found that for ^{2}H(p,p′), distortions hardly affected the shape, but reduced the magnitude by ~30% with respect to plane waves; and Pugh *et al.* [Pug73] fitted ^{2}H(p,2p) data with a PWIA calculation reduced by ~20%). Alternatively, we could try to find a real Woods-Saxon potential (as required by THREEDEE) which gives approximately the correct N-N phase shifts.

Pursuing the latter option, we chose $r_R = 1.7$, $a_R = 0.3$, as was used by Darden *et al.* [Dar88] for p + n, and then ran the optical model search code SNOOPY8 [Sch82] to determine V as a function of the effective lab energy over the required range (20–180 MeV). The resulting energy-dependent potential, which is fitted by $V = 5.2 + 157/\sqrt{E}$, gave a reasonable reproduction of N-N phase shifts [Bro76] despite the crude method (SNOOPY8 is appropriate for a spin-zero target).

For $E < 65$ MeV [Pod75] [Wes83]:

V	$53.75 - 0.869E$ $+0.004E^2$	r_R	1.488	a_R	0.144
W	$0.06146E^{1.365}$	r_I	1.501	a_I	0.378
W_D	0				
V_{ex}	$-0.065V$	r_{ex}	1.488	a_{ex}	0.144
V_{SO}	$0.07566E^{1.305}$	r_{SO}	1.049	a_{SO}	0.289
W_{SO}	0	r_C	1.3		
		β_{NONLOC}	0.85		

For $E \geq 65$ MeV [Van82] [Wes83]:

V	$67.01 - 11.91 \ln E$	r_R	1.481	a_R	0.199
W	$12.65 - 0.02478E$ $+3.413 \times 10^{-5}E^2$	r_I	1.828	a_I	0.233
W_D	0				
V_{ex}	$-1129E^{-1.361}$	r_{ex}	0.930	a_{ex}	0.562
V_{SO}	$17.47 - 2.343 \ln E$	r_{SO}	1.007	a_{SO}	0.255
W_{SO}	-0.76	r_C	1.3		
		β_{NONLOC}	0.85		

Table 4.2: *Optical potential for $p + {}^3H$ in the exit channels of the (p,2p) reaction. This potential was also used for $p + {}^3He$, $n + {}^3He$, $t + p$ and $h + n$. For the latter two cases (cluster knockout) the energy dependence was scaled as described in the text.*

V	$1.4 + 114/\sqrt{E}$ for $E \leq 50$ MeV; $412.8/E^{0.75} - 5.37$ for $E > 50$ MeV.	r_R	1.6	a_R	0.5
W	$0.1769E^{0.767}$	r_I	1.6	a_I	0.5
W_D	0				
V_{ex}	0				
V_{SO}	6.0	r_{SO}	1.6	a_{SO}	0.5
W_{SO}	0	r_C	1.72		
		β_{NONLOC}	0.85		

Table 4.3: *Optical potential [Wes83] [Roo86] for p + d in the exit channel of the (p,pd) reaction.*

V	6.68	r_R	1.66	a_R	0.69
W	3.2	r_I	1.66	a_I	0.69
W_D	0	β_{NONLOC}	0.54		

Table 4.4: *Optical potential [Cow77] for d + d in the exit channel of the (p,pd) reaction.*

On comparing the results of some trial calculations, with plane waves on the one hand, and with this derived potential on the other, we found very little difference in the shapes of the energy-sharing distributions, and ~20% difference in absolute magnitudes. Consequently, we decided that it was not worth using such a risky potential for so little difference in the results, and we thus used plane waves for all the p + p and p + n exit channels.

For the t + p and h + n legs of the final states, we used the same potentials as for p + ^{3}H (Table 4.2), with the energy scaled to take into account the reversed situation, i.e. E as given in Table 4.2 is the effective lab en-

ergy of a proton incident on a stationary triton; for the same centre-of-mass energy of the two scattering particles, the effective lab energy of a triton incident on a stationary proton would be three times greater. Thus we used the potential with $E = E_t/3$ (with no corrections for nonlocality).

The use of the same potential for h + n was considered reasonable, since van Oers *et al.* [Van82] were unable to differentiate between suitable parameters for p + ^{3}H and p + ^{3}He (the charge and magnetic radii of ^{3}H and ^{3}He are approximately the same and the effect of an isospin coupling term could not be separated from the scatter in their results).

Finally, we need optical potentials for calculating ^{4}He(p,pn)^{3}He; although we have no data from this reaction, we have calculated its contribution to the inclusive (p,p′) spectra (see Section 4.11.1), using the (p,2p) results as a guide to the appropriate spectroscopic factors. For p + ^{3}He and n + ^{3}He in the final states, the same potential was used as for p + ^{3}H; again the assumption is that the isospin coupling is weak.

All the above-mentioned energy-dependent potentials were added to a subroutine of THREEDEE, so that they could be automatically evaluated at the correct "effective lab energy".

4.3 Bound State Wave Functions

The bound state wave function $\phi_{L\Lambda}(\vec{r})$ (Equation 1.2) for ^{4}He(p,2p) is theoretically the overlap integral of the ^{4}He and nnp-cluster wave functions. However, the solution of the Schrödinger equation with realistic potentials for the four-nucleon system remains a formidable challenge. Faddeev techniques have been applied to the three-nucleon problem, but for ^{4}He it is more usual [Aka84] [Sch86] to resort to variational wave functions calculated by Monte Carlo or Quasi-Random Number methods.

It has also recently been shown [Gry89] that a single-particle potential with a repulsive core can be used to derive the ^{4}He momentum distribution to about the same accuracy as that obtained with the many-body techniques.

Despite the progress being made, however, the bound state wave functions calculated by these methods are still less accurate than those which may be derived phenomenologically [Lim73] from electron scattering data, by fitting the ^{4}He charge form factor.

We chose the parametrization used by van Oers *et al.* [Van82], rather than the Eckart parametrization of Lim [Lim73] (even though Lim's function does better [Van82] at high momenta), because it is on firmer theoretical ground—the data which were used for extracting the parameters were first corrected [Gre82] for meson exchange currents. In any case, we shall show in Section 4.7 that the two wave functions give reassuringly similar results.

The radial wave function of van Oers *et al.* is of the form

$$U(r) = \sum_{i=1}^{5} \alpha_i \exp(-\beta_i r)$$

where $\alpha_i = (4.84, -23.0, 47.3, -45.9, 16.8)$ and $\beta_i = 0.846 + 1.42(i-1)$.

As it is estimated [Sch86] that the nnp-cluster in ^{4}He is in the triton state ~80% of the time (>90% for low momentum components), we have also used this bound state wave function to describe the triton in ^{4}He, for the (p,pt) calculations. Furthermore, because its derivation [Gre82] assumes isospin invariance, it has also been used as the overlap integral for calculating the (p,pn) and (p,ph) cross sections.

For the d + d bound state wave function in the (p,pd) calculations, we Fourier Transformed the momentum distribution measured for ^{4}He(p,pd) at 156 MeV by Frascaria *et al.* [Fra75], which is a Gaussian with FWHM =

210 Mev/c, to get

$$U(r) = 0.767\, r \exp(-0.204\, r^2).$$

In doing this, we assume that the *distorted* momentum distribution measured by Frascaria *et al.* is the same shape as the undistorted distribution. This is probably not unreasonable. Firstly, the measurement was made at a quasifree angle, for which distortion effects should not be too severe. Secondly, even at lower energy (100 MeV), Pugh *et al.* [Pug73] fitted their ^{4}He(p,2p) distorted momentum distributions quite satisfactorily with a PWIA calculation.

To conclude, we note that the small but controversial D-state admixture [Wel88] in the ^{4}He ground state has been ignored for the purpose of our calculations. Although theoretical estimates of it [Ass87] [Pie87] [Wac88] range from 2% to 14%, the most recent experimental evidence [Bar87] [Wel88] favours the lower limit. Even if it were 14%, however, it is doubtful whether the DWIA calculation would be sensitive to such a nuance.

4.4 Two-body Cross Sections

THREEDEE has access to experimental N-N phase shifts, so for calculations involving the knockout of a nucleon, the two-body t matrix is calculated automatically. For the evaluation of cross sections involving cluster knockout, we added subroutines which interpolated experimental cross sections for p + d, p + t and p + h elastic scattering. Because the data were rather sparse, and unevenly spaced in energy, we found that linear interpolation was more reliable than the quadratic interpolation used for the N-N phase shifts.

For the p + d cross sections, we used mainly the compilation of Remler and Miller [Rem74] to establish a data base extending from 8 MeV to 198 MeV at centre-of-mass scattering angles from 23°–150°. It should be noted that, although the incident proton energy was 100 MeV, the IEP approximation requires cross sections at up to ~200 MeV in some extreme cases, because of the momentum of the bound cluster. The full data set consisted of angular distributions at the following energies: 8, 14, 19 MeV [Grü83]; 22 MeV [Bun68]; 65 MeV [Shi82]; 77, 95, 146, 155 and 198 MeV [Rem74]. The angular distribution at 198 MeV extended from only 80°–155°; cross sections for smaller angles were extrapolated from the 155 MeV data.

The data base for p + t elastic scattering was not as extensive. Angular distributions for 50°–160° were found at the following energies: 13, 16, 20 MeV [Det71]; 30 MeV [Dar72a]; 40, 57 MeV [Dar72b] and 156 MeV [Lan70]. Note the large gap between 57 and 156 MeV. Unfortunately, the values required for the IEP straddle this gap; as the cross section falls by more than an order of magnitude between the two energies, the linearly interpolated values may be seriously in error. The FEP, on the other hand, requires cross sections in the range ~10–70 MeV, and can thus be trusted to a greater extent.

The situation for p + h is somewhat better, because there are some data available around 100 MeV. The data base consists of angular distributions (30°–153°) at the following energies: 14, 16, 20 MeV [Hut71]; 31 MeV [Har70]; 35, 48 MeV [Mor75]; 85 MeV [Vot74]; 100 MeV [Gol70] and 156 MeV [Lan70].

4.5 Running THREEDEE

Before running the calculations, we optimized the input in THREEDEE for maximum efficiency, while retaining an accuracy >99% compared to results for a more conservative choice of numerical parameters. We found that twelve Gaussian points in each of r, θ and ϕ were sufficient for the integration of the distorted wave integral. The expansions of the distorted wave functions were found to converge after 10–15 partial waves, and the bound state wave functions (in steps of 0.1 fm) could be truncated at $r =$ 8 fm. DWIA calculations were then performed to cover all the reactions and geometries for which there were analyzed data, for $T_P = 10$ to 60 MeV in 5 MeV steps at $\theta_P = 45°$, and for $T_P = 10$ to 55 MeV at $\theta_P = 60°$. Each energy point took 15–20 seconds of cpu time on the VAX-750 computer.

4.6 Comparison of DWIA calculations with experimental data

4.6.1 ^{4}He(p,2p)^{3}H

In Figures 3.9 to 3.11, the calculations with the Final Energy Prescription for the two-body scattering are plotted as the solid curves, and those for the Initial Energy Prescription are plotted as dashed curves (cross sections are given in the laboratory system). There is very little difference in shape between the curves for each prescription; both give satisfactory overall fits to the data over the whole angular range covered. The calculated distributions are sometimes narrower than the experimental distributions and they peak at a slightly lower energy T_P. They also tend to turn upwards at either end of the energy scale, particularly at forward angles, a trend

which is not generally reflected in the data. We shall show in Section 4.7 that this is caused mainly by the energy-dependent optical potential of the low-energy particle in the final state.

The spectroscopic factors for the two prescriptions (indicated on the plots) are almost the same at large angles, but differ by nearly a factor of 2 at the smallest angles, which is as expected: off-shell effects on the two-body interaction are emphasized [Red70] at forward angles, and are particularly significant when the binding energy is relatively high, as is the case for ^{4}He. The two on-shell prescriptions are believed to represent the extremes, with the proper half-shell cross sections lying somewhere in between [Red70] [Bho76].

In Figure 4.1, the spectroscopic factors are plotted as a function of secondary angle θ_S for each primary angle θ_P. They are clearly angle-dependent, rising more or less linearly with increasing secondary angle. The error bars represent one third of the estimated maximum possible error in normalizing the DWIA distributions to the data.

The lines are least-squares fits (weighted by the inverse relative errors) for a constant spectroscopic factor, and for a linear angle dependence respectively. In the final chapter, we shall return to the subject of these angle-dependent spectroscopic factors.

4.6.2 ^{4}He(p,pd)^{2}H

The DWIA calculations are compared with the (p,pd) data in Figures 3.12 to 3.14. Although the agreement is not as good as for proton knockout, it is still quite reasonable.

The two-body cross section is not determined as accurately as in (p,2p), which probably explains most of the differences between the two prescriptions. The IEP, in particular, is interpolated in sparse elastic scattering

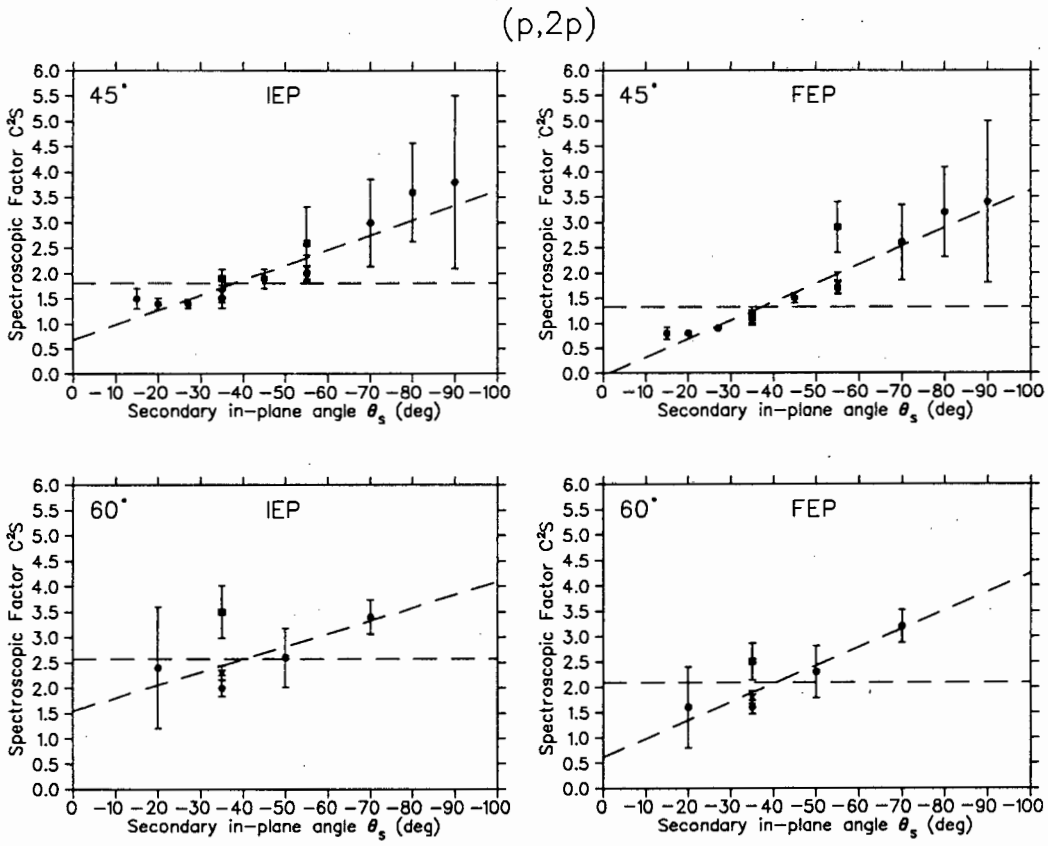

Figure 4.1: *Spectroscopic factors for (p,2p) at primary angles 45° and 60°, for each of the two prescriptions (as indicated), plotted against secondary in-plane angle θ_S. The in-plane angles are plotted as dots, and the out-of-plane angles are represented by crosses (for $\beta_S = 15°$), and by squares (for $\beta_S = 30°$). The lines are least-squares fits as described in the text.*

data. Also, the cross section has a steeper energy dependence than the N-N cross sections, which would tend to emphasize the differences. The IEP appears to give the better fits to the data, except at the most forward deuteron angles, where the FEP is superior. For $\theta_P = 60°$, the difference is not so much in the shape as in the position of the peak.

The spectroscopic factors are not as systematic as for (p,2p), with the ratio between the two prescriptions varying between 7 and 2. As can be seen in Figure 4.2, at $\theta_P = 45°$ the FEP spectroscopic factors are reasonably constant, mostly lying within a standard deviation of 0.3; at $\theta_P = 60°$, they are generally higher, being clustered around 0.6.

On the other hand, for the IEP at 45°, they decrease more or less linearly with increasing secondary angle, and at 60° there is no clear trend. The spectroscopic factor for $(60°; -35°; 30°)$ is noticeably higher than the others, because the DWIA predicts a more rapid drop in the distorted momentum distribution than is seen in the data as it goes out of plane from the quasifree angle $(60°; -35°; 0°)$.

4.6.3 ^{4}He(p,pt)^{1}H

The DWIA calculations are compared with the (p,pt) data in Figures 3.15 to 3.17. At forward angles, neither prescription describes the shape of the data very well. From $\theta_S = -35°$ outwards, the agreement is reasonable, with the FEP generally doing better than the IEP for primary angle 45°, and the IEP doing better at 60°. At $(45°; -70°; 0°)$ most of the yield is probably due to final state interactions between the two nucleons (see Section 4.9).

The kinks in the FEP curves, e.g. at $(45°; -35°; 0°)$, are caused by the interpolation of the two-body cross section in sparse elastic scattering data, and are thus an indication of the uncertainty in this component of the

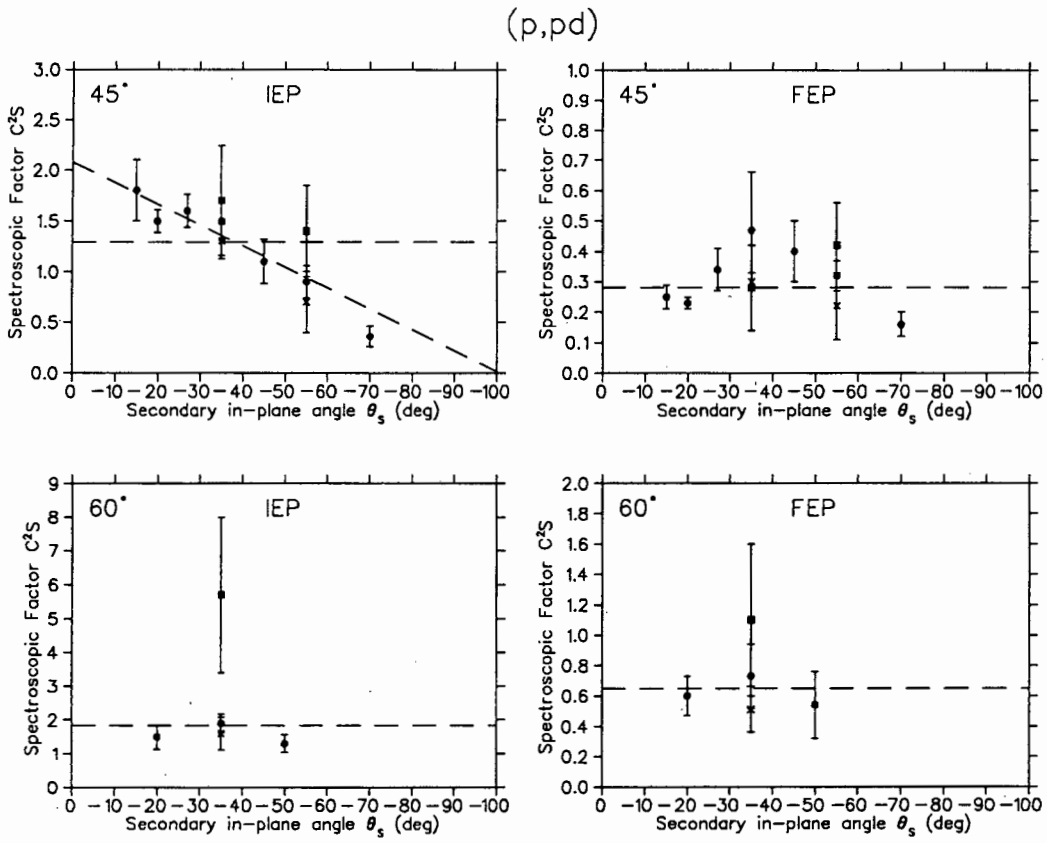

Figure 4.2: *Spectroscopic factors for (p,pd) at primary angles 45° and 60°, for each of the two prescriptions (as indicated), plotted against secondary in-plane angle θ_S. Other details are as given in Figure 4.1.*

factorized cross section.

The biggest problem with these fits is the steep rise in the DWIA cross section towards high proton energy, which is not as pronounced in the data. This is caused by the distorted wave integral increasing more rapidly than would be expected from an inspection of the recoil momenta. Possibly, it indicates that the triton optical potential is no longer appropriate at such low energies.

The spectroscopic factors are shown in Figure 4.3. They are erratic,

mainly because it is difficult to normalize a curve which is rising steeply at the point where the data reach their high-energy cutoff. The normalization thus depends critically on the cutoff energy. This can be seen most clearly for $(60°; -35°; 30°)$ and $(60°; -70°; 0°)$, where the lower cutoffs in the data (Figure 3.17) cause the extracted spectroscopic factors to be far out of line with the others. These two values were thus not used in the least-squares calculations of the average spectroscopic factors. The same problem is also evident, to a lesser extent, at $(45°; -55°; 30°)$ and $(45°; -80°; 0°)$.

4.6.4 ^{4}He(p,ph)n

Figure 3.18 shows the comparison between the DWIA calculations and the experimental (p,ph) data. There is good agreement at $(45°; -55°; 15°)$, and at $(45°; -65°; 0°)$ [after final state interactions have been accounted for (Section 4.9)]. At $(60°; -55°; 15°)$ the agreement would probably look reasonable too, if the component due to final state interactions were shown. At $(45°; -65°; 15°)$ the DWIA calculation does not reproduce the experimental distribution very well.

The spectroscopic factors are shown in Figure 4.4. For $\theta_P = 45°$, the average spectroscopic factors for the three distributions are 0.52 and 0.21 for the IEP and FEP respectively, but these are not the values which we have used for integrating the inclusive yields (Section 4.11.1). Rather, we took the values for (p,pt), because they are based on a wider range of distributions, and scaled them according to the difference between (p,ph) and (p,pt) at the angles for which we had both distributions. These scaled values are indicated by the dotted lines in Figure 4.4.

For $\theta_P = 60°$, there is no (p,pt) distribution corresponding to the single (p,ph) distribution, so we used the spectroscopic factors as extracted from the (p,ph) comparisons. Nevertheless, these are reasonably close to the

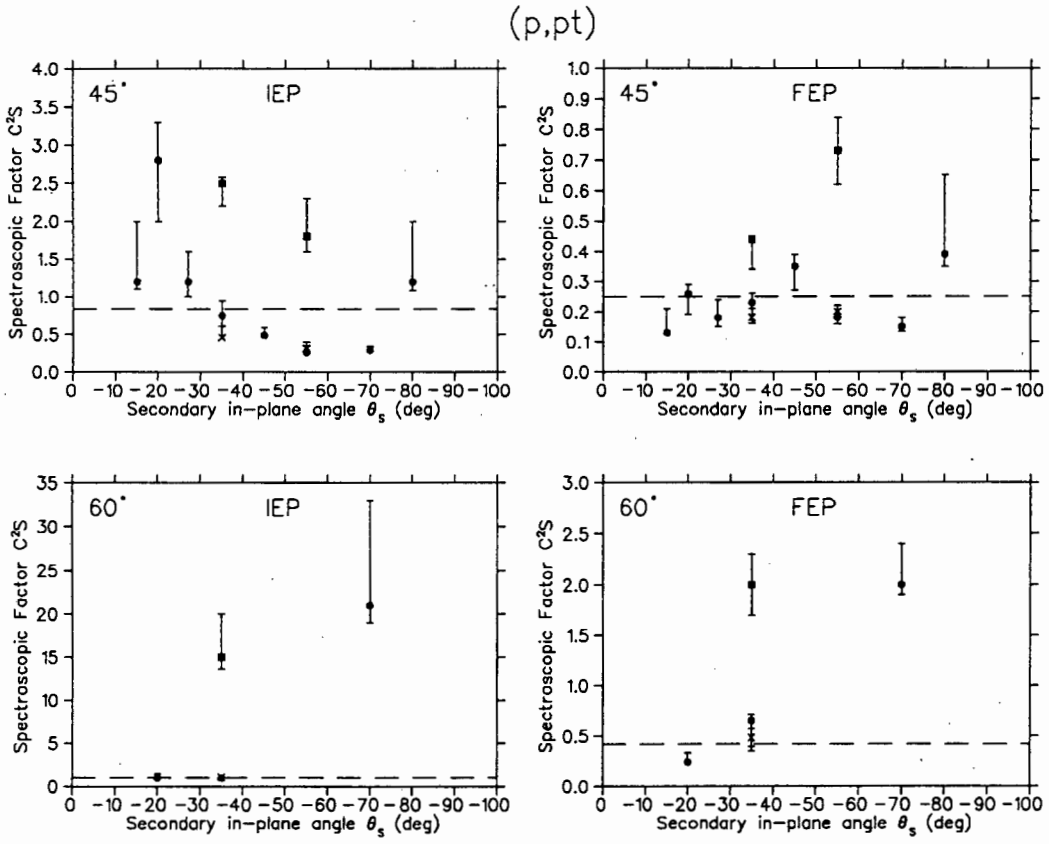

Figure 4.3: *Spectroscopic factors for (p,pt) at primary angles 45° and 60°, for each of the two prescriptions (as indicated), plotted against secondary in-plane angle θ_S. Other details are as given in Figure 4.1.*

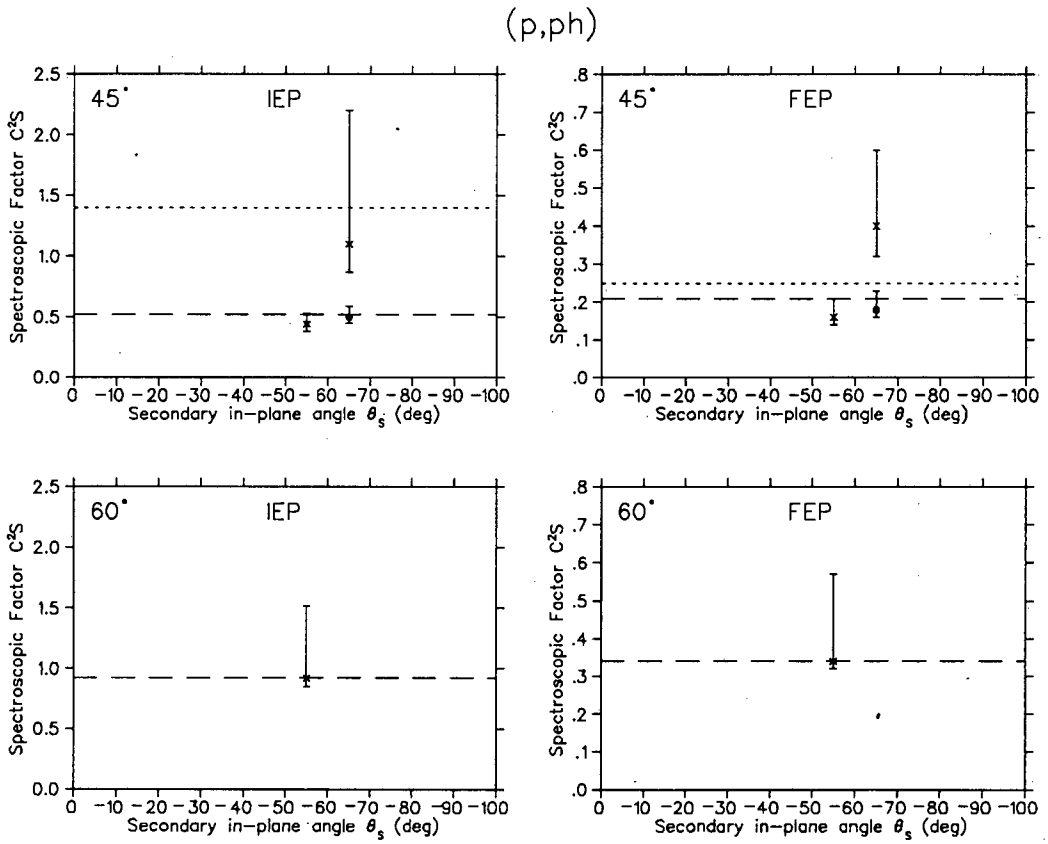

Figure 4.4: *Spectroscopic factors for (p,ph) at primary angles 45° and 60°, for each of the two prescriptions (as indicated), plotted against secondary in-plane angle θ_S. The meaning of the dotted lines is explained in the text. Other details are as given in Figure 4.1.*

average values extracted from the (p,pt) data: 0.92 versus 1.02 for the IEP, and 0.34 versus 0.42 for the FEP.

4.7 Sensitivity to the distorting potentials and bound state wave function

The criterion for judging the sensitivity of DWIA calculations to the distorting potentials is the extent to which changes in the potential parameters cause changes in the *shapes* of the energy-sharing distributions, rather than in the magnitudes. For example, Bhowmik *et al.* [Bho76] tried a number of different potentials for the exit channels of ^{12}C(p,2p) at 100 MeV, and found that the magnitude of their calculated angular correlation varied by a factor of 2; as the shape remained more or less constant, however, this was not considered to be indicative of undue sensitivity to these potentials.

Using this criterion, we claim that the DWIA calculations are insensitive to the potential used for the incoming wave, as a simultaneous change in all the well depths of 25% hardly affects the shapes of our energy-sharing distributions, but changes the magnitudes by 10–30%. Thus we may be confident that the adjustment of the well depths by the ratio m_B/m_A, as described in Section 4.2, does not invalidate the distorting potential in the entrance channel.

The outgoing distorted waves for the (p,2p) reaction do indicate some sensitivity to the well depths of the p + t optical potentials (see Figure 4.5): at the quasifree angle $(45°; -27°; 0°)$, a simultaneous reduction of V, W, V_{SO}, W_{SO} and V_{ex} by 25% in both exit channels (which is, after all, a fairly drastic change, and perhaps even unreasonably large) causes the peak to broaden, and to shift downwards in primary proton energy by ~5 MeV (dashed curve) in addition to the 50% increase in overall magnitude which

is reflected in the spectroscopic factors C^2S.

The shift in the peak position is consistent with the investigations of Kroll and Wall [Kro70] for changes in the strength of the real potentials; they found that the sensitivity to the imaginary potentials was limited to changes in absolute magnitude.

This shape sensitivity confirms our suspicion that the turn-up in the distributions towards either end of the energy scale is related to these potentials. Further investigation proves the turn-up to be an artefact of the energy-dependent potential breaking down for the outgoing proton with low energy.

The distribution calculated with potentials fixed at an average energy of 40 MeV (dotted line) is better behaved at the extremes, but does not fit the data as well as does the energy-dependent calculation in the more important peak region.

At $(45°; -70°; 0°)$, on the other hand, there is minimal change in shape, and only a 20% change in magnitude when the outgoing potentials are changed in the same way.

The calculations seem to be much less sensitive to the p + d and d + d potentials of the (p,pd) reaction. For $(45°; -35°; 0°)$, the dashed and dotted lines indicate the effect of varying each of these potentials in turn by 25%. Even the magnitudes barely change, which implies that the spectator deuteron plays a much reduced rôle in distorting the quasifree process in comparison with the spectator triton in the (p,2p) reaction.

The sensitivity of the (p,2p) calculation to the bound state wave function is shown in Figure 4.6 for two angles. There are minimal differences in shape between calculations with the wave function of van Oers *et al.* [Van82], and with that of Lim [Lim73], which is not surprising, because van Oers *et al.* noticed a difference only at high momenta (>400 MeV/c).

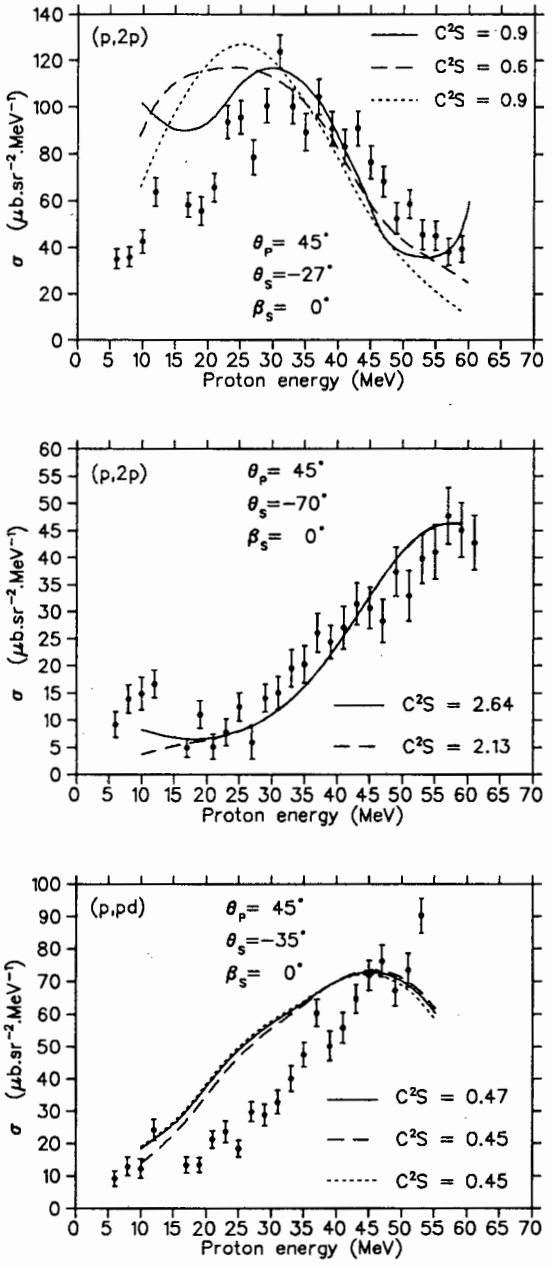

Figure 4.5: *Sensitivity to the optical potentials in the exit channels for (p,2p), top and centre, and (p,pd), below. The solid curves represent our standard FEP calculations. For (p,2p), the dashed curves are the result of changing the well depths by 25%, and are renormalized as indicated; the dotted curve is the result of using average-energy potentials. For (p,pd), the dashed and dotted curves are for 25% changes to the $p+d$ and $d+d$ potentials respectively.*

The use of Lim's parametrization increases the magnitude (i.e. reduces the spectroscopic factor) by 15% at the quasifree angle, but has no differential effect at the larger angle.

4.8 Corrections to the DWIA

It has been shown theoretically [Jac76] that the effect of spin-orbit interactions on the DWIA cross sections could be important. With the advent of the program THREEDEE [Cha82], which makes provision for spin-orbit terms in the optical potentials, several authors [Cha79] [Van82] [Wes85] [Sam86] [Cow89] have investigated the sensitivity of their calculated DWIA cross sections to these interactions, with diverse results. It seems that one can expect normalizations to change by about 10–30%, but the direction of the change is unpredictable. The effects are not as a rule limited to regions of high recoil momenta, as was found [Van82] in the specific case of ^{4}He(p,2p) at $\geq$250 MeV.

We find that the effect of turning off the spin-orbit terms in the potentials is to increase the calculated cross sections at the peak by $\sim$20% for the (p,2p) quasifree angle, by $\sim$10% for $(45°; -70°; 0°)$ and by $\sim$3% for (p,pd) at $(45°; -70°; 0°)$ (see Figure 4.7). The changes in shape and magnitude agree with the findings of Chant and Roos [Cha83] for (p,2p) energy-sharing distributions from $l = 0$ transitions.

It is worth remembering that the optical potential with the spin-orbit term off probably no longer fits the elastic scattering data from which it was derived, and is now inferior to a potential which has been derived with V_{SO} and W_{SO} held at zero during the original search on parameters. This is another reason why we retained the spin-orbit terms in the optical potentials (see Section 4.2), even for calculations of the factorized cross

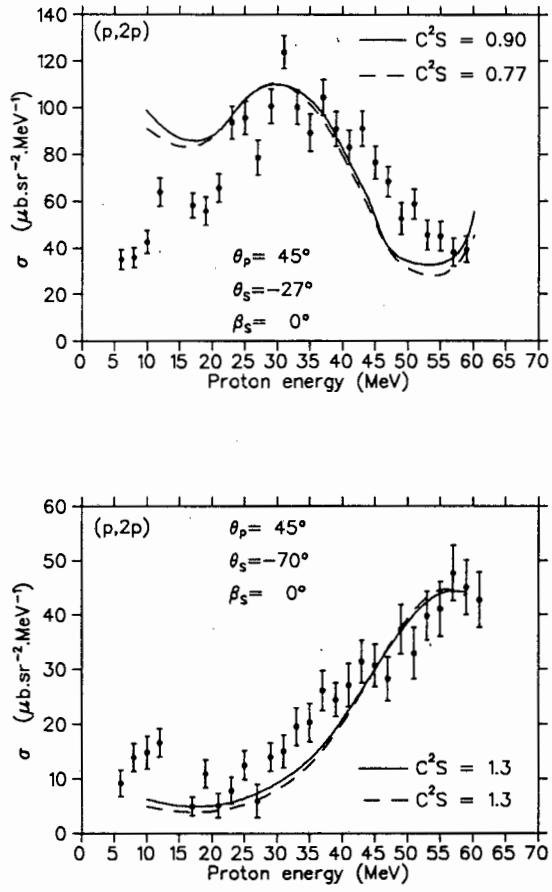

Figure 4.6: *Sensitivity of the (p,2p) calculations to the bound state wave function. The solid curves represent our standard FEP calculations with the wave function of van Oers et al. [Van82]; the dashed curves are for the parametrization of Lim [Lim73], renormalized as indicated.*

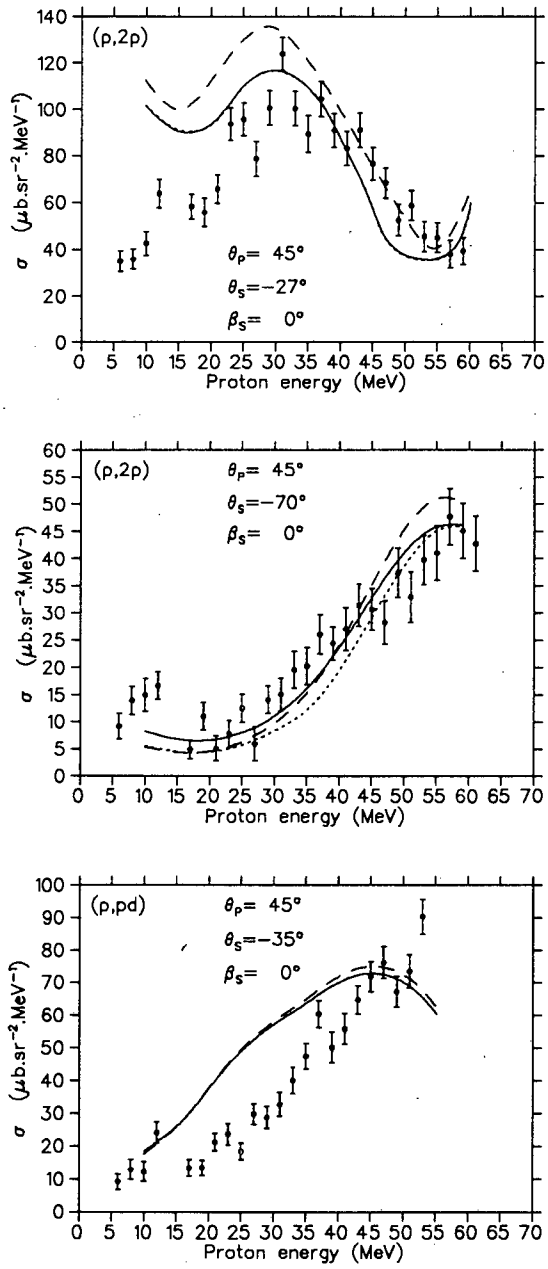

Figure 4.7: *The effect of turning off the spin-orbit terms in the optical potentials. The solid curves represent the standard calculations for the "factorized cross section", with full spin-orbit potentials; the dashed curves are for no spin-orbit terms. The dotted curves illustrate the difference obtained when the proper "coherent cross section" is calculated with the full spin-orbit potentials.*

section (which is formally incorrect).

In Figure 4.7 we also show the proper coherent cross section [Cha83], as a dotted curve. It is obvious that the solid curve (factorized cross section with spin-orbit potentials) yields results far closer to the "proper" results than the more theoretically-correct dashed curve (factorized cross section with no spin-orbit terms in the distorting potentials).

Figure 4.8 shows the effect of turning off the corrections for the nonlocality of the optical potentials. At the (p,2p) quasifree angle $(45°; -27°; 0°)$, the turn-up at the extremes is exacerbated, but the magnitude is hardly affected, whereas at $(45°; -70°; 0°)$ the magnitude increases ~20%, accompanied by slight shape differences. For (p,pd) at $(45°; -35°; 0°)$, the effect on both magnitude and shape is small.

Thus the calculations do not seem to display great sensitivity to the nonlocality of the optical potentials, which was also the conclusion of van Oers *et al.* [Van82] for ^{4}He(p,2p) at 250, 350 and 500 MeV.

4.9 Final State Interactions

In a number of the energy-sharing distributions for three-nucleon-cluster knockout, there is evidence of some extra structure which is not caused by the quasifree mechanism. This is particularly evident for (p,pt) at $(45°; -70°; 0°)$, Figure 3.16, and for (p,ph) at $(45°; -65°; 0°)$, Figure 3.18.

Calculations of the relativistic kinematics reveal that the final relative energy between the recoil nucleon and the primary proton reaches a minimum in the region of these structures. Consequently we have evaluated the Watson-Migdal [Wat52] [Mig55] final state interactions for the (p,ph) case, where the neutron-proton relative energy is only 0.6 MeV at $T_P = 25$ MeV.

Following Bernas *et al.* [Ber70], we write the triple differential cross

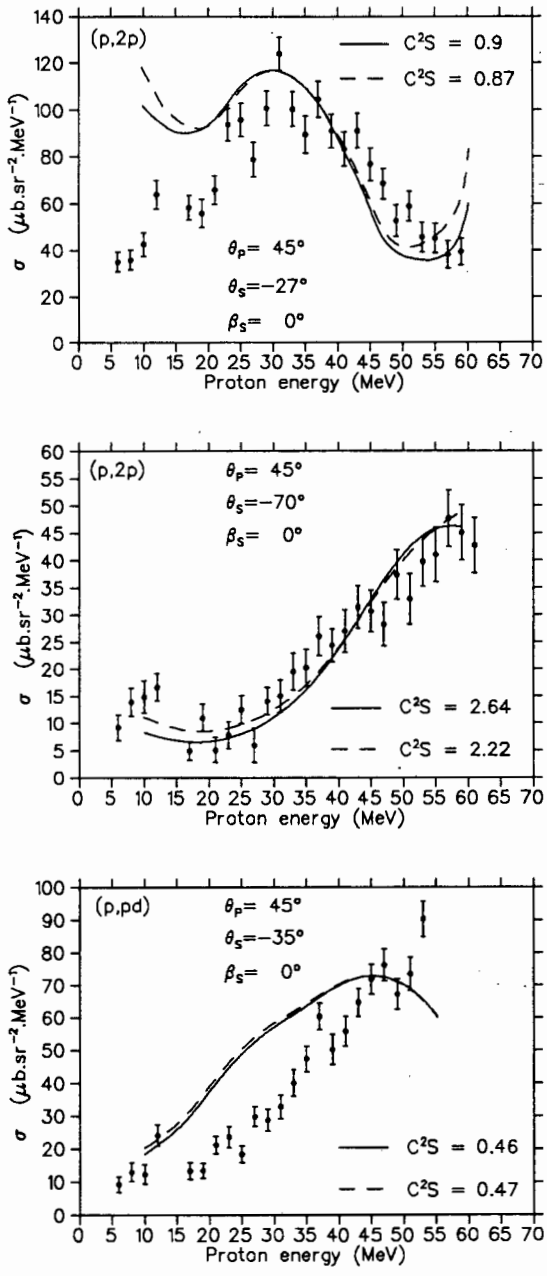

Figure 4.8: *The effect of turning off the corrections for nonlocality in the optical potentials. The solid curves represent the standard calculations with nonlocality corrections; the dashed curves are for no nonlocality corrections, and are renormalized as indicated.*

section for the final state interaction:

$$\frac{d^3\sigma}{d\Omega_c d\Omega_d dE_c} \propto \rho(E_c)\frac{1}{k^2 + (\frac{1}{2}k^2 r_{0s} - 1/a_s)^2}$$

where ρ is the three-body phase space factor, $k = p/\hbar$ for relative neutron-proton momentum p, r_{0s} is the singlet np effective range and a_s is the singlet np scattering length.

The implicit assumption [Wat52] [Mig55] in the proportionality is that the transition matrix element for the primary reaction (i.e. the production mechanism for these three-body final states) remains constant over the relative momentum range being studied. Furthermore, we have ignored the triplet contribution to the np scattering, as the singlet state is known [Ber70] to be predominant (most of the triplet np strength is in the bound deuteron).

The values for $r_{0s} = 2.76$ fm and $a_s = -23.72$ fm have been taken from the effective-range analysis of Lomon and Wilson [Lom74]. In Figure 3.18 the contribution of these final state interactions is shown at $(45°; -65°; 0°)$ (the calculation extends to np relative energies of 5 MeV, which can still be safely considered [Ber70] as purely s-wave scattering). The calculated spectrum has been normalized to the peak in the data, and when it is added incoherently to the DWIA calculation for the quasifree scattering, the overall fit to the data is very good.

4.10 Double-counting

Consider a ^{4}He(p,pd)^{2}H reaction for which the final state proton is detected in the primary telescope at θ_P, the knocked-out deuteron emerges at lab angle θ_d, and the spectator deuteron recoils at lab angle θ_R: if the knocked-out deuteron enters a secondary telescope situated at θ_S, i.e. $\theta_d = \theta_S$, we

have a normal (p,pd) coincidence event. However, if the *recoil* deuteron finds its way into the secondary telescope instead ($\theta_R = \theta_S$), we are then double-counting the knockout process which contributes to the yield at another geometry ($\theta_P; \theta_d$).

Fortunately, however, for s-state knockout the cross section (being roughly proportional to the momentum distribution) peaks around zero recoil momentum, so that most recoil deuterons are lost below the low-energy detection thresholds of the secondary telescopes. Double-counting, if it is at all significant, will be worst at the high-energy cutoff end of the energy-sharing distributions in Figures 3.12 to 3.14 (corresponding to low deuteron energy) and will decrease rapidly towards lower proton energies as the corresponding recoil deuteron energy increases.

To assess the importance of this "contaminant" in our quasifree knockout data, we calculated the momentum $\vec{p}_d$ of the detected deuteron corresponding to the uppermost datum in each of our distributions and compared it with the momentum $\vec{p}_u$ of the undetected deuteron in the three-body final state. From equation 1.1, the proportion of double-counted events in the total for that energy-bin is then roughly

$$\frac{|\phi(-\vec{p}_u)|^2}{|\phi(-\vec{p}_d)|^2 + |\phi(-\vec{p}_u)|^2}.$$

In the worst case, $(45°; -55°; 30°)$, this proportion was 0.4 for the highest datum at $T_P = 57$ MeV, dropping to 0.2 for the next point down, at 55 MeV, which illustrates the rapid disappearance of the problem as one moves away from the very edge of the energy-sharing distribution.

For all other geometries, the double-counting proportion never exceeded 0.2 for the extreme high-energy datum. Consequently, we have ignored this feature in the (p,pd) data as we do not believe that it significantly affects the comparisons with the DWIA calculations already described.

Similarly, we may expect the (p,2p) data to be "contaminated" by recoil protons from the reaction ^{4}He(p,pt)^{1}H and vice versa. Calculations in the same vein as for (p,pd) have shown that in the worst cases, the proportion of double-counting was around 0.2 for the extreme high-energy datum in each distribution, so we have ignored the problem of double-counting throughout our analyzed data.

4.11 Reconstructing the Inclusive Spectra

4.11.1 Quasifree knockout

We have shown that the DWIA is capable of describing the quasifree mechanism reasonably well for all possible knocked-out particles from ^{4}He (except for neutrons, which have not been investigated) over the solid angle range of major yield. Having extracted spectroscopic factors for each reaction type, we may now determine the total contribution of quasifree knockout to the inclusive yield simply by integrating the coincidence cross sections over the solid angles of the various secondary particles (Equation 1.5).

There is some ambiguity, however, in how one should treat the distortion of the (now unobserved) secondary particle. As the inclusive cross section depends only on the primary proton emerging cleanly from the nucleus, it does not matter whether the secondary particle is subsequently rescattered or even absorbed [Kro70]. Thus the use of a complex optical potential to distort the outgoing wave function is inappropriate, and one should use either a plane wave or at most a purely real potential. Wesick [Wes83] opted for the former, although it has been suggested [Hor80] [Def 69] [Don70] that the purely real potential is more consistent theoretically.

We, too, have chosen to use plane waves for the undetected particle, based on the investigation illustrated in Figure 4.9. We chose $(45°; -20°; 0°)$

as representative of the forward-angle data, where the turn-up at low and high energies, caused by inadequate optical potentials, has been shown to be the most severe (Section 4.7). Apart from a normalization difference, the full complex potential and the purely real potential give similar results. However, taking plane waves for the secondary proton causes the DWIA curve to be better behaved at high T_P (low secondary proton energy), which now reproduces the coincidence data more reliably.

As the difference in normalization between this curve and that from the purely real potential is <20%, we chose to use plane waves on pragmatic grounds. The severe turn-up in the other curves would have had unpredictable consequences when integrated over the solid angle of the secondary proton.

We have also followed Wesick *et al.* [Wes85] in using n-n rather than p-p phase shifts for the two-body t matrix in the (p,p′) calculations, as they found that the Coulomb interaction caused unphysical spikes in the integrated yield. The neglect of this long-range interaction is justified on the grounds that the impulse approximation describes essentially a short-range mechanism.

We differ from Wesick, however, in the choice of the solid angle ranges of integration. He selected end-points based on a plane wave calculation to determine where the cross section had dropped to 1% of its peak value, which corresponded to recoil momenta in the range 200–300 MeV/c. The distorted wave cross section was usually <5% of its maximum at these points.

We started by integrating between end-points which encompassed all that phase space for which recoils of <200 MeV/c were possible (see Figure 2.1). Then we repeated the calculation with even wider end-points to ensure that the integration had converged sufficiently.

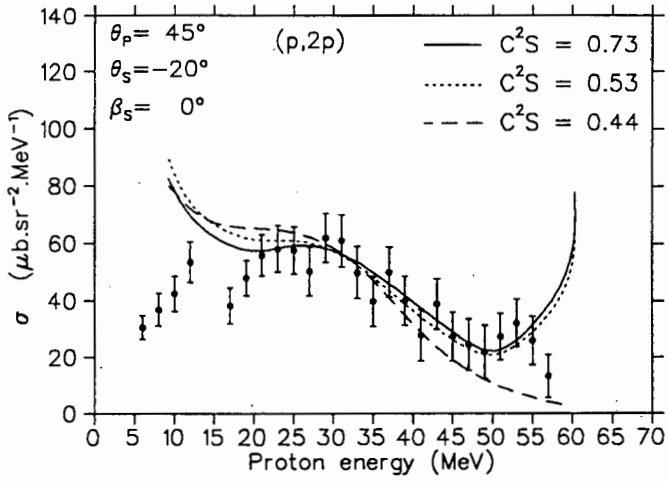

Figure 4.9: *Options for the exit channel of the unobserved particle: the solid curve shows the standard FEP calculation which was used for comparison with the coincidence data (complex optical potential); the dotted curve is for a purely real potential, renormalized by 30%, and the dashed curve is for plane waves, renormalized by 40%.*

This exercise showed that there was a need for caution at geometries for which the secondary proton was emitted at positive angles, on the same side of the beam as the primary proton. Figure 4.10 shows how the distorted wave integral turns upwards towards increasingly positive angles, despite the fact that the recoil momentum is continuously increasing (which causes the plane wave calculation to drop off as expected).

We attribute this to a possible breakdown [Roo77b] in the DWIA at these geometries, as we see the same trend for the other reactions too (cluster knockout), and in calculations [Law89] for heavier targets in other experiments. In one of those other experiments, ^{197}Au(p,2p) data were acquired with the coincident detectors on the same side of the beam: no

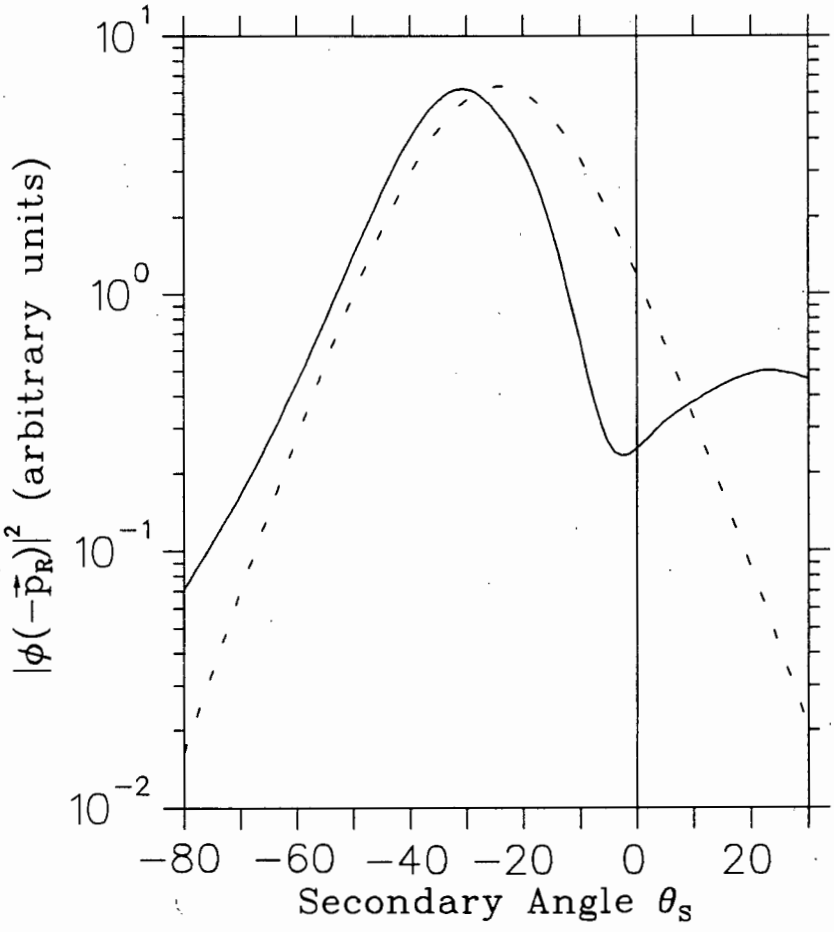

Figure 4.10: *Illustration of the upward excursion in the DWIA cross sections (solid curve) for positive angles of the secondary particle (i.e. emission on the same side of the beam as the primary proton). The plane wave calculation (dashed curve) has been normalized to the DWIA curve, and shows the expected continuous fall-off with increasing recoil momentum. These calculations were performed for 20 MeV primary protons emitted at 45°.*

evidence was seen for a corresponding increase in the coincidence yield.

Consequently, we have truncated the integrations over solid angle at $\theta_S = 0°$, which causes the integrated yields to be underestimated by not more than a few percent, as the major part of the yield is concentrated around low recoil momenta on the opposite side of the beam from the primary telescope.

Table 4.5 gives the end-points and the number of Gaussian integration points used for the calculations of the inclusive yields at 45°. The spectroscopic factors which were used at 45° and 60° are also indicated. For the (p,pn) calculation, the spectroscopic factor was assumed to be the same as for (p,2p).

					$C^2S(45°)$		$C^2S(60°)$	
Reaction	θ_S(Min)	Nθ	β_S(Max)	Nβ	IEP	FEP	IEP	FEP
(p,2p)	−110°	12	50°	6	1.80	1.32	2.57	2.09
(p,pn)	−110°	12	50°	6	1.80	1.32	2.57	2.09
(p,pd)	−90°	10	40°	5	1.29	0.28	1.84	0.65
(p,pt)	−86°	10	42°	6	0.84	0.25	1.02	0.42
(p,ph)	−86°	10	42°	6	1.40	0.25	0.92	0.34

Table 4.5: *The end-points used for integrating over θ_S and β_S; the number of Gaussian points used for each angle range; and the spectroscopic factors C^2S for each of the approximations, IEP and FEP .*

For (p,pd), (p,pt) and (p,ph), the computation of the high energy portion of the (p,p′) spectrum was complicated by the fact that kinematic limits were reached during integration over the specified solid angle, which would cause THREEDEE to terminate on error. Thus the spectrum had to be calculated piecemeal: up to the limiting energy, for the full range of integration, and then for a series of smaller ranges to get the higher energy points in T_P. Particular care was taken to account for all the solid angle

contributing to the uppermost point, so that we could have confidence in the inclusive yields constructed in this way.

The results are shown in Figures 4.11 and 4.12 for $\theta_P = 45°$ and 60° respectively. The curve labelled "Sum" represents the sum of the calculated contributions from the quasifree knockout of protons, neutrons, deuterons, tritons and helions, added incoherently.

At 45°, the IEP calculation accounts for ~60% of the inclusive yield between 10 and 55 MeV, and the FEP ~80%. The difference stems mainly from the (p,pn) contribution, for which the IEP and FEP spectroscopic factors, taken to be the same as for (p,2p), are possibly not accurate. Another discrepancy is in the contribution from triton and helion knockout at high energy, which reflects uncertainties in the two-body t matrix (off-shell effects combined with interpolation errors in sparse elastic scattering data). For both prescriptions, it is clear that most of the quasifree knockout contribution at high energy is in the form of cluster knockout, confirming the speculations of Wesick *et al.*

For $\theta_P = 60°$, one sees a similar picture, with the total estimated contribution from quasifree knockout being ~60% (IEP) or ~70% (FEP) of the experimentally measured yield.

We have not added the contributions from final state interactions. Although we showed in Section 4.9 that they could be significant at certain coincidence geometries, their estimated contributions to the integrated yield are insignificant over the energy region being studied (10 to 55 MeV).

Next, we refined our calculations by taking into account the angle dependence of the spectroscopic factors for nucleon knockout. We split the solid angle range of the unobserved particle into seven sectors in θ_S and summed the contributions from each, using average spectroscopic factors (for each sector) given by the linear least-squares fits shown in Figure 4.1.

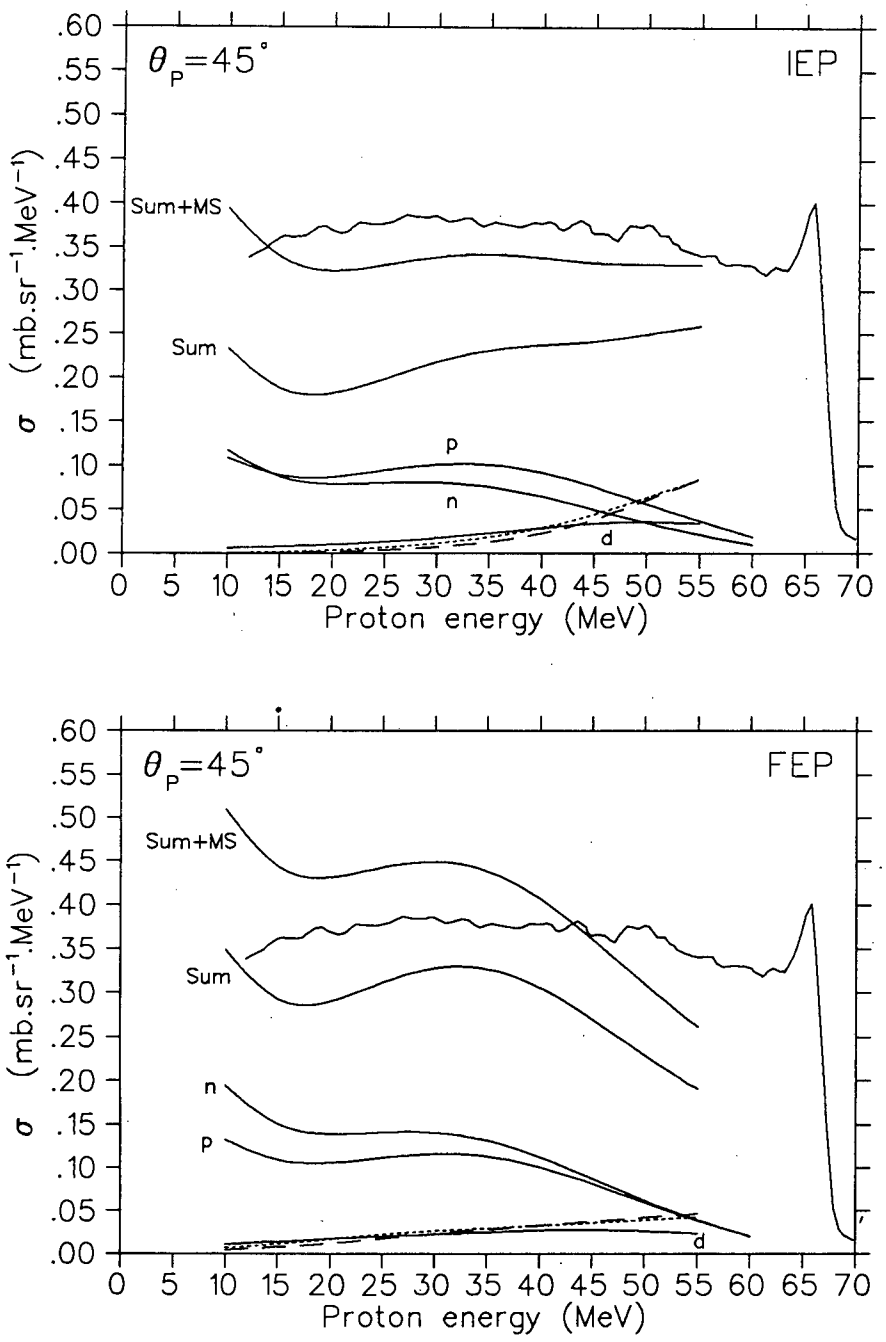

Figure 4.11: *Inclusive cross sections at 45°, compared with the data of Wesick et al. [Wes85], for the IEP (above) and the FEP (below). The curve labelled* 'Sum' *represents the sum of the contributions from the quasifree knockout of protons* ('p'), *neutrons* ('n'), *deuterons* ('d'), *tritons (dashed) and helions (dotted).* 'Sum + MS' *includes the estimated contribution from multiple scattering, added incoherently to the quasifree contributions.*

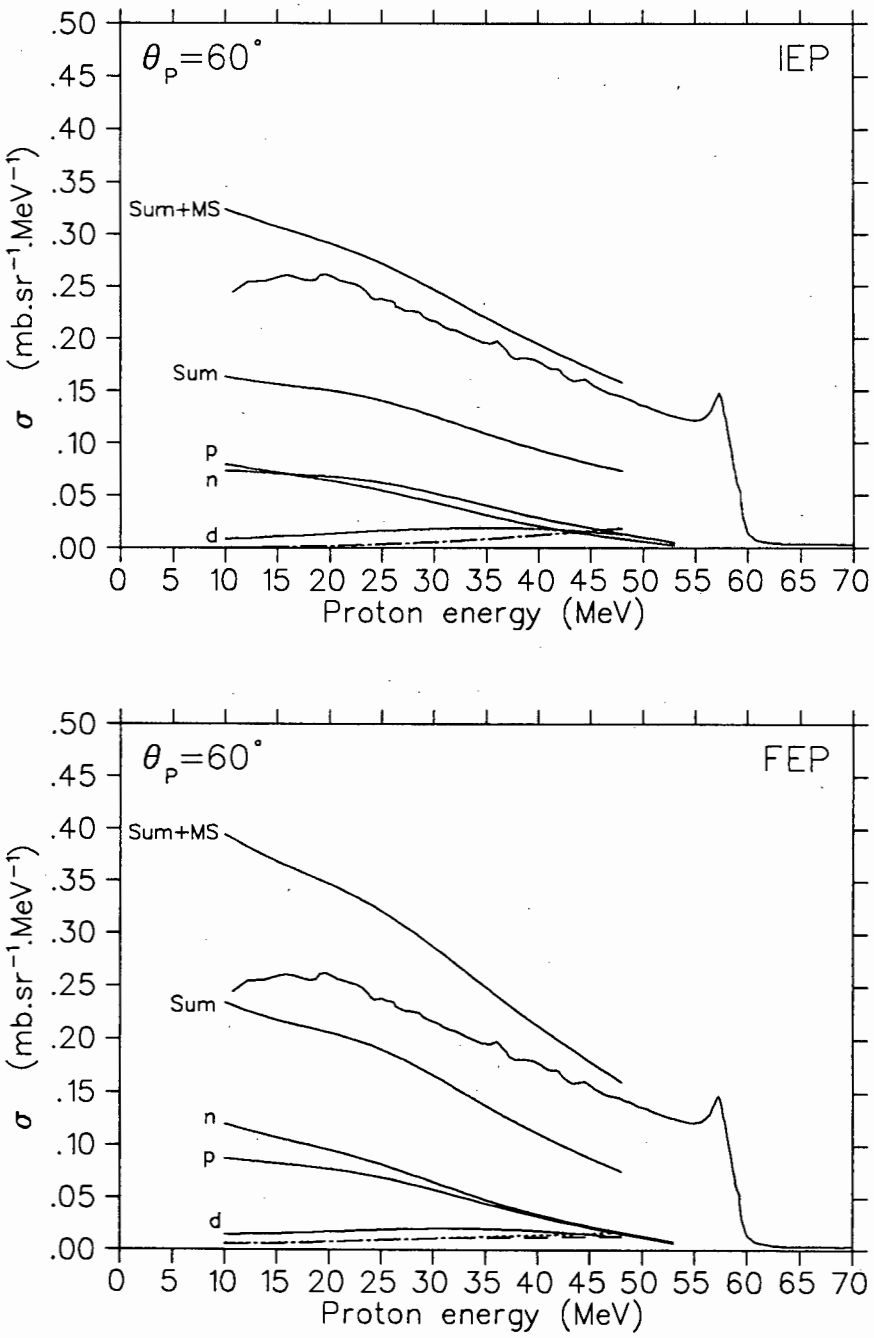

Figure 4.12: *Inclusive cross sections at 60°, compared with the data of Wesick et al. [Wes85], for the IEP (above) and the FEP (below). The curves are labelled in the same way as in Figure 4.11.*

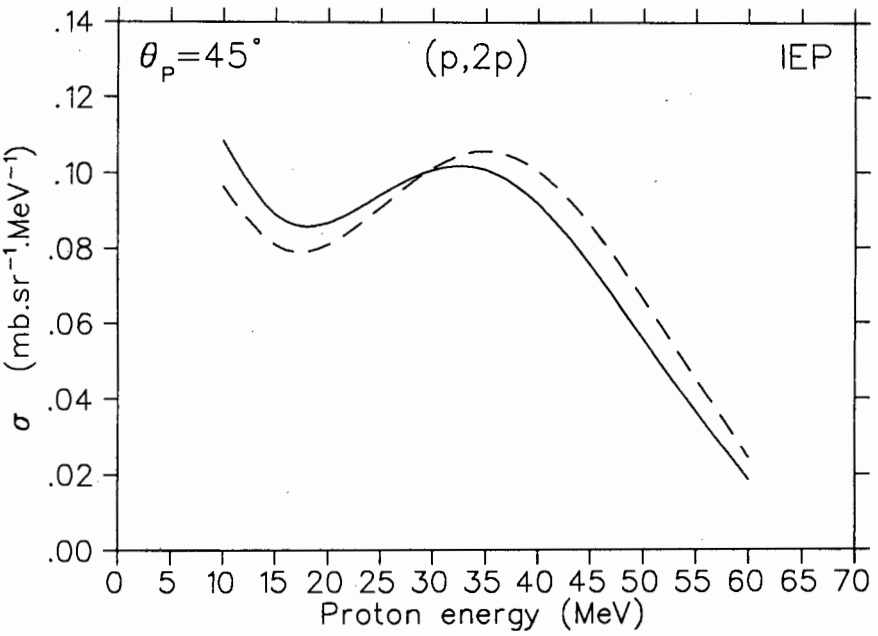

Figure 4.13: *A comparison between the inclusive (p,2p) yields at 45°, for a constant IEP spectroscopic factor (solid curve), and for angle-dependent spectroscopic factors (dashed curve).*

The comparison of the (p,2p) calculations with constant, or angle-dependent spectroscopic factors is shown for $\theta_P = 45°$ in Figure 4.13, indicating shape changes in the 10–30% range. It might seem surprising that the difference is not more profound, as the spectroscopic factors change by about a factor of 3 between $\theta_S = -15°$ and $-90°$. However, this relative insensitivity is a further consequence of the major yield being concentrated into a fairly small region of laboratory coordinate space. For $\theta_P = 45°$, for instance, most of the cross section comes from secondary protons emitted with lab angles between $-25°$ and $-55°$. Over this range, the least-squares constant spectroscopic factor is not too different from the linearly-dependent fit (see Figure 4.1).

For this reason, we did not repeat the exercise for cluster knockout. In any case, for (p,pd) there is not much angle dependence except in the IEP at 45° (see Figure 4.2), and for the three-nucleon clusters the extracted spectroscopic factors are too erratic for a meaningful estimate of the angle dependence.

Figures 4.14 and 4.15 show the same results as already presented, except that the (p,2p) and (p,pn) contributions have been calculated with the angle-dependent spectroscopic factors. In some energy regions, the total quasifree knockout contribution ('Sum') is changed by up to 30%, but the overall features of the curves are not very different from those generated with constant spectroscopic factors.

4.11.2 Multiple Scattering

We have seen that the total contribution of quasifree knockout to the inclusive continuum yields is between 60% and 80%. All the other reaction channels, which mainly involve direct breakup, or the excitation of the residual nucleus, leading to sequential decay, are loosely called "multiple scattering".

In order to test whether multiple scattering would fill in the remainder of the yield, we made a crude estimate of this contribution in our data, as follows:

Firstly, we assumed that the average proton multiplicity was 2, i.e. the primary proton was emitted along with one other proton (on average) from the various breakup channels: $p+t$, $p+d+n$, $p+p+n+n$, $d+d$ and $n+h$ (recall [Fia73] that ^{4}He has no bound excited states). Thus the multiple scattering portion of the (p,2p) data could be used for estimating the yield to be added to the quasifree components.

Secondly, the breakup of the target was assumed to arise from either

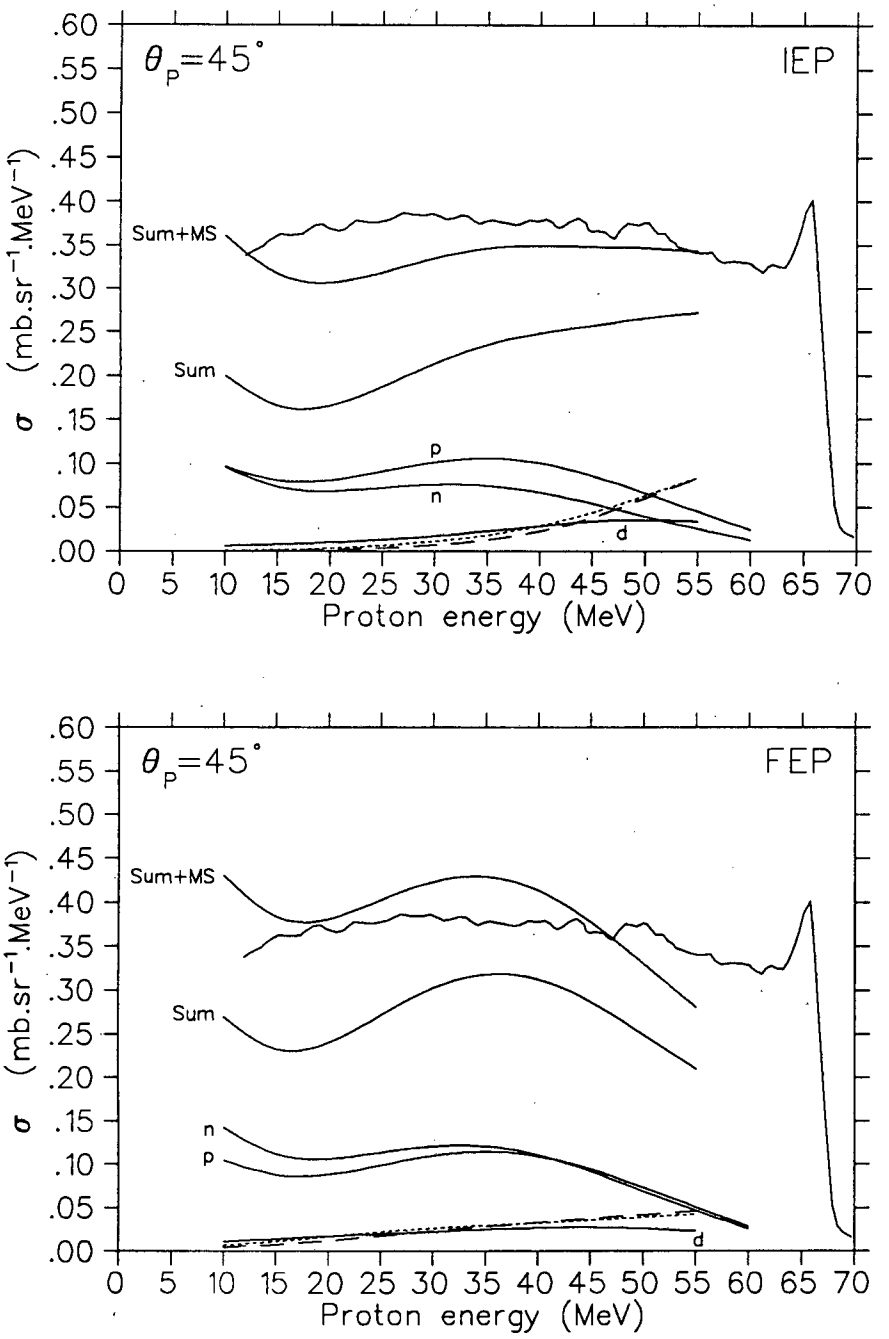

Figure 4.14: *The same as Figure 4.11, except that the nucleon knockout components are calculated with angle-dependent spectroscopic factors.*

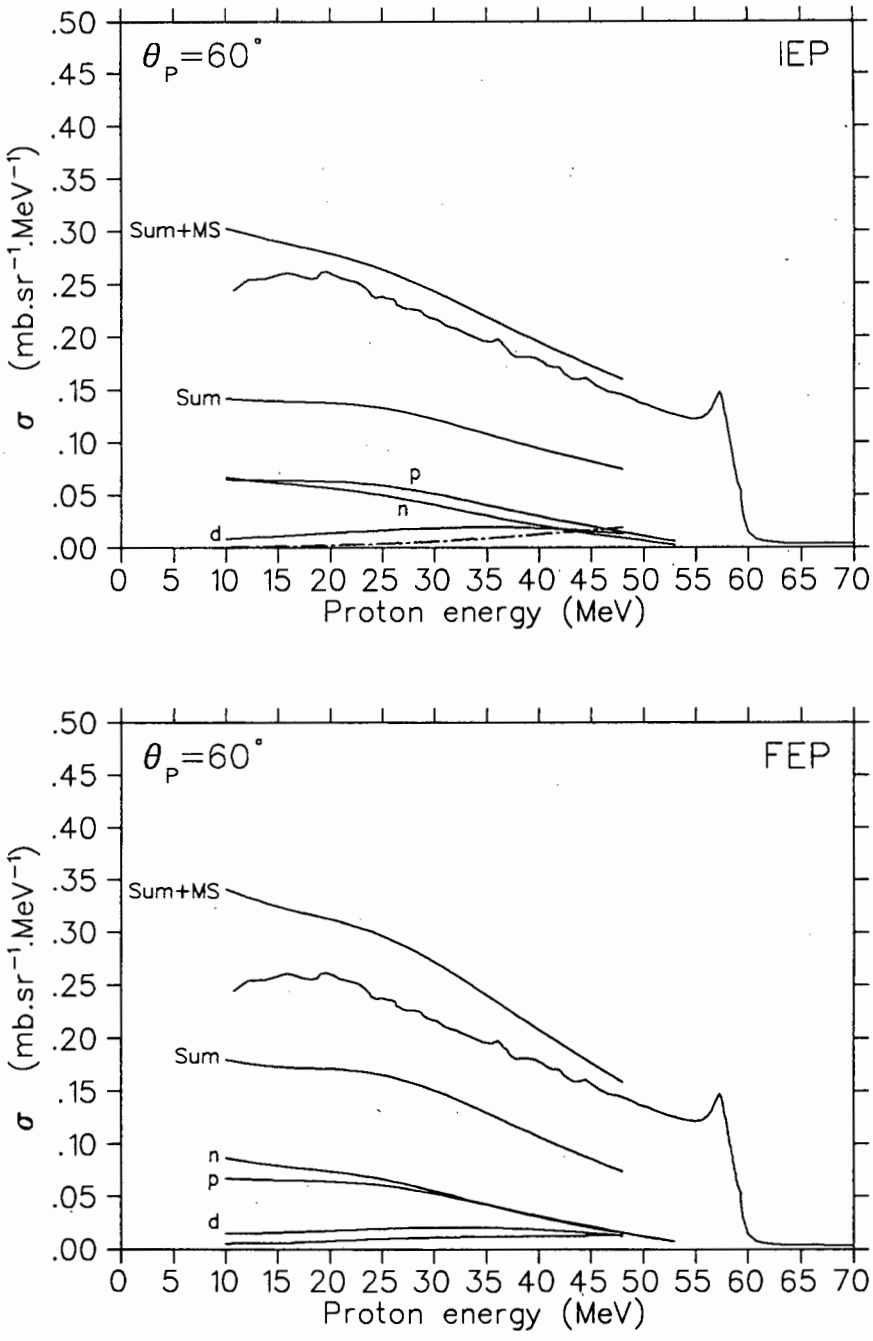

Figure 4.15: *The same as Figure 4.12, except that the nucleon knockout components are calculated with angle-dependent spectroscopic factors.*

an initial quasifree scattering, followed by further collisions with the recoiling spectator, or from "other mechanisms". Now the former mechanism has already been partially included in the calculated inclusive yields by our taking plane waves for the unobserved particle in the integration over solid angle, which thus allows for multiple scattering of this particle too. If we think of this quasifree doorway mode in terms of the Ciangaru picture [Cia84b], which treats the struck nucleon as an intranuclear projectile scattering inelastically off the residual nucleus, then it is clear that such a multiple scattering component will be forward-peaked.

However, the "other mechanisms" which still need to be included are assumed to be isotropic in phase space. Thus to select only these contributions, we need to take the multiple scattering yield at a relatively backward coincidence angle and integrate it over phase space. We consequently selected data at $(45°; -80°; 0°)$ and $(60°; -70°; 0°)$ for the purpose of this exercise. Figure 4.16 shows the region of the summed-energy distribution at $(45°; -80°; 0°)$ which was projected onto the primary proton energy axis in the same way as for the quasifree locus as described in Section 3.8. The curved gate delineates a portion of the multiple scattering data which were doubled to compensate for the data lost in the energy gap, and below the threshold of the secondary telescope. Random coincidences were subtracted as before, but no attempt was made to correct for the reaction tails in the NaI detectors.

The energy dependences of the resulting projected spectra were then approximated by linear least-squares fits and an integration was performed (for two sample points, $T_P = 20$ MeV and $T_P = 50$ MeV) over 4π solid angle with the appropriate phase space factors.

The final values for the integrated yield due to multiple scattering, at the two sample energy points, were again assumed to define a linear energy

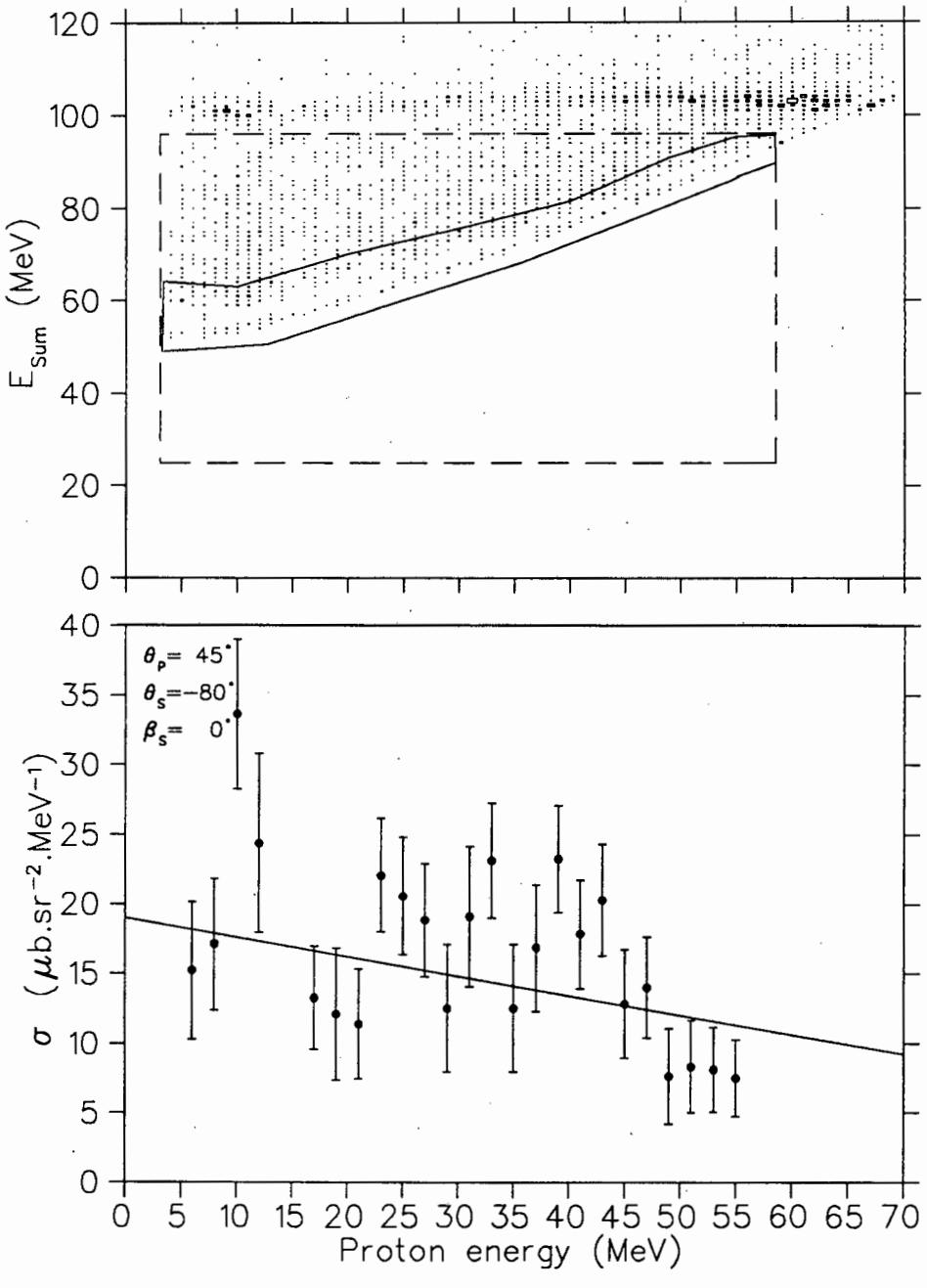

Figure 4.16: *Illustration of how the multiple scattering contribution was extracted from the 2-D summed-energy distribution (above) at* $(45°; -80°; 0°)$. *The indicated region below the quasifree knockout locus was projected onto the energy axis of the primary proton, to yield the spectrum shown below (data inside the curved gate were doubled — see text). Also shown below is a linear least-squares fit to the multiple scattering distribution.*

dependence. Quite coincidentally, the results of these estimates for $\theta_P = 45°$ and for $\theta_P = 60°$ were identical:

$$\frac{d^2\sigma}{d\Omega_P dE_P} = (0.181 - 0.002\,T_P)\ \text{mb.sr}^{-1}.\text{MeV}^{-1}.$$

The incoherent sum of this estimated multiple scattering contribution and the quasifree knockout cross sections is shown as the upper curve ('Sum + MS') in Figures 4.11 to 4.15.

In order to compare the quality and consistency of the final results for the various prescriptions and spectroscopic factor dependences, we have renormalized them to the inclusive data for presentation in Figure 4.17. The normalization factors are given in Table 4.6.

45°	IEP	Constant	1.09
		Ang.-Dep.	1.09
	FEP	Constant	0.90
		Ang.-Dep.	0.93
60°	IEP	Constant	0.87
		Ang.-Dep.	0.90
	FEP	Constant	0.76
		Ang.-Dep.	0.81

Table 4.6: *Normalization factors for the calculated inclusive cross sections shown in Figure 4.17. At each angle, the two prescriptions are calculated with both constant spectroscopic factors and angle-dependent spectroscopic factors (for the nucleon-knockout component).*

At 45°, the IEP reproduces the flat continuum spectrum better than the FEP, although it overestimates the low-energy portion. For both the constant and the angle-dependent spectroscopic factors, the IEP curves were ~10% low before renormalization, and the FEP curves were ~10%

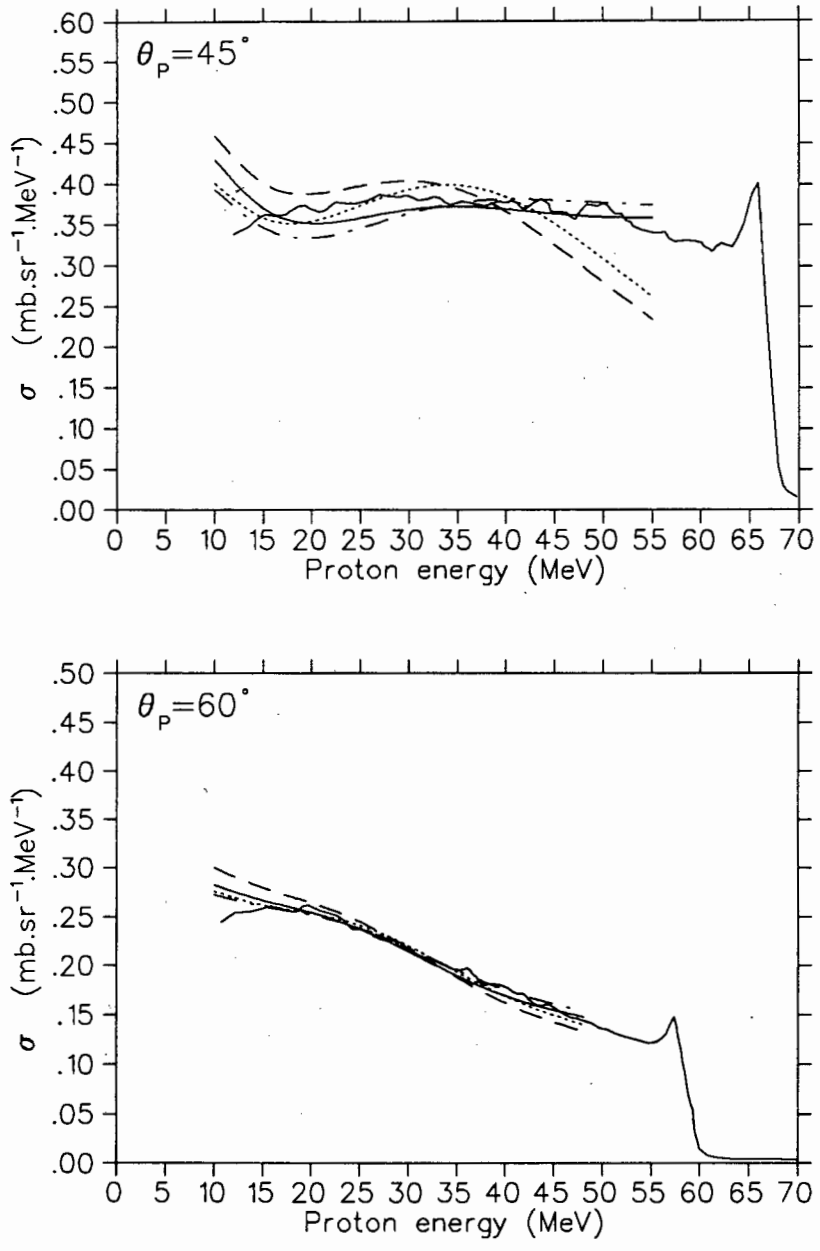

Figure 4.17: *Final comparisons of the calculated inclusive spectra at 45° (above) and 60° (below). The curves are normalized to the experimental data with the factors given in Table 4.6, and represent the sum of all the quasifree knockout contributions and the estimated multiple scattering contribution, as follows:*

Solid curve: IEP with constant spectroscopic factors C^2S;

Dash-dotted curve: IEP with angle-dependent C^2S;

Dashed curve: FEP with constant C^2S;

Dotted curve: FEP with angle-dependent C^2S.

high. Thus if we consider the two prescriptions as delimiting the uncertainty in the on-shell treatment of the two-body t matrices, then the experimental spectrum lies squarely on the average of the two. The shapes of the FEP curves are reasonable, but they both underpredict the high-energy portion of the spectrum. In this instance, the use of angle-dependent spectroscopic factors (dotted curve) does improve the quality of the fit somewhat.

At 60° the slope of the experimental distribution is reproduced almost exactly by both prescriptions with both methods of treating the spectroscopic factors, except at the lowest energies, where they fail to turn down as the data do. All the calculations overpredict the total yield, however, and need to be renormalized by between 10% and 25% to give the agreement as shown.

Chapter 5

Discussion and Conclusions

5.1 Applicability of the DWIA

In Chapter 4 we saw that the DWIA does quite well in modelling the quasifree knockout of protons from ^{4}He, although there are problems at the extreme ends of the primary proton energy scale, particularly for forward angles of the coincident secondary proton. For the knockout of deuterons, the calculations give a reasonable fit to the data, but they underestimate the high-energy yields at many of the coincidence angles. On the other hand, for triton and helion knockout, it is the calculation which rises somewhat more rapidly than the data towards high primary proton energy, although the overall fits are still reasonable.

Therefore we claim that the DWIA is adequate for the exercise of calculating the quasifree scattering component of the inclusive spectra. It was possible to extract reasonably consistent spectroscopic factors, and judging by the differences between the calculations for the two prescriptions, the inclusive yields could be integrated to an accuracy of 10–20% overall, with larger errors for specific reaction channels at some energies.

In many ways, it is surprising that the DWIA performs as well as it does for these reactions at 100 MeV, as there are a number of reasons for treating the calculations with circumspection:

Firstly, some doubt has been expressed [Roo74] [Wes85] [Kit85] about the applicability of distorted-wave techniques to a system as light as ^{4}He, because the small number of open reaction channels may give rise to strong interference effects. Thus the use of an optical potential to account for initial- and final-state interactions is hardly appropriate, as the spectator nucleons would be expected to influence the reaction individually rather than via a "mean field" (which is an acceptable picture for heavier nuclei).

On the other hand, the system is not light enough to allow distortions to be ignored altogether. Plane wave (PWIA) calculations typically over-

predict the coincidence yield by about a factor of 5, and the position of the peak is not given as well as in the DWIA.

Another problem caused by the light system is that the "kinetic energy approximation" [Cha77], which is necessary for factorizing the distorted wave integral, might be expected to break down. It consists of neglecting a term in the final state Hamiltonian which couples the kinetic energies of the two emitted particles c and d [in the reaction $A(a,cd)B$]. The approximation is valid if the mass of the spectator nucleus m_B is large compared to m_c and m_d, and is thus also known [Red70] as the heavy-core approximation. Nevertheless, it can still be valid, even for a "light core", if particles c and d are emitted at approximately 90° to each other in the centre-of-mass [Cha77]. Hence we would expect the breakdown to be limited to the unusual geometries, such as at very forward angles for the secondary particle. Furthermore, the approximation becomes exact in the plane-wave limit, so that the smallish distortions in light systems might also remedy the situation to a certain extent.

Then there are the problems associated with low energies, particularly in the exit channels:

The impulse approximation allows the knockout process to be treated as a free scattering, but strong distortions caused by the core nucleons may shift the two-body t matrix fully off-shell [Mil81]. In other words, the quasifree scattering takes place inside the distorting potentials, which may modify the wave functions such that momentum and energy are not conserved [Lim66], and the asymptotic scattering angle and momentum transfer are therefore not applicable. This is a broader interpretation of an "off-shell" effect than that caused merely by the binding energy of the struck nucleon, with its resultant momentum mismatch [Red70]. It implies that the factorization approximation is invalid, so that a proper calculation

would need to evaluate the two-body matrix elements coherently with those of the distorted waves, as has been done by Kudo *et al.* [Kud86], using an effective N-N interaction.

Young and Redish [You74] have investigated the validity of the DWIA for ^{4}He(p,2p) at 65 and 100 MeV by comparing it with exact Faddeev calculations, and they find that it is a reasonably good approximation at 100 MeV, but not very good at 65 MeV. However, they considered only quasifree symmetric angles. Earlier comparisons [Lim66] between calculations in the distorted-wave t-matrix approximation, and in the DWIA, indicate that the DWIA should still be adequate at 100 MeV; but when one of the outgoing particles has low kinetic energy, i.e. at the extremes of the energy-sharing distributions, the distortions are probably severe enough to invalidate the DWIA, and effects such as focusing [McC59] [Lim66] [Mil81] of the distorted wave functions may lead to large uncertainties in the calculations, particularly [Lim66] at forward angles.

With regard to "unusual" geometries, Kitching *et al.* [Kit85] observe that one cannot expect the DWIA to perform well for kinematics which sample the minima or the high-momentum tails of the momentum distributions, as the small cross sections for the "clean" quasifree process would be significantly contaminated by multiple scattering contributions, such as the rescattering of particles originally "emitted" in a direction of high yield. Possibly the best examples of this point are the out-of-plane geometries in our sets of data, where one sees the quasifree peaks becoming progressively washed out with increasing angles β_S.

In the case of cluster knockout, there are several arguments against the DWIA as an appropriate formalism:

Clusters will be deformed by the nuclear medium in which they are embedded [Kit85] and will have a large chance of breaking up before escaping

from the strong nuclear field, which implies that the impulse approximation is inappropriate. [On the other hand, the fact that the spectator is light means that distortion in the exit channel may be minimal, even for low energies of the knocked-out cluster, so that there is a good chance that the cluster will get out of the nucleus cleanly.] The large size of a cluster and consequent nonlocality of the two-body interaction also violates the spirit of the impulse approximation; and the heavy-core approximation is even less valid than for nucleon knockout. From a computational point of view, there is the added difficulty of sparse cross section data for the proton-cluster scattering.

It is gratifying that, in spite of all these objections, the DWIA gives a reasonable fit to the (p,pd) data, and it is surprising that it even comes close to reproducing the (p,pt) and (p,ph) distributions.

To summarize, we have demonstrated experimentally that the DWIA is applicable to the reaction ^{4}He(p,p'x) at 100 MeV over most of the phase space containing the major yield, despite strong theoretical objections. Nevertheless, it would be unwise to extend these calculations to geometries far from those which have been tested here, as there are indications that the DWIA may break down rapidly, particularly towards forward angles of the knocked-out particle, and on the same side of the beam as the primary proton. Furthermore, the calculation is expected to be less accurate when one of the outgoing particles has low energy. Thus the extreme ends of the calculated energy-sharing distributions should be viewed with caution.

5.2 Angle-dependent Spectroscopic Factors

For the reaction ^{4}He(p,2p), the angle dependence of the extracted spectroscopic factors is quite pronounced: for example, we see an increase of a factor of 3–4 (see Figure 4.1) between the quasifree angle $(45°; -27°)$ and the largest angle measured, $(45°; -90°)$.

A similar trend is found [Cow89] for ^{12}C(p,2p) at 200 MeV; and for the same reaction at 100 MeV, Devins *et al.* [Dev79] find that the spectroscopic factor derived from angular correlation data at symmetric angles is double that derived from data at asymmetric angles.

This angle-dependent trend is also a feature of comparisons between DWIA calculations and inclusive (p,p′) measurements. Wesick *et al.* [Wes85] see a factor of 3–6 increase (depending on the prescription used for the two-body interaction) in the spectroscopic factor between 17.5° and 60°, for ^{4}He(p,p′) at 100 MeV. They speculate that the rising spectroscopic factor may be caused by multiple scattering contributions in the low energy part of their spectra, which would be most pronounced at the larger angles.

For ^{12}C(p,p′) at 90 and 200 MeV, Förtsch *et al.* [För88] find a similar trend with increasing scattering angle. However, the angle-dependence is not as severe as in the work of Wesick *et al.* on the lighter target, which casts doubt on the proposed explanation simply in terms of multiple scattering contributions, which should increase with target mass.

We have seen in Sections 4.7 and 4.8 that the DWIA calculations at different angles are sensitive in varying degrees to such features of the optical potentials as nonlocality corrections, spin-orbit terms, and the energy-dependent real central and imaginary potentials. The use of a different bound state wave function also changes the spectroscopic factor at some angles more than at others. Nevertheless, it is implausible that the combination of all these uncertainties would account for more than a 50% relative

change between the spectroscopic factors extracted at the various angles. Therefore, the explanation for a factor of 3 variation in spectroscopic factor must be sought elsewhere.

Inspection of the least-squares fits to the (p,2p) spectroscopic factors shown in Figure 4.1 reveals that the angle dependence has roughly the same slope for $\theta_P = 45°$ and 60°. Furthermore, the offset between the two sets is close to 15°, which is the difference between the two primary angles. To illustrate this point, in Figure 5.1 we have plotted all the FEP spectroscopic factors on a single graph against the separation angle $\theta_P - \theta_S$. Clearly, the physics behind the angle dependence is related to this separation angle.

Also indicated on the plot is the approximate separation angle at which the coincidence cross section peaks for each of the sets $\theta_P = 45°$ and $\theta_P = 60°$. As the bulk of the coincidence yield for $\theta_P = 60°$ is biased towards larger separation angles, where the spectroscopic factors are higher, it is evident that the *inclusive* cross section, i.e. the integrated coincidence yield, as measured by Wesick *et al.*, will require a larger spectroscopic factor to normalize the DWIA calculation at 60°, than at 45°.

Thus we have shown that the angle dependence of the spectroscopic factors in the inclusive calculations of Wesick *et al.*, and in the exclusive calculations of this work, have their origin in one and the same phenomenon, which is a dependence on the separation angle $\theta_P - \theta_S$. This in turn is suggestive of a dependence on the recoil momentum.

As the spectroscopic factor is determined by normalizing the DWIA calculation to the experimental cross section at the peak of the energy-sharing distribution, it is instructive to look at the separate factors in the factorized cross section (Equation 1.4) at these peak values. In Table 5.1, we group some data sets for $\theta_P = 45°$ and 60° into pairs with more or less the same separation angle. For each data set, we list the peak cross section

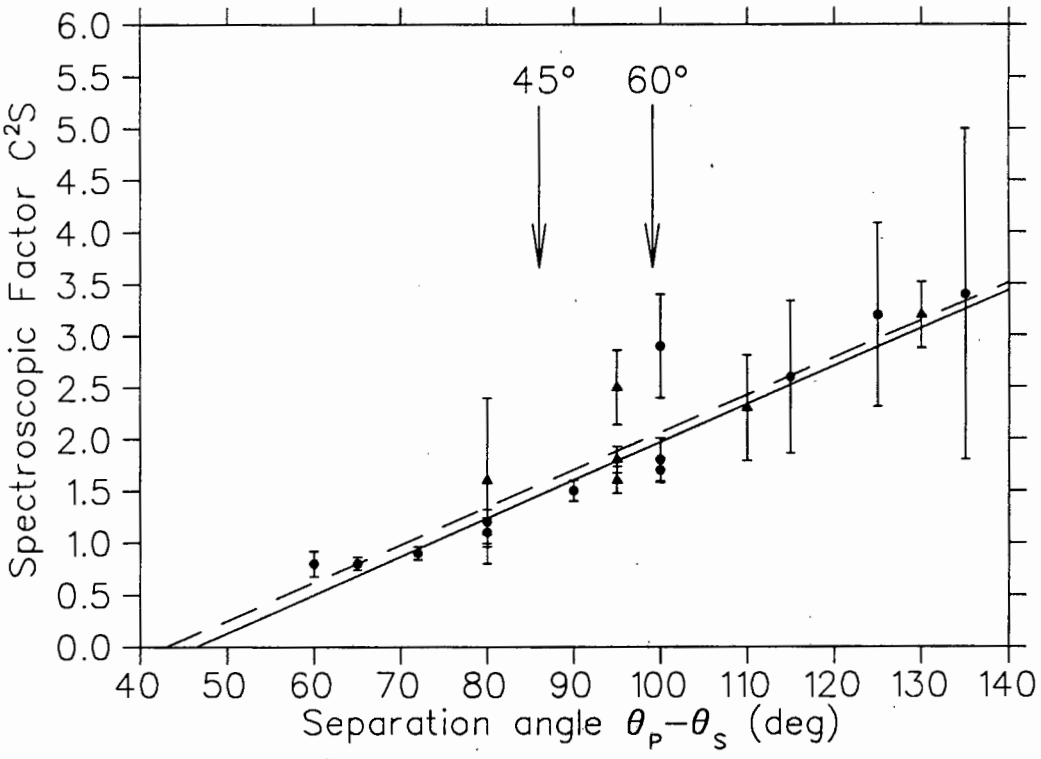

Figure 5.1: *The dependence of the spectroscopic factors on the separation angle $\theta_P - \theta_S$. The FEP spectroscopic factors for $\theta_P = 45°$ are plotted as dots, with the solid line least-squares fit; the corresponding spectroscopic factors for $\theta_P = 60°$ are plotted as triangles, with the dashed line fit. The arrows indicate where the cross section peaks for each set of coincidence angles.*

in the measured distribution, and the corresponding recoil momentum at the peak. These values are seen to be consistent for a particular separation angle, irrespective of the primary angle θ_P.

$(\theta_P;\theta_S)$	$\theta_P-\theta_S$	σ_{Exp}	$\vec{p}_R$	$\lvert\phi(-\vec{p}_R)\rvert^2$	σ_{pp}	C^2S
(45°; −27°)	72°	110	32	6.7	7.3	0.9
(45°; −55°)	100°	100	92	4.9	4.7	1.7
(60°; −35°)	95°	110	72	5.4	5.0	1.6
(45°; −70°)	115°	47	151	1.4	4.3	2.6
(60°; −50°)	110°	55	134	2.2	4.4	2.3
(45°; −80°)	125°	35	198	0.9	4.3	3.2
(60°; −70°)	130°	15	228	0.4	4.1	3.2

Table 5.1: *The dependence of the factors in the DWIA cross section on the separation angle $\theta_P - \theta_S$. σ_{Exp} is the experimental cross section ($\mu b.sr^{-2}.MeV^{-1}$) at the peak of each tabulated coincidence angle, and the other columns are, in order: the recoil momentum (MeV/c), the distorted momentum distribution (arbitrary units), the two-body cross section ($mb.sr^{-1}$) and the FEP spectroscopic factor.*

In the DWIA calculations, four factors are multiplied together to give the cross section (Equation 1.4): the value of the distorted momentum distribution at the appropriate recoil momentum, the two-body cross section, the kinematic factor (which remains almost constant for the angles shown here and is thus not tabulated), and the spectroscopic factor. The kinematics of the two-body interaction (and thus the cross section σ_{pp}) also remain fairly constant over these angles (Table 5.1), so we conclude that the angle dependence of the spectroscopic factors suggests a discrepancy between the data and the calculated distorted momentum distribution. Our results show that generally the DWIA falls off much too rapidly with respect to the

data beyond ~100 MeV/c. Thus the increasing trend in the spectroscopic factors towards large angles is possibly a consequence of these angles being sensitive to only the higher-momentum components of the bound state wave function.

Larger than expected high-momentum components have been seen in almost all other measurements of ^{4}He(p,2p):

At 600 MeV, Perdrisat *et al.* [Per69] found that the momentum distribution deviated from a fitted Gaussian shape above about 100 MeV/c. In a proper DWIA calculation, Roos [Roo74] obtained a better shape, using the Lim wave function [Lim73] for the bound state, but still could not reproduce the momentum components above ~200 MeV/c.

The momentum distribution was also found to be wider than the DWIA calculation in a comparison [Tyr66] at 460 MeV. At 156 MeV, Frascaria *et al.* [Fra75] were able to fit the distorted momentum distribution only after employing an unrealistic oscillator wave function for the bound state, as the wave function of Lim [Lim73] once again underpredicted the high-momentum components.

Not surprisingly, the plane wave calculations of Pugh *et al.* [Pug73] are also too narrow in comparison with the 100 MeV data, but that could be just a consequence of neglecting distortions.

The state of the art measurements for this reaction remain those of van Oers *et al.* [Van82] at 250, 350 and 500 MeV. The data deviate significantly from their calculated momentum distributions above ~200 MeV/c. Although the Lim wave function reduces the discrepancy at high momentum (>400 MeV/c) in comparison with the wave function corrected for meson exchange currents (which is the one we used, too—see Section 4.3), it does no better in the 200—400 MeV/c range. Consequently, we would not expect to improve our own fits by switching to the Lim wave function.

Measurements of the distorted momentum distribution by means of the ^{4}He(e,e'p) reaction are troubled by an apparent sensitivity [Van88] [Mag89] to the kinematics of the reaction. Once this puzzle has been resolved, the ^{4}He(e,e'p) data may help to elucidate the present problem.

A number of possible explanations [Van82] have been put forward for the enhanced contributions to the data at high recoil momenta. Apart from general flaws in the DWIA description of the reaction, such as the inadequacy of the optical potentials and the bound state wave function, the most likely cause would seem to be that other mechanisms, which are not accounted for in the DWIA, manifest themselves at high momenta, where the DWIA cross section becomes small.

Several rescattering and exchange terms have been proposed [Van82]. Conceptually, the simplest of these is the picture in which one of the emerging protons scatters elastically from the recoil nucleus. Intuitively this occurrence should be fairly common: we have already seen that distortion plays a significant rôle in these reactions, yet there are few open channels for inelastic scattering from such a light nucleus. A large proportion of the distortion would thus consist of elastic rescattering. Mougey [Mou80], for instance, has demonstrated that the enhanced high momentum components seen in the reaction ^{12}C(e,e'p) may be accounted for by the addition of a rescattered component to the DWIA momentum distribution.

The DWIA assumes that flux lost to distortion is removed from the quasifree locus; it makes no attempt to account for the reappearance of this flux elsewhere, which is probably a reasonable approach for heavier targets, where the proportion of elastic rescattering would be small.

Even for light targets, one would normally not worry about this second-order mechanism, provided that the kinematics were such as to favour the clean quasifree mechanism, e.g. where low recoil momenta are possible.

Thus we return to the observations made in Section 5.1, that the DWIA should not be expected to perform well at "unusual" geometries where the clean quasifree knockout cross section is low, which makes it vulnerable to contamination from competing mechanisms.

For the other reactions (p,pd), (p,pt) and (p,ph), it is not as clear whether there is a relationship between the spectroscopic factors and the recoil momentum. In only one case is there an obviously angle-dependent trend: for (p,pd) at $\theta_P = 45°$ (see Figure 4.2). Here, the IEP spectroscopic factors *decrease* with increasing separation angle, which implies perhaps that the DWIA distorted momentum distribution is too broad. This is quite likely, considering the manner in which the bound state wave function was deduced from a momentum distribution which was, itself, already distorted (see Section 4.3).

In conclusion, we speculate that the origin of the angle-dependent spectroscopic factors is traceable to an inability of the DWIA to reproduce the high-momentum components of the distorted momentum distribution. Although the reason for this failure cannot be pinpointed with certainty, it is suspected that contributions from other diagrams, such as rescattering of one of the outgoing protons, might constitute the remainder of the yield at these momenta.

5.3 The Quasifree Scattering component in the inclusive spectra

The main conclusions of this study, with regard to the composition of the inclusive spectra, have already been stated in Section 4.11. They may be summarized as follows:

- Quasifree scattering accounts for the bulk (~70%) of the inclusive continuum yields from the reaction ^{4}He(p,p') at 100 MeV.

- The knockout of nucleons contributes most of the yield at low energies of the scattered primary proton, but cluster knockout dominates the yield at higher energies.

We now consider some aspects of these findings in more detail, and relate them to theoretical estimates.

Firstly, to put the preceding discussion on spectroscopic factors into perspective, it is worth stressing that the integration over the solid angle of the unobserved particle (in order to get the inclusive yield) is not very sensitive to the angle dependence of the spectroscopic factors, because most of the yield is concentrated into a relatively small solid angle range, which is adequately characterized by an average spectroscopic factor.

Most of the uncertainty in the estimated shape and magnitude of the inclusive quasifree scattering component arises from two sources: the spectroscopic factors for the (p,pn) contributions, and the high-energy cluster knockout contributions.

We justify using the (p,2p) spectroscopic factors for (p,pn) also (on the self-conjugate target ^{4}He), on the basis of the arguments put forward by Kitching *et al.* [Kit85], who claim that all the factors (Equation 1.4) in the DWIA cross section for the two reactions should be about the same, except for the free N-N cross section, which of course is treated properly in THREEDEE. Other differences would depend on the bound state wave functions for the proton or the neutron, and on the different optical potentials for scattering off the mirror residual nuclei. We have seen in Section 4.3 that the bound state wave function is taken to be the same for the proton or the neutron in ^{4}He, as isospin invariance was assumed in its derivation. It is argued [Kit85] that the effect of the small difference in binding energy

is essentially cancelled by the Coulomb force suppressing the tail of the proton wave function. Similarly, as discussed in Section 4.2, the same optical potential was used for the distortions in the final states of the (p,pn) reaction as was used for $p + {}^3H$ in the (p,2p) reaction, since the isospin coupling was found [Van82] to be weak.

Despite these arguments, it would have been preferable if experimental (p,pn) coincidence spectra had been available, so that spectroscopic factors could have been extracted directly. It is doubtful, however, whether such measurements would have altered the substance of the conclusions which we have already drawn from this work. Thus from a pragmatic point of view, it is probably not worth setting up a difficult neutron experiment for the sole purpose of generating the data for the present comparison, as the gain is likely to be disappointing.

The other major source of uncertainty, namely fitting the high-energy portion of the (p,pt) and (p,ph) distributions, manifests itself in the divergent shapes of the IEP and FEP integrated yields at high energies of the primary proton (see Figure 4.17). It would not be a simple matter to remedy this situation. Firstly, there is the difficulty (see Section 4.6.3) of normalizing the calculated DWIA curves to the steeply rising knockout data. Then there is the sparseness of the elastic scattering data which introduces large uncertainties in the two-body cross sections for each on-shell prescription. Finally, it is probable that other aspects of the DWIA require careful scrutiny, because of the theoretical objections raised in Section 5.1. Fortunately, these uncertainties are not so large as to challenge the broad conclusions which we have made, although they do prevent an *accurate* estimate of the proportion of quasifree scattering in the total yield.

For the primary angle 45°, the total quasifree contributions amount to 60% and 80% of the measured inclusive yield, for the IEP and FEP

respectively. If the two prescriptions are taken to represent the extremes, then we may propose an estimate of $70 \pm 10\%$ for the total contribution from quasifree knockout. At $\theta_P = 60°$, the prescriptions give 60% and 70% respectively, which is also compatible with the figure $70 \pm 10\%$.

It should be remembered that these contributions to the inclusive spectra also include some of what would be called multiple scattering in a coincidence experiment, as we are interested in observing only the primary proton cleanly, and are not concerned with what happens to the secondary particle in the final state. In the context of the DWIA as applied to inclusive spectra, then, the remainder of the yield ($30 \pm 10\%$) is presumed to consist of multiple scattering events involving the primary proton. We have shown in Section 4.11.2, that an independent estimate of this multiple scattering contribution (from a rough analysis of the coincidence data below the quasifree locus) corroborates the estimate of $30 \pm 10\%$ for $\theta_P = 45°$, but seems to overestimate the relative contribution at 60°, giving ~60% instead of the expected 30–40%. We do not think that much importance should be attached to this discrepancy, in the light of the crudeness of the latter estimate.

We conclude that the relative contributions of quasifree scattering and multiple scattering to the inclusive yields are ~70% and ~ 30% respectively (between 10 MeV and ~50 MeV). Of the quasifree component, ~75% comes from nucleon knockout and the rest comes from cluster knockout. At 10 MeV, the (p,pN) contribution is over 90%, whereas at the highest energies it is only 20–40%, with the bulk of the quasifree yield coming from the knockout of deuterons, tritons and helions.

The shapes of our calculated total spectra agree reasonably well with the measured spectrum at 45°, and very well at 60° (see Figure 4.17). The lack of a visible quasifree peak, which bothered Wesick *et al.* [Wes85], is

seen to have a simple explanation: the (p,pN) distribution does indeed have a maximum (at ~30 MeV for $\theta_P = 45°$, see Figure 4.11), but this is washed out by the cluster knockout contributions picking up towards higher energies of the primary proton. Although some semblance of this peak remains in the FEP curve, it disappears altogether in the IEP prediction. This confirms the observation made in the Introduction, that the lack of a quasifree peak does not necessarily imply that the reaction mechanism is dominated by multiple scattering. The fact that the measured spectrum at 45° continues without dropping (beyond the high-energy cutoff of these calculations) may well be caused by the excitation of high-lying unbound states in ^{4}He, as suggested by Wesick *et al.*

It is interesting to make a rough comparison between our results on ^{4}He and the predictions of some preequilibrium models for heavier targets. All of these models, whether semiclassical or quantum mechanical, compute the continuum spectrum as arising from a series of N-N interactions, with a certain probability of emission after each step, so the probability for quasifree scattering is obtained simply by truncating the series after one step. Our results thus represent a semi-empirical determination of the fraction of the yield attributable to the first step.

Recognizing the importance [Bla73] [Gru86] of the first one or two steps in this series, Chiang and Hüfner [Chi80] have developed a simple theory which allows the calculation of continuum spectra from the sum of just three terms, representing single scattering, double scattering and compound nucleus formation, respectively. The calculation of the first two steps is based on the notion of an average trajectory; and the probability of an interaction is related to the mean free path in the nuclear medium. Despite the unsophisticated approach, these calculations have been reasonably successful in fitting inclusive continuum spectra generated by 15–100 MeV incident

protons and neutrons on a range of targets from ^{12}C to ^{209}Bi (in some cases doing better than the more complicated exciton model).

Chiang and Hüfner conclude that single scattering dominates the cross section except at large energy losses, where multi-step mechanisms take over, as one might expect. For instance, they estimate that for mean free paths in the range 3–5 fm (the upper limit is probably most appropriate [Gee89] for 100 MeV incident energies), the proportion of quasifree scattering in the total yields is 60–70% for a ^{12}C target, 50–60% for ^{54}Fe and 30–40% for ^{209}Bi. These estimates seem a little high in the light of our estimate of $70 \pm 10\%$ for the very light nucleus ^{4}He.

Recently, Smith and Bozoian [Smi89] have taken a similar approach, which was first proposed by Wu [Wu80]: they replace the first step of the exciton model calculation (the 2p1h term) by an explicit calculation for quasifree scattering, while the multiple scattering contribution is calculated in the normal way by the exciton model, from the 3p2h term onwards. The quasifree scattering is calculated in a Fermi-gas model for the nuclear response function, with the absorption being given by a modified Glauber theory. The calculation is renormalized to yield the correct reaction cross section by modifying only the depletion factors in the exciton part of the series.

From the results of these calculations, it is claimed that the quasifree term dominates the inclusive continuum yields from various nuclei at incident energies between 60 and 200 MeV. For instance the proportion of quasifree scattering from ^{27}Al at 90 MeV is claimed to be $\sim$70%; for ^{54}Fe at 62 MeV it is $\sim$60%, which again is somewhat higher than might be expected from our results. However, the fits to the data are generally not good, and it thus seems difficult to justify the way in which the calculations were renormalized, where it was assumed that the absolute magnitude of

the quasifree part was correct.

It would be interesting to compare our results with predictions of various preequilibrium models for the first step of the series in ^{4}He, although the lightness of the system probably has implications which are even more serious for these models than for the DWIA.

5.4 Alternative Approaches

^{4}He is an awkward target nucleus from a theoretical point of view because, as we have seen in Section 5.1, it is too light to be modelled correctly in the DWIA, yet too complex for an exact solution of the scattering problem.

Young and Redish [You74] have performed Faddeev calculations for ^{4}He(p,2p)^{3}H at 65 and 100 MeV by reducing the reaction to a quasi-three-body problem. This approach goes a long way towards an exact solution, although there are obviously still some drastic approximations. The bound state is viewed as an inert triton core plus a proton, and the three particles interact via pairwise separable potentials. In order to make the calculation tractable, the proton-triton potential is limited to relative $l \leq 2$.

The object of the calculations was to test the accuracy of the DWIA, which was thus derived in the Faddeev formalism for comparison with the exact calculation (in order to simulate the impulse approximation, the N-N interaction was turned on only once). For the quasifree symmetric angle at 100 MeV, it was found that the DWIA gave the correct shape, and the magnitude was within 20% of the exact calculation. Young and Redish conclude that the DWIA is a reasonably good approximation at 100 MeV, although it is inadequate for the extraction of reliable spectroscopic factors. Nevertheless, this is an encouraging result with respect to the work presented here.

Fukunaga *et al.* [Fuk86] have used Faddeev techniques to model ^{4}He(p,p′) and ^{4}He(p,pt)^{1}H at 65 MeV. They were able to fit the data well in the region of final state interactions, but there was no evidence in their data of quasifree cluster knockout.

In conclusion, it appears that in principle more accurate and appropriate calculations than the DWIA are possible for modelling the various breakup channels induced by 100 MeV protons on ^{4}He. It would be interesting to compare the present results with the full Faddeev calculations when these become available.

Chapter 6

Summary

Exclusive measurements have been made of the reactions ^{4}He(p,2p), (p,pd), (p,pt) and (p,ph) at 100 MeV. The primary protons were measured at two angles, 45° and 60°, in coincidence with secondary protons, deuterons, tritons or helions covering a wide range of angles on the opposite side of the beam, both in- and out-of-plane.

The purpose of the measurements was to explore the validity of the Distorted Wave Impulse Approximation (DWIA) as a description of these quasifree knockout reactions, at all geometries where the knockout cross section is significant. It was trusted that the model would be found to be adequate, even for unusual geometries, so that reliable spectroscopic factors could be extracted. Thus it would be possible to determine the shape and magnitude of the quasifree scattering contribution to the *inclusive* ^{4}He(p,p′) spectra by integrating the DWIA cross sections over the solid angles of the various types of secondary particle.

The interest in the relative importance of quasifree scattering and multiple scattering in the inclusive spectra at 100 MeV was generated by the inclusive measurements of Wesick *et al.* [Wes85], which showed no evidence of quasifree peaks, even though these were predicted by the DWIA. It was speculated that the contributions from cluster knockout could be a factor in the flat shape of the measured spectra. Furthermore, Wesick *et al.* were puzzled by the angle dependence of the normalizations that were required to fit the DWIA calculations to the inclusive spectra.

It was thus recognized that coincidence measurements would be needed in order to elucidate these problems. The various contributions from nucleon knockout, cluster knockout and multiple scattering would then be measured directly.

Six telescopes, each consisting of two silicon detectors and a NaI detector, were used to measure protons at primary angles 45° and 60°, in

coincidence with protons, deuterons, tritons or helions at secondary angles ranging from $-15°$ to $-90°$ in plane, and from $0°$ to $30°$ out-of-plane. The target consisted of a gas cell filled with high-purity helium at $\sim$1 bar of pressure.

The event tapes, which contained the data taken during the experiment, were analyzed to produce energy-sharing distributions of the cross sections for quasifree knockout. The projections of the two-dimensional quasifree knockout loci were made onto the energy axis of the primary proton.

DWIA calculations were performed for comparison with the energy-sharing distributions. The (p,2p) calculations are expected to be more accurate than those for cluster knockout because of the availability of precise N-N phase shifts, whereas the two-body interactions for (p,pd), (p,pt) and (p,ph) were interpolated from sparse elastic scattering data. Two different on-shell prescriptions were used for determining an appropriate scattering angle and centre-of-mass energy for the two-body interaction: the Initial Energy Prescription (IEP) and the Final Energy Prescription (FEP).

For the (p,2p) reaction, the comparison between the experimental data and the curves calculated by means of the DWIA is satisfactory over the entire solid angle range of the energy-sharing distributions. However, the DWIA results tend to turn upwards at the extremes of the energy scale, particularly at forward angles, which is a trend not reflected in the experimental data. The spectroscopic factors which are required to normalize the DWIA curves to the experimental energy-sharing distributions are angle-dependent, with an increasing trend towards larger secondary angles.

The DWIA calculations for the (p,pd) reaction are in reasonable agreement with the data, although they are not as good as for proton knockout. There are bigger differences between the curves for the two on-shell prescriptions, and the spectroscopic factors are not as systematic as for (p,2p).

They are reasonably constant with angle, however, except for the IEP at primary proton angle 45°, which tends to decrease towards larger secondary angles.

For the (p,pt) and (p,ph) reactions, the DWIA curves are in poor agreement with the data at forward angles, but from secondary angles of $-35°$ outwards, the agreement is reasonable. There are large uncertainties in the extracted spectroscopic factors because of the difficulty in normalizing the curves to the data, which rise steeply towards the high-energy cutoff of the energy-sharing distributions. At some angles, the data indicate strong contributions from final state interactions. A Watson-Migdal calculation of the final state interaction was added incoherently to the DWIA results and gave good overall agreement with these experimental distributions.

The sensitivity of the DWIA calculations to details of the distorting potentials was investigated. It was found that the calculations were not sensitive to the optical potential in the entrance channel, but that there was some sensitivity in predicted magnitude and peak position to changes in the outgoing potentials for the (p,2p) reaction. The cluster knockout calculations are not as sensitive to the potentials in the exit channel. Furthermore, the calculations are not very sensitive to details of the bound state wave functions.

The nonlocality corrections changed some of the cross sections by $\sim$20%, and the effect of the spin-orbit interactions in the optical potentials was found to vary with angle from 3% to 20%.

The angle dependence of the spectroscopic factors probably results from an inability of the DWIA to reproduce the high-momentum components of the distorted momentum distribution. This also provides a ready explanation of the angle dependence found by Wesick *et al.* in the inclusive measurements. It is suspected that the extra yield at high momenta is the

result of contributions from mechanisms not described in the DWIA, such as the rescattering of one of the outgoing particles.

Despite theoretical misgivings about applying distorted wave techniques to light systems, it is concluded that the DWIA is an adequate formalism for modelling the quasifree knockout reactions induced by 100 MeV protons on ^{4}He. Although there were indications that the model was starting to break down under extreme kinematic conditions, it nevertheless gave a reasonable description of the various knockout cross sections over the range of major yield.

Consequently, it was appropriate to calculate the quasifree knockout contribution to the *inclusive* spectra, by integrating the DWIA cross sections over the solid angles of the secondary particles, using the average spectroscopic factors extracted from the coincidence data. For the (p,pn) reaction, it was assumed that the spectroscopic factors were the same as for (p,2p).

A comparison of these calculations with the inclusive spectra measured by Wesick *et al.* reveals that quasifree scattering accounts for 60–80% of the yield at 45°, and 60–70% at 60°. Improved calculations which allow for the angle dependence of the spectroscopic factors give similar results.

The major sources of uncertainty in these calculations are the spectroscopic factors for neutron knockout, and the cluster knockout contributions at high energies of the scattered proton.

At low energies of the scattered proton (10 MeV), more than 90% of the quasifree yield comes from nucleon knockout, whereas at higher energies, it is the knockout of deuterons, tritons and helions which contributes most of the yield.

A rough estimate of the multiple scattering yield was made from further analysis of the coincidence data. When this is added to the quasifree com-

ponent, the measured inclusive yield at 45° is reproduced to within 10%, but the yield at 60° is overestimated by 10–25%. At 45°, the flat shape of the inclusive spectrum is well reproduced by the IEP results of the DWIA plus the estimated multiple scattering component. The lack of a discernible quasifree peak is seen to arise from the superposition of the cluster knockout contributions on the high-energy side of the quasifree nucleon knockout peak.

The FEP predictions are not as close to the shape of the inclusive spectrum at 45°: they indicate that some of the characteristic quasifree shape should be retained. At 60°, the DWIA calculations with both the IEP and the FEP reproduce the shape of the inclusive spectrum very well when added to the estimated multiple scattering contributions.

Thus we have shown that the featureless inclusive spectra from ^{4}He(p,p′) at 45° and 60° are compatible with the interpretation of a reaction mechanism dominated by quasifree scattering.

Finally, we summarize the principal conclusions of this work as follows:

- The DWIA is an appropriate formalism for modelling the quasifree knockout reactions ^{4}He(p,p′x) at 100 MeV, over a wide kinematic range.

- The continuum ^{4}He(p,p′) cross sections at 45° and 60° are dominated by quasifree scattering ($70 \pm 10\%$), with $\sim 30\%$ arising from multiple scattering.

- The contribution of cluster knockout to the inclusive yields is significant. Although nucleon knockout constitutes over 90% of the quasifree component at 10 MeV, at high energies of the scattered proton it makes up only 20–40% of the quasifree yield, with the balance coming from the knockout of deuterons, tritons and helions.

- The absence of discernible quasifree peaks in the inclusive spectra is probably due to the cluster knockout contributions filling in the yield at higher energies.

- The angle dependences of the spectroscopic factors for both the inclusive (p,p′) and the exclusive (p,2p) calculations may be due to the DWIA underpredicting the wings of the distorted momentum distribution. It is likely that other mechanisms, such as rescattering of one of the final state protons, contribute the remaining yield at high recoil momentum.

Appendix A

Cross Section Tables

T_P (MeV)	σ (μb.sr^{-2}.MeV^{-1})					
	$\theta_S = -15°$ $\beta_S = 0°$	$\theta_S = -20°$ $\beta_S = 0°$	$\theta_S = -27°$ $\beta_S = 0°$	$\theta_S = -35°$ $\beta_S = 0°$	$\theta_S = -35°$ $\beta_S = 15°$	$\theta_S = -35°$ $\beta_S = 30°$
6.0		30.6 ± 4.2	35.0 ± 4.3	47.0 ± 4.7	52.2 ± 5.1	
8.0		36.9 ± 5.7	35.9 ± 4.4	73.9 ± 5.5	50.4 ± 5.2	
10.0		42.4 ± 6.2	42.6 ± 5.1	62.8 ± 5.5	63.9 ± 5.6	
12.0		53.5 ± 7.1	63.8 ± 6.2	102.3 ± 6.3	54.7 ± 5.5	
17.0		38.2 ± 6.3	58.3 ± 5.3	49.4 ± 5.1	39.3 ± 4.5	
19.0		48.0 ± 6.2	55.9 ± 6.0	71.1 ± 5.6	49.2 ± 4.9	
20.0	31.7 ± 6.4					
21.0		55.9 ± 7.2	65.8 ± 6.0	86.3 ± 6.1	49.9 ± 5.3	
23.0		58.2 ± 8.0	93.6 ± 6.9	100.6 ± 6.5	56.0 ± 5.8	7.3 ± 2.1
25.0		57.6 ± 8.3	95.6 ± 7.2	112.1 ± 7.2	58.9 ± 5.5	6.2 ± 2.1
27.0		50.4 ± 8.5	78.6 ± 7.5	129.3 ± 7.4	76.5 ± 6.2	14.7 ± 2.8
28.0	22.4 ± 7.5					
29.0		62.0 ± 8.6	100.6 ± 7.5	133.5 ± 7.4	73.8 ± 6.7	14.3 ± 3.1
31.0		61.0 ± 9.1	123.9 ± 7.1	140.6 ± 7.8	65.7 ± 6.0	16.9 ± 3.6
33.0		49.9 ± 9.1	100.2 ± 7.5	145.5 ± 8.2	85.5 ± 6.7	22.4 ± 3.9
35.0		39.8 ± 8.8	89.3 ± 8.0	157.1 ± 8.0	83.6 ± 6.5	26.6 ± 4.0
36.0	30.8 ± 7.6					
37.0		50.1 ± 8.7	104.4 ± 7.7	146.1 ± 7.7	88.9 ± 6.7	26.5 ± 4.4
39.0		40.1 ± 8.6	90.9 ± 7.4	157.6 ± 7.9	81.5 ± 6.7	20.7 ± 4.0
41.0		27.8 ± 9.3	83.1 ± 7.3	137.5 ± 7.9	80.9 ± 6.6	32.3 ± 4.5
43.0		38.9 ± 8.8	91.1 ± 7.4	142.2 ± 7.8	84.5 ± 6.4	25.4 ± 4.1
44.0	28.8 ± 7.0					
45.0		27.4 ± 8.8	76.6 ± 7.0	131.7 ± 7.3	76.7 ± 6.2	27.8 ± 4.5
47.0		24.5 ± 9.3	68.4 ± 6.5	117.9 ± 7.0	73.3 ± 6.6	28.6 ± 4.4
49.0		21.8 ± 9.5	52.7 ± 6.8	118.2 ± 6.7	70.7 ± 6.2	26.5 ± 4.7
51.0		27.4 ± 8.3	58.9 ± 6.4	109.6 ± 7.0	73.6 ± 6.3	23.1 ± 4.2
52.0	25.7 ± 6.0					
53.0		32.1 ± 8.5	45.6 ± 6.5	76.6 ± 6.4	64.7 ± 5.6	24.8 ± 4.5
55.0		25.9 ± 8.6	45.0 ± 6.3	70.7 ± 6.3	58.8 ± 5.7	27.6 ± 4.5
57.0		13.2 ± 7.7	38.1 ± 6.0	72.9 ± 6.0	56.4 ± 5.5	36.1 ± 4.6
59.0			39.4 ± 5.7	68.4 ± 5.6	57.1 ± 5.6	32.7 ± 5.0
61.0				57.3 ± 5.9	46.7 ± 5.3	32.1 ± 4.5
63.0				58.2 ± 5.6		

Table A.1: *(p,2p) cross sections for $\theta_P = 45°$. The values are plotted in Figure 3.9.*

T_P (MeV)	σ (μb.sr^{-2}.MeV^{-1})						
	$\theta_S = -45°$	$\theta_S = -55°$	$\theta_S = -55°$	$\theta_S = -55°$	$\theta_S = -70°$	$\theta_S = -80°$	$\theta_S = -90°$
	$\beta_S = 0°$	$\beta_S = 0°$	$\beta_S = 15°$	$\beta_S = 30°$	$\beta_S = 0°$	$\beta_S = 0°$	$\beta_S = 0°$
6.0	12.9 ± 3.4	21.0 ± 2.7	24.6 ± 3.2		9.2 ± 2.4	6.3 ± 1.8	
7.0							2.2 ± 0.9
8.0	34.3 ± 4.2	24.4 ± 3.2	18.7 ± 2.5		13.9 ± 2.5	11.8 ± 2.5	
10.0	58.7 ± 5.9	25.6 ± 3.0	38.9 ± 3.8		14.9 ± 3.0	16.6 ± 2.8	
11.0							5.4 ± 1.0
12.0	55.1 ± 5.7	42.2 ± 3.9	33.3 ± 3.9		16.6 ± 2.5	10.6 ± 2.8	
17.0	26.0 ± 4.3	16.1 ± 2.5	16.0 ± 2.6	4.3 ± 1.2	4.9 ± 1.7	3.5 ± 2.2	
18.0							3.0 ± 0.9
19.0	38.4 ± 4.9	14.8 ± 3.1	18.3 ± 2.8	1.4 ± 1.0	11.0 ± 2.5	4.4 ± 1.6	
21.0	33.8 ± 5.5	21.9 ± 3.4	25.2 ± 3.0	4.2 ± 1.8	5.1 ± 2.3	5.8 ± 1.7	
22.0							2.4 ± 1.0
23.0	54.2 ± 6.5	33.5 ± 3.7	21.2 ± 3.0	3.1 ± 1.5	7.8 ± 2.5	4.3 ± 1.8	
25.0	70.7 ± 6.4	30.5 ± 3.5	26.5 ± 3.3	4.6 ± 1.9	12.5 ± 2.6	4.6 ± 2.1	
26.0							5.6 ± 0.9
27.0	85.8 ± 7.3	35.5 ± 3.9	28.2 ± 3.5	8.9 ± 2.3	5.9 ± 3.1	6.2 ± 1.5	
29.0	113.4 ± 7.5	38.9 ± 4.2	26.4 ± 3.4	6.6 ± 2.2	14.1 ± 2.5	8.7 ± 2.0	
30.0							2.5 ± 1.0
31.0	115.3 ± 7.9	41.7 ± 3.9	38.6 ± 3.8	9.5 ± 2.3	15.0 ± 3.0	8.0 ± 2.2	
33.0	124.2 ± 8.2	49.7 ± 4.3	34.2 ± 4.1	16.3 ± 2.4	19.5 ± 3.4	4.6 ± 2.1	
34.0							5.1 ± 1.3
35.0	139.4 ± 8.7	55.6 ± 4.5	36.6 ± 4.0	17.7 ± 2.6	20.3 ± 3.4	10.2 ± 1.9	
37.0	155.9 ± 9.4	62.1 ± 4.8	49.0 ± 4.5	18.5 ± 2.9	26.1 ± 3.6	12.7 ± 2.7	
38.0							2.2 ± 0.9
39.0	144.2 ± 9.3	70.0 ± 5.2	50.4 ± 4.6	20.1 ± 3.0	24.4 ± 3.1	8.2 ± 2.6	
41.0	148.5 ± 9.3	72.5 ± 5.5	50.7 ± 4.6	18.1 ± 3.2	27.1 ± 3.9	13.8 ± 2.4	
42.0							8.1 ± 1.4
43.0	151.1 ± 9.4	80.0 ± 5.4	51.8 ± 4.9	18.9 ± 3.1	31.4 ± 3.9	12.1 ± 2.1	
45.0	161.7 ± 9.2	88.2 ± 5.8	55.8 ± 4.7	25.6 ± 3.5	30.7 ± 3.8	15.3 ± 2.7	
46.0							10.9 ± 1.5
47.0	172.6 ± 9.2	77.7 ± 5.7	65.1 ± 5.4	30.0 ± 3.8	28.2 ± 4.0	17.1 ± 3.0	
49.0		96.1 ± 5.6	60.2 ± 5.1	23.2 ± 3.7	37.3 ± 4.5	14.7 ± 3.4	
50.0							9.4 ± 1.6
51.0		95.4 ± 5.8	58.3 ± 5.3	24.8 ± 4.1	32.9 ± 4.7	18.4 ± 3.6	
53.0		99.4 ± 5.8	68.9 ± 5.4	36.0 ± 4.3	39.8 ± 4.5	23.7 ± 3.5	
54.0							15.2 ± 2.0
55.0	143.7 ± 9.1	93.2 ± 5.7	59.0 ± 5.6	31.1 ± 4.2	41.0 ± 5.0	23.0 ± 4.3	
57.0	115.7 ± 8.2	86.9 ± 5.9	59.4 ± 5.3	32.2 ± 4.4	47.7 ± 5.2	32.2 ± 3.9	
58.0							13.4 ± 1.9
59.0	91.3 ± 7.6	83.2 ± 5.8	66.2 ± 5.2	37.5 ± 4.1	45.0 ± 5.1	34.1 ± 3.9	
61.0	79.1 ± 7.0		64.7 ± 5.4	35.3 ± 4.4	42.7 ± 5.1	28.5 ± 4.0	

Table A.2: *(p,2p) cross sections for $\theta_P = 45°$. The values are plotted in Figure 3.10.*

T_P (MeV)	σ (μb.sr^{-2}.MeV^{-1})					
	$\theta_S = -20°$ $\beta_S = 0°$	$\theta_S = -35°$ $\beta_S = 0°$	$\theta_S = -35°$ $\beta_S = 15°$	$\theta_S = -35°$ $\beta_S = 30°$	$\theta_S = -50°$ $\beta_S = 0°$	$\theta_S = -70°$ $\beta_S = 0°$
6.0		115.5 ± 6.4	71.4 ± 5.3		32.4 ± 4.3	
7.0	35.9 ± 4.5			27.4 ± 2.8		5.6 ± 1.1
8.0		154.6 ± 7.4	86.6 ± 5.7		36.5 ± 4.3	
10.0		111.1 ± 6.8	63.5 ± 5.2		53.1 ± 5.2	
11.0				15.5 ± 2.8		6.1 ± 1.4
12.0		76.1 ± 5.8	40.3 ± 4.3		40.6 ± 4.8	
17.0		73.6 ± 5.6	44.1 ± 4.6		33.7 ± 4.2	
18.0	20.1 ± 5.7			16.6 ± 2.7		8.5 ± 1.4
19.0		100.0 ± 6.4	51.2 ± 4.7		33.4 ± 4.0	
21.0		109.5 ± 6.5	53.5 ± 4.9		41.8 ± 4.4	
22.0	37.8 ± 6.6			23.1 ± 3.0		7.9 ± 1.5
23.0		98.5 ± 6.2	50.6 ± 5.2		32.1 ± 3.9	
25.0		94.0 ± 6.4	51.5 ± 4.9		43.5 ± 4.7	
26.0	45.8 ± 6.7			24.9 ± 3.1		5.4 ± 1.8
27.0		106.8 ± 6.9	62.9 ± 5.3		49.9 ± 5.0	
29.0		103.0 ± 6.7	53.6 ± 4.8		51.5 ± 5.4	
30.0	40.5 ± 7.1			27.6 ± 3.0		7.3 ± 1.8
31.0		101.5 ± 6.4	55.1 ± 5.1		45.9 ± 5.5	
33.0		97.9 ± 6.2	54.8 ± 4.8		53.3 ± 5.3	
34.0	40.5 ± 6.8			19.5 ± 2.7		10.2 ± 2.5
35.0		87.0 ± 6.3	50.5 ± 4.5		53.7 ± 4.9	
37.0		75.2 ± 6.1	49.5 ± 4.8		48.8 ± 5.2	
38.0	37.6 ± 7.0			26.1 ± 2.8		12.0 ± 2.2
39.0		73.0 ± 5.9	40.0 ± 4.5		51.4 ± 5.1	
41.0		62.4 ± 5.5	37.8 ± 4.8		37.0 ± 5.2	
42.0	26.2 ± 6.4			20.2 ± 2.8		12.8 ± 2.1
43.0		63.6 ± 5.0	37.9 ± 4.5		54.8 ± 5.1	
45.0		49.4 ± 4.5	45.9 ± 4.3		43.7 ± 4.9	
46.0	23.2 ± 6.2			17.6 ± 2.9		15.7 ± 2.3
47.0		49.0 ± 4.7	33.3 ± 4.2		44.3 ± 5.1	
49.0		44.2 ± 4.9	42.6 ± 4.2		35.0 ± 4.8	
50.0	15.1 ± 5.7			18.3 ± 2.6		14.5 ± 2.3
51.0		40.5 ± 4.4	32.2 ± 4.0		30.0 ± 5.2	
53.0		33.4 ± 4.3			38.9 ± 4.7	
54.0						15.4 ± 2.4

Table A.3: *(p,2p) cross sections for $\theta_P = 60°$. The values are plotted in Figure 3.11.*

T_P (MeV)	σ (μb.sr^{-2}.MeV^{-1})					
	$\theta_S = -15°$ $\beta_S = 0°$	$\theta_S = -20°$ $\beta_S = 0°$	$\theta_S = -27°$ $\beta_S = 0°$	$\theta_S = -35°$ $\beta_S = 0°$	$\theta_S = -35°$ $\beta_S = 15°$	$\theta_S = -35°$ $\beta_S = 30°$
6.0			19.6 ± 2.8	9.3 ± 2.3	3.0 ± 1.7	0.5 ± 0.9
7.0	15.7 ± 4.4	12.6 ± 2.5				
8.0			12.7 ± 3.0	13.0 ± 2.9	7.4 ± 1.8	3.0 ± 1.2
10.0			20.7 ± 3.6	12.3 ± 2.9	8.3 ± 2.4	0.4 ± 1.1
11.0	15.6 ± 4.3	13.3 ± 2.9				
12.0			24.5 ± 3.5	24.2 ± 3.3	13.3 ± 2.7	5.8 ± 1.9
17.0			12.3 ± 2.5	13.4 ± 2.4	9.4 ± 2.0	5.9 ± 1.7
18.0	8.4 ± 4.5	15.5 ± 2.2				
19.0			19.3 ± 2.9	13.4 ± 2.3	9.4 ± 2.0	5.9 ± 1.7
20.0						
21.0			21.1 ± 3.0	21.3 ± 2.7	15.8 ± 2.6	3.4 ± 1.3
22.0	11.9 ± 3.8	14.8 ± 2.3				
23.0			22.4 ± 3.1	23.7 ± 3.2	16.8 ± 2.8	2.8 ± 1.4
25.0			31.1 ± 3.2	18.4 ± 2.6	15.5 ± 2.7	7.3 ± 1.9
26.0	15.5 ± 5.3	19.7 ± 2.5				
27.0			30.1 ± 3.5	29.8 ± 3.2	24.3 ± 3.2	4.3 ± 1.7
28.0						
29.0			26.6 ± 3.1	28.8 ± 3.3	17.6 ± 3.1	4.4 ± 1.5
30.0	15.5 ± 4.3	22.8 ± 2.6				
31.0			28.5 ± 3.9	32.8 ± 3.6	21.7 ± 3.3	8.3 ± 2.0
33.0			35.3 ± 3.4	40.1 ± 4.1	16.0 ± 2.7	8.3 ± 2.0
34.0	8.3 ± 3.1	19.7 ± 2.6				
35.0			34.7 ± 3.5	47.4 ± 3.9	27.2 ± 3.6	6.7 ± 2.0
36.0						
37.0			39.0 ± 4.1	60.4 ± 4.2	24.2 ± 3.4	8.7 ± 2.2
38.0	13.1 ± 4.0	22.1 ± 2.5				
39.0			40.8 ± 4.0	50.2 ± 4.6	23.2 ± 3.3	7.2 ± 2.1
41.0			48.0 ± 4.0	55.9 ± 4.7	25.6 ± 3.5	10.3 ± 2.2
42.0	17.9 ± 5.6	19.9 ± 2.7				
43.0			48.8 ± 4.1	64.7 ± 4.3	33.3 ± 4.0	6.5 ± 2.3
44.0						
45.0			39.3 ± 4.2	71.9 ± 4.6	32.4 ± 3.9	7.9 ± 2.0
46.0	17.9 ± 4.6					
47.0			42.3 ± 4.2	76.2 ± 4.9	33.1 ± 4.0	10.4 ± 2.7
49.0			38.2 ± 4.0	67.3 ± 4.8	37.6 ± 4.4	9.0 ± 2.5
51.0			29.2 ± 3.9	73.6 ± 5.1	37.0 ± 4.3	15.6 ± 2.9
53.0				90.4 ± 5.4	34.0 ± 4.3	14.1 ± 3.2
55.0					39.0 ± 4.4	23.3 ± 3.7
57.0					44.6 ± 4.5	23.0 ± 3.6
59.0					53.8 ± 5.3	

Table A.4: *(p,pd) cross sections for $\theta_P = 45°$. The values are plotted in Figure 3.12.*

T_P (MeV)	σ (μb.sr^{-2}.MeV^{-1})				
	$\theta_S = -45°$	$\theta_S = -55°$	$\theta_S = -55°$	$\theta_S = -55°$	$\theta_S = -70°$
	$\beta_S = 0°$	$\beta_S = 0°$	$\beta_S = 15°$	$\beta_S = 30°$	$\beta_S = 0°$
6.0	4.7 ± 1.4	0.7 ± 1.1	0.3 ± 1.2	0.5 ± 1.1	
7.0					1.3 ± 0.5
8.0	3.8 ± 2.0	3.3 ± 1.0	1.2 ± 1.0	1.7 ± 0.7	
10.0	9.8 ± 2.6	3.8 ± 1.2	3.8 ± 1.3	3.0 ± 1.2	
11.0					1.0 ± 0.4
12.0	8.0 ± 2.4	5.5 ± 1.2	2.9 ± 1.2	2.1 ± 1.1	
17.0	6.8 ± 2.0	4.1 ± 1.1	2.7 ± 0.9	0.4 ± 0.8	
18.0					0.4 ± 0.7
19.0	10.1 ± 2.6	2.2 ± 0.8	2.0 ± 1.1	2.0 ± 0.8	
21.0	11.0 ± 2.4	3.8 ± 1.0	1.9 ± 1.5	2.0 ± 0.8	
22.0					1.1 ± 0.5
23.0	12.7 ± 2.3	3.5 ± 1.0	3.2 ± 1.2	3.0 ± 1.0	
25.0	13.1 ± 2.8	3.8 ± 1.8	4.4 ± 1.1	2.0 ± 1.1	
26.0					1.3 ± 0.5
27.0	13.4 ± 3.2	5.1 ± 1.2	3.8 ± 1.3	2.8 ± 1.4	
29.0	15.1 ± 3.1	5.6 ± 1.4	5.0 ± 1.2	3.0 ± 1.2	
30.0					0.4 ± 0.6
31.0	22.3 ± 3.4	8.6 ± 1.7	4.3 ± 1.6	4.6 ± 1.2	
33.0	25.8 ± 3.5	11.8 ± 1.9	5.3 ± 1.2	4.3 ± 1.2	
34.0					1.1 ± 0.8
35.0	28.3 ± 3.6	11.0 ± 2.0	8.2 ± 1.6	4.7 ± 1.4	
37.0	33.0 ± 3.9	11.9 ± 1.9	9.3 ± 2.0	5.0 ± 1.5	
38.0					2.5 ± 0.8
39.0	41.4 ± 4.6	19.2 ± 2.4	9.3 ± 2.0	8.0 ± 1.8	
41.0	50.8 ± 4.9	19.9 ± 2.5	11.4 ± 2.0	4.2 ± 1.9	
42.0					2.7 ± 0.7
43.0	58.5 ± 5.1	27.0 ± 2.9	12.2 ± 2.4	9.9 ± 2.0	
45.0	55.9 ± 5.3	33.6 ± 3.0	14.7 ± 2.1	5.9 ± 2.2	
46.0					4.2 ± 1.3
47.0	77.1 ± 6.3	32.0 ± 3.4	15.6 ± 2.3	7.6 ± 1.8	
49.0	91.8 ± 6.4	38.9 ± 3.6	17.6 ± 2.6	13.4 ± 2.5	
50.0					5.9 ± 1.4
51.0	92.2 ± 6.6	49.9 ± 3.9	22.7 ± 2.8	9.4 ± 2.2	
53.0		51.8 ± 4.0	26.5 ± 3.1	26.2 ± 3.0	
54.0					12.1 ± 1.7
55.0			37.5 ± 3.7	24.8 ± 3.3	
57.0			40.6 ± 3.6	26.1 ± 3.3	

Table A.5: *(p,pd) cross sections for $\theta_P = 45°$. The values are plotted in Figure 3.13.*

T_P (MeV)	σ (μb.sr^{-2}.MeV^{-1})				
	$\theta_S = -20°$ $\beta_S = 0°$	$\theta_S = -35°$ $\beta_S = 0°$	$\theta_S = -35°$ $\beta_S = 15°$	$\theta_S = -35°$ $\beta_S = 30°$	$\theta_S = -50°$ $\beta_S = 0°$
6.0		15.0 ± 3.0	8.0 ± 2.2	5.0 ± 1.7	2.0 ± 1.4
7.0	18.6 ± 2.8				
8.0		11.0 ± 2.8	10.8 ± 1.8	1.8 ± 1.8	2.8 ± 1.1
10.0		16.2 ± 2.7	9.5 ± 2.0	5.4 ± 1.7	4.0 ± 1.3
12.0		15.0 ± 2.4	7.3 ± 1.9	2.8 ± 1.4	2.0 ± 0.9
17.0		17.5 ± 2.4	10.7 ± 1.8	3.0 ± 1.6	5.6 ± 1.5
18.0	16.2 ± 3.0				
19.0		18.6 ± 2.3	10.7 ± 1.8	5.8 ± 1.9	4.0 ± 1.3
21.0		24.7 ± 2.8	7.9 ± 1.9	3.5 ± 1.8	3.5 ± 1.6
22.0	18.5 ± 3.3				
23.0		32.8 ± 3.2	14.6 ± 2.4	3.7 ± 1.7	6.8 ± 1.6
25.0		35.0 ± 3.3	20.1 ± 2.5	7.9 ± 2.3	9.1 ± 2.2
26.0	27.3 ± 3.2				
27.0		41.5 ± 3.7	18.5 ± 2.7	10.4 ± 2.3	12.4 ± 2.2
29.0		50.3 ± 3.9	14.0 ± 2.2	10.8 ± 2.1	9.6 ± 2.0
30.0	27.5 ± 3.2				
31.0		48.3 ± 3.7	20.7 ± 2.5	8.1 ± 2.2	12.2 ± 2.5
33.0		45.5 ± 3.8	23.1 ± 2.8	11.7 ± 3.0	18.6 ± 2.9
34.0	24.8 ± 3.4				
35.0		65.8 ± 4.5	23.7 ± 2.8	11.1 ± 2.6	18.2 ± 2.9
37.0		57.0 ± 4.2	26.1 ± 3.1	9.4 ± 2.2	24.6 ± 3.3
38.0	21.2 ± 3.2				
39.0		61.4 ± 4.3	26.2 ± 2.9	12.2 ± 2.4	21.6 ± 2.9
41.0		48.8 ± 4.0	23.5 ± 2.8	12.9 ± 2.7	22.4 ± 3.0
42.0	20.7 ± 3.2				
43.0		62.7 ± 4.4	21.6 ± 2.7	14.2 ± 2.5	23.7 ± 3.5
45.0		51.6 ± 4.0	25.6 ± 2.9	19.1 ± 2.7	30.4 ± 3.5
46.0	18.5 ± 2.7				
47.0		49.3 ± 3.8	24.7 ± 2.9		38.7 ± 4.1
49.0		50.5 ± 3.9	25.1 ± 3.0		32.0 ± 3.7
51.0		37.5 ± 3.5			39.2 ± 4.1
53.0					55.4 ± 4.8

Table A.6: *(p,pd) cross sections for $\theta_P = 60°$. The values are plotted in Figure 3.14.*

T_P (MeV)	σ (μb.sr^{-2}.MeV^{-1})					
	$\theta_S = -15°$ $\beta_S = 0°$	$\theta_S = -20°$ $\beta_S = 0°$	$\theta_S = -27°$ $\beta_S = 0°$	$\theta_S = -35°$ $\beta_S = 0°$	$\theta_S = -35°$ $\beta_S = 15°$	$\theta_S = -35°$ $\beta_S = 30°$
6.0		4.7 ± 1.8	2.0 ± 1.2	1.3 ± 1.3	1.0 ± 1.1	1.5 ± 0.9
7.0	3.6 ± 3.6					
8.0		5.3 ± 1.7	0.8 ± 1.6	1.9 ± 1.2	2.1 ± 1.0	1.0 ± 0.7
10.0		4.5 ± 2.0	4.0 ± 1.7	2.4 ± 1.1	2.6 ± 1.0	6.4 ± 1.8
11.0	7.1 ± 2.9					
12.0		8.5 ± 2.5	5.6 ± 1.8	4.1 ± 1.3	4.7 ± 1.4	3.3 ± 1.5
17.0		7.1 ± 1.9	4.9 ± 1.3	2.3 ± 1.3	0.4 ± 0.4	2.9 ± 1.2
18.0	13.0 ± 3.9					
19.0		9.2 ± 2.1	9.3 ± 1.7	4.4 ± 1.1	2.5 ± 1.0	3.9 ± 1.4
21.0		7.8 ± 2.0	7.7 ± 2.3	6.8 ± 1.6	3.8 ± 1.3	3.4 ± 1.3
22.0	15.4 ± 4.3					
23.0		5.7 ± 2.5	8.4 ± 1.9	7.5 ± 1.9	2.5 ± 1.0	4.9 ± 1.5
25.0		10.7 ± 2.3	11.9 ± 1.8	5.2 ± 1.9	4.2 ± 1.3	2.9 ± 1.2
26.0	20.1 ± 4.9					
27.0		12.5 ± 2.2	14.7 ± 2.2	8.7 ± 1.9	5.5 ± 1.5	6.3 ± 1.8
29.0		15.3 ± 2.6	16.9 ± 2.5	11.3 ± 1.8	6.1 ± 1.8	8.1 ± 2.2
30.0	8.3 ± 3.1					
31.0		13.2 ± 2.4	10.7 ± 2.2	15.3 ± 2.3	4.2 ± 1.3	5.3 ± 1.6
33.0		17.8 ± 2.2	19.1 ± 2.4	18.7 ± 2.4	6.8 ± 1.7	5.2 ± 1.8
34.0	8.3 ± 3.1					
35.0		12.8 ± 2.7	20.2 ± 2.9	16.3 ± 2.1	8.1 ± 1.8	10.0 ± 2.5
37.0		14.7 ± 2.2	17.5 ± 2.4	23.9 ± 2.8	9.3 ± 2.0	4.7 ± 1.7
38.0	11.9 ± 3.7					
39.0		18.5 ± 2.5	19.8 ± 2.6	25.8 ± 2.9	14.6 ± 2.6	11.0 ± 2.6
41.0		13.8 ± 2.4	24.4 ± 2.6	28.1 ± 2.9	16.3 ± 2.8	11.9 ± 2.7
42.0	9.5 ± 3.4					
43.0		9.9 ± 2.4	26.2 ± 2.8	30.1 ± 3.0	13.6 ± 2.7	17.1 ± 2.9
45.0		9.3 ± 2.1	19.6 ± 2.8	36.7 ± 3.4	15.7 ± 2.9	20.4 ± 3.3
46.0	9.5 ± 3.4					
47.0			21.0 ± 2.7	41.1 ± 3.4	24.3 ± 3.2	17.4 ± 3.1
49.0			19.5 ± 2.5	43.3 ± 3.9	25.6 ± 3.3	30.7 ± 4.1
51.0				48.3 ± 3.9	27.1 ± 3.5	32.2 ± 4.1
53.0				41.5 ± 3.8	29.1 ± 3.7	
55.0				50.0 ± 4.0	30.0 ± 3.8	
57.0				52.0 ± 4.4	42.8 ± 4.9	
59.0				56.0 ± 4.4		

Table A.7: *(p,pt) cross sections for $\theta_P = 45°$. The values are plotted in Figure 3.15.*

T_P (MeV)	σ (μb.sr^{-2}.MeV^{-1})					
	$\theta_S = -45°$ $\beta_S = 0°$	$\theta_S = -55°$ $\beta_S = 0°$	$\theta_S = -55°$ $\beta_S = 15°$	$\theta_S = -55°$ $\beta_S = 30°$	$\theta_S = -70°$ $\beta_S = 0°$	$\theta_S = -80°$ $\beta_S = 0°$
6.0	2.1 ± 0.9	5.6 ± 1.6	3.2 ± 1.0	6.3 ± 1.6	3.6 ± 2.1	
8.0	1.7 ± 0.8	3.5 ± 1.2	4.4 ± 1.4	4.3 ± 1.2	5.3 ± 1.4	
10.0	1.3 ± 0.7	5.4 ± 1.2	2.9 ± 1.2	6.6 ± 1.6	4.4 ± 1.9	11.9 ± 2.3
12.0	2.1 ± 0.9	5.6 ± 1.4	8.2 ± 1.7	7.3 ± 1.9	12.8 ± 2.4	15.9 ± 2.6
17.0	0.8 ± 0.6	5.9 ± 1.3	4.7 ± 1.2	4.3 ± 1.4	5.6 ± 1.5	4.7 ± 1.3
19.0	1.2 ± 1.3	5.4 ± 1.2	3.7 ± 1.3	4.9 ± 1.3	4.9 ± 1.4	5.0 ± 1.3
21.0	2.9 ± 1.1	6.2 ± 1.3	4.1 ± 1.1	4.6 ± 1.2	13.9 ± 2.3	2.8 ± 1.4
23.0	4.2 ± 1.3	5.6 ± 1.4	6.1 ± 1.3	6.5 ± 1.5	12.0 ± 2.1	2.9 ± 1.0
25.0	4.2 ± 1.3	6.7 ± 1.5	5.2 ± 1.2	10.1 ± 1.8	15.4 ± 2.4	5.8 ± 1.4
27.0	2.9 ± 1.5	6.7 ± 1.3	7.0 ± 1.6	2.6 ± 1.5	16.9 ± 2.5	4.7 ± 1.3
29.0	4.2 ± 1.3	10.2 ± 1.7	5.8 ± 1.3	5.9 ± 1.4	12.4 ± 2.2	5.0 ± 1.3
31.0	7.1 ± 2.0	5.4 ± 1.2	6.1 ± 1.3	6.5 ± 1.5	16.2 ± 2.5	11.5 ± 2.0
33.0	10.1 ± 2.1	7.5 ± 1.4	5.7 ± 1.8	7.2 ± 1.7	19.9 ± 2.9	6.1 ± 1.7
35.0	8.8 ± 2.2	6.9 ± 1.5	6.1 ± 1.3	7.9 ± 1.8	21.1 ± 2.8	6.1 ± 1.5
37.0	10.1 ± 2.3	6.9 ± 1.5	6.4 ± 1.4	8.4 ± 2.2	25.9 ± 3.3	8.3 ± 2.0
39.0	15.6 ± 2.8	6.0 ± 1.9	7.6 ± 1.5	9.6 ± 2.1	21.1 ± 2.8	7.9 ± 1.7
41.0	26.2 ± 3.3	8.6 ± 1.5	7.3 ± 1.5	11.7 ± 2.3	21.9 ± 2.9	6.5 ± 1.5
43.0	38.4 ± 4.3	14.3 ± 2.0	8.4 ± 1.9	11.0 ± 2.3	17.3 ± 2.7	7.9 ± 1.9
45.0	34.2 ± 4.0	14.7 ± 2.3	9.4 ± 1.7	16.9 ± 3.1	9.9 ± 2.8	10.2 ± 1.9
47.0	49.1 ± 4.8	20.4 ± 2.7	14.4 ± 2.2	21.5 ± 2.9	12.5 ± 2.2	
49.0	58.9 ± 5.1	29.8 ± 2.8	14.0 ± 2.5	29.4 ± 3.2	16.2 ± 2.7	
51.0	57.3 ± 5.2	34.1 ± 3.3	19.6 ± 2.9	28.0 ± 3.5	15.4 ± 2.8	
53.0	78.3 ± 5.8	46.8 ± 3.6	21.8 ± 2.8		19.2 ± 3.2	
55.0	89.8 ± 6.5	55.9 ± 3.9	39.0 ± 3.6		23.5 ± 3.3	
57.0	88.2 ± 6.6	57.0 ± 4.0	42.7 ± 4.0		21.8 ± 2.9	
59.0		42.7 ± 3.4				
61.0		51.5 ± 4.1				

Table A.8: *(p,pt) cross sections for $\theta_P = 45°$. The values are plotted in Figure 3.16.*

T_P (MeV)	σ (μb.sr^{-2}.MeV^{-1})				
	$\theta_S = -20°$	$\theta_S = -35°$	$\theta_S = -35°$	$\theta_S = -35°$	$\theta_S = -70°$
	$\beta_S = 0°$	$\beta_S = 0°$	$\beta_S = 15°$	$\beta_S = 30°$	$\beta_S = 0°$
6.0		3.1 ± 1.9	3.7 ± 1.1	3.6 ± 1.1	21.7 ± 3.6
7.0	2.3 ± 1.0				
8.0		8.6 ± 2.0	3.4 ± 1.0	2.9 ± 1.4	16.0 ± 3.0
10.0		2.4 ± 1.1	2.4 ± 0.9	4.0 ± 1.7	12.1 ± 2.3
12.0		2.4 ± 1.1	2.4 ± 1.1	3.2 ± 1.1	8.5 ± 2.0
17.0		3.8 ± 1.3	2.7 ± 0.9	2.6 ± 1.2	5.8 ± 1.6
18.0	8.7 ± 1.9				
19.0		6.6 ± 1.8	3.9 ± 1.1	3.3 ± 1.3	9.0 ± 2.7
21.0		6.3 ± 2.2	3.9 ± 1.1	4.2 ± 1.2	13.0 ± 2.4
22.0	10.8 ± 1.8				
23.0		10.4 ± 2.2	3.3 ± 1.0	12.7 ± 2.1	12.1 ± 2.3
25.0		16.5 ± 2.8	3.0 ± 1.0	7.4 ± 1.6	11.0 ± 2.6
26.0	13.4 ± 1.9				
27.0		10.8 ± 2.3	9.1 ± 1.8	7.4 ± 1.6	19.2 ± 2.9
29.0		11.0 ± 2.7	5.7 ± 1.3	8.3 ± 1.9	11.6 ± 2.3
30.0	11.7 ± 1.8				
31.0		15.6 ± 2.7	5.1 ± 1.2	10.4 ± 2.0	11.0 ± 2.6
33.0		16.0 ± 2.8	9.7 ± 1.7	12.8 ± 2.5	18.3 ± 2.9
34.0	6.6 ± 2.0				
35.0		20.8 ± 3.1	8.5 ± 1.6	15.3 ± 2.6	18.3 ± 2.9
37.0		29.3 ± 3.7	7.6 ± 1.7	23.9 ± 3.0	17.1 ± 3.8
38.0	11.6 ± 2.1				
39.0		25.3 ± 3.7	13.0 ± 2.1		
41.0		35.5 ± 4.1	14.8 ± 2.4		
42.0	12.3 ± 1.9				
43.0		31.0 ± 4.1	12.7 ± 2.2		
45.0		39.9 ± 4.4	20.7 ± 2.5		
47.0		37.8 ± 4.5			
49.0		53.8 ± 5.1			
51.0		52.7 ± 5.2			
53.0		64.2 ± 5.7			
55.0		89.6 ± 7.0			

Table A.9: *(p,pt) cross sections for $\theta_P = 60°$. The values are plotted in Figure 3.17.*

T_P (MeV)	σ (μb.sr^{-2}.MeV^{-1})			
	$\theta_P = 45°$	$\theta_P = 45°$	$\theta_P = 45°$	$\theta_P = 60°$
	$\theta_S = -55°$	$\theta_S = -65°$	$\theta_S = -65°$	$\theta_S = -55°$
	$\beta_S = 15°$	$\beta_S = 0°$	$\beta_S = 15°$	$\beta_S = 15°$
6.0	2.3 ± 1.1	12.4 ± 2.0	7.3 ± 1.9	6.5 ± 2.0
8.0	5.8 ± 1.7	9.9 ± 2.1	7.2 ± 2.0	7.1 ± 1.7
10.0	7.3 ± 1.5	9.7 ± 2.0	13.1 ± 2.0	8.3 ± 1.9
12.0	5.6 ± 1.3	9.9 ± 1.7	8.2 ± 1.9	2.9 ± 1.1
17.0	0.8 ± 1.2	8.0 ± 1.5	6.8 ± 1.4	2.7 ± 1.6
19.0	3.5 ± 1.0	9.7 ± 2.4	6.7 ± 1.6	4.5 ± 1.4
21.0	2.3 ± 1.1	9.9 ± 2.1	5.2 ± 1.5	4.9 ± 1.4
23.0	3.1 ± 1.4	19.7 ± 2.5	6.6 ± 1.8	5.8 ± 1.5
25.0	3.2 ± 1.0	26.7 ± 2.9	6.7 ± 1.6	6.6 ± 1.6
27.0	3.8 ± 1.1	25.3 ± 2.6	11.5 ± 2.0	4.1 ± 1.3
29.0	7.6 ± 1.5	30.7 ± 3.0	8.2 ± 1.8	7.0 ± 1.7
31.0	4.7 ± 1.2	25.4 ± 2.9	8.2 ± 1.8	5.2 ± 1.9
33.0	4.3 ± 1.4	22.1 ± 2.7	10.6 ± 2.0	7.0 ± 1.7
35.0	4.4 ± 1.1	17.1 ± 2.2	10.1 ± 1.7	7.3 ± 2.1
37.0	7.6 ± 1.5	18.9 ± 2.4	10.4 ± 2.3	5.4 ± 1.5
39.0	5.8 ± 1.7	16.4 ± 2.3	11.7 ± 2.2	6.9 ± 2.0
41.0	6.7 ± 1.6	14.9 ± 2.0	6.4 ± 1.8	7.4 ± 1.8
43.0	9.1 ± 1.6	13.2 ± 2.1	11.7 ± 2.3	10.1 ± 2.6
45.0	6.0 ± 2.0	15.1 ± 2.2	10.7 ± 2.0	10.9 ± 3.4
47.0	12.5 ± 2.2	14.4 ± 2.0	15.9 ± 2.6	
49.0	7.2 ± 2.1	11.2 ± 2.1	10.8 ± 1.8	
51.0	20.8 ± 2.7	17.8 ± 2.2	13.3 ± 2.3	
53.0	21.7 ± 2.9	21.3 ± 2.6		
55.0	22.6 ± 2.9	27.1 ± 3.0		
57.0	30.8 ± 3.0			

Table A.10: *(p,ph) cross sections. The values are plotted in Figure 3.18.*

References

[Aka84] Yoshinori Akaishi, Nucl. Phys. **A416** (1984) 409c.

[Ale80] Y. Alexander, J. W. Van Orden, Edward F. Redish and Stephen J. Wallace, Phys. Rev. Lett. **44** (1980) 1579.

[And81] B. D. Anderson, A. R. Baldwin, A. M. Kalenda, R. Madey, J. W. Watson, C. C. Chang, H. D. Holmgren, R. W. Koontz and J. R. Wu, Phys. Rev. Lett. **46** (1981) 226.

[Ass87] H. J. Assenbaum and K. Langanke, Phys. Rev. C **36** (1987) 17.

[Bar87] C. A. Barnes, K. H. Chang, T. R. Donoghue, C. Rolfs and J. Kammeraad, Phys. Lett. B **197** (1987) 315.

[Ber70] M. Bernas, D. Bachelier, J. K. Lee, P. Radvanyi, M. Roy-Stéphan, I. Brissaud and C. Détraz, Nucl. Phys. **A156** (1970) 289.

[Ber72] F. E. Bertrand, W. R. Burrus, N. W. Hill, T. A. Love and R. W. Peelle, Nucl. Instrum. & Methods **101** (1972) 475.

[Ber73] F. E. Bertrand and R. W. Peelle, Phys. Rev. C **8** (1973) 1045.

[Bho76] Ranjan K. Bhowmik, C. C. Chang, J.-P. Didelez and H. D. Holmgren, Phys. Rev. C **13** (1976) 2105.

[Bir64] J. B. Birks, *The Theory and Practice of Scintillation Counting*, Pergamon Press (Oxford, 1964) pp.437–440.

[Bla73] M. Blann, Nucl. Phys. **A213** (1973) 570.

[Bla75] Marshall Blann, Annu. Rev. Nucl. Sci. **25** (1975) 123.

[Bla87] L. C. Bland, J. Breeden, K. Murphy, W. W. Jacobs, B. Raue, J. Sowinski, J. Templon, S. Vigdor and J. Wilkerson, Indiana Univ. Cyclotron Facility Newsletter **40** (1987) p.6.

[Bot86a] A. H. Botha, H. N. Jungwirth, J. J. Kritzinger, D. Reitmann and S. Schneider, Proc. 11th Intern. Conf. on Cyclotrons and their Applications (Tokyo, 1986) p.9.

[Bot86b] A. H. Botha, S. J. Burger, Z. B. du Toit, D. Reitmann, P. J. Celliers, P. M. Cronje and H. N. Jungwirth, Proc. 11th Intern. Conf. on Cyclotrons and their Applications (Tokyo, 1986) p.515.

[Bro76] G. E. Brown and A. D. Jackson, *The Nucleon-Nucleon Interaction*, North-Holland Publishing Company (Amsterdam, 1976) p.210.

[Bun68] S. N. Bunker, J. M. Cameron, R. F. Carlson, J. Reginald Richardson, P. Tomaš, W. T. H. van Oers and J. W. Verba, Nucl. Phys. **A113** (1968) 461.

[Cam77] J. M. Cameron, P. Kitching, R. H. McCamis, C. A. Miller, G. A. Moss, J. G. Rogers, G. Roy, A. W. Stetz, C. A. Goulding and W. T. H. van Oers, Nucl. Instrum. & Methods **143** (1977) 399.

[Car79] T. A. Carey, Ph.D. thesis, University of Maryland, 1979.

[Car84] T. A. Carey, P. G. Roos, N. S. Chant, A. Nadasen and H. L. Chen, Phys. Rev. C **29** (1984) 1273.

[Cha77] N. S. Chant and P. G. Roos, Phys. Rev. C **15** (1977) 57.

[Cha79] N. S. Chant, P. Kitching, P. G. Roos and L. Antonuk, Phys. Rev. Lett. **43** (1979) 495.

[Cha82] N. S. Chant, *Code THREEDEE*, University of Maryland (unpublished).

[Cha83] N. S. Chant and P. G. Roos, Phys. Rev. C **27** (1983) 1060.

[Che50] Geoffrey F. Chew, Phys. Rev. **80** (1950) 196.

[Che81] T. Chen, R. E. Segel, P. T. Debevec, John Wiggins, P. P. Singh and J. V. Maher, Phys. Lett. **103B** (1981) 192.

[Chi80] H. C. Chiang and J. Hüfner, Nucl. Phys. **A349** (1980) 466.

[Cia83] G. Ciangaru, C. C. Chang, H. D. Holmgren, A. Nadasen, P. G. Roos, A. A. Cowley, S. Mills, P. P. Singh, M. K. Saber and J. R. Hall, Phys. Rev. C **27** (1983) 1360.

[Cia84a] G. Ciangaru, C. C. Chang, H. D. Holmgren, A. Nadasen and P. G. Roos, Phys. Rev. C **29** (1984) 1289.

[Cia84b] G. Ciangaru, Phys. Rev. C **30** (1984) 479.

[Cow77] A. A. Cowley, P. G. Roos, N. S. Chant, R. Woody, III., H. D. Holmgren and D. A. Goldberg, Phys. Rev. C **15** (1977) 1650.

[Cow80a] A. A. Cowley, C. C. Chang, H. D. Holmgren, J. D. Silk, D. L. Hendrie, R. W. Koontz, P. G. Roos, C. Samanta and J. R. Wu, Phys. Rev. Lett. **45** (1980) 1930.

[Cow80b] A. A. Cowley, C. C. Chang and H. D. Holmgren, Phys. Rev. C **22** (1980) 2633.

[Cow88] A. A. Cowley, J. V. Pilcher, J. J. Lawrie and D. M. Whittal, Phys. Lett. B **201** (1988) 196.

[Cow89] A. A. Cowley, J. V. Pilcher, J. J. Lawrie and D. M. Whittal, Phys. Rev. C **40(4)** (1989) xxx (to be published).

[Dar72a] R. Darves-Blanc, Nguyen Van Sen, J. Arvieux, J. C. Gondrand, A. Fiore and G. Perrin, Nucl. Phys. **A191** (1972) 353.

[Dar72b] R. Darves-Blanc, Nguyen Van Sen, J. Arvieux, A. Fiore, J.C. Gondrand and G. Perrin, Lett. Nuova Cimento **4** (1972) 16.

[Dar88] S. E. Darden, O. Karban, C. Blyth, J. B. A. England, J. M. Nelson and S. Roman, Nucl. Phys. **A486** (1988) 285.

[Def69] Taber de Forest, Jr., Nucl. Phys. **A132** (1969) 305.

[Den88] J. W. A. den Herder, H. P. Blok, E. Jans, P. H. M. Keizer, L. Lapikás, E. N. M. Quint, G. van der Steenhoven and P. K. A. de Witt Huberts, Nucl. Phys. **A490** (1988) 507.

[Det71] J. L. Detch, Jr., R. L. Hutson, Nelson Jarmie and J. H. Jett, Phys. Rev. C **4** (1971) 52.

[Dev79] D. W. Devins, D. L. Friesel, W. P. Jones, A. C. Attard, I. D. Svalbe, V. C. Officer, R. S. Henderson, B. M. Spicer and G. G. Shute, Aust. J. Phys. **32** (1979) 323.

[Don70] T. W. Donnelly, Nucl. Phys. **A150** (1970) 393.

[Fes80] Herman Feshbach, Arthur Kerman and Steven Koonin, Ann. Phys. (N.Y.) **125** (1980) 429.

[Fia73] S. Fiarman and W. E. Meyerhof, Nucl. Phys. **A206** (1973) 1.

[För88] S. V. Förtsch, A. A. Cowley, J. V. Pilcher, D. M. Whittal, J. J. Lawrie, J. C. van Staden and E. Friedland, Nucl. Phys. **A485** (1988) 258.

[Fra75] R. Frascaria, P. G. Roos, M. Morlet, N. Marty, A. Willis, V. Comparat and N. Fujiwara, Phys. Rev. C **12** (1975) 243.

[Fru84] Salvatore Frullani and Jean Mougey, *Advances in Nuclear Physics, Volume* **14**, eds. J. W. Negele and Erich Vogt, Plenum Press (New York, 1984) p.1.

[Fuk86] K. Fukunaga, S. Kakigi, T. Ohsawa, A. Okihana, T. Sekioka, H. Nakamura-Yokota and S. Tanaka, Nucl. Phys. **A456** (1986) 48.

[Gee89] D. F. Geesaman, R. Gilman, M. C. Green, R. J. Holt, J. P. Schiffer, B. Zeidman, G. Garino, M. Saber, R. E. Segel, E. J. Beise, G. W. Dodson, S. Hoibraten, L. D. Pham, R. P. Redwine, W. W. Sapp, C. F. Williamson, S. A. Wood, N. S. Chant, P. G. Roos, J. D. Silk, M. Deady and X. K. Maruyama, Phys. Rev. Lett. **63** (1989) 734.

[Gol70] N. P. Goldstein, A. Held and D. G. Stairs, Can. J. Phys. **48** (1970) 2629.

[Gre82] J. M. Greben, Phys. Lett. **115B** (1982) 363.

[Gre83] R. E. L. Green, D. H. Boal, R. L. Helmer, K. P. Jackson and R. G. Korteling, Nucl. Phys. **A405** (1983) 463.

[Gri66] J. J. Griffin, Phys. Rev. Lett. **17** (1966) 478.

[Grü83] W. Grüebler, V. König, P. A. Schmelzbach, F. Sperison, B. Jenny, R. E. White, F. Seiler and H. W. Roser, Nucl. Phys. **A398** (1983) 445.

[Gru86] H. Gruppelaar, P. Nagel and P. E. Hodgson, Rivista del Nuova Cimento **9** (1986) 1.

[Gry89] M. Grypeos and K. Ypsilantis, J. Phys. G **15** (1989) 1397.

[Har70] S. A. Harbison, R. J. Griffiths, N. M. Stewart, A. R. Johnston and G. T. A. Squier, Nucl. Phys. **A150** (1970) 570.

[Hor80] Y. Horikawa, F. Lenz and Nimai C. Mukhopadhyay, Phys. Rev. C **22** (1980) 1680.

[Hou71] E. Hourany, T. Yuasa, J. P. Didelez, M. Hage Ali, F. Reide and F. Takeuchi, Nucl. Phys. **A162** (1971) 624.

[Hut71] R. L. Hutson, Nelson Jarmie, J. L. Detch, Jr. and J. H. Jett, Phys. Rev. C **4** (1971) 17.

[Jac65] Daphne F. Jackson and Tore Berggren, Nucl. Phys. **62** (1965) 353.

[Jac66] Gerhard Jacob and Th. A. J. Maris, Rev. Mod. Phys. **38** (1966) 121.

[Jac73] Gerhard Jacob and Th. A. J. Maris, Rev. Mod. Phys. **45** (1973) 6.

[Jac76] Daphne F. Jackson, Nucl. Phys. **A257** (1976) 221.

[Jan82] Joseph F. Janni, At. Data Nucl. Data Tables **27** (1982) 147.

[Kal83] A. M. Kalend, B. D. Anderson, A. R. Baldwin, R. Madey, J. W. Watson, C. C. Chang, H. D. Holmgren, R. W. Koontz, J. R. Wu and H. Machner, Phys. Rev. C **28** (1983) 105.

[Kit80] P. Kitching, C. A. Miller, W. C. Olsen, D. A. Hutcheon, W. J. McDonald and A. W. Stetz, Nucl. Phys. **A340** (1980) 423.

[Kit85] P. Kitching, W. J. McDonald, Th. A. J. Maris and C. A. Z. Vasconcellos, *Advances in Nuclear Physics, Volume* **15**, eds. J. W. Negele and Erich Vogt, Plenum Press (New York, 1985) p.43.

[Kra89] G. J. Kramer, H. P. Blok, J. F. J. van den Brand, H. J. Bulten, R. Ent, E. Jans, J. B. J. M. Lanen, L. Lapikás, H. Nann, E. N. M. Quint, G. van der Steenhoven, P. K. A. de Witt Huberts and G. J. Wagner, Phys. Lett. B **227** (1989) 199.

[Kro70] F. R. Kroll and N. S. Wall, Phys. Rev. C **1** (1970) 138.

[Kud86] Yoshiteru Kudo and Kiro Miyazaki, Phys. Rev. C **34** (1986) 1192.

[Kud88] Yoshiteru Kudo, Noriyo Kanayama and Takashi Wakasugi, Phys. Rev. C **38** (1988) 1126.

[Kud89] Yoshiteru Kudo, Noriyo Kanayama and Takashi Wakasugi, Phys. Rev. C **39** (1989) 1162.

[Lan70] H. Langevin-Joliot, Ph. Narboni, J. P. Didelez, G. Duhamel, L. Marcus and M. Roy-Stephan, Nucl. Phys. **A158** (1970) 309.

[Law89] J. J. Lawrie, private communication.

[Leo87] W. R. Leo, *Techniques for Nuclear and Particle Physics Experiments*, Springer-Verlag (Berlin, 1987) p.189.

[Lim66] K. L. Lim and I. E. McCarthy, Nucl. Phys. **88** (1966) 433.

[Lim73] T. K. Lim, Phys. Lett. **44B** (1973) 341.

[Lom74] E. Lomon and Richard Wilson, Phys. Rev. C **9** (1974) 1329.

[Lyo86] Louis Lyons, *Statistics for nuclear and particle physicists*, Cambridge Univ. Press (Cambridge, 1986) p.3.

[Mac84] H. Machner, D. Protić, G. Riepe, J. P. Didelez, N. Frascaria, E. Gerlic, E. Hourani and M. Morlet, Phys. Lett. **138B** (1984) 39.

[Mac85] H. Machner, Phys. Rep. **127** (1985) 309.

[Mag89] A. Magnon, M. Bernheim, M. K. Brussel, G. P. Capitani, E. de Sanctis, S. Frullani, F. Garibaldi, A. Gerard, H. E. Jackson, J. M. Legoff, C. Marchand, Z. E. Meziani, J. Morgenstern, J. Picard, D. Reffay, S. Turck-Chieze, P. Vernin and A. Zghiche, Phys. Lett. B **222** (1989) 352.

[McC59] Ian E. McCarthy, Nucl. Phys. **11** (1959) 574.

[Mei87] R. J. Meijer, A. van den Brink, E. A. Bakkum, P. Decowski, K. A. Griffioen and R. Kamermans, Nucl. Instrum. & Methods in Phys. Res. **A256** (1987) 521.

[Mig55] A. B. Migdal, Sov. Phys.-JETP, **1** (1955) 2.

[Mil81] C. A. Miller, Nucl. Phys. **A353** (1981) 157c.

[Mor75] J. R. Morales, T. A. Cahill, D. J. Shadoan and H. Willmes, Phys. Rev. C **11** (1975) 1905.

[Mou80] J. Mougey, Nucl. Phys. **A335** (1980) 35.

[Per62] F. Perey and B. Buck, Nucl. Phys. **32** (1962) 353.

[Per69] C. F. Perdrisat, L. W. Swenson, P. C. Gugelot, E. T. Boschitz, W. K. Roberts, J. S. Vincent and J. R. Priest, Phys. Rev. **187** (1969) 1201.

[Pie87] J. Piekarewicz and S. E. Koonin, Phys. Rev. C **36** (1987) 875.

[Pil89a] J. V. Pilcher, Ph.D. thesis, University of Cape Town, 1989.

[Pil89b] J. V. Pilcher, A. A. Cowley, D. M. Whittal and J. J. Lawrie, Phys. Rev. C **40(4)** (1989) xxx (to be published).

[Pod75] B. S. Podmore and H. S. Sherif, *Few Body Problems in Nucl. and Particle Phys.*, edited by R. J. Slobodrian, B. Cujec and K. Ramavataram (Quebec, Aug. 1975) p.517.

[Pug73] H. G. Pugh, P. G. Roos, A. A. Cowley, V. K. C. Cheng and R. Woody, Phys. Lett. **46B** (1973) 192.

[Pun88] V. Punjabi, K. A. Aniol, A. Bracco, C. A. Davis, M. B. Epstein, H. P. Gubler, J. P. Huber, W. P. Lee, D. J. Margaziotis, C. F. Perdrisat, P. R. Poffenberger, H. Postma, H. J. Sebel, A. W. Stetz and W. T. H. van Oers, Phys. Rev. C **38** (1988) 2728.

[Raa87] D. A. Raavé, *The Control and Auxiliary Equipment of the National Accelerator Centre Precision 1.5m Scattering Chamber*,

Master Diploma in Electrical Engineering dissertation, Cape Technikon (1987), unpublished.

[Red70] Edward F. Redish, G. J. Stephenson, Jr. and Gerald M. Lerner, Phys. Rev. C **2** (1970) 1665.

[Rem74] E. A. Remler and R. A. Miller, Ann. Phys. (N.Y.) **82** (1974) 189.

[Roo74] P. G. Roos, Phys. Rev. C **9** (1974) 2437.

[Roo76] P. G. Roos, D. A. Goldberg, N. S. Chant, R. Woody III., and W. Reichart, Nucl. Phys. **A257** (1976) 317.

[Roo77a] P. G. Roos, N. S. Chant, A. A. Cowley, D. A. Goldberg, H. D. Holmgren and R. Woody, III., Phys. Rev. C **15** (1977) 69.

[Roo77b] P. G. Roos, in *Momentum Wave Functions - 1976*, edited by D. W. Devins, AIP Conf. Proc. No. 36 (Am. Institute Phys., New York, 1977), p. 32.

[Roo86] P. G. Roos, private communication.

[Roo87] P. G. Roos, S. Afr. J. Phys. **10** (1987) 80.

[Sam82] C. Samanta, N. S. Chant, P. G. Roos, A. Nadasen and A. A. Cowley, Phys. Rev. C **26** (1982) 1379.

[Sam86] C. Samanta, N. S. Chant, P. G. Roos, A. Nadasen, J. Wesick and A. A. Cowley, Phys. Rev. C **34** (1986) 1610.

[Sch82] P. Schwandt, *Code SNOOPY8*, IUCF Report No. 82-3 (1982), unpublished.

[Sch86] R. Schiavilla, V. R. Pandharipande and R. B. Wiringa, Nucl. Phys. **A449** (1986) 219.

[Seg82] R. E. Segel, T. Chen, L. L. Rutledge, Jr., J. V. Maher, John Wiggins, P. P. Singh and P. T. Debevec, Phys. Rev. C **26** (1982) 2424.

[Seg85] R. E. Segel, S. M. Levenson, P. Zupranski, A. A. Hassan, S. Mukhopadhyay and J. V. Maher, Phys. Rev. C **32** (1985) 721.

[Sil59] Edward A. Silverstein, Nucl. Instrum. & Methods, **4** (1959) 53.

[Shi82] H. Shimizu, K. Imai, N. Tamura, K. Nisimura, K. Hatanaka, T. Saito, Y. Koike and Y. Taniguchi, Nucl. Phys. **A382** (1982) 242.

[Smi89] R. D. Smith and M. Bozoian, Phys. Rev. C **39** (1989) 1751.

[Spe81] Josef Speth and Adriaan van der Woude, Rep. Prog. Phys. **44** (1981) 719.

[Tak89] T. Takaki, Phys. Rev. C **39** (1989) 359.

[Tra89] M. Trabandt, W. Scobel, M. Blann, B. A. Pohl, R. C. Byrd, C. C. Foster and R. Bonetti, Phys. Rev. C **39** (1989) 452.

[Tyr66] H. Tyrén, S. Kullander, O. Sundberg, R. Ramachandran, P. Isacsson and T. Berggren, Nucl. Phys. **79** (1966) 321.

[Van82] W. T. H. van Oers, B. T. Murdoch, B. K. S. Koene, D. K. Hasell, R. Abegg, D. J. Margaziotis, M. B. Epstein, G. A. Moss, L. G. Greeniaus, J. M. Greben, J. M. Cameron, J. G. Rogers and A. W. Stetz, Phys. Rev. C **25** (1982) 390.

[Van88] J. F. J. van den Brand, H. P. Blok, R. Ent, E. Jans, G. J. Kramer, J. B. J. M. Lanen, L. Lapikás, E. N. M. Quint, G. van der Steenhoven and P. K. A. de Witt Huberts, Phys. Rev. Lett. **60** (1988) 2006.

[Vot74] L. G. Votta, P. G. Roos, N. S. Chant and R. Woody, III., Phys. Rev. C **10** (1974) 520.

[Wac88] B. Wachter, T. Mertelmeier and H. M. Hofmann, Phys. Lett. B **200** (1988) 246.

[Wal66] N. S. Wall and P. R. Roos, Phys. Rev. **150** (1966) 811.

[Wat52] Kenneth M. Watson, Phys. Rev. **88** (1952) 1163.

[Wel88] H. R. Weller, R. M. Whitton, J. Langenbrunner, Evans Hayward, W. R. Dodge, S. Kuhn and D. R. Tilley, Phys. Lett. B **213** (1988) 413.

[Wes83] J. S. Wesick, Ph. D. thesis, University of Maryland, 1983.

[Wes85] J. S. Wesick, P. G. Roos, N. S. Chant, C. C. Chang, A. Nadasen, L. Rees, N. R. Yoder, A. A. Cowley, S. J. Mills and W. W. Jacobs, Phys. Rev. C **32** (1985) 1474.

[Wol52] Peter A. Wolff, Phys. Rev. **87** (1952) 434.

[Wu79] J. R. Wu, C. C. Chang and H. D. Holmgren, Phys. Rev. C **19** (1979) 698.

[Wu80] J. R. Wu, Phys. Lett. **91B** (1980) 169.

[Yoo89] Sung Hoon Yoo, A. Williams, S. Mordechai, C. Fred Moore, C. L. Morris, S. J. Seestrom-Morris, M. K. Jones, S. M. Sterbenz, D. Dehnhard, D. S. Oakley and A. Fazely, Phys. Rev. Lett. **63** (1989) 738.

[You74] Stephen K. Young and Edward F. Redish, Phys. Rev. C **10** (1974) 498.